Mathematical modelling of the tumour microenvironment: the causes and consequences of tumour acidity

Maymona Al-Husari

Department of Mathematics and Statistics

University of Strathclyde

Glasgow, UK

October 2012

This thesis is submitted to the University of Strathclyde for the degree of Doctor of Philosophy in the Faculty of Science.

This thesis is the result of the author's original research. It has been composed by the author and has not been previously submitted for examination which has led to the award of a degree.

Signed:
Date:

Acknowledgements

I would like to thank my supervisor, Dr Steven Webb, for his advice and guidance throughout the period of my research. I am grateful to EPSRC for providing the financial assistance for this work. I am also thankful to all my friends and family for their inspiration and support.

Abstract

Extracellular acidity and high levels of lactate are commonly observed in solid tumours. Some tumours also exhibit a reversed cellular pH gradient with an intracellular pH that is higher than the extracellular. This has been shown to play a crucial part in not only the invasive and metastatic cascade of tumours, but also on their response to therapies. In this thesis, we present four different mathematical models that examine the possible causes of tumour acidity and its effect on cell metabolism and tumour invasion.

In the second chapter, we derive an ordinary differential equation model that explicitly focus on the interplay between H^+-ions and lactate. We subject the model to qualitative and quantitative analysis and, in particular, we study the effect in the variations of key parameter estimates on the emergence of a reversed transmembrane pH gradient within the tumour. The model predicts that a reversed pH gradient is attainable under aerobic conditions when sources of H^+-ions other than those from glycolysis are decreased and the lactate/H^+ cell membrane transporter (MCT) activity is increased—but we find the intra- and extracellular pH values in this case to be too alkaline to be physiological. Under anaerobic conditions, we find that decreasing the sources of H^+-ions other than those from glycolysis and also the glycolytic rate gives rise to a reversed cellular pH gradient, but again for intra- and extracellular pH values that are far from realistic biologically.

In the third chapter, we present an extension to the first model by including the spatial diffusion of hydrogen ions and lactate. This spatial extension also predicts

a reversed transmembrane pH gradient but this time for more realistic intra- and extracellular pH values. We find that low levels of blood lactate can give rise to a reversed pH gradient throughout the spatial domain independent of the levels of tissue lactate. Likewise, we have found the existence of a negative pH gradient to be strongly dependent on the combined activity of a lactate/H^+ cell membrane transporter and other sources of H^+-ion.

In the fourth chapter, we study the role of oxygen and pH on early tumour growth using a hybrid cellular automaton model. We examine whether the levels of oxygen, intra- or extracellular pH are the dominating metabolites driving tumour growth and phenotypic transformations. This model predicts that when tumour cells are strongly sensitive to changes in the intracellular pH, a low activity of the Na^+/H^+ cell membrane transporter (NHE) or a high rate of anaerobic glycolysis can give rise to a "fingering" morphology. Furthermore, we show that as the activity of the MCT transporter increases, all the tumour cells within the spheroid can exhibit a reversed transmembrane pH gradient.

In the fifth chapter, we examine the effect of extracellular acidity on tumour invasion focusing, in particular, on cellular adhesion, matrix-degrading enzyme activity and cellular proliferation. Our numerical simulations using a cellular Potts model show that, under acidic extracellular pH, cell-ECM adhesion strength has a comparable effect on tumour invasiveness as the rate at which the ECM is degraded by proteolytic enzymes. We also show that tumour cells cultured under physiological pH tend to be larger and develop a "diffuse" morphology compared to those cultured at acidic pH which display protruding "fingers" at the advancing tumour front.

Contents

List of abbreviations

CA	Cellular Automata
ECM	Extracellular Matrix
H^+	Hydrogen ions
NHE	Na^+/H^+ exchanger
MCT	Monocarboxylate Transporter (also known as the lactate/H^+ symporter)
MMP	Matrix Metalloproteinase
pH	Potential of hydrogen ions, defined as -log[H^+]
pH_i	pH inside the cell
pH_e	pH outside the cell

List of Figures

List of Tables

Chapter 1

Introduction

According to the International Agency for Research on Cancer (IARC), there were 12.4 million new cancer cases and 7.6 million cancer deaths in 2008 worldwide [25]. By 2030, the number of cancer cases and deaths worldwide are expected to more than double [25]. It has been estimated that more than 33% of the UK population will develop cancer during their lifetime [1]. There has been, however, a remarkable improvement in the treatment and diagnosis of cancer which has contributed to a steady decline in the death rates in the last three decades. Still, the major cause of treatment failure in cancer patients is the spread of the primary cancer to different regions of the body and the destructive effect it has on the normal tissue [97].

Much evidence indicates that a tumour manifests following multiple alterations in the genetic make up of several cells [157]. Also, many lines of evidence now suggest that the tumour microenvironment plays a major role in tumour development and can either be favourable or detrimental to tumour growth [194]. The tumour microenvironment is considerably different from that of normal tissue [160]. As more mutated cells accumulate, the normal organisation of the tissue gradually becomes disrupted. Vascular supply to tumours is often poorly formed and chaotic with the result that tumours may contain regions of poor nutritional supply and hypoxia (low oxygen) [42]. Tumour cells often adapt to hypoxia by switching to a less-efficient pathway of energy production (i.e. anaerobic glycolysis) and as a

result produce excess hydrogen ions and lactate [73]. To ensure cell viability, these ions are extruded extracellularly (i.e. outside the cell) via several cell membrane transporters. With a compromised vasculature and an up-regulated glycolysis, this is thought to create an acidic extracellular environment [236].

Acidic extracellular environment and high lactate levels have been shown to play a crucial part in the invasive and metastatic cascade of some tumours. Several enzymes which are known to facilitate the degradation of the structural barrier (known as the extracellular matrix) between the tumour and the vasculature are activated and secreted in large quantities under acidic extracellular conditions [116]. Moreover, extracellular acidity can trigger cells to strongly adhere to the extracellular matrix [126, 166] and weakly adhere to each other [46, 47, 48], thus further facilitating metastasis. Not only does acidosis play a role in the macroscopic scale of tumour progression but it has also been shown to be involved in early tumorigenesis. For example, exposure to hypoxia and low pH has been implicated in increased DNA mutations and a subsequent lack of DNA repair in mammalian cells [194, 257, 258]. Furthermore, lactate has been shown to stimulate several signalling pathways involved in tumour progression [133, 134, 237]. In addition, hypoxia and acidity have been shown to render cells resistant to cancer treatment such as radiotherapy [185, 228] and chemotherapy [251].

Mathematical modelling at various temporal and spatial scales are increasingly being used to understand the intricate phases of cancer development. The work contained in this thesis will focus on better understanding what causes extracellular acidity and the role it plays in the invasion process. I now outline our approach in this thesis.

1.1 Thesis outline

The remainder of this chapter is dedicated to an overview of the complex topic of cancer and the microenvironment. We begin by introducing some of the key properties of the disease from a biological perspective. In particular, we discuss the pH regulatory mechanisms involved in maintaining a viable intracellular pH (i.e. pH inside the cell) and the cellular changes that are thought to cause an acidic extracellular pH (i.e. pH outside the cell). Unlike normal tissue, some solid tumours are known to have an intracellular pH that is higher than the extracellular, a phenomenon referred to as "a negative transmembrane pH gradient" or "a reversed transmembrane pH gradient" [24, 248]. Also presented are the consequences of this aberrant pH gradient on both the tumour and normal tissue. We then move on to discuss relevant mathematical models on tumour acidity.

In Chapter 2, we develop an ordinary differential equation model that explicitly focuses on the interplay between H^+-ions and lactate. We subject the model to qualitative and quantitative analysis and, in particular, we study the effect from variations of key parameter estimates on the emergence of a reversed transmembrane pH gradient within the tumour.

In Chapter 3, we present an extension to the model developed in Chapter 2 to include the diffusion of hydrogen ions and lactate across the tissue. Apart from increasing the biological realism of the model by incorporating spatial effects, this extension allows us to examine whether extracellular lactate levels spatially correlate with the extracellular pH and whether the distribution of the various transporters which regulate the intracellular pH across the tumour tissue has an effect on the cellular pH gradient. We also investigate the effect of intercellular gap junctions on the cellular pH gradient and the spatial distribution of extracellular lactate and hydrogen-ions.

In Chapter 4, we study the role of oxygen and pH on early tumour growth using a hybrid cellular automaton model. We examine whether the levels of oxygen,

intracellular or extracellular pH are the dominating metabolites driving tumour growth and invasion. The degree of invasiveness is measured by the appearance of a "fingered" morphology. In particular, we study the effect of variations in some of the key parameters in the model, such as those associated with maintaining a viable intracellular pH, in the evolution of the tumour spheroid and the emergence of a reversed transmembrane pH gradient.

In Chapter 5, we study the effect of cellular adhesion, matrix-degrading enzyme activity and cellular proliferation on tumour invasion. We do this by using a cellular Potts model which allows each biological cell to occupy more than one lattice point and hence allows them to change shape. By way of model validation, we begin the chapter by simulating and reproducing the cellular Potts model of cancer invasion described by Turner *et al.* [233]. In this model the pH conditions are assumed to be neutral (i.e. pH_e 7.4). We use experimental evidence to find new parameter values under acidic extracellular pH and investigate the effect of acidity on cellular adhesion, matrix-degrading enzyme activity and cellular proliferation.

We conclude the thesis in Chapter 6 by discussing possible future extensions and the potential implication of our work.

1.2 Biological background on cancer

There are over 50 trillion cells in the adult human body performing numerous operations [125]. In order for those cells to continue functioning normally, they must pass multiple checkpoints [16]. If a cell is damaged and cannot be repaired, it dies [16]. This programmed cell death, known as apoptosis, is crucial to all cells in the body, acting to eradicate cells that are a threat to the organism. Each day, approximately 50 to 70 billion cells undergo apoptosis in the average human adult [192]. This process is evaded when multiple irreversible alterations to the genetic make-up of cells occur, known as DNA mutations [101]. This allows mutated cells to grow uncontrollably and accumulate in a lump of cells called a

"tumour" [178].

Tumours are categorised as benign or malignant depending on their ability to invade the surrounding tissue and spread to distant parts of the body. Cancer is the Latin word for "crab", most likely used to reflect the finger-like projections from a tumour mass [178]. The oldest description of cancer was discovered in an ancient Egyptian textbook between 3000–1500 BC, with the earliest evidence of the disease found in fossilised bone tumours in human mummies [153]. Malignant, or cancerous tumours, have the ability to invade neighbouring tissues and establish new colonies in the body and is very difficult to treat effectively [16]. Benign tumours, however, are usually harmless unless they grow large and start exerting pressure on vital organs. But even then, they are often still treated efficiently by conventional therapies such as chemotherapy, surgery, or radiotherapy.

1.2.1 Angiogenesis

As tumour cells proliferate rapidly, the tumour becomes large and it becomes impossible for nutrients to diffuse into the centre and waste to be removed. In 1971, Folkman [64] suggested that in order for tumours to flourish and grow beyond 1–2 mm in diameter, tumours produce signalling molecules that stimulate the growth of nearby blood vessels. This complex process of vessel formation is known as "angiogenesis" and is triggered by various signals, including low pO_2, low pH and low glucose [38]. Such low conditions facilitate the secretion of several tumour angiogenic growth factors (TAFs) such as the Vascular Endothelial Growth Factor (VEGF) and Fibroblast Growth Factor (FGF) by the tumour cells themselves or the neighbouring normal cells [38]. The expression and secretion of TAFs are thought to be triggered under hypoxic conditions, mainly by Hypoxia Inducible Factors such as HIF-1α which are known to also activate several other signalling pathways [45]. When TAFs are released, endothelial cells (which line the blood vessels) secrete matrix-degrading enzymes (known as proteolytic enzymes). These enzymes degrade the basement membrane (that supports the blood vessel) and

the extracellular matrix, allowing endothelial cells to migrate away from the blood vessel and into the tumour. Endothelial cells then divide, align and form new blood vessels which then link together to form looped structures called anastomoses [38].

These newly formed blood vessels are anything but normal. They are "leaky", are not rigid enough to withstand significant tissue stress, are badly formed or have absent basement membranes or endothelial lining [187, 236]. As a result, most tumours can contain both highly perfused regions and others with compromised perfusion. This can then give rise to variable levels of metabolites, such as oxygen, pH, lactate and glucose, within the same tumour.

1.2.2 Invasion and metastasis

The basement membrane that separates the tumour from the vasculature must be degraded if a tumour cell is to leave the primary mass and gain access to the blood vessel. Once inside the blood stream, tumour cells are susceptible to clearance by the body's own immune system and only the very aggressive tumour cells survive [56]. To establish themselves in another location of the body, tumour cells must leave the blood stream. All these processes are believed to involve a complex interaction between a variety of proteolytic enzymes, growth factors, cell-cell and cell-matrix adhesion components [97].

Proteolytic enzymes

Apart from their well-known role in facilitating tumour cell invasion [59], proteolytic enzymes are also implicated in many other pathological conditions such as rheumatoid arthritis, pancreatitis, diabetes mellitus and muscular dystrophy [154]. There are four main classes of proteolytic enzymes: the serine proteases which include the plasminogen activators, the cysteine proteases (which are mostly lysosomal cathepsins), the aspartic proteases and the metalloproteinase (MMP) [253]. Table 1.1 summarises the role of each these proteases in degrading components

of the extracellular matrix including fibronectin, laminin, collagen and elastin. These enzymes are generally released in an inactive form which require activation by other proteases [59]. For example, cathepsin D is known to mediate the activation of procathepsin B [235]. Once activated, cathepsin B can then act as an activator of other proteases. That is, active cathepsin B can activate pro-uPA, which is secreted as an inactive proenzyme [205]. Then, active uPA can convert plasminogen into plasmin. Cathepsin B and plasmin are also capable of degrading several components of the ECM and can also activate pro-MMPs [59]. As well as having activators, proteolytic enzyme also have tissue inhibitors that regulate their activity. It is thought that the imbalance that exists between the rate of activation and inhibition of proteolytic enzyme is of major significance in cancer development [211].

The most important and extensively studied proteolytic enzymes involved in matrix degradation are the MMPs and lysosomal cathepsins [59]. There are 23 identified human MMP genes which are known to act extracellularly and digest both matrix and non-matrix proteins [156]. The expression of MMPs is transcriptionally maintained by a number of cell activators, including cell-cell adhesions, cell-ECM adhesions, growth factors, inflammatory cytokines and hormones [156]. The activity of MMPs are also maintained via inhibition by endogenous inhibitors and tissue inhibitors of metalloproteinases (TIMPs for short) [211]. Increased production of MMPs has been linked to the invasive and metastatic behaviour in some tumours [59, 116, 154, 256]. On the other hand, decreased expression of tissue inhibitors of MMP-2 (TIMPs-2) has been found in gastric carcinomas [155] and esophageal and gastric adenocarcinomas [95]

The exact mechanism by which MMPs facilitate cellular invasion is not clear [54]. However, the overexpression of MMP-3 in mammary epithelial cells has been shown to lead to activation and upregulation of other MMPs and the loss of cell-cell contacts, partly due to the degradation of E-cadherin [154]. On the other hand, inhibition of MMP-12 has been shown to give rise to reduced macrophage inva-

sion through matrigel both *in vitro* and *in vivo* [209]. Based on these studies a large number of MMP inhibitors have been designed and a few have been clinically tested in patients with cancer or arthritis. Unfortunately, these have shown little efficacy [14]. The failure of these clinical trials may partly be due to the absence of selective inhibitors [14].

The activity of MMPs is strongly pH-dependent, with an optimal activity within the physiological pH range (pH 7.2–7.5) [54]. However, an *in vitro* study by Martinez-Zaguilan *et al.* [142] shows a considerable rise in the relative amount of active MMP in human melanoma cells when exposed to acidic extracellular medium [142]. A more recent study by Giusti *et al.* [88] also shows that MMP-2 and MMP-9 activities increase in tumour-shed vesicles after exposure to acidic extracellular pH. Moreover, a study by Rofstad *et al.* [195] found that acidic extracellular pH promotes experimental pulmonary metastasis in human melanoma cells through an acidity-induced upregulation of the proteolytic enzymes MMP-2, MMP-9, cathepsin B, and cathepsin L; and acidity-induced up-regulation of proangiogenic factors VEGF-A and IL-8. For a full review of the role of proteolytic enzymes, see [59].

Table 1.1: Proteases that are involved in degrading the ECM components. Table courtesy of [211].

Protease family	**Protease**	**Protease function**
Aspartyl	Cathepsin D	Degradation of ECM components
		Conversion of cysteine procathepsins into cathepsins
Cysteine	Cathepsins B, L, H, K	Degradation of ECM components
		Conversion of pro-MMPs into MMPs
Serine	Plasmin	Degradation of ECM components
		Activation of uPA
		Conversion of inactive elastase into elastase
	uPA	Conversion of plasminogen into plasmin
	tPA	Conversion of plasminogen into plasmin
Neutrophil serine	Elastase	Degradation of ECM components
		Cathepsin G
MMPs		Degradation of collagens and other ECM proteins
		Activation of another pro-MMP's into MMPs
	Collagenases [MMP-1, 8, 13]	Degradation of collagens I, II, III, VII, X and gelatins
	Stromelysins [MMP-3, 10]	Degradation of proteoglycans, laminin, gelatins, collagens III, IV, V, IX, fibronectin, entactin, SPARC, collagenase-1
	Gelatinases [MMP-2, 9]	Degradation of gelatins, collagens: IV, V, VII, X, fibronectin, elastin, procollagenase-3
	Membrane-type [MMP-14–17,24,25]	Degradation of collagen I, II, III, gelatins, aggrecan,fibronectin, laminin, vitronectin, MMP-2,13, tenascin, nidogen
	Others [MMP-7,11,12,19,20,23]	Degradation of proteoglycans, laminin, fibronectin, gelatins, collagens IV, elastin, entactin, tenascin

Cell adhesion

There is accumulating evidence suggesting that alterations in the adhesive properties of tumour cells correlate with tumour progression [9, 17, 41, 217]. Cell adhesion has shown to be important in cell growth, cell migration, apoptosis, im-

mune responses and cell differentiation in vertebrate cells [174]. There are over 50 identified cell adhesion molecules (CAMs) that can be divided into four major superfamilies: the immunoglobulins (Ig), cadherins, selectins, and integrins [174]. All members of the CAM superfamilies can mediate cell-cell binding except integrins which can only mediate cell-ECM binding [191]. CAMs bind to either the same protein, known as homophilic adhesion, or to a different protein, called heterophilic adhesion [174].

Cadherin genes are considered as tumour suppressor genes [241] and a loss of their expression or activity has been correlated with increased tumour cell migration [20]. The expression of the most abundant adheren adhesion molecule in the epithelia is E-cadherin, and this is downregulated in most epithelial cancers [20]. Several studies have shown that restoring functional E-cadherin adhesion hinders the invasive phenotype of many different cancers [241]. Furthermore, the expression of cadherin in tumour cells can also be used to identify the histologic nature of tumours and can be used as a differential diagnostic marker between tumours of similar phenotype but different histogenesis [172, 173]. Moreover, cadherins bind with intracellular proteins known as catenins, which link the cadherin molecule to the actin micro-filaments and mediate signal transduction mechanisms that regulate cell growth and differentiation [204]. Data suggests that several potential signalling pathways could be modulated by E-cadherin complex [40]. For example, E-cadherin can increase the expression of the epidermal growth factor receptor and induce its ligand independent activation [121].

Integrins, on the other hand, mediate the adhesion of cells to the ECM and immunoglobulin superfamily molecules [174]. Integrin expression and activity have important roles in the different steps of tumour progression, including initiation [100, 108]. High expression of integrins is shown to be correlated with the progression of breast cancer [191], hepatocellular carcinoma [82], murine melanoma cell [126] and prostate cancer [261]. Recent studies have also shown that integrins mediate cell signalling molecules that are stimulated by growth factors and onco-

genes particularly during tumour initiation [191].

Extracellular acidity has been shown to trigger cells to strongly adhere to the extracellular matrix [126, 166] and weakly adhere to each other [46, 47, 48], thus further facilitating metastasis [17]. Recent studies have shown that culturing human liver hepatocellular carcinoma at pH 6.6 enhances their migratory potential with activation of tyrosine phosphorylation of β-catenin and E-cadherin [46, 47, 48]. Several studies have also shown that the cell-ECM adhesions are strongest at acidic extracellular pH [166, 218]. In particular, a study by Paradise *et al.* [166] show that the extracellular pH of human melanoma cells not only modulates cell adhesion molecules but can also affect their morphology and migratory potential. That is, cells were found to reach their maximum motility at $\mathrm{pH}_e \sim 7.0$ but hardly migrate at pH_e 6.6 or 7.5. Long-time exposure to pH 6.5 is shown to cause cells to exhibit an elongated morphology. In addition, migration and morphology was found to be correlated with the strength of cell-matrix interactions [166]. Also, adhesion was found to be the strongest at extracellular pH 6.6 [166].

1.2.3 Cell metabolism

Glycolysis is a complex process whereby one mole of glucose is metabolised to produce adenosine triphosphate (ATP) molecules. In addition to being a major source of energy in the cell [16], ATP has other essential roles: it is required for the synthesis of DNA (replication) and RNA (protein synthesis); it regulates certain biochemical pathways; it is essential for the active transport of some ions across the cell membrane (e.g. the Vacuolar H^+ ATPase, the Na^+/K^+ ATPase and the Ca^{2+} ATPase) [16].

Under plentiful supply of oxygen, cells generally convert one molecule of glucose to carbon dioxide and 38 ATP molecules. This can be written in a simplified form as:

$$\mathrm{Glucose} + 6\mathrm{O}_2 \rightarrow 6\mathrm{CO}_2 + 38\mathrm{ATP}. \tag{1.1}$$

In the absence of oxygen, glucose is converted into lactic acid with the production of only two ATP molecules. This is represented as:

$$\text{Glucose} \rightarrow 2\text{lactic acid} + 2\text{ATP}, \tag{1.2}$$

where lactic acid quickly dissociates to form lactate and H^+ ions.

During aerobic metabolism, about eight H^+-ions are produced for every oxygen molecule used. However, the intracellular and extracellular pH still remains nearly constant. This is because there is an intricate balance between the rate at which H^+-ions are produced and removed during ATP resynthesis and reoxidation of reduced coenzymes [105]. Anaerobic metabolism (glycolysis), however, yields a net of two H^+-ions per glucose molecule consumed.

Warburg's Nobel prize-winning work in the 1920s showed that, in contrast to normal cells, tumour cells exhibit an altered metabolism marked by an increased glucose uptake and raised glycolysis [247]. In fact, this feature is clinically exploited in the detection of tumours using fluorodeoxyglucose Positron Emission Tomography (FDG-PET) imaging in clinical radiology [13, 120, 128]. Such imaging has also demonstrated an association between tumour aggressiveness and the rate of glucose consumption [73, 122]. Warburg's work also showed that even in the presence of plentiful supply of oxygen, tumour cells still undergo anaerobic glycolysis to yield only 2 ATP molecules in total [247]. This is 19 times less efficient than the aerobic metabolism and the vastly growing tumour then strives to maintain the production of ATP by up-regulating their glycolytic pathway. As a result, more lactic acid is produced and the tumour can become very acidic. In fact, tumours were initially thought to have an acidic intracellular pH, but this was then found to reflect primarily the extracellular pH because those measurements were made using micro-electrodes which are too large to insert in most cells [260]. The invention of non-invasive measurements of intracellular pH (pH_i) by magnetic resonance spectroscopy (MRS) has shown that tumour pH_i can actually be alkaline [93].

The cause of extracellular acidity in tumours is still not entirely known [220]. Lactic acid is not the only source of extracellular acidity in tumours. Experiments showed that glycolysis-deficient Chinese hamster lung fibroblasts, when transfected into mice, produce an acidic extracellular pH around 6.7 despite an insignificant production of lactic acid [159]. These cells, however, were found not to be able to acidify their extracellular space *in vitro*. Furthermore, a subsequent study showed that Chinese hamster ovary cells which are deficient in lactate dehydrogenase (LDH, which catalyses the breakdown of glucose to lactate) consume negligible amounts of glucose and produce insignificant levels of lactic acid [254]. Nevertheless, the extracellular environment became acidic when these cells were transplanted into mice but not *in vitro* [254]. These experiments clearly show that there is a discrepancy between the levels of lactate and extracellular pH in some tumours. An alternative candidate for tumour acidosis has shown to be carbon dioxide [103, 159, 254].

1.2.4 Mechanisms of intracellular pH regulation

The metabolically produced hydrogen ions must be removed from the cell interior to ensure a physiological pH_i and cell viability. This is because many cellular processes such as those associated with metabolism [196], the cell cycle [63, 109] and cell proliferation [22, 135] are all pH sensitive. Furthermore, most mammalian cells in tissue culture have been shown not to be able to proliferate at an extracellular pH less than 6.6 [22]. Cells, therefore, have evolved several short and long term mechanisms to maintain their pH_i within the normal physiological range (pH 7.2–7.4). Short term homoeostasis involves a rapid reversible defence mechanism that immediately minimises changes in the intracellular pH [22]. This involves cellular buffering which can be divided into three types: physicochemical buffering, H^+-ion consuming metabolic reactions and intracellular organellar sequestration or release of H^+-ions [202].

The most essential and abundant physicochemical intracellular buffer is phos-

phoric acid (H_3PO_4) which has a pKa close to the normal intracellular pH, i.e. 7.2 (pKa is defined as the negative logarithm of the acid dissociation constant, Ka) [23]. Amino acids, such as lysine, arginine, and histidine, aspartate and glutamate, are also important physicochemical buffers [23]. Normal cellular metabolism also produces buffering molecules, including carbon dioxide, acetic, lactic and citric acids [202]. The extracellular pH is also maintained through the intricate interactions of plasma carbon dioxide partial pressure (pCO_2) and bicarbonate ions (HCO_3^-) [202]. This is facilitated by carbonic anhydrase enzymes (CA), some of which are known to be over-expressed in malignant tumours and are associated with poor prognosis [225]. Organellar buffering, on the other hand, is the sequestration of H^+-ions into intracellular vesicles [23]. There is also accumulating evidence suggesting that such vesicles, which contain matrix-degrading enzymes, tend to relocate to the surface of the cell to aid invasion [90, 154, 232].

As mentioned earlier, cellular buffering is a short term immediate response employed before long term pH regulating mechanisms are activated. Long-term mechanisms consist of transport proteins that are based either at the cellular membrane or at the vacuolar membrane inside the cell. They can be divided into two broad categories: those that do not require energy in the form of ATP to drive the transport, such as the Na^+/H^+ antiporter, the lactate/H^+ symporter, the Na^+-dependant $HCO_3{}^-/Cl^-$ exchanger, Na^+-independent $HCO_3{}^-/Cl^-$ exchanger; and those that require ATP to facilitate their diffusion, such as the plasma membrane and vacuolar type H^+ ATPase pump [23]. Some of these transporters are illustrated schematically in Figure 1.1.

The universal membrane protein, Na^+/H^+ exchanger (NHE for short) exports one H^+ ion outside the cell in return of one Na^+ ion [12]. This antiporter is found in most cell types [22] and plays an essential role in the regulation of cytoplasmic pH, and a change in its activity has been shown to have a drastic effect on cell metabolism and viability [12]. It is also shown to be implicated in mitogenesis and cell volume regulation [226]. The Na^+/H^+ antiporter is freely reversible depending

on both the Na^+ and H^+ gradients. However, most mammalian cells maintain an inward Na^+ gradient which stimulates H^+ ion efflux. This process is tightly mediated by pH and the antiporter's activity changes by more than three orders of magnitude between pH 7 and 8 (recall that $pH = -\log[H^+]$), and is totally down-regulated below pH 6.5 [12]. Moreover, a study by Busco *et al.* [35] finds the NHE expression and activity to be essential for invadopodia-mediated ECM degradation. An upregulated NHE activity is also important for the invasiveness of cervical cancer cell [49]. The NHE also is shown to play a part in the migration of human melanoma cells [218] and fibroblasts [57].

Amongst the many transmembrane ion exchangers is the lactate/H^+ symporter (also known as the Monocarboxylate Transporter or MCT for short) [246]. This symporter works by transporting lactate and hydrogen ions together in the same direction, depending on the gradient of each ion. This process is freely reversible with equilibrium being attained when $[\text{lactate}_i]/[\text{lactate}_e]=[H^+_e]/[H^+_i]$. There is growing evidence suggesting that elevated tissue lactate levels are associated with a high risk of metastasis [207, 246] and a reduced response to radiotherapy [185]. Moreover, Cardone *et al.* [37] suggest that the lactate/H^+ symporter and the Na^+/H^+ antiporter cause tumour acidity which in turn stimulates metastasis. Also, MCT expression has been shown to be significantly increased in cervical carcinomas [175] and colorectal carcinomas [176]. In particular, MCT1 was directly related to the presence of vascular invasion in cervical cancers [175].

We will focus in this thesis on the role of the NHEs and MCTs in tumour pH regulation, but will briefly mention now some alternative pH-regulatory mechanisms expressed in mammalian cells. Another membrane transporter which is shown to be present in several cell lines, but not all, is the Na^+-driven HCO_3^-/Cl^- exchanger, which helps to raise the intracellular pH upon intracellular acidification [22]. This transporter works by extruding Cl^- ions extracellularly and importing $HCO_3{}^-$ into the cell which acts as a buffer for the intracellular H^+. Similar to the Na^+/H^+ exchanger, the activity of the Na^+-dependent $HCO_3{}^-/Cl^-$ exchanger

decreases as the normal resting value of pH_i is approached. At higher levels of pH_i, the Na^+-dependant HCO_3^-/Cl^- exchanger is more active than the Na^+/H^+ antiporter. Since the pH_e within solid tumours is usually in the range 6.5-7.0 and the fact that the activity of Na^+-dependant HCO_3^-/Cl^- exchanger is reduced at pH_e lower than 7.0 compared to Na^+/H^+ antiporter suggests that the latter transporter plays a major role in regulating intracellular pH in such regions.

Hydrogen ions can also be packaged into vesicles by vacuolar H^+ ATPase or they can be extruded across the cellular membrane by a similar membrane-type H^+ ATPase. The vacuolar ATPase transports H^+-ions from the cytosol into lysosomes, thus acidifying lysosomes, and generating a low lysosomal pH that is necessary for the optimum activity of lysosomal hydrolytic enzymes such as cathepsin proteases [90]. Tumour cells have been reported to have a high expression of V-type H^+ ATPase [186].

So far we have concentrated on mechanisms that regulate pH_i in response to an acid load. Cells are rarely faced with the problem of alkaline loading under physiological conditions. Nevertheless, the cellular ion gradient is such that the Na^+-independent HCO_3^-/Cl^- exchanger will take Cl^- into the cell and the HCO_3^- out and thus bring the intracellular pH back to normal levels. However, this exchanger is found to be inhibited in most cell lines at low pH_i [24].

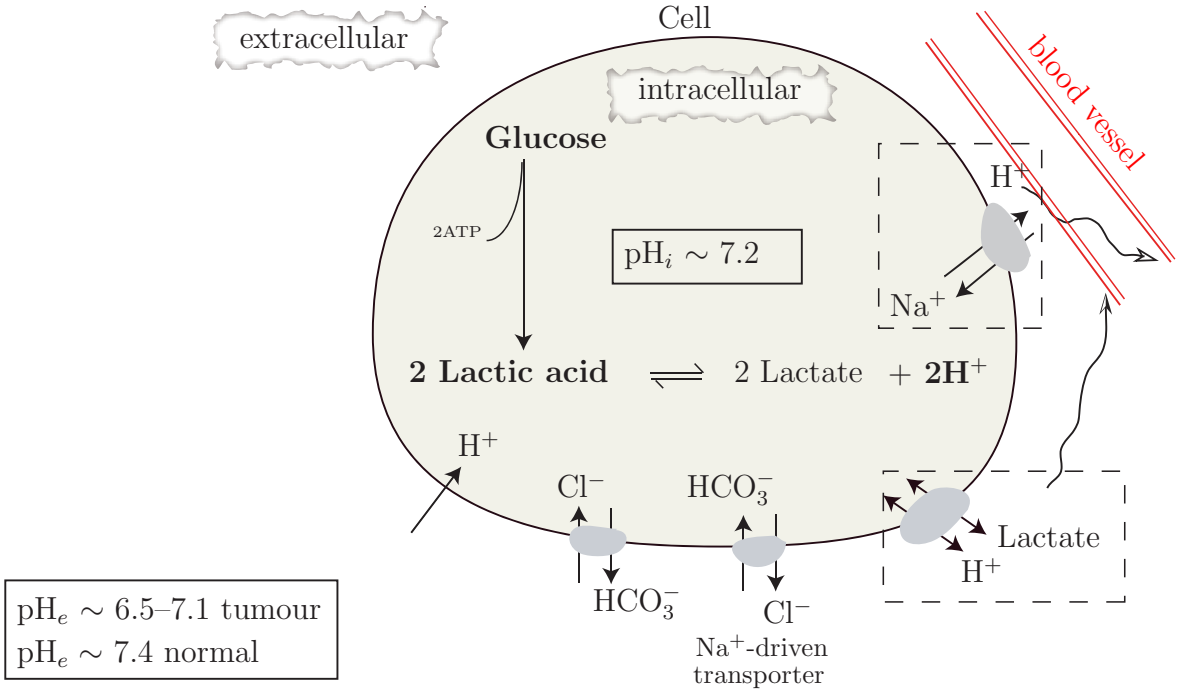

Figure 1.1: Some of the long-term mechanisms which are known to maintain the intracellular pH in mammalian cells at physiological levels. When H^+-ions are produced from glycolysis, they may be removed by: the lactate/H^+ exchanger which transports lactate and H^+-ions in or out of the cell depending on their gradient; the Na^+/H^+ exchanger which takes in Na^+-ions in return of H^+-ions; or they may be buffered by HCO_3^- which enters the cells via the Na^+-driven HCO_3^-/Cl^- exchanger. When pH_i becomes alkaline, HCO_3^- may be removed via the Na^+-independent exchanger. In this thesis, we focus on the activity of the two membrane transporters highlighted by a dashed box.

1.2.5 Effect of tumour pH on treatment efficacy

Traditional anti-cancer treatments include: chemotherapy (the use of drugs to kill tumour cells), radiotherapy (the use of radiation to kill tumour cells) and hyperthermia (the use of heat to kill tumour cells), or a combination of the three [151]. Unlike bacterial infections, which can be eradicated using antibiotics, cancer is a

collection of more than 100 diseases that varies in complexity from one patient to the next. Also, it has proved difficult for an anti-cancer treatment to totally exert toxic effects against the tumour without damaging normal tissue [30]. Developing new anti-cancer therapies often involves pinpointing the differences between normal and malignant growth and targeting the abnormalities. Hypoxia and acidity have recently emerged as a key targeting abnormality, and are currently being exploited for the treatment of cancer [81, 110, 186, 216, 226].

Chemotherapeutic drugs enter the tumour cell either via passive diffusion or active transport, and once inside the cell they are subjected to various intracellular metabolisms [151]. Since cellular membranes are only permeable to "uncharged" molecules [16], it is important for a drug to remain in the "uncharged" form before crossing the membrane. The "charged" form of a drug is not membrane permeable and will accumulate in the extracellular space, therefore exerting little or no cytotoxic effects [151]. Therefore, the transport of a drug by passive diffusion is enhanced at extracellular pH values that leave the drug in the "uncharged" form in the extracellular space [186]. There are many different types of anti-cancer drugs, amongst them are the weak acids and weak bases which are known to be sensitive to cellular pH gradients [251]. The pH difference between normal and tumour tissues, and particularly the cellular pH gradient difference in the tumour itself may provide selective treatment for tumours [226]. For example, the pH gradient has been shown to alter the intracellular-extracellular distribution of weak acids or bases agents [186, 231].

There is now ample evidence suggesting that low pH_e plays an essential role in rendering cells sensitive to hyperthermia [36, 65, 80]. The studies by [65, 80] suggest that the extent of tumour heat sensitivity is greater at low pH_e (pH in the range of 6.5–7.0 that is often found in solid tumours) and at lower temperatures. There are other studies which suggest that tumour response to hyperthermia depends on the intracellular pH rather than the extracellular and that the effect of hyperthermia at low pH_e is significantly greater when pH_i is artificially lowered

by, for example, blocking the Na^+/H^+ exchanger [50, 98].

On the other hand, low pH_e has been shown to render tumour cells resistant to radiotherapy, but not to the same extent as hypoxia [226]. Moreover, it seems that resistance depends on the relationship between the time cells become acidic and the time radiation is administered [106]. For example, an experiment by [106] showed that Chinese hamster ovary cells had an increased survival rate when exposed to acidic pH_e following irradiation than during or before radiation. All of these findings are valid under aerobic conditions, however, under hypoxic conditions, acidity has been shown not to increase the radioresistance of tumour cells [198].

1.3 Mathematical modelling of tumour development

As we have seen in the previous section, cancer is a complex disease encompassing several biological processes that occur at various spatial and temporal scales, ranging from the subcellular, cellular and tissue scale. The growing number of biological research articles published every year on cancer development call for a quantitative method to integrate the ever-expanding literature. Mathematical modelling can be such a quantitative method and a useful tool to test hypotheses which can be time-consuming or impossible to implement experimentally. Mathematical modelling can also provide predictions which can be validated by further experimental studies.

The contributions of mathematical modelling to the understanding of tumour growth and development dates back at least 60 years. Some of the earliest models (for example, [33, 64, 92, 228]) focus mainly on how culture conditions (such as oxygen and nutrients) can affect the growth of multicellular spheroids (MCS). Several studies have since emerged to describe the many levels of complexity, from the intracellular signalling pathways to the macroscopic invasion processes. Of

these, models explore particular aspects of tumour growth and dynamics such as immunotherapy (e.g. see [27, 32, 119]), angiogenesis (e.g. see [43, 138]) and invasion (e.g. see [77, 188, 189, 190, 214]). Most models can be grouped into two broad categories, those describing the behaviour of individual cells (discrete models), and those averaging the spatial and temporal behaviour of cells (continuum models). The complexity of cancer as a disease often calls for the combination of the two approaches (i.e. hybrid models). We will briefly summarise the techniques used. For a comprehensive review, see for example [3, 10, 132, 44, 182, 197].

Continuum models typically consist of reaction-diffusion or reaction-diffusion-convection or integro-differential equations. This approach is particularly useful for describing clinically visible tumours, but is not suitable for tracking the behaviour of a small number of cells growing at an early stage of tumorigenesis. This, however, can be addressed by utilising a "discrete" approach which allows the behaviour of individual cells to be tracked using a set of predefined biophysical rules. Discrete models are usually categorised into two groups: lattice-based (cellular automata) and lattice-free. In lattice-based modelling, the cells or subcellular elements are limited to a regular lattice. In lattice-free models, cells are approximated by deformable spheres, ellipses or aggregates of spheres. Hybrid models, on the other hand, have the potential to combine the best features of both discrete and continuum models.

There are only relatively few mathematical models that consider tumour acidity. Amongst these are the work of [71, 158, 214, 249, 250]. In this chapter, we discuss a number of studies based on their relevance to this thesis and their contribution to our understanding of acidity in tumours. We focus on the modelling assumptions, governing equations and summarise the main findings. We split the summary into two parts: continuum models and discrete lattice-based models.

1.3.1 Relevant continuum models

Webb *et al.* (1999) [250]

We consider the study by Webb *et al.* [250] which investigates the various pH regulatory mechanisms adopted by tumour and normal cells in maintaining the intracellular pH at physiological levels. The main differences between normal and tumour cells, in their model, are the inefficient tumour vasculature, and the increased tumour production of H^+-ions from glycolysis. Denoting by I and E the concentrations of intracellular and extracellular H^+-ions respectively, the model has the general functional form

$$\frac{dI}{dt} = -\underbrace{P_1(I,E)}_{Na^+\text{driven } Cl^-/HCO_3^-} - \underbrace{P_2(I,E)}_{Na^+/H^+\text{exchanger}} + \overbrace{P_3(I)}^{Na^+\text{independent } Cl^-/HCO_3^-} + \underbrace{S_1(V)}_{H^+\text{from glycolysis}} + \overbrace{\beta E}^{H^+\text{leakage}}, \tag{1.3}$$

$$\frac{dE}{dt} = \underbrace{P_1(I,E)}_{Na^+\text{driven } Cl^-/HCO_3^-} + \underbrace{P_2(I,E)}_{Na^+/H^+\text{exchanger}} - \overbrace{P_3(I)}^{Na^+\text{independent } Cl^-/HCO_3^-} - \underbrace{S_2(V)E}_{\text{removal by vasculature}} - \overbrace{\beta E}^{H^+\text{leakage}}, \tag{1.4}$$

where V represents the degree of vascularity. Due to the difficulty in parameterising the model, a qualitative approach is adopted: $S_1(V)$ is assumed to be a monotone decreasing function of V, whereas $S_2(V)$ is taken to be directly proportional to V, and the qualitative functional forms of $P_i (i = 1, 2, 3)$ are estimated using experimental findings from [24]. That is, $P_1(I, E)$ is taken such that the maximum influx of HCO_3^--ions by the Na^+-driven Cl^-/HCO_3^- exchanger (in response to an intracellular acid load) occurs when $pH_i \sim 7.0$ and the activity of the exchanger slowly decreases as pH_i increases or decreases. Similarly, $P_2(I, E)$ is taken such that the maximum efflux of H^+-ions by the Na^+/H^+ exchanger (in response to an intracellular acid load) occurs when $pH_i \sim 6.75$ and slowly decreases as pH_i increases or decreases. Moreover, $P_1(I, E)$ and $P_2(I, E)$ are both assumed to decrease exponentially and linearly, respectively, as pH_e becomes low. $P_3(I)$

is assumed to be an exponentially decreasing function describing the reduction in the activity of the Na^+-independent Cl^-/HCO_3^- (in response to an intracellular alkaline load) at low pH_i.

The main aim of their study is to capture the well-established experimental observations that the intracellular pH in some solid tumour cells is higher than in some normal cells and in particular higher than the tumour extracellular pH [226]. In their first set of qualitative analysis, the authors focus on the influence of increased lactic acid production in tumour cells, compared to normal cells, on resting pH_i. Although the authors find that tumour cells are able to maintain a physiological pH_i despite an acidic pH_e, they find that there is very little difference between the pH_i of tumour and normal cells. This prompted them to consider the role of the lactate/H^+ symporter in regulating pH_i and whether its inclusion is sufficient to produce a reversed cellular pH gradient. They incorporate a term of the form $\alpha S_1(V)G(E)$ into the equations, where α is a positive rate constant denoting the rate of activity of the lactate/H^+ symporter and $G(E)$ is an exponentially decreasing function describing the reduction in the activity of this transporter at low pH_e. Failing to obtain the desired reversed cellular pH gradient in hypoxic cases, the authors neglect the effects of the lactate/H^+ symporter and introduce a term in the form of $\lambda H(I)$ into (1.3) to reflect the intracellular sequestration of H^+-ions by intracellular acidic vesicles. The parameter λ is a positive rate constant and $H(I)$ is a Hill function with co-efficient one to model the saturation of the sequestration process. They then show that the most active mechanism of pH_i regulation within hypoxic tumour cells is this transfer of H^+-ions from the cytosol into acidic organelles.

Neville (2003) [158]

Motivated by the lack of explicit account of glucose and the lack of quantitative analysis in the study by Webb *et al.* [250], Neville [158] models the process of glycolysis, in normal and tumour cells, focusing not only on the dynamics of lactic

acid but also on intra- and extracellular glucose dynamics. In Neville's model, the rate of glycolysis and extracellular acid removal by the surrounding vasculature distinguishes normal cells from tumour cells. The model consists of five ordinary differential equations describing intracellular H^+-ions (I), extracellular H^+-ions (E), H^+-ions contained in lysosomes (L), intracellular glucose (G_I) and extracellular glucose (G_E). The equations read as follows:

$$\begin{aligned}\frac{dI}{dt} &= \underbrace{\mu_E(E-I)}_{H^+\text{leakage}} - \underbrace{\frac{C_3 I}{C_4+I^2}}_{Na^+/H^+\text{exchanger}} + \underbrace{\frac{2C_1 G_I}{C_2+I}}_{H^+\text{from glycolysis}} - \underbrace{\theta(G_I)\frac{I_{max} I}{C_5+I}}_{H^+\text{degradation by lysosomes}} \\ &\quad + \underbrace{\gamma(I,L),}_{H^+\text{excreted from intracellular lysosomes}} \qquad (1.5)\end{aligned}$$

$$\frac{dE}{dt} = -\mu_E(E-I) + \frac{C_3 I}{C_4+I^2} - \underbrace{C_6 E,}_{\text{removal by vasculature}} \qquad (1.6)$$

$$\frac{dL}{dt} = \theta(G_I)\frac{I_{max} I}{C_5+I} - \gamma(I,L), \qquad (1.7)$$

$$\frac{dG_I}{dt} = \underbrace{\mu_G(G_E-G_I)}_{\text{glucose diffusing into cell}} - \underbrace{\frac{C_1 G_I}{C_2+I},}_{\text{glucose consumed via glycolysis}} \qquad (1.8)$$

$$\frac{dG_E}{dt} = \underbrace{A}_{\text{source of glucose}} - \mu_G(G_E-G_I), \qquad (1.9)$$

where $A, \mu_E, \mu_G, C_j (j \in 1,2,3,4,5,6)$, and I_{max} are positive rate constants. We briefly discuss the physical meanings of the above terms:

1. $\mu_E(E-I)$: μ_E reflects the rate at which H^+-ions leak intracellularly due to the negative potential of the cell membrane.

2. $\dfrac{C_3 I}{C_4+I^2}$: the rate at which H^+-ions leave the cell via the Na^+/H^+ exchanger. The parameters C_3 and C_4 are estimated from the data in [24].

3. $\dfrac{2C_1 G_I}{C_2+I}$: the rate at which two H^+-ions are produced via glycolysis and is taken to be directly proportional to the concentrations of intracellular glucose

and inversely proportional to intracellular H^+-ions to reflect the fact that decreasing pH_i decreases the glucose consumption rate [39]. The parameter C_2 is the H^+ level at which the glycolytic rate is half maximal and C_1 is the maximal rate of glycolysis.

4. $\theta(G_I)\dfrac{I_{max}I}{C_5+I}$: intracellular digestion of H^+-ion by lysosomes. It is assumed to saturate if intracellular H^+-ions concentration increases. Also, $\theta(G_I)$ is a Hill function which saturates with increasing intracellular glucose concentration.

5. $\gamma(I,L)$: lysosomal secretion of H^+-ions into the intracellular space is taken to be directly proportional to the difference in the concentration of H^+-ions in the lysosomes and in the intracellular space.

6. C_6E: the rate of removal of H^+-ions (C_6) is assumed to be lower in tumours than normal tissue.

7. A: this constant describes the rate at which glucose is supplied to the extracellular domain.

Using perturbation techniques, Neville predicts that, due to a higher glycolytic rate, tumour cells can withstand a greater increase in intracellular acidity compared to normal cells—consistent with the findings by [250]. Furthermore, numerical solutions to the system in (1.5)–(1.9) reveal that the concentrations of intracellular H^+-ions and that in the lysosomes change at a much slower rate relative to the other metabolites in the model. The author attributes this finding to the ability of cells to maintain the intracellular pH at physiological levels. More importantly, Neville's quantitative approach to pH modelling recovers the often-observed reversed pH gradient, and supports the same reasoning behind this as shown by Webb *et al.* [250]. That is, a tumour's increased reliance on the glycolytic pathway and a poor clearance rate of H^+-ions are major factors contributing to a reversed cellular pH gradient.

Gatenby & Gawlinski (1996) [71]

The study by Gatenby & Gawlinski [71] is the first to consider acidity as a mechanism mediating tumour invasion. A set of coupled reaction-diffusion equations describe the spatial distribution of normal tissue (N_1), tumour tissue (N_2), and excess H^+-ion concentration (L). The general model framework is:

$$\frac{\partial N_1}{\partial t} = \underbrace{r_1 N_1 \left(1 - \frac{N_1}{K_1}\right)}_{\text{growth}} - \underbrace{d_1 L N_1,}_{\text{death from excess } H^+} \tag{1.10}$$

$$\frac{\partial N_2}{\partial t} = \underbrace{r_2 N_2 \left(1 - \frac{N_2}{K_2}\right)}_{\text{growth}} + \underbrace{\nabla \cdot \left[D_2 \left(1 - \frac{N_1}{K_1}\right) \nabla N_2\right]}_{\text{movement}}, \tag{1.11}$$

$$\frac{\partial L}{\partial t} = \underbrace{r_3 N_2}_{\text{production}} - \underbrace{d_3 L}_{\text{removal by vasculature}} + \underbrace{D_3 \nabla^2 L,}_{\text{diffusion}} \tag{1.12}$$

where r_1, r_2 and r_3 denote the growth rates of normal tissue, tumour tissue and the rate of acid production respectively. The K_1, K_2 are the normal and tumour tissue carrying capacities respectively, D_2 the tumour cell diffusion coefficient, D_3 the H^+-ion diffusion co-efficient, r_3 the rate of H^+-ion production and d_3 the rate of removal of H^+-ions by vasculature and buffering. At the heart of their model are two assumptions: 1. normal cells do not diffuse; 2. tumour cells cannot diffuse when normal cells are at their carrying capacity and only diffuse when normal cells are diminished.

Non-dimensionalising equations (1.10)–(1.12) identifies a critical parameter, $\delta_1 = d_1 r_3 K_2 / d_3 r_1$. Linear stability analysis yields four steady state solutions:

1. Absence of normal and tumour tissue, and acid (unconditionally unstable).

2. Normal tissue existing at its carrying capacity with the lack of tumour tissue and acid (unconditionally unstable).

3. Co-existence of tumour and normal tissue with the presence of acid (stability depends on the parameter δ_1).

4. Total diminishment of normal tissue and the existence of tumour tissue at its carrying capacity and the presence of acid (unconditionally stable).

For $\delta_1 < 1$, steady state number 3 is stable and the tumour and normal tissue co-exist in a benign state. For $\delta_1 > 1$, steady state number 3 is unstable and evolves to that of a total elimination of the normal tissue (steady state number 4). Moreover, travelling wave solutions predict a smooth pH gradient extending from the tumour edge into the peritumoral tissue. This is consistent with the *in vivo* pH profiles of VX2 rabbit carcinoma obtained earlier by Martin & Jain [140]. More crucially, the model suggests that, provided $\delta_1 > 1$, a hypocellular gap exists between the advancing tumour front and the receding normal tissue. Gatenby & Gawlinski [71] subsequently showed that 67% of the 21 human squamous cell carcinoma examined were judged to have this gap *in vitro*. This study is an excellent illustration of how a mathematical model can be formulated using biological hypotheses and the solution of which can then drive experimental designs.

Smallbone *et al.* (2005) [214]

Smallbone *et al.* [214] argue that the acid-mediated tumour invasion model developed by [71] does not accurately represent the growth pattern of benign tumours. Assuming that the tumour acts as an incompressible fluid and that spherical symmetry prevails, Smallbone *et al.* [214] model the tumour as a sphere consisting of proliferating cells and necrotic material. The driving mechanism of tumour invasion is taken to depend purely on the levels of hydrogen ions (H) which evolve according to the following reaction-diffusion equation:

$$\frac{\partial H}{\partial t} = \underbrace{r_t T}_{\mathrm{H^+ from\ glycolysis}} - \underbrace{r_v V H}_{\text{removal by vasculature}} + \underbrace{\frac{D_H}{R^2}\frac{d}{dR}\left(R^2\frac{dH}{dR}\right)}_{\text{diffusion}}, \tag{1.13}$$

where, V denotes the vascular density which is taken to distinguish an avascular growth from a vascular one, r_V the rate of removal of H^+-ions by the vasculature, r_T the rate of H^+-ions production from glycolysis, D_H the diffusion co-efficient of

H^+-ions (assumed constant) and T the viable tumour cell density. At the heart of their model is the assumption that metabolically produced H^+-ions can both promote and inhibit tumour growth. That is, normal cells cannot withstand the harsh acidic environment created by the tumour tissue and hence die, allowing the tumour to expand into the resulting empty space. On the other hand, if H^+-ions accumulate within the tumour tissue due to a reduced removal rate by the vasculature then auto-toxicity occurs and tumour tissue can then die.

Analysis of this simple model predicts three tumour growth patterns. In an avascular tumour, a benign growth always prevails if the rate of tumour acid removal is low. In a vascular tumour, whether a benign growth prevails or not depends on a predefined threshold for tumour cell death due to acidity (h_T): if $h_T < 1$, the tumour turns out to be benign; if $h_T \geq 1$, the tumour invades the entire normal tissue. In contrast, a tumour does not grow if it is so small that the acid levels do not become high enough to induce normal cell death.

Moreover, a hypocellular gap is predicted to exist between the advancing tumour front and the normal tissue—in line with [71]. However, this gap is predicted to be of a similar size to the tumour, and larger than the experimentally determined estimates of 100 μm. This then lead the authors, in a subsequent study [213], to consider modelling the tumour as a multicellular sphere consisting of not only proliferative and necrotic cells but also quiescent cells which are known to be less metabolically active and thus are likely to produce less acid than proliferative cells. They show that the amended model in [213] results in a hypocellular gap matching the size observed in experimental studies.

1.3.2 Relevant discrete lattice-based models

Interested by Neumann's model of self-replicating robots [242], Conway developed the first 2-D discrete model of interacting biological cells known as the "game of life" model [70]. Since then, individual-based models, such as cellular automata (CA for short), have been used to model various biological phenomenon, such as

morphogenesis (e.g. see [203]), predator-prey invasion (e.g. see [208]), excitable media (e.g. see [76]) and many others (e.g. see [4] for a review). Most of these models also use a"continuum" approach for extracellular metabolite and substrate concentrations since traditional CA methods lack the ability to deal with continuously varying elements such as substrate diffusion and consumption. The first work using an individual based CA model in cancer modelling was developed by Düchting and Vogelsaenger [58], who used it to investigate the effects of radiotherapy. Since then, many CA models have been developed to examine the various aspects of tumour development such as the tumour morphology (e.g. [62]), the glycolytic phenotype (e.g. [170]), tumour cell adhesion (e.g. [8]), and the cell-cycle (e.g. [181]).

The cellular Potts model (otherwise known as the Glazier-Graner-Hogeweg model or GGH for short) is a type of CA model which was developed by Glazier and Graner in 1992 to model cell sorting [91]. Based on energy-minimisation techniques, the main advantage of the Potts model is that it allows biological cells to be represented as spatially-extended objects with variable shapes. The Potts model has been used extensively to model morphogenesis as well as tumour growth.

In this section, we focus on lattice-based tumour growth models. For a comprehensive review on other methods such as agent based, lattice-gas or immersed boundary models see the comprehensive review by Lowengrub *et al.* [132].

Patel *et al.* (2001)

The acid-mediated continuum model developed by Gatenby and Gawlinski [71] suggests that, in a clinically apparent tumour mass, tumour-induced acidity plays a significant role in invasion and destruction of normal tissue. However, it is not obvious whether this is also the case when a tumour is relatively small in size. Patel *et al.* [170] therefore develop a hybrid CA model to study the role of H^+ production and host tissue vascularity in the growth and invasive capacity of a small cluster of tumour cells. The automaton elements of the model include normal cells, tumour

cells, empty space and native microvessels. Diffusion of glucose (G) and H^+ ions (H_t) to and from the microvessels, and their consumption or production by cells, is governed by the following reaction-diffusion differential equations:

$$\frac{\partial G(\mathbf{r},t)}{\partial t} = \underbrace{D_G \nabla^2 G(\mathbf{r},t)}_{\text{diffusion}} - \underbrace{k(\mathbf{r})G(\mathbf{r},t)}_{\text{consumption}}, \tag{1.14}$$

$$\frac{\partial H_t(\mathbf{r},t)}{\partial t} = \underbrace{D_H \nabla^2 H_t(\mathbf{r},t)}_{\text{diffusion}} + \underbrace{h(\mathbf{r})}_{H^+ \text{ production}}, \tag{1.15}$$

where, D_G and D_H are the diffusion co-efficients of glucose and H^+-ions respectively, $k(\mathbf{r})$ is taken such that it is non-zero only when a tumour or normal cell is present, with tumour cells consuming ten times more glucose than normal cells. Also, $h(\mathbf{r})$ is non-zero only when a tumour is present. Glucose is delivered and H^+-ions are removed through the boundary conditions imposed at the vessel walls. Note that because glucose and H^+-ions diffuse at a faster rate relative to cell growth, the time derivatives in (1.14)–(1.15) are set to zero. The phenotypic evolution of individual cells then depends on the steady state local concentrations of glucose and H^+.

The model predicts that the growth of an initial cluster of 21 tumour cells (in a 200×200 automaton) is able to generate an environment that allows the tumour to advance by destroying the normal tissue. A wide variety of tumour morphologies are obtained: a compact mass with regions of central necrosis, those with "diffuse" necrosis and those with "cords" (which are cylindrical cuffs of tumour cells surrounding a blood vessel [16]). It also turns out that the tumour morphology crucially depends on the rate of H^+-ion production and its removal.

Gerlee *et al.* (2008) [79]

Gerlee *et al.* [79] examine the emergence of the tumour glycolytic phenotype in cancer using a complex CA model based on a feed-forward neural network. The model also consists of discrete individual tumour cells, continuous chemical fields

(oxygen, glucose and H^+-ions) and ECM density. The time evolution of oxygen (c), glucose (g) and hydrogen ions (h) are governed by the following partial differential equations:

$$\begin{aligned}
\frac{\partial c}{\partial t} &= \underbrace{D_c \nabla^2 c}_{\text{diffusion}} + \underbrace{f_c(x,y,t),}_{\text{production or consumption}} \\
\frac{\partial g}{\partial t} &= \underbrace{D_g \nabla^2 g}_{\text{diffusion}} + \underbrace{f_g(x,y,t),}_{\text{production or consumption}} \\
\frac{\partial h}{\partial t} &= \underbrace{D_h \nabla^2 h}_{\text{diffusion}} + \underbrace{f_h(x,y,t),}_{\text{production or consumption}}
\end{aligned}$$

where $D_i (i \in c, g, h)$ are the respective diffusion co-efficients. The ECM density is assumed to degrade at a rate proportional to the excess H^+-ion concentration. The authors find that the tumour environment affects both its growth and evolutionary dynamics. More specifically, low oxygen levels allow for the development of a "fingered" morphology, while a dense extracellular matrix density gives rise to more compact tumours with wider fingers.

Jiang *et al.* (2005) [219]

The first cellular Potts model to describe a three-dimensional avascular tumour growth was developed by Stott *et al.* [219]. Their model reproduces the classical three layered tumour structure (with a necrotic core, an intermediate layer of quiescent cells and an outer layer of proliferative cells). Jiang *et al.* [112] further extends this Potts model to include a subcellular model of a protein expression regulatory network for the cell-cycle as well as incorporating growth promoters and inhibitors through continuum reaction-diffusion equations. At the extracellular scale, the model considers the diffusion, consumption, and production of nutrients, metabolites, growth promoters, and inhibitors, presented in a generic form,

$$\frac{\partial u}{\partial t} = \underbrace{D \nabla^2 u}_{\text{diffusion}} + \underbrace{f(x,y,z),}_{\text{production or consumption}} \tag{1.16}$$

where, D is the diffusion co-efficient of the chemical u, and $f(x, y, z)$ is the metabolic rate which depends on the state of the cell (i.e. whether each cell is proliferative, quiescent or necrotic). The chemicals considered include oxygen, nutrients, lactate, growth and inhibitory factors.

Biological cells interact with one another through their surface membrane, and this is modelled using a coupling constant, $J_{\tau(\sigma_{ij}),\tau(\sigma_{i'j'})}$, to quantify the adhesive energy between cells in a Hamiltonian function, E (see Chapter 5 for detailed description of these terms). This energy function is made up of the cell-cell adhesion energies and cell volume. That is,

$$E = \sum_{ij} \sum_{i'j'} \underbrace{J_{\tau(\sigma_{ij}),\tau(\sigma_{i'j'})} \left(1 - \delta_{\tau(\sigma_{ij}),\tau(\sigma_{i'j'})}\right)}_{\text{cell adhesion}} + \sum_{\text{all domains } \lambda \neq 0} \underbrace{\lambda \left(v_\sigma - V_T\right)^2}_{\text{cell volume}}, \quad (1.17)$$

In the first term, the outer sum runs over all occupied sites in the lattice, whereas the inner sum is over the eight nearest neighbours of (i, j). The Kronecker delta, $\delta_{\tau(\sigma_{ij}),\tau(\sigma_{i'j'})}$, is equal to one when $\sigma_{ij} = \sigma_{i'j'}$ and zero otherwise. This ensures that only surface interactions between different biological cells contribute to the cell-cell adhesion energy. Parameter values were estimated to best fit experimental measurements of spheroids *in vitro* such that the model reproduces an avascular tumour consisting of a necrotic core surrounded by a quiescent and a proliferative rim.

1.4 In this thesis

The microenvironment of tumours varies considerably from normal tissue, with tumours having pronounced variations in hypoxia and acidity. Cells respond to hypoxia by switching to anaerobic metabolism which then leads to the production of high amounts of lactic acid and this is thought to lower the extracellular pH. The pioneering study of Warburg [247], however, showed that upregulated glycolysis in many aggressive tumours can occur even with ample supply of oxygen. Cells also respond to the upregulated lactic acid production by upregulating sev-

eral membrane-bound transporters which raises the intracellular pH [49, 176, 184]. With a poor tumour vasculature and an altered tumour cell metabolism, this may then lead to cells having an extracellular pH that is lower than the intracellular. This is called a 'reversed cellular pH gradient' and has been implicated in tumour cell proliferation [85], apoptosis [123, 167], cell morphology [218] and migration [218]. Increased lactate levels have also been correlated with incidence of metastasis in some cancers [245, 246].

There has been considerable mathematical modelling efforts to understand the effect of extracellular acidity on tumour development. However, none of the previous models have examined the role of lactate in regulating the intracellular pH to a physiological level and its effect on the onset of a 'reversed cellular pH gradient'. In this thesis, we develop a mathematical model that examines the role of various membrane-based ion transporters in tumour pH regulation, in particular, with a focus on the interplay between lactate and H^+ ions and whether the lactate/H^+ symporter activity is sufficient to give rise to the observed reversed pH gradient that is observed in some tumours.

In Chapter 2, we develop an ordinary differential equation model that explicitly focuses on the interplay between H^+-ions and lactate. In Chapter 3, we present an extension to this model by including the diffusion of hydrogen ions and lactate across the tissue. In Chapter 4, we study the role of oxygen and pH on early tumour growth using a hybrid cellular automaton model. We examine whether the levels of oxygen, intracellular or extracellular pH are the dominating metabolites driving tumour growth and invasion. In Chapter 5, we use the cellular Potts model to study the effect of cellular adhesion, matrix-degrading enzyme activity and cellular proliferation on tumour invasion.

Chapter 2

A mathematical model examining the interplay between H^+-ions and lactate

2.1 Introduction

The microenvironment of tumours trigger various signals which can promote invasion [142, 160] and reduce tumour response to therapies [29, 104]. An altered pH homoeostasis is increasingly becoming a distinct feature of some cancer cells. While the intracellular pH in normal differentiated cells is generally ~ 7.2 and is less alkaline than the extracellular pH ($pH_e \sim 7.4$) [23], the intracellular pH of some malignant tumour cells can be greater than 7.4 and is found to be more alkaline than the extracellular pH ($pH_e \sim 6.5$–7.1) [86, 168]. That is, a 'reversed' pH gradient ($pH_i > pH_e$) exists and is thought to confer a survival advantage to the tumour over normal tissue [179, 187]—an acidic pH_e is believed to enhance the invasive behaviour of tumour cells [142, 195] and render them resistant to some chemotherapeutics [243]. On the other hand, an elevated pH_i can have permissive effects on proliferation [180, 184] and the evasion of apoptosis [123, 143].

Unlike normal cells, it is well-established that malignant tumour cells undergo anaerobic glycolysis despite plentiful oxygen supply [73]. This yields excess levels of hydrogen ions and lactate which must be exported outside the cell in order to maintain cell viability. Cells have evolved several short and long term mechanisms to maintain their pH_i within the normal physiological range (pH 7.2–7.4). In this chapter, we focus on the well-studied Na^+/H^+ exchanger and the lactate/H^+ symporter which are increasingly implicated in tumour progression [49, 118, 147, 176]. We investigate the effect of their activity on tumour pH reversal.

Previous models which consider tumour acidity are [71, 158, 214, 249, 250] (see Section 1.3 for details on these models). Gatenby & Gawlinski [71] derive an acid-mediated tumour invasion model which provides a simple mechanism linking altered glucose metabolism with the ability of tumour cells to form invasive cancers. The modelling of Webb *et al.* [249, 250] includes descriptions of intracellular and extracellular pH and their effects on invasion. However, the various cell-membrane transporters are represented in a rather simple fashion. Moreover, they do not include lactate as a variable, but instead include the lactate/H^+ symporter as a function depending wholly on extracellular H^+ and the degree of functioning vasculature. The role of sequestration of H^+-ions into lysosomes is also considered in [250]. The modelling of Neville *et al.* [158] considers the evolution of intracellular and extracellular glucose as well as hydrogen ions.

In this chapter, we present a new model for pH regulation that explicitly focuses on the interplay between H^+-ions and lactate. We develop the mathematical model in Section 2.2 and present some of the qualitative features of H^+ and lactate. Numerical simulations show that the pH solutions initially change very rapidly relative to lactate. Detailed analysis of this behaviour in Section 2.4.2 show that the initial concentration of intra and extracellular lactate plays a crucial role in the sharp transient. More importantly, our model has the potential to reproduce the well-documented reversed pH gradient but for values outside the physiological pH range (6.9–7.4)—suggesting, instead, that other cellular mechanisms may play

an important role in this behaviour.

2.2 Model development

Our model framework is that of a single tumour cell or normal cell with two compartments—intracellular and extracellular—and we focus on the regulation of lactate and H^+-ions between these two compartments (see Figure 1.1 for a schematic). We consider the temporal evolution of H^+-ions which we denote by H_σ, $\sigma \in \{I, E\}$ where I, E denotes intracellular and extracellular concentrations, and lactate (L_σ) where $\sigma \in \{I, E\}$.

The cells studied in this model can be tumour or normal depending on parameter choices and whether the vasculature, V, is bigger or smaller than a chosen threshold degree of vasculature (V^g) which we use to control whether the cell undergoes glycolysis (for $V < V^g$) or aerobic metabolism (for $V \geq V^g$). In line with Webb *et al.* [249, 250] and Neville *et al.* [158], we assume that extracellular ions are removed from the interstitial space at a rate directly proportional to V.

Our model differs from previous studies in that we explicitly include lactate. This allows a better representation of the MCT (i.e., the lactate/H^+ symporter) and its role in pH regulation and, in particular, whether the action of the MCTs are able to reproduce a reversed pH gradient which is characteristic of some tumours [93].

Derivation of the lactate/H^+ term

Consider the following closed system which describes the transport of H^+-ions and lactate across the cell membrane from the intracellular to the extracellular space via the MCT transporter:

$$[L_I] + [H_I] \underset{k_{-1}}{\overset{k_1}{\rightleftharpoons}} [L_I H_I] \overset{k_2([L_I H_I]-[L_E H_E])}{\longleftrightarrow} [L_E H_E] \underset{k_1}{\overset{k_{-1}}{\rightleftharpoons}} [L_E] + [H_E], \tag{2.1}$$

where $[\cdot]$ denotes concentration and $L_\sigma H_\sigma$ represents intracellular and extracellular lactic acid, for $\sigma = I, E$ respectively. The k_2 parameter denotes the rate of activity of the lactate/H^+ symporter and we assume that this activity is directly proportional to the concentration difference of lactic acid across the cell membrane. The rate at which lactic acid dissociates into lactate and H^+-ions is denoted by k_{-1} and the rate of the reversible reaction is denoted by k_1. We then use the law of mass action to derive the following equations from the reactions shown in (2.1), namely:

$$\begin{aligned}
\frac{d[H_I]}{dt} &= -k_1[L_I][H_I] + k_{-1}[L_I H_I], && (2.2)\\
\frac{d[L_I]}{dt} &= -k_1[L_I][H_I] + k_{-1}[L_I H_I], && (2.3)\\
\frac{d[L_I H_I]}{dt} &= k_1[L_I][H_I] - k_{-1}[L_I H_I] - k_2([L_I H_I] - [L_E H_E]), && (2.4)\\
\frac{d[H_E]}{dt} &= k_{-1}[L_E H_E] - k_1[H_E][L_E], && (2.5)\\
\frac{d[L_E]}{dt} &= k_{-1}[L_E H_E] - k_1[H_E][L_E], && (2.6)\\
\frac{d[L_E H_E]}{dt} &= -k_{-1}[L_E H_E] + k_1[H_E][L_E] + k_2([L_I H_I] - [L_E H_E]). && (2.7)
\end{aligned}$$

Given that k_1 and k_{-1} are known to be large (i.e. lactic acid dissociates freely, with an equilibrium constant of 1.38×10^{-4} mol/l, to form lactate and H^+-ions) [206], this allows us to assume that $[L_I H_I]$ and $[L_E H_E]$ are quasi-steady. Hence, solving equations (2.4) and (2.7) algebraically for $[L_I H_I]$ and $[L_E H_E]$ we get

$$[L_I H_I] = \frac{k_1}{k_{-1}}([L_I][H_I] + [L_E][H_E]) - [L_E H_E],$$

where

$$[L_E H_E] = \frac{k_1 k_2}{k_{-1}\left(2k_2 + k_{-1}\right)}\left([L_I][H_I] + [L_E][H_E]\left(1 + \frac{k_{-1}}{k_2}\right)\right).$$

So that the lactate/H^+ efflux term after a little algebra, $k_1[L_I H_I] - k_{-1}[L_I H_I]$, becomes

$$k_3([H_I][L_I] - [H_E][L_E]),$$

where $k_3 = k_1k_2/(2k_2 + k_{-1})$ and we will use this expression for lactate/H^+ efflux via the MCT in our full model.

The full model equations read as follows:

$$\begin{aligned}\frac{dH_I}{dt} &= \underbrace{l_H(H_E - H_I)}_{H^+\text{leakage}} - \underbrace{f_1\mathrm{H}(H_I - H_E)(H_I - H_E)}_{Na^+/H^+\text{antiporter}} - \underbrace{k_3(H_IL_I - H_EL_E)}_{\text{MCT}} \\ &+ \underbrace{\frac{2\Phi_G\mathrm{H}(V^g - V)}{H_I + b}}_{\text{Excess } H^+\text{via glycolysis}} + \underbrace{d_1,}_{\text{Other sources of } H^+} \end{aligned} \tag{2.8}$$

where $\mathrm{H}(\cdot)$ denotes a Heaviside function,

$$\begin{aligned}\frac{dH_E}{dt} &= -\underbrace{l_H(H_E - H_I)}_{H^+\text{leakage}} + \underbrace{f_1\mathrm{H}(H_I - H_E)(H_I - H_E)}_{Na^+/H^+\text{antiporter}} + \underbrace{k_3(H_IL_I - H_EL_E)}_{\text{MCT}} \\ &- \underbrace{R_1(V)H_E,}_{\text{Removal by vasculature}} \end{aligned} \tag{2.9}$$

$$\begin{aligned}\frac{dL_I}{dt} &= \underbrace{\frac{2\Phi_G\mathrm{H}(V^g - V)}{H_I + b}}_{\text{Production from glycolysis}} + \underbrace{d_4}_{\text{Other sources of lactate}} - \underbrace{\alpha_4L_I}_{\text{Lactate degradation}} \\ &- \underbrace{k_3(H_IL_I - H_EL_E),}_{\text{MCT}} \end{aligned} \tag{2.10}$$

$$\frac{dL_E}{dt} = \underbrace{k_3(H_IL_I - H_EL_E)}_{\text{MCT}} - \underbrace{R_2(V)L_E.}_{\text{Removal by vasculature}} \tag{2.11}$$

To close our system, we assume appropriate initial concentration of the chemicals that correspond to levels typically found in normal cells, that is:
$H_I = H_I^0$ mol/l, $H_E = H_E^0$ mol/l, $L_I = L_I^0$ mol/l, $L_E = L_E^0$ mol/l.

We now explain, in turn, how we derived each of the model terms in equations (2.8)– (2.11):

1. $l_H(H_E - H_I)$. This term describes the rate at which H^+ ions enter the cell due to the internally negative potential of the cell membrane. In line with Neville *et al.* [158], we assume that this occurs at a rate directly proportional

to the difference in the hydrogen ion concentration across the cell membrane. The permeability of the cell membrane to H^+ ions is approximately 10^{-14} m/s [125]. Dividing this by the typical width of the bilayer ($\sim$ 10 nm) [125] gives an estimation for l_H as 10^{-6} s^{-1}.

2. $f_1 \mathrm{H}(H_I - H_E)(H_I - H_E)$. This term models the rate at which H^+-ions are exported outside the cell via the Na^+/H^+ exchanger (NHE for short) and we assume that the rate of H^+ efflux is directly proportional to the H^+ gradient across the cell membrane, i.e. $H_I - H_E$. This is a sensible assumption since experiments carried out by Boyer & Tannock [24] report that the rate of H^+ efflux is linearly proportional to the transmembrane H^+ gradient ($H_I - H_E$) in MGHU1 human bladder carcinoma cells. For simplicity, we assume that the outward Na^+ gradient is always positive. Therefore, this term is taken to be proportional to the hydrogen ion gradient only. The Heaviside is used to prevent any H^+ influx which is typically not observed via this transporter. The constant f_1 is a parameter which denotes the rate of H^+ flux, and carries the units of s^{-1}.

3. $k_3(H_I L_I - H_E L_E)$. This term represents the rate at which hydrogen ions are extruded along with lactate ions. These ions are transported via a Monocarboxylate Transporter (MCT) located at the plasma membrane. A study by McDermott *et al.* [144] shows that lactate transport is saturable with respect to increasing concentrations of lactate and hydrogen ions, but for simplicity we assume a linear relationship. This term can also be seen as an approximation of the MCT efflux expression derivable from a recent kinetic model in [240]. The constant k_3 (units of $mol^{-1}/l^{-1}/s$) describes the rate at which hydrogen ions and lactate are exported or imported.

4. d_1. This term implicitly accounts for other sources of H^+ ions in the cell. For example, this could include the catalysed hydration of cell generated CO_2 into H^+-ions and bicarbonate ions by Carbonic Anhydrase enzymes

(CA) [223]. There are 16 isoforms of mammalian CAs, some are expressed internally while others are membrane-tethered with an extracellular catalytic site [148]. In particular, the internally expressed CA I and CA II are shown to be predictive of local growth of oral squamous cell carcinoma [130] and is correlated with biological aggressiveness of colorectal cancer [18].

5. $\frac{2\Phi_G \mathrm{H}(V^g - V)}{H_I + b}$. This term models the net production of H^+ ions via the process of glycolysis. Glycolysis is a metabolic pathway involving a complex chain of chemical reactions that produces energy rich molecules (ATP) [125]. Studies by Kaminkas [114] showed that glucose transport and consumption in cultured Ehrlich ascites-tumour cells are pH dependent. Decreasing pH_i is found to decrease the rate of glucose consumption [22, 39]. In particular, the key glycolytic enzyme phosphofructokinase is found to be critically pH sensitive [19]. As mentioned before, in our model, we assume a threshold degree of vasculature (V^g), above which a cell will undergo aerobic metabolism, and below which anaerobic glycolysis will prevail. In the presence of an oxygen supply ($V \geq V^g$), there is no net production of H^+ ions as aerobic metabolism is shown not to produce any net H^+-ions [105]. However, in low oxygen concentrations ($V < V^g$), two H^+-ions are produced from the dissociation of lactic acid [105]. We assume glucose to be plentiful, which is reasonable given the observed large diffusion distance of glucose [236]. The constant Φ_G represents the maximal rate of glycolysis and b corresponds to the concentration of H^+ ions needed to achieve one half of the maximum rate of glycolysis. We use the results of [39] for EMT6/R0 mouse mammary tumour cells to estimate Φ_G and b. In this study, it is noted that glucose is consumed at a rate of 2×10^{-14} g/cell/s at a pH of 7.2. One mol of glucose has a relative molecular mass of 180 g and one cell has a volume of roughly 10^{-15} m^3 [131]. This corresponds to a glucose consumption rate of 1.1×10^{-4} $\mathrm{mol/m^3/s}$. If we choose $b = 10^{-7}$ mol/l then $\Phi_G = 10^{-14}$ $(\mathrm{mol/l})^2/\mathrm{s}$.

6. $R_\sigma(V)$, $\sigma = 1, 2$ for H^+-ions and lactate, respectively. These terms represent the rate at which hydrogen and lactate ions are removed from the interstitial space. We assume, along with [158, 250, 214], that once H^+ ions and lactate are extruded, they are removed linearly by the supporting vasculature, that is, $R_\sigma(V) = \rho_\sigma V$, where $\sigma = 1, 2$. However, the vasculature of tumour is believed to be highly disordered and compromised [187, 236], which results in uneven perfusion and a poor clearance rate. This allows us to take V to be much lower in tumours than in normal tissue.

7. d_4. This term corresponds to the production of lactate under normal physiological conditions. In non-stressed or non-shocked animals, significant lactate is produced to maintain a concentration of 0.7 mM [206]. It has been estimated [206] that lactate is produced in the resting man at the following rates (mM/h/kg): skeletal mass, 3.13; brain, 0.14; red cell mass, 0.18; and 0.11 for blood elements, renal medulla, intestinal mucosa and skin. Total lactate production in a 70-kg man is approximately 1,300 mM/day [206].

8. $\alpha_4 L_I$. This term implicitly describes the rate at which lactate is converted back to pyruvate or is degraded. We currently have no available data to approximate this value and so we vary it in our analysis.

2.3 Analysis of the model

We begin by considering the qualitative features of the long-time steady state solutions of the model. At equilibrium, the steady states $(H_I^*, H_E^*, L_I^*, L_E^*)$ for equations (2.8)–(2.11) are obtained by setting $\frac{dH_I}{dt} = \frac{dH_E}{dt} = \frac{dL_I}{dt} = \frac{dL_E}{dt} = 0$. Adding equations (2.8) and (2.9) then gives

$$H_E^* = \begin{cases} \dfrac{d_1}{\rho_1 V}, & V \geq V^g, \\ \dfrac{d_1}{\rho_1 V} + \dfrac{2\Phi_G}{\rho_1 V (H_I^* + b)}, & V < V^g. \end{cases} \tag{2.12}$$

Adding (2.10) and (2.11) and solving for L_I^* gives

$$L_I^* = \begin{cases} \left(d_4 - \rho_2 V L_E^*\right)/\alpha_4, & V \geq V^g, \\ \left(\dfrac{2\Phi_G}{H_I^* + b} + d_4 - \rho_2 V L_E^*\right)/\alpha_4, & V < V^g. \end{cases} \tag{2.13}$$

Now, substituting (2.13) and (2.12) into (2.11) gives

$$L_E^* = \begin{cases} \dfrac{q\rho_1 V H_I^*}{rH_I^* + u}, & V \geq V^g, \\ \dfrac{(qH_I^{*2} + wH_I^*)\rho_1 V}{rH_I^{*2} + sH_I^* + p}, & V < V^g. \end{cases} \tag{2.14}$$

where,

$q = k_3 d_4$, $r = \rho_1\rho_2 k_3 V^2$, $u = \alpha_4 d_1 k_3 + \alpha_4\rho_1\rho_2 V^2$, $w = 2\Phi_G + d_4 b$,

$s = \rho_1\rho_2 V^2 k_3 b + \alpha_4 d_1 k_3 + \alpha_4\rho_1\rho_2 V^2$,

$p = \alpha_4\rho_1\rho_2^2 V^2 b + \alpha_4 d_1 k_3 b + 2\alpha_4\Phi_G k_3$.

In order to calculate the steady state for H_I^*, equations (2.12), (2.13) and (2.14) must be substituted back into the steady state version of (2.8)–(2.11) (i.e. with the time derivatives set to zero). This yields an extremely long intractable algebraic expression and so we can not obtain an analytical solution for H_I^*. We thus resort to numerical methods in order to understand the model behaviour.

2.3.1 Parameter rescaling

We now perform a numerical study of this system to explore the behaviours. To facilitate this, we rescale the system according to the following rescalings: $\tilde{H}_I = H_I/b$, $\tilde{H}_E = H_E/b$, $\tilde{L}_I = \alpha_4 L_I/d_4$, $\tilde{L}_E = \alpha_4 L_E/d_4$, $\tilde{t} = \alpha_4 t$, where the tildes

represent rescaled variables with which the model equations become

$$\begin{aligned}
\frac{d\tilde{H}_I}{d\tilde{t}} &= \tilde{l}_H(\tilde{H}_E - \tilde{H}_I) - \tilde{f}_1 \mathrm{H}(\tilde{H}_I - \tilde{H}_E)(\tilde{H}_I - \tilde{H}_E) \\
&\quad -\tilde{k}_3\psi(\tilde{H}_I\tilde{L}_I - \tilde{H}_E\tilde{L}_E) + \frac{2\tilde{\Phi}_G\psi \mathrm{H}(V^g - V)}{\tilde{H}_I + 1} + \tilde{d}_1, \qquad (2.15) \\
\frac{d\tilde{H}_E}{d\tilde{t}} &= -\tilde{l}_H(\tilde{H}_E - \tilde{H}_I) + \tilde{f}_1 \mathrm{H}(\tilde{H}_I - \tilde{H}_E)(\tilde{H}_I - \tilde{H}_E) \\
&\quad +\tilde{k}_3\psi(\tilde{H}_I\tilde{L}_I - \tilde{H}_E\tilde{L}_E) - \tilde{R}_1(V)\tilde{H}_E, \qquad (2.16) \\
\frac{d\tilde{L}_I}{d\tilde{t}} &= \frac{2\tilde{\Phi}_G \mathrm{H}(V^g - V)}{\tilde{H}_I + 1} + 1 - \tilde{L}_I - \tilde{k}_3(\tilde{H}_I\tilde{L}_I - \tilde{H}_E\tilde{L}_E), \qquad (2.17) \\
\frac{d\tilde{L}_E}{d\tilde{t}} &= \tilde{k}_3(\tilde{H}_I\tilde{L}_I - \tilde{H}_E\tilde{L}_E) - \tilde{R}_2(V)\tilde{L}_E, \qquad (2.18)
\end{aligned}$$

where,

$$\tilde{l}_H = \frac{l_H}{\alpha_4},\ \ \tilde{f}_1 = \frac{f_1}{\alpha_4},\ \ \tilde{k}_3 = \frac{k_3 b}{\alpha_4},\ \ \tilde{\Phi}_G = \frac{\Phi_G}{b d_4},$$
$$\tilde{d}_1 = \frac{d_1}{b\alpha_4},\ \ \psi = \frac{d_4}{b\alpha_4},\ \ \tilde{\rho}_1 = \frac{\rho_1}{\alpha_4},\ \ \tilde{\rho}_2 = \frac{\rho_2}{\alpha_4}.$$

The initial concentrations become:

$$\tilde{H}_I^0 = H_I^0/b,\ \ \tilde{H}_E^0 = H_E^0/b,\ \ \tilde{H}_I^0 = H_I^0/b,\ \ \tilde{L}_I^0 = \alpha_4 L_I^0/d_4,\ \ \tilde{L}_E^0 = \alpha_4 L_E^0/d_4.$$

We will henceforth drop the tildes for notational convenience.

Parameter estimates

Given the large number of parameters posed in the model, it has proved difficult to obtain concrete values for all our parameters. However, we are able to obtain values for some of the parameters using literature data, see Section 2.2 for details. The remaining parameters are determined by pre-assuming normoxic and hypoxic steady state values for pH_e, pH_i, L_I and L_E. Ball park estimates for these values

are readily available in the literature. For instance, assuming that for a normal tissue in a normoxic environment: pH_e^*=7.4 (H_E^*=$10^{-7.4}$ mol/l), pH_i^*=7.2 (H_I^*=$10^{-7.2}$ mol/l), L_I^*= 1×10^{-3} mol/l, L_E^*= 1.4×10^{-3} mol/l [221] and we take $V = 1$ for normoxia. Now, with $b = 10^{-7}$ mol/l we have $\tilde{H}_I^* = 0.6310, \tilde{H}_E^* = 0.3981$, and now taking $\tilde{L}_E^* = 1$ we have $d_4/\alpha_4 \sim O(10^{-3}) \equiv 1.4 \times 10^{-3}$ and $\tilde{L}_I^* = 0.7143$. Adding equations (2.17) and (2.18) at steady state gives $1 - \tilde{L}_I^* - \tilde{\rho}_2 V \tilde{L}_E^* = 0$ and substituting for $\tilde{L}_I^*, \tilde{L}_E^*$ and V we have $\tilde{\rho}_2 = 0.2857$. Then substituting for $\tilde{H}_E^*$, $\tilde{H}_I^*$, $\tilde{L}_I^*$, $\tilde{L}_E^*$ and $\tilde{\rho}_2$ in equation (2.18) at steady state we have that $\tilde{k}_3 = 5.4316$. Now adding equations (2.15) and (2.16) at steady state we get $\tilde{d}_1 = \tilde{\rho}_1 \tilde{H}_E^*$ and substituting for $\tilde{H}_E^*$ we have that $\tilde{d}_1 = 0.3981\tilde{\rho}_1$. Assuming that the activity of $\text{Na}^+/\text{H}^+ \approx$ MCT, i.e. $\tilde{f}_1(\tilde{H}_I^* - \tilde{H}_E^*) \approx \tilde{k}_3(\tilde{H}_I^* \tilde{L}_I^* - \tilde{H}_E^* \tilde{L}_E^*)$ and after substitutions, we get $\tilde{f}_1 = 1.7174 \times 10^4$. Using estimates for l_H from [125] and assuming that $\tilde{l}_H \equiv 10^{-6} \tilde{f}_1$, we obtain from equation (2.15) at steady state $\tilde{d}_1 = 7.9978 \times 10^3$.

Now, for $V < V^*$ we would expect $\text{pH}_e^* = 6.60$ and $\text{pH}_i^* = 6.52$ respectively [149]. Adding equations (2.15) and (2.16) at steady state we get $\tilde{d}_1 = \tilde{\rho}_1 V \tilde{H}_E^* - 2\tilde{\Phi}_G \psi/(\tilde{H}_I + 1)$ which then gives $\tilde{\Phi}_G = 0.2823$.

A summary of all of the non-dimensional parameters are given in Table 2.1–we refer to this set of parameters as the 'base' set.

Table 2.1: Dimensionless values of the model parameters in (2.15)–(2.18).

Parameter	Value
$\tilde{l}_H$	1.7174×10^{-2}
$\tilde{f}_1$	1.7174×10^{4}
$\tilde{k}_3$	5.4316
$\tilde{d}_1$	7.9996×10^{3}
$\tilde{\rho}_1$	2.0095×10^{4}
$\tilde{\rho}_2$	0.2857
$\tilde{\Phi}_G$	0.2823
ψ	1.4×10^{4}
V^g	0.5

2.4 Numerical solution

We construct numerical solutions to the system (2.15)–(2.18) in MATLAB using the parameter values in Table 2.1. Using those parameters, a linearisation of our system yields real and negative eigenvalues of varying order of magnitudes. Hence, we use a stiff multistep ODE solver, ode15s, based on backward numerical differentiation formulas. The numerical accuracy of the solution was confirmed by reducing the ODE solver tolerances and we noted a convergence of the solutions to that shown in Figure 2.1. A typical solution is shown in Figure 2.1, (a) for $V \geq V^g$ and (b) for $V < V^g$. Note that for the full model, we assume a resting $\mathrm{pH}_i = 7.2$, $\mathrm{pH}_e = 7.4$, for $V \geq V^g$ (normoxia) and $\mathrm{pH}_i = 6.52$, $\mathrm{pH}_e = 6.60$, for $V < V^g$ (hypoxia) [149, 221]. We hard-wire the final steady state solutions into this simulation, but it is interesting to note the differences in how pH and lactate attain these steady state values. We observe that the solutions of pH_I and pH_E initially change very rapidly, whilst L_I and L_E vary over a longer timescale (see Figure 2.1). We use singular perturbation techniques in Section 2.4.2 to analyse

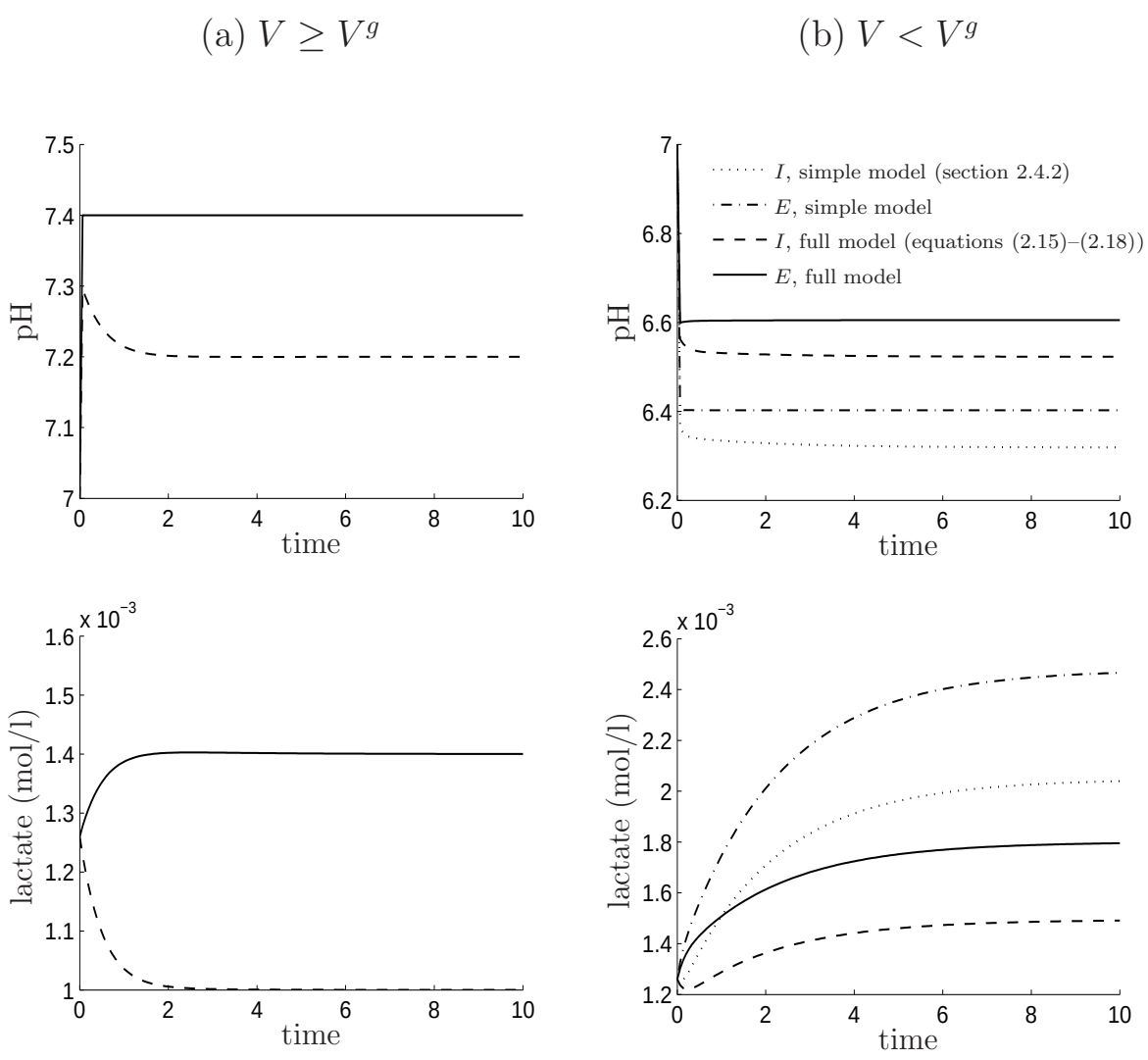

Figure 2.1: A typical numerical solution for (a) $V \geq V^g$ and (b) $V < V^g$ for the full (equations 2.15–2.18) and simplified model (section 2.4.2) showing the sharp initial transient in the H^+-ions solution relative to lactate. (——, extracellular, full model), (− − −, intracellular, full model), (·····, intracellular, simple model), (–·–·–, extracellular, simple model). The parameter values used are shown in Table 1—we refer to this as the 'base' set of parameter values. Initial conditions: $H_I^0 = 0.63, H_E^0 = 0.63, L_I^0 = 0.9, L_E^0 = 0.9$. We note from Figure 2.1(b) that by removing the $H_I + 1$ factor from the glycolysis term (giving the simple model) the qualitative behaviour of the model is unchanged for the range of parameters considered.

this behaviour in more detail. Before we do this, given the uncertainty in some of the parameter estimates, we perform a parameter sensitivity analysis to identify the key rate parameters in the system.

2.4.1 Sensitivity analysis

In this Section, we vary individual parameters in turn and note their effects on the steady state solutions of the model. We illustrate the sensitivity of the model behaviour for the $V < V^g$ case in Figure 2.2 as a percentage change in each of the chosen parameter values from their base value. Given the similarity between the $V \lesseqgtr V^g$ cases, we only show the $V < V^g$ case for brevity. The parameters that we illustrate are those that show the most variation in the solutions—these are, $f_1, k_3, \rho_1, \rho_2, d_1$ and V, which respectively represent the rate of activity of the NHE; and that of MCT; the rate of removal of H^+-ions; and that of lactate; background production of H^+-ions; and finally the degree of vasculature. The sensitivity of the model behaviour for the $V \geq V^g$ is qualitatively similar to that shown in Figure 2.2, except that H_E^* is insensitive to any parameter variations except for d_1, ρ_1 and V. That is, variations in d_1, ρ_1 and V result in qualitatively different lactate behaviour for the $V \lesseqgtr V^g$ cases. More specifically, increasing ρ_1 above its 'base' value (see Table 2.1) results in low steady state levels of intracellular lactate under normoxic conditions (not shown), whilst a high value of intracellular lactate is attained under hypoxia. This means that a purely glycolytic tumour will still have high levels of intracellular lactate despite increased H^+-ions removal rate. Numerical simulations indicate that increasing H^+-ions removal rate under hypoxic conditions results in a high NHE activity, which leaves less intracellular H^+-ions to bind with lactate for extrusion via the MCT. Moreover, increasing d_1 results in a large L_E^* under normoxic conditions (not shown), whilst the opposite is true under hypoxic conditions. This implies that the MCT extrudes H^+ ions (along with lactate) more rapidly under normoxic conditions compared to hypoxic. Our sensitivity analysis also predicts that increasing the blood perfusion for an already

highly glycolytic tumour, whilst keeping perfusion below the hypoxic threshold, results in low intra and extracellular H^+-ions and intracellular lactate, but an unexpectedly high extracellular lactate levels. This is because as extracellular H^+-ions and lactate are cleared, intracellular lactate and H^+-ions continue to be produced glycolytically, and hence the activity of the MCT becomes much higher which gives rise to the observed higher extracellular lactate.

2.4.2 Singular perturbation analysis of a simplified model

We note from the numerical simulations in Figure 2.1 that there is an initial sharp transient in the pH solution profile relative to the slower change in the lactate solutions. We now analyse this behaviour in more detail. To facilitate the analysis, we remove the factor $1/(H_I+1)$ from the glycolysis term. We note that by doing so the qualitative behaviour of the solutions is not affected for the range of parameters considered (see dotted and dash-dotted solutions in Figure 2.1(b)). Also, it turns out to be more convenient to work with the following variables for total H^+ and lactate and the difference between intracellular and extracellular concentrations, namely:

$$H_T = H_I + H_E,\ L_T = L_I + L_E,\ H_D = H_I - H_E,\ L_D = L_I - L_E.$$

The model contains a number of large and small parameters (see Table 2.1) and we exploit this by introducing a small parameter $\epsilon \ll 1$ and rescale the parameters as follows $l_H = \hat{l_H}\epsilon^2$, $f_1 = \hat{f}_1/\epsilon^4$, $\psi = \hat{\psi}/\epsilon^4$, $\Phi_G = \hat{\Phi_G}\epsilon$, $d_1 = \hat{d}_1/\epsilon^3$, $\rho_1 = \hat{\rho}_1/\epsilon^4$, $\rho_2 = \hat{\rho}_2\epsilon$, $V = \hat{V}\epsilon$, where the parameters represented by 'hats' are all of $O(1)$ and $\epsilon = 0.1$. Upon substitution into (2.15)–(2.18), and representing the equations in

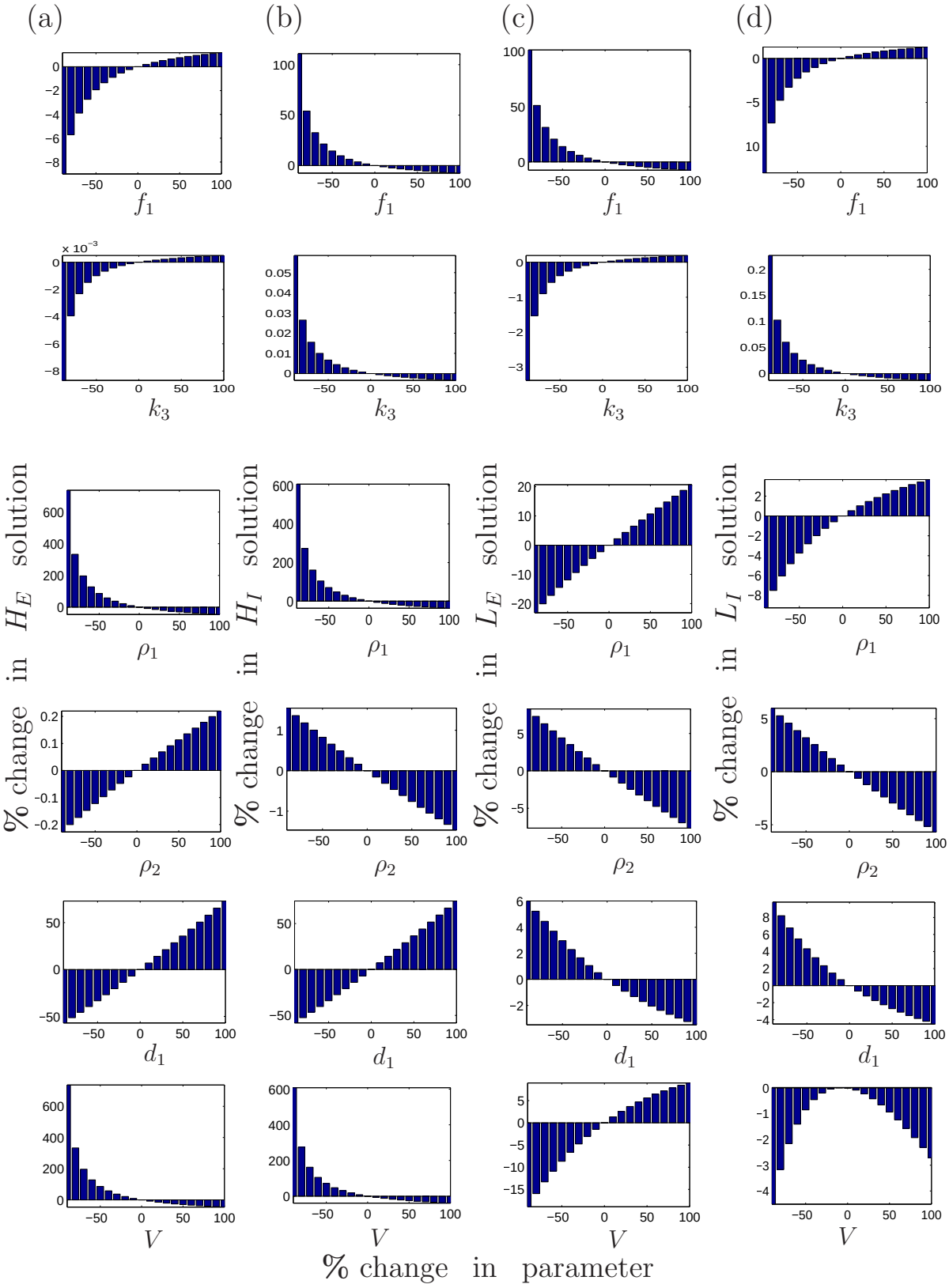

Figure 2.2: Sensitivity analysis of the full model. For each parameter, the percentage change in its value from the base case is plotted on the x-axis, and the corresponding percentage change in the steady state solution is plotted on the y-axis. We only show the results for $V < V^g$ as they are, in general, qualitatively similar to $V \geq V^g$.

terms of H_T, H_D, L_T and L_D we obtain

$$\epsilon^3 \frac{dH_T}{dt} = 2\hat{\Phi}_G \hat{\psi} \mathrm{H}(\hat{V}^g - \hat{V}) + \hat{d}_1 - \frac{\hat{\rho}_1 \hat{V}}{2}(H_T - H_D), \tag{2.19}$$

$$\epsilon^4 \frac{dH_D}{dt} = 2\hat{\Phi}_G \hat{\psi} \epsilon \mathrm{H}(\hat{V}^g - \hat{V}) + \hat{d}_1 \epsilon + \frac{\hat{\rho}_1 \hat{V}}{2} \epsilon (H_T - H_D) - 2H_D(\hat{l}_H \epsilon^6 + f_1) - k_3 \hat{\psi}(H_T L_D + H_D L_T), \tag{2.20}$$

$$\frac{dL_T}{dt} = 2\hat{\Phi}_G \epsilon \mathrm{H}(\hat{V}^g - \hat{V}) + 1 - \frac{1}{2}(L_T + L_D) - \frac{\hat{\rho}_2 \hat{V}}{2} \epsilon^2 (L_T - L_D), \tag{2.21}$$

$$\frac{dL_D}{dt} = 2\hat{\Phi}_G \epsilon \mathrm{H}(\hat{V}^g - \hat{V}) + 1 - \frac{1}{2}(L_T + L_D) + \frac{\hat{\rho}_2 \hat{V}}{2} \epsilon^2 (L_T - L_D) - k_3(H_T L_D + H_D L_T). \tag{2.22}$$

The problem is clearly singular since the small parameter ϵ multiplies the derivative terms in the H_T and H_D equations. This means that the dependent variables, H_T and H_D, undergo rapid changes over very small timescale (as we indeed observe in Figure 2.1). These rapid changes cannot be handled by slow time scales, but can be tackled using a stretched time scale. Specifically, we look for solutions in the form of an asymptotic expansion such as

$$u_\sigma(t;\epsilon) = u_\sigma^0(t) + \epsilon u_\sigma^1(t) + \epsilon^2 u_\sigma^2(t) + \epsilon^3 u_\sigma^3(t) + \ldots, \tag{2.23}$$

where $u = H, L$ and $\sigma = T, D$ and we first rescale time using $t = \epsilon^\alpha \tau$, $\alpha > 0$.

2.4.2.1 Inner solution

We look for the inner solution of (2.19)–(2.22) valid near $t = 0$, with the objective of understanding in more detail the sharp initial transient in the intra and extracellular pH solutions. We rescale time by letting $t = \epsilon^\alpha \tau$ and after substituting into (2.19)–(2.22) we find that the distinguished limit is reached when $\alpha = 4$. Now, with $t = \epsilon^4 \tau$, putting $\epsilon = 0$ in the resulting equations we have

$$L_D^0 = 0, \;\; L_T^0 = L_T^0(0), \;\; H_D^0 = 0 \text{ and } H_T^0 = H_T^0(0), \tag{2.24}$$

where $H_T^0(0)$ and $L_T^0(0)$ correspond to the initial values of H_T^0 and L_T^0 respectively.

Equating $O(\epsilon)$ terms for H_T and solving gives

$$H_T^1 = \left(2\hat{\Phi}_G\hat{\psi}\mathrm{H}(\hat{V}^g - \hat{V}) + \hat{d}_1 - \hat{\rho}_1\hat{V}H_T^0\right)\tau. \tag{2.25}$$

Equating $O(\epsilon)$ terms for H_D gives

$$\frac{dH_D^1}{d\tau} = 2\hat{\Phi}_G\hat{\psi}\mathrm{H}(\hat{V}^g - \hat{V}) + \hat{d}_1 + \frac{\hat{\rho}_1\hat{V}}{2}H_T^0 - (k_3\hat{\psi}L_T^0 + 2\hat{f}_1)H_D^1. \tag{2.26}$$

Solving for H_D^1 with $H_D^1(0) = 0$, we then get

$$H_D^1 = \frac{(\hat{\rho}_1\hat{V}H_T^0 + 4\hat{\Phi}_G\hat{\psi}\mathrm{H}(\hat{V}^g - \hat{V}) + 2\hat{d}_1)(1 - \mathrm{e}^{-(k_3\hat{\psi}L_T^0 + 2\hat{f}_1)\tau})}{2(2\hat{f}_1 + k_3\hat{\psi}L_T^0)}, \tag{2.27}$$

where H_T^0 and L_T^0 are given in (2.24).

Equating $O(\epsilon)$ terms for L_T and L_D gives $L_T^1 = L_D^1 = 0$.

Now, equating $O(\epsilon^2)$ terms for H_T gives

$$\frac{dH_T^2}{d\tau} = -\frac{\hat{\rho}_1\hat{V}\,(H_T^1 - H_D^1)}{2}, \tag{2.28}$$

subject to $H_T^2(0) = 0$. Substituting for H_D^1, H_T^1 and solving for H_T^2 we then get

$$\begin{aligned} H_T^2 \;=\; & \frac{\hat{\rho}_1\hat{V}}{8(k_3\hat{\psi}L_T^0 + 2\hat{f}_1)^2}\Big(k_3\hat{\psi}L_T^0\tau\big(\hat{\rho}_1k_3\hat{\psi}\hat{V}H_T^0L_T^0\tau + 4\hat{\rho}_1\hat{f}_1\hat{V}H_T^0\tau + 2\hat{\rho}_1\hat{V}H_T^0 \\ & +8\hat{\Phi}_G\hat{\psi}\mathrm{H}(\hat{V} - \hat{V}^g) + 4\hat{d}_1 - 4k_3\hat{\Phi}_G\hat{\psi}^2\mathrm{H}(\hat{V} - \hat{V}^g)L_T^0\tau - 8\hat{d}_1\hat{f}_1\tau^2 - 8\hat{d}_1\hat{f}_1 \\ & -2\hat{d}_1k_3\hat{\Phi}_G\hat{\psi}\mathrm{H}(\hat{V} - \hat{V}^g)\tau\big) + 8\hat{d}_1\hat{f}_1\tau + 4\hat{\rho}_1\hat{f}_1^2\hat{V}H_T^0\tau^2 - 4\hat{d}_1 - 2\hat{\rho}_1\hat{V}H_T^0 \\ & +(2\hat{\rho}_1\hat{V}H_T^0 + 8\hat{\Phi}_G\hat{\psi}\mathrm{H}(\hat{V} - \hat{V}^g) + 4\hat{d}_1)\mathrm{e}^{-(k_3\hat{\psi}L_T^0 + 2\hat{f}_1)} + 4\hat{\rho}_1\hat{f}_1\hat{V}H_T^0\tau \\ & -16\hat{f}_1\hat{\Phi}_G\hat{\psi}\mathrm{H}(\hat{V} - \hat{V}^g)(\hat{\psi}k_3L_T^0\tau^2 + \tau^2 - 1) - 8\hat{\Phi}_G\hat{\psi}\mathrm{H}(\hat{V} - \hat{V}^g)\Big). \end{aligned} \tag{2.29}$$

Equating $O(\epsilon^2)$ terms for H_D gives

$$\frac{dH_D^2}{d\tau} = \frac{\hat{\rho}_1\hat{V}\,(H_T^1 - H_D^1)}{2} - (2\hat{f}_1 + k_3\hat{\psi}L_T^0)H_D^2, \tag{2.30}$$

which, on solving subject to $H_D^2(0) = 0$, we get

$$\begin{aligned} H_D^2 &= \frac{\hat{\rho}_1\hat{V}}{4(k_3\hat{\psi}L_T^0+2\hat{f}_1)^2}\Big(\big(8\hat{\Phi}_G\hat{\psi}\mathrm{H}(\hat{V}^g-\hat{V})+4\hat{d}_1\big)\big(\mathrm{e}^{-(k_3\hat{\psi}L_T^0+2\hat{f}_1)\tau}-1\big) \\ &+\big(4k_3\hat{\Phi}_G\hat{\psi}^2\mathrm{H}(\hat{V}^g-\hat{V})L_T^0\tau+2\hat{d}_1k_3\hat{\psi}L_T^0\tau+8\hat{f}_1\hat{\Phi}_G\hat{\psi}\mathrm{H}(\hat{V}^g-\hat{V})\tau \\ &-8\hat{\Phi}_G\hat{\psi}\mathrm{H}\big(\hat{V}^g-\hat{V}\big)-2\hat{\rho}_1\hat{f}_1\hat{V}H_T^0\tau-\hat{\rho}_1\hat{V}k_3\hat{\psi}H_T^0L_T^0\tau+4\hat{d}_1\hat{f}_1\tau \\ &-4\hat{d}_1\big)\big(\mathrm{e}^{-(k_3\hat{\psi}L_T^0+2\hat{f}_1)\tau}+1\big)\Big). \end{aligned} \tag{2.31}$$

Equating $O(\epsilon^2)$ terms for L_T and L_D then gives $L_T^2 = 0, L_D^2 = 0$.

Equating $O(\epsilon^3)$ terms in the H_T equation gives

$$\frac{dH_T^3}{d\tau} = -\frac{\hat{\rho}_1\hat{V}\,(H_T^2-H_D^2)}{2}. \tag{2.32}$$

Substituting for H_D^2, H_T^2 and solving for H_T^3 subject to $H_T^3(0) = 0$, we get

$$\begin{aligned} H_T^3 &= -\frac{\hat{\rho}_1^2\hat{V}^2}{48(k_3\hat{\psi}L_T^0+2\hat{f}_1)^3}\Big(\big(24k_3\hat{\Phi}_G\hat{\psi}^2L_T^0\tau+6k_3\hat{\rho}_1\hat{V}\hat{\psi}H_T^0L_T^0\tau+24\hat{d}_1(\hat{f}_1\tau+1) \\ &+48\hat{\Phi}_G\hat{\psi}(1+\hat{f}_1\tau)+12k_3\hat{d}_1\hat{\psi}L_T^0\tau+12\hat{f}_1\hat{\rho}_1\hat{V}H_T^0\tau\big)\mathrm{e}^{-(k_3\hat{\psi}L_T^0+2\hat{f}_1)\tau} \\ &+24\hat{d}_1\hat{f}_1\tau+24k_3\hat{\Phi}_G\hat{\psi}^2L_T^0\tau+12\hat{d}_1k_3\hat{\psi}L_T^0\tau-12\hat{f}_1\hat{\rho}_1\hat{V}H_T^0\tau \\ &+24\hat{f}_1^2\hat{\rho}_1\hat{V}H_T^0\tau^2-16\hat{f}_1^3\hat{d}_1\tau^3+8\hat{f}_1^3\hat{\rho}_1\hat{V}H_T^0\tau^3-4k_3^3\hat{\Phi}_G\hat{\psi}^4{L_T^0}^3\tau^3 \\ &-2\hat{d}_1k_3^3\hat{\psi}^3{L_T^0}^3\tau^3-24\hat{f}_1k_3^2\hat{\Phi}_G\hat{\psi}^3{L_T^0}^2\tau^3-12k_3^2\hat{f}_1\hat{d}_1\hat{\psi}^2{L_T^0}^2\tau^3 \\ &-48\hat{f}_1^2k_3\hat{\Phi}_G\hat{\psi}^2L_T^0\tau^3-24\hat{d}_1\hat{f}_1^2k_3\hat{\psi}L_T^0\tau^3-32\hat{f}_1^3\hat{\Phi}_G\hat{\psi}\tau^3+48\hat{f}_1\hat{\Phi}_G\hat{\psi}\tau \\ &+k_3\hat{\rho}_1\hat{V}\hat{\psi}H_T^0L_T^0\big(6k_3\hat{\psi}L_T^0\tau^2+24\hat{f}_1\tau^2+6\hat{f}_1k_3\hat{\psi}L_T^0+k_3^2\hat{\psi}^2{L_T^0}^2\tau^3 \\ &+12\hat{f}_1^2\tau^3-6\big)-24\hat{d}_1-48\hat{\Phi}_G\hat{\psi}\Big). \end{aligned} \tag{2.33}$$

Equating $O(\epsilon^3)$ terms in the H_D equation gives

$$\frac{dH_D^3}{d\tau} = \frac{\hat{\rho}_1\hat{V}\,(H_T^2-H_D^2)}{2} - (2\hat{f}_1+k_3\hat{\psi}L_T^0)H_D^3, \tag{2.34}$$

subject to $H_D^3(0) = 0$. This can be readily solved after substituting for H_D^2 and H_T^2 from above (solution not shown for brevity).

Equating $O(\epsilon^3)$ terms in the L_T and L_D equations gives $L_T^3 = 0, L_D^3 = 0$. Equating $O(\epsilon^4)$ terms in the H_T equation then gives

$$\frac{dH_T^4}{d\tau} = -\frac{\hat{\rho}_1 \hat{V}\,(H_T^3 - H_D^3)}{2}. \tag{2.35}$$

Again, after substituting for H_D^3, H_T^3, (2.35) can be easily solved subject to $H_T^4(0) = 0$ (solution not shown for brevity).

Equating $O(\epsilon^4)$ in the H_D equation gives

$$\frac{dH_D^4}{d\tau} = \frac{\hat{\rho}_1 \hat{V}\,(H_T^3 - H_D^3)}{2} - (2\hat{f}_1 + k_3\hat{\psi}L_T^0)H_D^4 - k_3\hat{\psi}H_T^0 L_D^4, \tag{2.36}$$

subject to $H_D^4(0) = 0$. Here, L_T^4 and L_D^4 respectively satisfy $\frac{dL_T^4}{d\tau} = 1 - L_T^0/2$ and $\frac{dL_D^4}{d\tau} = 1 - L_T^0/2$, subject to $L_T^4(0) = 0$ and $L_D^4(0) = 0$ respectively, which in solving gives

$$L_T^4 = \Big(1 - \frac{L_T^0}{2}\Big)\tau \text{ and } L_D^4 = \Big(1 - \frac{L_T^0}{2}\Big)\tau. \tag{2.37}$$

Equation (2.36) can then be readily solved after substituting for H_D^3, H_T^3 and L_D^4 (solution not shown for brevity).

Now, equating $O(\epsilon^5)$ terms for L_T gives

$$\frac{dL_T^5}{d\tau} = 2\hat{\Phi}_G \mathrm{H}(\hat{V}^g - \hat{V}), \tag{2.38}$$

subject to $L_T^5(0) = 0$, which on solving gives $L_T^5 = 2\hat{\Phi}_G \mathrm{H}(\hat{V}^g - \hat{V})\tau$.

Equating $O(\epsilon^5)$ terms for L_D^5 then gives

$$\frac{dL_D^5}{d\tau} = 2\hat{\Phi}_G - k_3 L_T^0 H_D^1, \tag{2.39}$$

subject to $L_D^5(0) = 0$, which upon solving gives

$$\begin{aligned} L_D^5 &= \frac{-1}{2(k_3\hat{\psi}L_T^0 + 2\hat{f}_1)^2}\Big(\big(k_3\hat{\rho}_1\hat{V}H_T^0 + 4k_3\hat{\Phi}_G\hat{\psi} + 2\hat{d}_1k_3\big)L_T^0\mathrm{e}^{-(k_3\hat{\psi}L_T^0+2\hat{f}_1)\tau} \\ &+\big(k_3^2\hat{\rho}_1\hat{V}\hat{\psi}L_T^0H_T^0\tau + 2\hat{f}_1k_3\hat{\rho}_1\hat{V}H_T^0\tau - 8\hat{f}_1k_3\hat{\Phi}_G\hat{\psi}\tau + 2\hat{d}_1k_3^2\hat{\psi}L_T^0\tau \\ &+4\hat{d}_1\hat{f}_1k_3\tau - k_3\hat{\rho}_1\hat{V}H_T^0L_T^0 - 4k_3\hat{\Phi}_G\hat{\psi} - 2\hat{d}_1k_3\big)L_T^0 - 16\hat{f}_1^2\hat{\Phi}_G\tau\Big). \quad (2.40) \end{aligned}$$

We equate $O(\epsilon^5)$ terms in the H_T and H_D equations and solve (solution not shown). The approximations for H_T and H_D compare very well with the numerical solution for $t \in [0, \epsilon^4]$ as shown in Figure 2.3 for $V \geq V^g$ (inclusive of all terms up to $O(\epsilon^5)$) and in Figure 2.4 for $V < V^g$ (inclusive of all terms up to $O(\epsilon^2)$).
Equating $O(\epsilon^6)$ terms in the L_D equation gives

$$\frac{dL_D^6}{d\tau} = L_T^0\left(\frac{\hat{\rho}_2\hat{V}}{2} - k_3H_D^2\right), \quad (2.41)$$

subject to $L_D^6(0) = 0$, which can be easily solved upon substitution for H_D^2.

Equating $O(\epsilon^6)$ terms in the L_T equation gives $\dfrac{dL_T^6}{d\tau} = -\hat{\rho}_2\hat{V}L_T^0/2$, which subject to $L_T^6(0) = 0$, solves to

$$L_T^6 = \frac{-\hat{\rho}_2\hat{V}L_T^0\tau}{2}. \quad (2.42)$$

We equate $O(\epsilon^7)$ and $O(\epsilon^8)$ terms in the L_D equation and present the approximate solutions in Figure 2.3 for $V \geq V^g$ (inclusive of all terms up to $O(\epsilon^8)$) and in Figure 2.4 for $V < V^g$ (inclusive of all terms up to $O(\epsilon^6)$).
The approximations for L_T, inclusive of all terms up to $O(\epsilon^6)$, compare very well with the numerical solutions for $t \in [0, \epsilon^4]$ as shown in Figure 2.3 for $V \geq V^g$ and Figure 2.4 for $V < V^g$.

With $H_I(t, \epsilon) = (H_T(t, \epsilon) + H_D(t, \epsilon))/2$, numerical inspections through variations in the magnitudes of the parameters that constitute $H_I(t, \epsilon)$ shows that, amongst other parameters, L_T^0 in particular plays a crucial role in the sharp transient in the H^+-ions profile. Recall that L_T^0 denotes the combined initial concen-

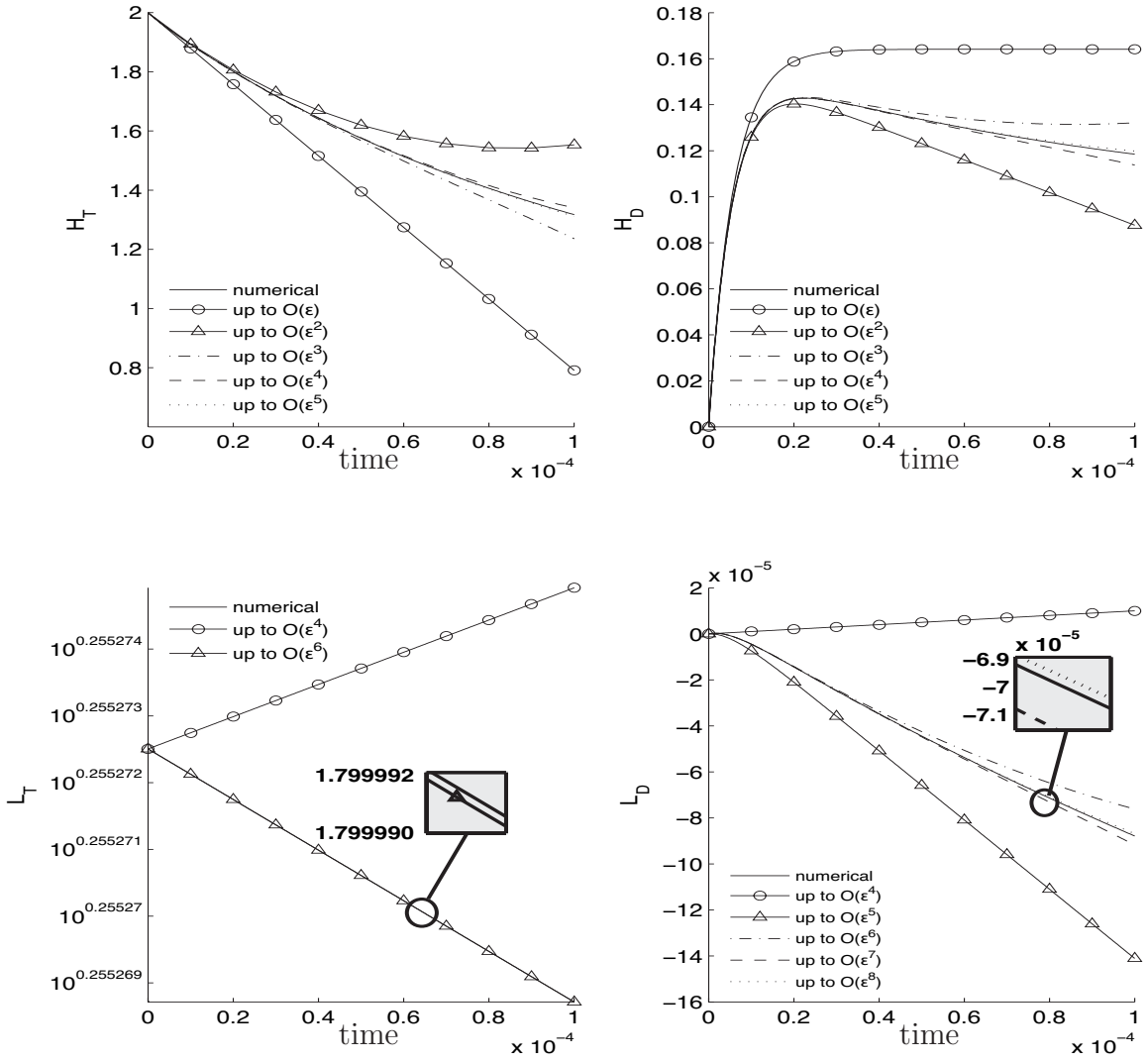

Figure 2.3: Inner solution for the normoxic case ($V \geq V^g$) in terms of increasing order of ϵ. Using perturbation analysis, we obtain an analytic approximation (shown in equations (2.25)–(2.42)) to the solution of the simpler system and compare them with the numerical solution. These solutions capture the interesting sharp transition in the pH solution that is observed in the full model for $t \in [0, \epsilon^4]$, where here we take $\epsilon = 0.1$.

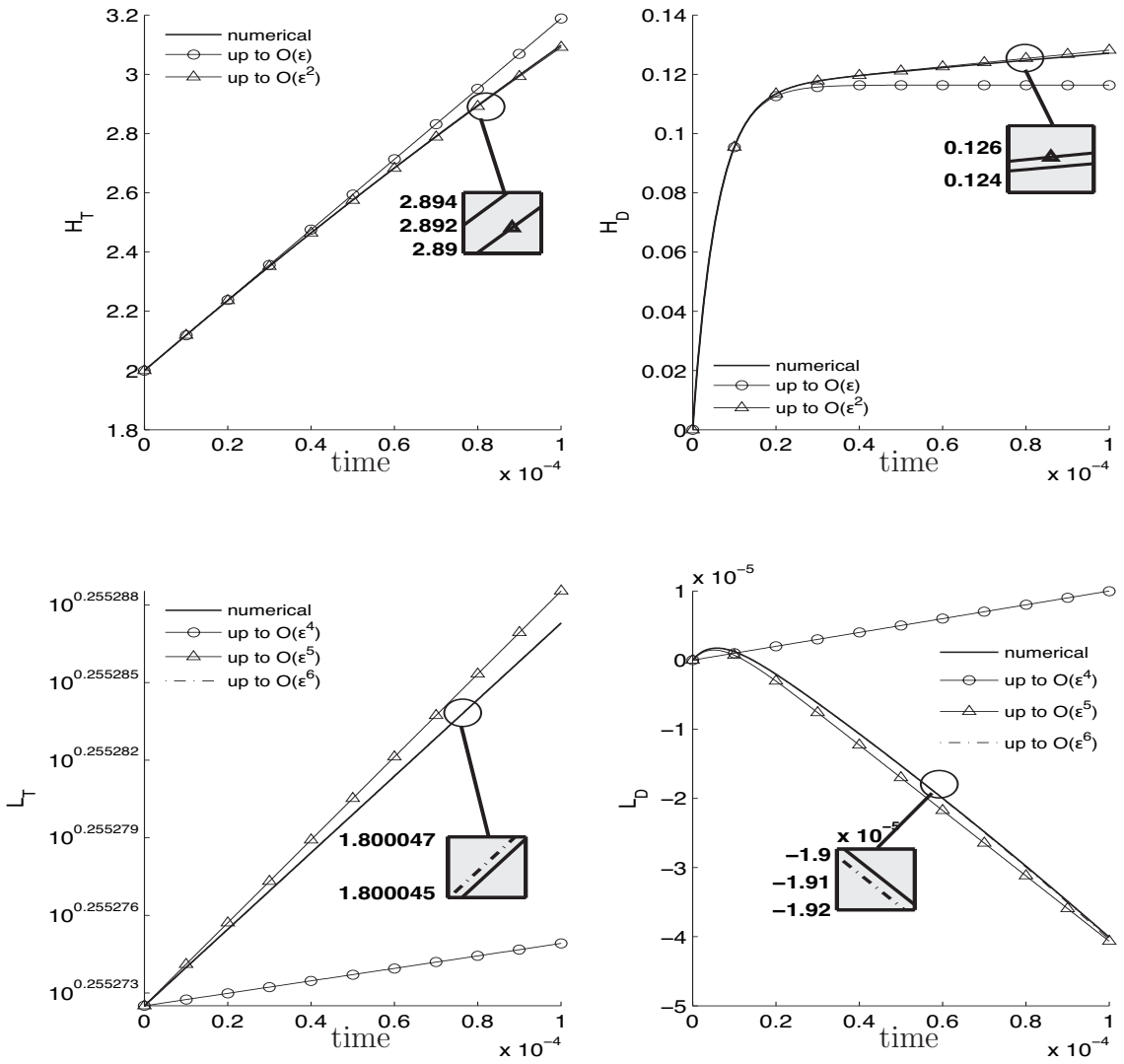

Figure 2.4: Same caption to Figure 2.3 but, here, we show the hypoxic case ($V < V^g$).

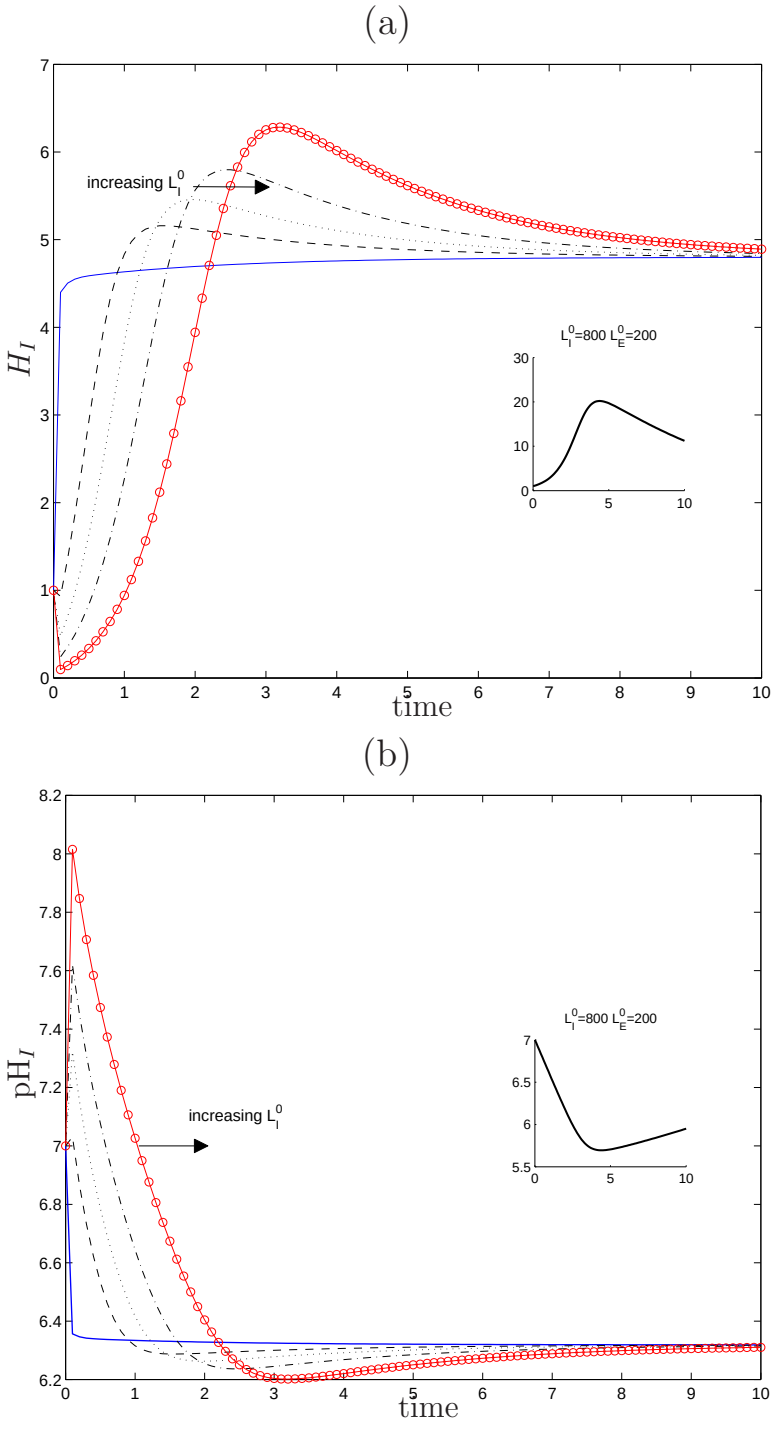

Figure 2.5: This simulation illustrates the effect of increasing the dimensionless initial concentration of intracellular lactate, L_I^0, from 0.9 (solid blue line) to 80 (solid circled line) on the steepness of (a) intracellular H^+-ions profile and (b) the corresponding pH, under hypoxic conditions. Here the initial extracellular lactate concentration, L_E^0, is 0.9. Inset shows a more shallower profile when L_I^0 as well as L_E^0 are increased to 800 and 200 respectively.

tration of intra and extracellular lactate. With the initial levels of extracellular lactate kept fixed, L_E^0, numerical simulations show that increasing the initial intracellular lactate levels, L_I^0, results in a shallow profile of H^+-ions (see Figure 2.5), which is much shallower when L_E^0 is increased (see inset of Figure 2.5). Numerical simulations illustrating the activity of the NHEs and MCTs reveal that, when L_I^0 and L_E^0 is low, the activity of the NHEs is much more rapid than the MCTs and that a sharp transient exists in the H^+-ions solution. On the other hand, a high L_I^0 and L_E^0 results in a much higher activity of the MCT (for a short time) and consequently a reversed pH gradient (for that period of time). Then, as extracellular H^+-ions and lactate build up, the MCTs import H^+-ions and lactate and hence provide intracellular H^+-ions for the NHEs to function again. Our results, therefore, suggest that the activity of the NHE indirectly controls the steepness of the initial transient of the pH solution.

2.4.2.2 Outer solution

Putting $\epsilon = 0$ in equations (2.19)–(2.22) yields the following set of differential algebraic equations

$$2\hat{\Phi}_G\hat{\psi} + \hat{d}_1 - \frac{\hat{\rho}_1\hat{V}(H_T^0 - H_D^0)}{2} = 0, \tag{2.43}$$

$$-2\hat{f}_1 H_D^0 - k_3\hat{\psi}(H_T^0 L_D^0 + H_D^0 L_T^0) = 0, \tag{2.44}$$

$$\frac{dL_T^0}{dt} = 1 - \frac{(L_T^0 + L_D^0)}{2}, \tag{2.45}$$

$$\frac{dL_D^0}{dt} = 1 - \frac{(L_T^0 + L_D^0)}{2} - k_3(H_T^0 L_D^0 + H_D^0 L_T^0). \tag{2.46}$$

Eliminating H_T^0 from equations (2.43) and (2.44) gives

$$H_D^0 = \frac{-2k_3\hat{\psi}L_D^0(2\hat{\Phi}_G\hat{\psi} + \hat{d}_1)}{\hat{\rho}_1\hat{V}(2\hat{f}_1 + k_3\hat{\psi}(L_T^0 + L_D^0))}. \tag{2.47}$$

Noting that $(L_T^0 + L_D^0) = 2L_I^0 > 0$ in (2.47) we notice that, to leading order,

1. $H_D^0 > 0$ if $L_D^0 < 0$ i.e. we have $H_E^0 < H_I^0$ if $L_I^0 < L_E^0$,

2. $H_D^0 < 0$ if $L_D^0 > 0$ i.e. we have $H_E^0 > H_I^0$ if $L_I^0 > L_E^0$.

Although this conclusion is to leading order, experiments carried out by Stubbs *et al.* [221] to determine whether lactate distribution across the cell membrane reflect the transmembrane pH in Hepatoma 9618a found that: $\mathrm{pH}_i = 7.10 > \mathrm{pH}_e = 6.79$ and $L_I = 8.36$ mM $> L_E =$3.39 mM, which is in line with our prediction that $H_E^0 > H_I^0$ if $L_I^0 > L_E^0$. We find later in this section that where a reversed pH gradient is attained, the steady state levels of intracellular lactate is always higher than the extracellular (see Figure 2.7).

The outer solutions evolve to the steady state solution which, in terms of the simple non-dimensional model, are

$$H_E^* = \begin{cases} \dfrac{d_1}{\rho_1 V}, & V \geq V^g, \\ \dfrac{d_1 + 2\Phi_G \psi}{\rho_1 V}, & V < V^g. \end{cases} \tag{2.48}$$

We note that, compared with the full model solution in equation (2.12), H_E^* here does not depend on H_I^* for the $V < V^g$ case. We also have, from (2.43)–(2.46)

$$L_I^* = \begin{cases} 1 - \rho_2 V L_E^*, & V \geq V^g, \\ 2\Phi_G + 1 - \rho_2 V L_E^*, & V < V^g, \end{cases} \tag{2.49}$$

and

$$L_E^* = \begin{cases} \dfrac{k_3 \rho_1 V H_I^*}{k_3 \rho_1 \rho_2 V^2 H_I^* + d_1 k_3 + \rho_1 \rho_2 V^2}, & V \geq V^g, \\ \dfrac{k_3 \rho_1 V (1 + 2\Phi_G) H_I^*}{\rho_1 \rho_2 V^2 k_3 H_I^* + 2 k_3 \Phi_G \psi + d_1 k_3 + \rho_1 \rho_2 V^2}, & V < V^g. \end{cases} \tag{2.50}$$

Finally, substituting (2.48), (2.49) and (2.50) into (2.16) yields a lengthy expression for H_I^* in terms of the model parameters. We show the variation of this H_I^* solution in Figure 2.6, for variations in (a) (f_1, V) and (b) (k_3, V); and in Figure 2.7, (a) (d_1, Φ_G) and (b) (d_1, k_3).

The simple model solutions are highly analogous to those of the full model in (2.12)–(2.14). The only difference is that when the glycolytic factor is dropped, the H^+-ions and lactate solutions are larger which is due to the lack of inhibitory effect of high intracellular H^+-ions on glycolysis (e.g. see Figure 2.1).

Figure 2.6 clearly shows that across a range of f_1, k_3 and V values, with better vascularisation, a tumour will have a higher pH_i and pH_e and lower intra- and extracellular lactate levels. This is supported by studies carried out by [83, 230] which shows that the intracellular pH of tumours depends on blood flow and an acute decline in blood flow results in a significant reduction in pH_i [230]. Figure 2.6(a) further indicates that an increase in f_1 raises pH_i because more H_I's are extruded. As a result, less intracellular hydrogen ions are available to bind with intracellular lactate for MCT to function and, hence, we observe that intracellular lactate builds up and extracellular lactate decreases. This observation is more apparent in the hypoxic case ($V < V^g$). There seems to be no effect on pH_e with increasing f_1, which is not surprising. In Figure 2.6(b), we see that varying k_3 has little effect on pH_i, pH_e and L_I^* but a more significant effect on L_E^*, which is more apparent in the $V \geq V^g$ region. Numerical simulations showing the activity of the NHEs and MCTs indicate that increasing k_3 results in a lower H^+-ion gradient and a lower MCT activity (the extent of the decrease is very small in the hypoxic case).

We show in Figure 2.7(a) the effect of varying Φ_G (rate of glycolysis) and d_1 (background production of H^+-ions) on the steady state solution of pH and lactate under hypoxic conditions. The pH gradient is reversed for relatively small Φ_G and d_1 which we find, from our numerical simulations, to be due to the increased activity of the MCTs. This is because a low source of intracellular H^+-ions and rate of glycolysis directly impacts the NHEs by lowering its activity. Clearly, the reversed pH gradient is above pH 8—outside the physiologically reasonable range. Figure 2.7(b) shows the effect of varying k_3 (rate of MCT activity) and d_1 (background production of H^+-ions) on the steady state solution of pH and lactate

under normoxic conditions. Note that varying k_3 and d_1 under hypoxic conditions does not result in a negative pH gradient (not shown). This is because our model predicts that the impact of the MCT on the regulation of pH_i is small in hypoxic regions (see Figure 2.6) compared to normoxic (in line with findings by Webb *et al.* in [250]). This appears to be due to the increased activity of the MCTs which is evident from the decreased L_I^* and increased L_E^*. Biologically, this implies that lowering sources of intracellular H^+-ions other than those resulting from glycolysis can give rise to highly alkaline reversed pH gradient. For example, lowering the Carbonic Anhydrase (CA) catalysed hydration of CO_2 into HCO_3^- and H^+-ions can enhance the efficacy of chemotherapeutics by alkalising the intra and extracellular pH. This is supported by an *in vitro* study by Parkkila *et al.* [169] which found that a potent CA inhibitor suppresses the relative invasion rate of renal carcinoma cell lines by 18–74%.

2.5 Discussion and conclusions

Some tumours are reported to have an acidic extracellular environment, which is often thought to give them a greater survival advantage [75]. It is believed that this is caused by elevated glycolysis which results in the up-regulation of certain cellular transporters. In this chapter, we have described a mathematical model that focuses on the interplay between H^+-ions and lactate in tumours. The main differences between normal and tumour cells in the model are: tumour cells rely heavily on the inefficient glycolytic pathway for energy production and also their clearance rate of extracellular ions is assumed to be poor. Qualitative analysis of the model shows that tumour cells have higher levels of lactate and lower pH, which is in line with experimental observations [75]. Further analysis of the steady state solutions shows that, the more vascularised the cell, the higher the intra and extracellular pH and the lower the lactate levels. This is supported by studies carried out by [83, 230] which shows that the intracellular pH of tumours depend

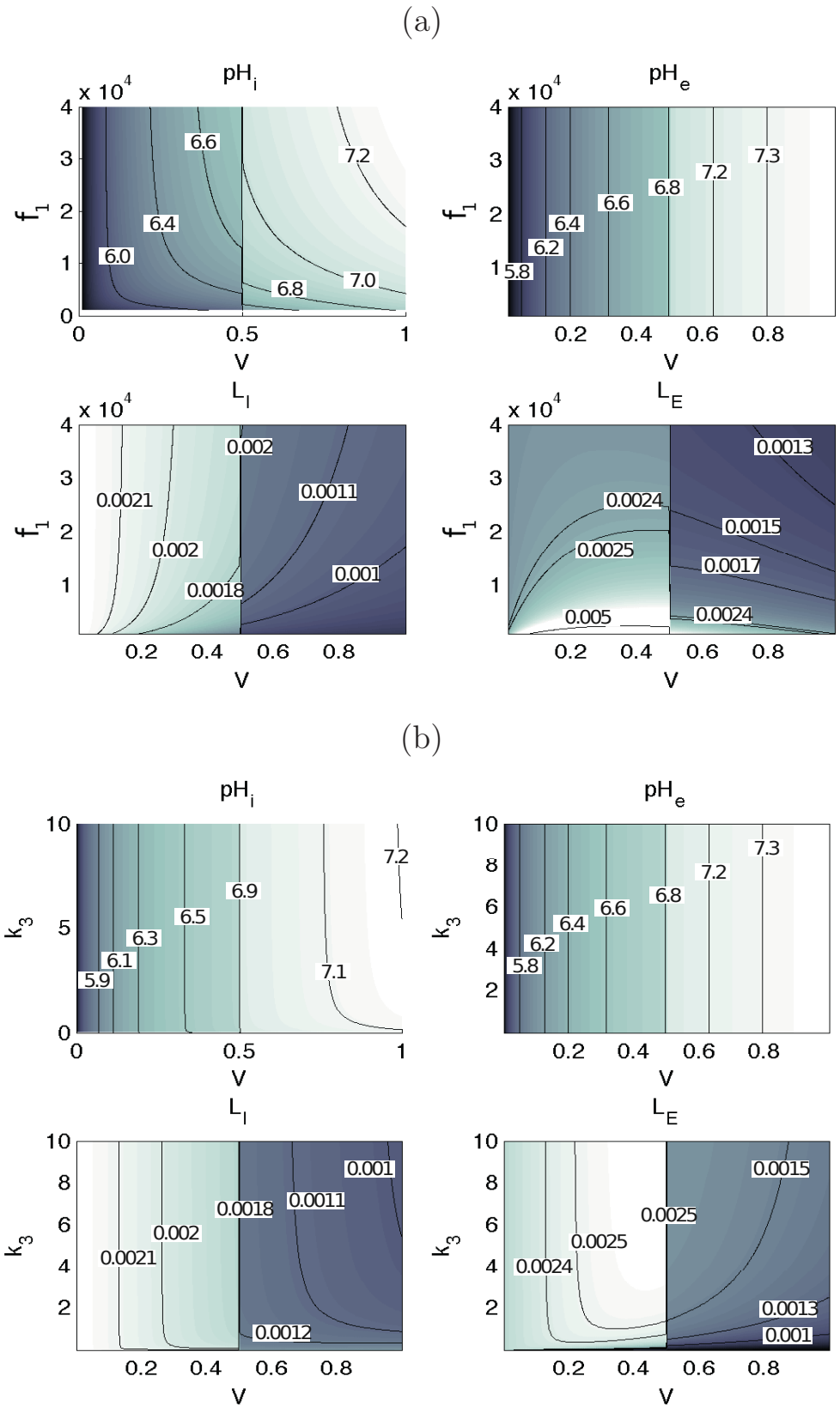

Figure 2.6: We illustrate the effect of varying key parameters (a) f_1 (NHE rate activity) *versus* V (vasculature); and (b) k_3 (MCT rate activity) *versus* V on the steady state solution of pH and lactate. In both simulations, vasculature spans from poorly formed blood vessels ($V < V^g = 0.5$) to very efficient ones ($V \geq V^g = 0.5$.)

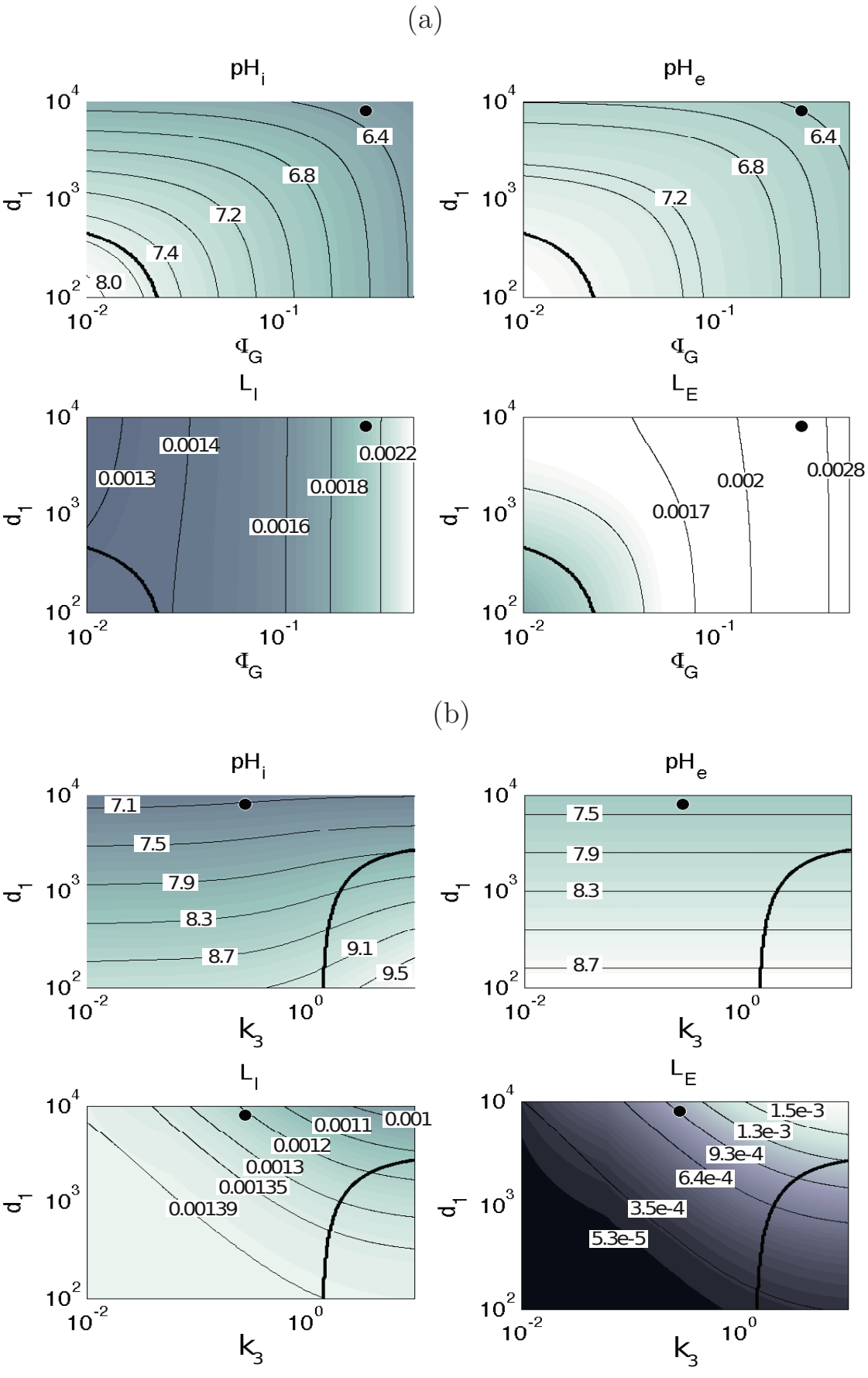

Figure 2.7: Caption on following page.

Figure 2.7: (Previous page). (a) The effect of varying Φ_G (rate of glycolysis) and d_1 (background production of H^+-ions) on the steady state solution of pH and lactate under hypoxic conditions using the simple model. Regions below the black thick curve represent a reversed pH gradient whilst above is otherwise. Values of pH and lactate for the 'base' case parameter set are represented by a black filled circle. Clearly the reversed pH gradient is above pH 8—outside the physiologically reasonable range. (b) Here we show the effect of varying k_3 (rate of MCT activity) and d_1 on the steady state solution of pH and lactate under normoxic conditions using the simple model.

on blood flow and an acute decline in blood flow results in a significant reduction in pH_i [230]. Our qualitative analysis also shows that decreasing the quantity of hydrogen ions produced from sources other than metabolism can cause the pH cellular gradient to be reversed.

Numerical simulations in Section 2.4 show that, after an initial transient, the intra and extracellular pH sharply attain their steady state value. To study this behaviour in more detail, we have considered a simplified model, in which we neglect the inhibitory effect of low intracellular pH on glycolysis. Investigation of this model using singular perturbation analysis has given considerable insight into the behaviour of the solution, and has provided a good analytical approximation to the solutions of the system. These solutions compare very well with the numerical simulations, and capture the interesting transition in the pH solution that is observed in the full model. We find that the initial concentrations of intra and extracellular lactate play a key role in this sharp transient. Numerical simulations show that a high initial value of intracellular lactate results in a sharp increase in the activity of the MCTs which gives rise to a transiently reversed pH gradient and as a result a suspended NHE activity. This seems to explain the shallow profile obtained when the initial concentration of intracellular lactate is increased, which is more shallow when extracellular lactate is also increased. Therefore, we

conclude that the activity of the Na^+/H^+ exchanger plays a key role in the sharp initial transient in the pH solution relative to lactate.

Analysis of the model show that, with the inclusion of lactate explicitly in the model, a reversed pH gradient is attainable under aerobic conditions when other sources of hydrogen ions are decreased and MCT activity is increased—but we find the pH conditions that this reversed gradient is found to be too alkaline to be viable and therefore is unrealistic. Under anaerobic conditions, we find that decreasing 'other sources of H^+-ions' and the glycolytic rate gives rise to a reversed cellular pH gradient, but again it is too alkaline to be biologically realistic. This suggests that another mechanism could be contributing to support a physiologically reasonable reversed pH gradient and we are driven in the next chapter to find if a more realistic spatial representation of the tumour may have an effect on reproducing a biologically realistic reversed pH.

A recent study by Colen *et al.* [51] indicates that glioma invasion was markedly impaired when lactate efflux was inhibited. More specifically, it was found to cause complete necrosis in some cases. A more recent study by Sonveaux *et al.* [215] shows that blocking lactate influx through MCT1 can lead to anti-angiogenic and anti-metabolic effects. Our study suggests that, for some values of background production of H^+-ions, decreasing the MCT activity will diminish the reversed pH gradient which is known to be implicated in tumour invasiveness [248].

Chapter 3

Spatial distribution of H^+-ions and lactate in a one-dimensional monolayer

3.1 Introduction

A variety of modelling techniques are now widely used to examine features of cancer progression. The ordinary differential equation model, presented in Chapter 2, shows that a reversed cellular pH gradient that is seen in some tumours is possible with the factors that we consider, but we find it in our model for biologically unrealistic parameter estimates. To increase the biological realism of our model we consider the fact that tissue has spatial structure. In so doing, we also examine the findings of Provent *et al.* [183] that, in some cases, the spatial concentrations of extracellular lactate and extracellular hydrogen ions are often uncorrelated. That is, regions with high extracellular acidity do not necessarily correlate with high levels of lactate [183]. In Section 3.3.3, we investigate the conditions under which this phenomenon is observed. It is suggested that this is because protons, which are exported outside cells along with lactate in hypoxic regions, re-enter the cells

indirectly via the HCO_3^-/Cl^- exchanger or simply leak back into the cell and then are transported cell-to-cell via gap junctions to make protons available for the NHE exchanger [183]. Another study by Grillon *et al.* [94] reports that the distribution of NHEs and MCTs in rat brain gliomas are heterogeneous—the relative intensity of NHE1 (isoform 1) peaks at an average distance of 0.33±0.027 mm from the edge of the tumour and expression of the MCT1 (which can transport lactate and H^+ either out of or into cells [99]) peaks further into the glioma (1.05±0.14 mm from the edge of the tumour). We incorporate these findings into the model in Section 3.3.5 and examine their effect on the cellular pH gradient. We finally investigate in Section 3.3.6 the effect of H^+-ion intercellular gap junctions on the cellular pH gradient reversal and the spatial distribution of extracellular lactate and H^+-ions.

3.2 Model formulation

For simplicity, we assume a one-dimensional Cartesian geometry, such that $0 \leq x \leq L$, where L denotes the distance away from the blood vessel which is located at $x = 0$. Our model has the form

$$\frac{dH_I}{dt} = \frac{2\Phi_G \mathrm{H}(V^g - V)}{H_I + b} + d_1 + \phi, \tag{3.1}$$

$$\frac{dL_I}{dt} = \frac{2\Phi_G \mathrm{H}(V^g - V)}{H_I + b} + d_4 - \alpha_4 L_I - \theta, \tag{3.2}$$

$$\frac{\partial H_E}{\partial t} = D_H \frac{\partial^2 H_E}{\partial x^2} - \phi, \tag{3.3}$$

$$\frac{\partial L_E}{\partial t} = D_L \frac{\partial^2 L_E}{\partial x^2} + \theta, \tag{3.4}$$

where,

$$\theta = k_3(H_I L_I - H_E L_E),$$

$$\phi = l_H(H_E - H_I) - f_1 \mathrm{H}(H_I - H_E)(H_I - H_E) - k_3(H_I L_I - H_E L_E),$$

and $\mathrm{H}(\cdot)$ is a Heaviside (as in Chapter 2).

The current model differs from that in Chapter 2 via the added diffusion terms of extracellular H^+-ions and lactate, with diffusion coefficients D_H and D_L respectively. Also, here the boundary conditions at $x = 0$ replace the removal terms, $R_\sigma(V)$, σ =1 and 2, used in Chapter 2 for extracellular H^+-ions and lactate respectively. Rather than including the complexity of an additional equation for oxygen, we simply assume a linear decreasing concentration of O_2 (denoted by V) from the blood vessel located at $x = 0$, namely $V = 1 + (\gamma - 1)x/L$, where $\gamma = \in [0, 1)$ (see Figure 3.1 for a schematic). With appropriate choices of γ, we can either simulate a tumour which is completely well-oxygenated (e.g. if $\gamma = 1$) or a tumour that is hypoxic for $V < V^g$ (i.e. $x^g < x \leq L$) and aerobic for $V \geq V^g$ (i.e. $0 \leq x \leq x^g$), where $x = x^g$ is the point at which $V = V^g$. As in Chapter 2, we assume that glucose supply is plentiful $\forall x \in [0, L]$. We impose boundary conditions to represent a tumour with a well-perfused blood vessel (on the left side of the tissue, $x = 0$) which supplies the tumour with oxygen and removes H^+-ions and lactate. That is

$$\begin{aligned}
\text{At } x = 0: \qquad D_H \frac{\partial H_E}{\partial x}(0,t) &= \rho_{Hl}(H_E(0,t) - H_{\infty l}),\\
D_L \frac{\partial L_E}{\partial x}(0,t) &= \rho_{Ll}(L_E(0,t) - L_{\infty l}),\\
\text{At } x = L: \qquad H_E(L,t) &= H_{\infty r},\\
-D_L \frac{\partial L_E}{\partial x}(L,t) &= \rho_{Lr}(L_E(L,t) - L_{\infty r}),
\end{aligned}$$

where $H_{\infty l}$ and $L_{\infty l}$ are, respectively, the concentrations of hydrogen ions and lactate inside the blood vessel at $x = 0$. Their rate of leakage into or out of the blood vessel at $x = 0$ is regulated by the parameters ρ_{Hl} and ρ_{Ll} respectively. A similar notation is used for lactate at the right hand side boundary condition, but with $L_{\infty r}$ denoting estimated tissue lactate levels. Based on an experimental observation, we take a fixed boundary condition at $x = L$ for the extracellular H^+ since findings show that at $L = 2$ mm, the extracellular pH is known to be around 6.5 (Personal Communication with Jonathan Coles, Institute of Photonics, University of Strathclyde).

We denote the initial values by their normal concentration in the tissue, namely, $H_I(x,0) = H_I^0$ mol/l, $H_E(x,0) = H_E^0$ mol/l, $L_I(x,0) = L_I^0$ mol/l, $L_E(x,0) = L_E^0$ mol/l.

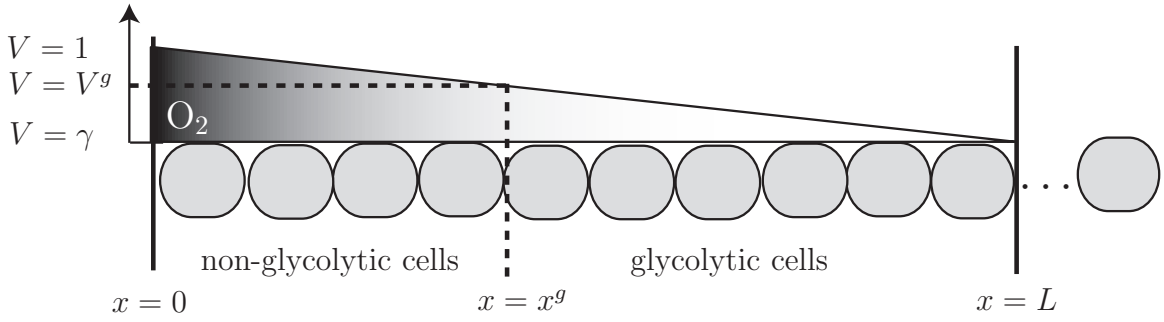

Figure 3.1: A schematic representation of the distribution of glycolytic ($V < V^g$) and non-glycolytic cells ($V \geq V^g$) in the 1-D spatial model (3.1)–(3.4). $x = 0$ denotes the location of the blood vessel.

Non-dimensionlisation

To facilitate the numerical study of the model, we rescale space, $\tilde{x} = \sqrt{\alpha_4/D_H}x$, where the tilde represents the rescaled space. This scales out the diffusion parameter for H^+-ions, D_H. The remaining variables are rescaled as in Chapter 2, namely

$$\tilde{H}_I = \frac{H_I}{b},\ \tilde{H}_E = \frac{H_E}{b},\ \tilde{L}_I = \frac{\alpha_4 L_I}{d_4},\ \tilde{L}_E = \frac{\alpha_4 L_E}{d_4},\ \tilde{t} = \alpha_4 t.$$

The dimensionless equations then read

$$\frac{d\tilde{H}_I}{d\tilde{t}} = \frac{2\tilde{\Phi}_G\psi \mathrm{H}(V^g - V)}{\tilde{H}_I + 1} + \tilde{d}_1 + \tilde{\phi}, \tag{3.5}$$

$$\frac{d\tilde{L}_I}{d\tilde{t}} = \frac{2\tilde{\Phi}_G \mathrm{H}(V^g - V)}{\tilde{H}_I + 1} + 1 - \tilde{L}_I - \tilde{\theta}, \tag{3.6}$$

$$\frac{\partial\tilde{H}_E}{\partial\tilde{t}} = \frac{\partial^2\tilde{H}_E}{\partial\tilde{x}^2} - \tilde{\phi}, \tag{3.7}$$

$$\frac{\partial\tilde{L}_E}{\partial\tilde{t}} = \tilde{D_L}\frac{\partial^2\tilde{L}_E}{\partial\tilde{x}^2} + \tilde{\theta}, \tag{3.8}$$

where,

$$\tilde{\theta} = \tilde{k}_3(\tilde{H}_I\tilde{L}_I - \tilde{H}_E\tilde{L}_E),$$

$$\tilde{\phi} = \tilde{l}_H(\tilde{H}_E - \tilde{H}_I) - \tilde{f}_1\mathrm{H}(\tilde{H}_I - \tilde{H}_E)(\tilde{H}_I - \tilde{H}_E) - \tilde{k}_3\psi(\tilde{H}_I\tilde{L}_I - \tilde{H}_E\tilde{L}_E).$$

We use the same rescalings as in Chapter 2 for the model parameters and, with these rescalings, the boundary conditions then become

$$\frac{\partial\tilde{H}_E}{\partial\tilde{x}}(0,\tilde{t}) = \tilde{\rho}_{Hl}(\tilde{H}_E(0,\tilde{t}) - \tilde{H}_{\infty l}), \ \frac{\partial\tilde{L}_E}{\partial\tilde{x}}(0,\tilde{t}) = \tilde{\rho}_{Ll}(\tilde{L}_E(0,\tilde{t}) - \tilde{L}_{\infty l}), \tag{3.9}$$

$$\tilde{H}_E(\tilde{L},\tilde{t}) = \tilde{H}_{\infty r}, \ \frac{\partial\tilde{L}_E}{\partial\tilde{x}}(\tilde{L},\tilde{t}) = -\tilde{\rho}_{Lr}(\tilde{L}_E(\tilde{L},\tilde{t}) - \tilde{L}_{\infty r}), \tag{3.10}$$

where,

$$\tilde{\rho}_{Hl} = \frac{\rho_{Hl}}{\sqrt{\alpha_4 D_H}}, \ \tilde{H}_{\infty l} = \frac{H_{\infty l}}{b}, \ \tilde{\rho}_{Ll} = \frac{\rho_{Ll}}{D_L}\sqrt{\frac{D_H}{\alpha_4}}, \ \tilde{L}_{\infty l} = \frac{\alpha_4 L_{\infty l}}{d_4}, \ \tilde{H}_{\infty r} = \frac{H_{\infty r}}{b},$$

$$\tilde{\rho}_{Lr} = \frac{\rho_{Ll}}{D_L}\sqrt{\frac{D_H}{\alpha_4}}, \ \tilde{L}_{\infty r} = \frac{\alpha_4 L_{\infty r}}{d_4}, \ \tilde{D}_L = \frac{D_L}{D_H}, \ \tilde{L} = \sqrt{\frac{\alpha_4}{D_H}}L.$$

And the initial conditions become

$$\tilde{H}_I(\tilde{x},0) = \tilde{H}_I^0, \ \tilde{H}_E(\tilde{x},0) = \tilde{H}_E^0, \ \tilde{L}_I(\tilde{x},0) = L_I^0, \ \tilde{L}_E(\tilde{x},0) = \tilde{L}_E^0, \tag{3.11}$$

where,

$$\tilde{H}_I^0 = \frac{H_I^0}{b}, \ \tilde{H}_E^0 = \frac{H_E^0}{b}, \ \tilde{L}_I^0 = \frac{\alpha_4 L_I^0}{d_4}, \ \tilde{L}_E^0 = \frac{\alpha_4 L_E^0}{d_4}.$$

3.3 Numerical solution

3.3.1 Spatial discretisation and numerical scheme

We divide the spatial domain into N uniformly spaced points with grid size, $\Delta x = L/(N-1)$. This allows the problem to be solved in MATLAB using a built-in ODE solver (ode15s) with four ODEs in time (for H_I, H_E, L_I, L_E) at each space point. The grid function $u(x_j, t)$, $u \in \{H_I, H_E, L_I, L_E\}$, denotes an approximation of u at x_j, where $1 \leq j \leq N$. For the diffusion terms of H_E and L_E, we use a simple finite difference approximation in the interior points using a second central difference of the form

$$\frac{\partial^2 u_j}{\partial x^2} \approx \frac{u_{j+1} - 2u_j + u_{j-1}}{\Delta x^2}; \quad 1 \leq j \leq N-1. \tag{3.12}$$

We approximate u_0 using a first order central difference

$$\frac{\partial u_1}{\partial x} \approx \frac{u_2 - u_0}{2\Delta x} = \rho_{vl}(u_1 - v_{\infty l}) \Rightarrow u_0 = u_2 - 2\Delta x \rho_{vl}(u_1 - v_{\infty l}), \tag{3.13}$$

where $v \in \{H, L\}$ and $v_{\infty l}$ is the corresponding blood level of H^+-ions or lactate respectively. We approximate $\partial^2 u_j/\partial x^2$ at $j = N$ in a similar manner.

3.3.2 Parameter estimates

From the literature, we are able to estimate some of the new parameters. We take the diffusion co-efficient of H^+ ions (D_H) to be 1.08×10^{-5} cm^2/s [127] and that of lactate (D_L) to be 8.8×10^{-6} cm^2/s [259]. We assume that cells near the blood vessel are well-oxygenated and that extracellular lactate and H^+-ions leak in or out of the blood vessel at a much higher rate than extracellular lactate does into the tissue at $x = L$ due to the leakiness of the tumour vasculature. The vessel permeability to lactic acid (ρ_{Ll}) is taken to be 1.19×10^{-4} cm/s [53], for which the non-dimensional equivalence is $4.4 \times 10^{-2}/\sqrt{\alpha_4}$. With a lack of available data, we also assume that H^+ ions have the same vessel permeability as lactate. Also, because of the lack of available data on the rate of lactate decay (α_4), we vary this parameter in Section 3.3.3 and note the effect on the overall model behaviour.

In general, normal blood lactate in unstressed patients is between 0.5–1.0$\times 10^{-3}$ mol/l, but for patients with critical illnesses, concentrations of less than 2.0$\times 10^{-3}$ mol/l are sometimes found [21]. With this in mind, we estimate lactate levels inside the blood vessel at $x = 0$, $L_{\infty l}$, to be 0.5–1.0$\times 10^{-3}$ mol/l [21], and lactate 2 mm away from the blood vessel, $L_{\infty r}$, to be 2.0$\times 10^{-3}$ mol/l [21]. Recall from our parameter estimates in Chapter 2 that $d_4/\alpha_4 \sim O(10^{-3}) \equiv 1.4 \times 10^{-3}$ mol/l, which gives $\tilde{L}_{\infty l} = 0.35$–$0.71$ and $\tilde{L}_{\infty r} = 1.42$ (in dimensionless form). The normal blood H^+ concentration in unstressed patients is found to be in the range of 3.55–4.5×10^{-8} mol/l [178] and we take this value to represent $H_{\infty l}$.

Almost fifty years following Warburg's pioneering work on tumour metabolism [247], extensive studies have concluded that glucose is a main energy source for malignant tumours [73, 74] and that 60% of cancer cells are glycolytic [55]. We therefore partition our tumour section so that 60% of the cells undergo anaerobic glycolysis and the remaining 40% do not. We simulate the model with appropriate non-dimensional initial conditions that represent normal tissue levels: $\tilde{H}_I^0 = 0.63$, $\tilde{H}_E^0 = 0.63$, $\tilde{L}_I^0 = 1$ and $\tilde{L}_E^0 = 1$. A summary of the non-dimensional parameter values used in the model is presented in Table 3.1. The remaining parameters are the same as those in Chapter 2 (see Table 2.1 for details).

We will work with the non-dimensional model hereafter but drop the tildes for notational convenience.

3.3.3 Spatial distribution of extracellular lactate and hydrogen ions

Given that there is some uncertainty in the values that we should take for the vessel permeabilities (ρ_{Hl} and ρ_{Ll})—mostly stemming from the uncertainty of the value of α_4 (i.e. recall that ρ_{Hl} (dimensionless) $= \rho_{Hl}/(\alpha_4 D_H)^{1/2}$ and ρ_{Ll} (dimensionless) $= \rho_{Ll}/(D_H/\alpha_4 D_L^2)^{1/2}$)—we first vary the dimensionless values of ρ_{Hl} and ρ_{Ll} in our analysis. In particular, we are interested to find if these parameters have

Table 3.1: Dimensionless parameter estimates used in the one-dimensional spatial model in (3.5)–(3.11). PC=personal communications with Jonathan Coles, Institute of Photonics, University of Strathclyde.

Description	**Symbol**	**Value**	**Ref.**
Vessel permeability to H^+ at $x = 0$	$\tilde{\rho}_{Hl}$	$4.4 \times 10^{-2}/\sqrt{\alpha_4}$	Estimate
Vessel permeability to lactate at $x = 0$	$\tilde{\rho}_{Ll}$	$4.4 \times 10^{-2}/\sqrt{\alpha_4}$	[53]
Tissue permeability to lactate at $x = L$	$\tilde{\rho}_{Lr}$	$4.4 \times 10^{-2}/\sqrt{\alpha_4}$	Estimate
Normal H^+ concentration in blood	$\tilde{H}_{\infty l}$	0.35–0.45	[226]
Lactate concentration in blood at $x = 0$	$\tilde{L}_{\infty l}$	0.35–0.71	[21]
Lactate concentration in the tissue at $x = L$	$\tilde{L}_{\infty r}$	1.42	[21]
H^+-ions concentration in the tissue at $x = L$	$\tilde{H}_{\infty r}$	3.16	PC
Diffusion co-efficient fraction	$\tilde{D}_L$	0.81	[127, 259]
Tissue size	$\tilde{L}$	0.02	PC

any effect on whether the extracellular pH is less acidic when extracellular lactate is high. Figure 3.2(a) shows how the spatial profile of extracellular pH at steady state is qualitatively reversed (i.e. from that with an increasing pH_E profile versus distance from the tumour edge x to that of a decreasing pH_E profile versus x) as ρ_{Hl} increases. It appears that this reversal occurs at roughly $\rho_{Hl} > 20$ (note that as ρ_{Hl} gradually increases from 20, pH_E slowly increases near the blood vessel and attains a minimum parabolic profile which gradually changes into a monotonically decreasing function as ρ_{Hl} further increases). The spatial profile of extracellular lactate, however, remains qualitatively unchanged (see Figure 3.2(b)) as ρ_{Hl} increases. Note that varying the rate of removal of lactate into the blood vessel, ρ_{Ll}, has no qualitative effect on the spatial profile of lactate and pH as illustrated in Figure 3.2(c)–(d)).

We show a typical simulation with large ρ_{Hl} and ρ_{Ll} (=O(10^3)) in Figure 3.3. We illustrate the profiles with and without the inclusion of the "glycolytic factor"

(i.e. the denominator $H_I + 1$ in the first term of equations (3.5) and (3.7)). Note that dropping this glycolytic factor from the model equations has no qualitative effect on the model behaviour. Hence, we work with the simplified model (i.e. with the glycolytic factor dropped) from this point on because we exploit the simpler form analytically later in this chapter. Note that dropping the "glycolytic factor" does, however, have a quantitative effect on the rate of activity of the NHE and MCT in the anaerobic region (see Figure 3.3(b)). This is because the inhibitory effects of low intracellular pH on glycolysis is neglected when the "glycolytic factor" is dropped. As a result, the intra- and extracellular pH is more acidic and the extracellular lactate becomes higher throughout the domain. We also observe that the levels of intracellular lactate in the aerobic region is slightly lower when the "glycolytic factor" is dropped which is attributed to the slightly higher MCT activity and lower NHE activity there.

Also note the "jump" in the intracellular concentration profiles and the activity of the membrane-based transporters observed at $x = x^g$. This is due to the switch from aerobic metabolism in the $x \leq x^g$ region to anaerobic metabolism in the $x > x^g$ region where oxygen levels are low. The extracellular lactate and pH display no significant observable "jump" in their profile due to the smoothed effect of diffusion. The key solution features are as follows: intracellular H^+-ions, extracellular H^+-ions and extracellular lactate are higher in the region further away from the blood vessel (i.e. in the $x > x^g$ region) than that in the aerobic region close to the blood vessel (both with and without the inclusion of the "glycolytic factor"). However, intracellular lactate levels increase in the anaerobic region but quickly drop to levels below that found close to the blood vessel (both with and without the inclusion of the "glycolytic factor"). This could be because the NHE activity near the blood vessel is high due to the larger H^+-ions transmembrane gradient as a result of an increased removal of extracellular H^+-ions into the blood vessel. Consequently, the MCT activity near the blood vessel becomes low because there are less intracellular H^+-ions available for extrusion and as a result intracellular

lactate levels near the blood vessel become high and decrease as the activity of the NHE decreases (away from the blood vessel).

On the other hand, we do observe a spatial correlation between the increase in extracellular pH and the increase in extracellular lactate as shown in Figure 3.4. This is in line with the findings of Provent *et al.* [183] which showed that the glucose-induced increase in extracellular lactate showed no associated decrease in extracellular pH. However, they suggest that the re-distribution of extracellular H^+-ions at sites remote from anaerobic lactate production is primarily due to the leakage of H^+-ions intracellularly and their subsequent transfer by gap junctions to make them available for extrusion by the NHEs. In contrast, our model predictions suggest that this same result can be observed in the absence of gap junctions, and instead with a reduced permeability of the blood vessels to H^+-ions and lactate. In a biological sense, we may interpret our results by suggesting that less-efficient blood vessels, which are indeed frequently found in tumours, are likely to give rise to a contrasting spatial distribution of extracellular pH and lactate.

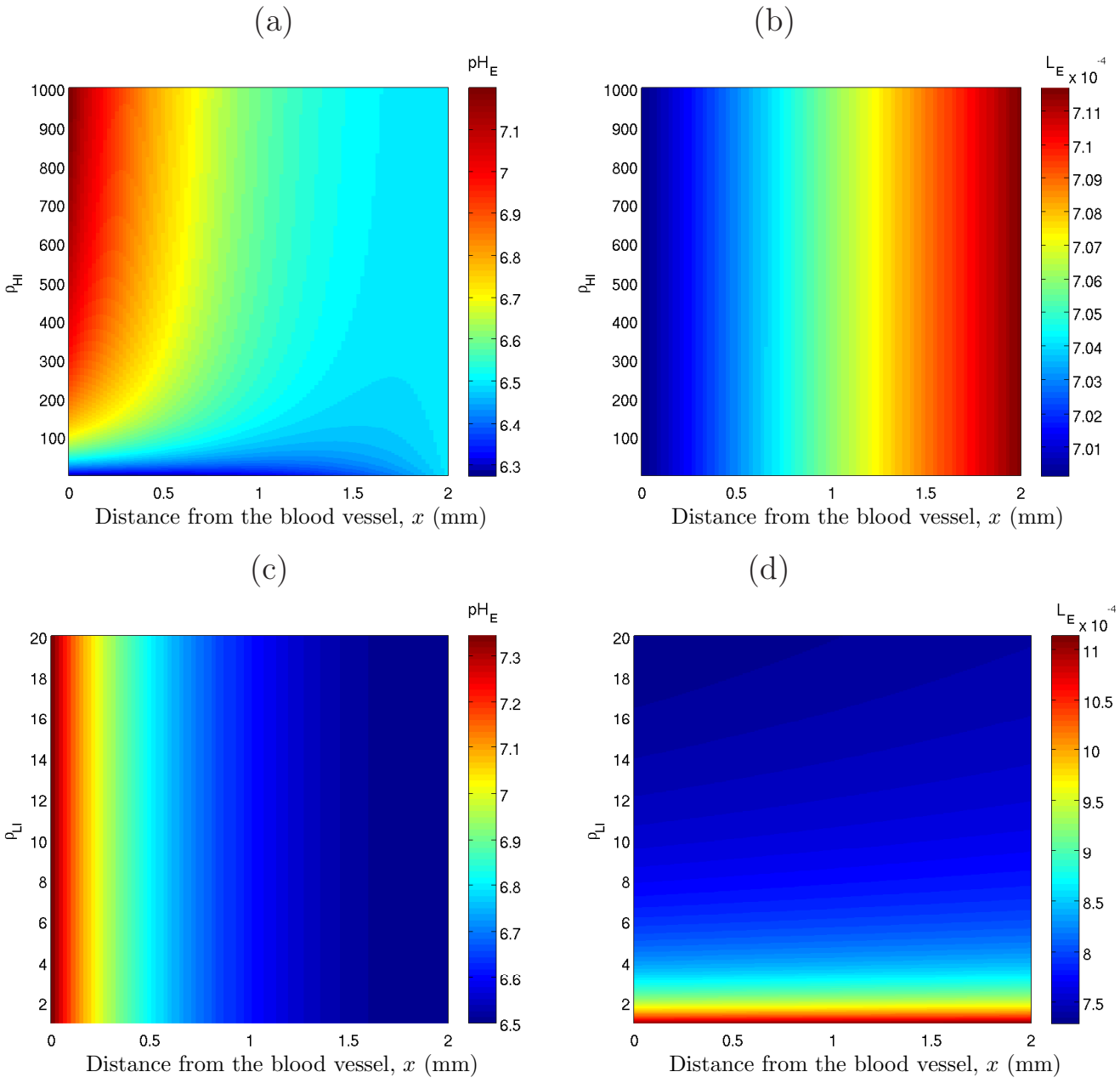

Figure 3.2: Plots showing the effect of varying the rate of H^+-ions leakage into the blood vessel (ρ_{Hl}) on the spatial profile of (a) pH_E and (b) L_E; and the effect of varying the rate of lactate leakage into the blood vessel (ρ_{Ll}) on the spatial profile of (c) pH_E and (d) L_E. In (a)– (b):$\rho_{Ll} = 4.4 \times 10^3$. In (c)–(d):$\rho_{Hl} = 4.4 \times 10^3$. Remaining parameter values are as in Table 3.1 and with $\rho_{Lr} = 0.44, L_{\infty l} = 0.5, L_{\infty r} = 1.42, H_{\infty l} = 0.398$. The prescribed model is simulated until the steady state solution is reached, starting from the initial conditions: $H_I^0 = 0.63$, $H_E^0 = 0.63$, $L_I^0 = 1$ and $L_E^0 = 1$. We determine whether the steady state solution is reached by considering the solution at time step, i, and time step, $i+1$. If the absolute difference in solution is less than some ε (we choose to be 10^{-6}), then the model stops running at the i^{th} step. With this value of ε, the metabolites reach a steady state at $t = 6$.

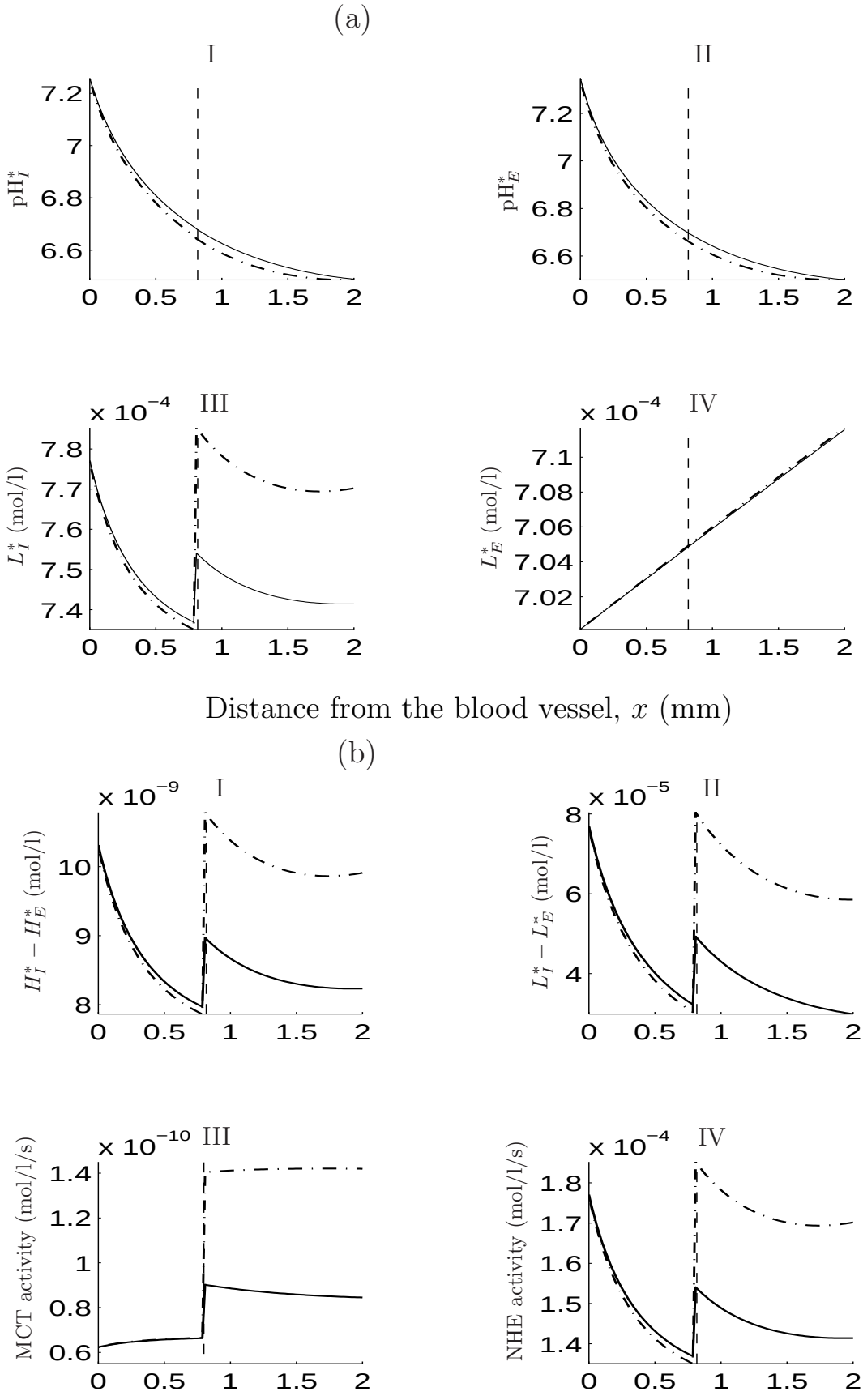

Figure 3.3: Caption on following page.

Figure 3.3: (Previous page). Numerical solution of the system (3.5)–(3.11), (——, glycolytic factor included) and (– · – ·, glycolytic factor dropped). Obtained using an ODE stiff solver from MATLAB. As in Chapter 2, we denote by the superscripted $*$ the steady state levels. The vertical dashed lines denote $x = x^g$, where here $x^g = (4\gamma + 6)/10$, with γ chosen to be 0.1 throughout the simulations in this chapter. (a) A spatial correlation exists between extracellular lactate levels and pH_E (e.g. compare (a)II and (a)IV). (b)I shows the hydrogen ion gradient, (b)II the lactate gradient, (b)III the MCT activity and (b)IV the NHE activity. Parameter values are as in Table 3.1 with $\rho_{Hl} = 4.4 \times 10^3, \rho_{Ll} = 4.4 \times 10^3, \rho_{Lr} = 0.44, L_{\infty l} = 0.5, L_{\infty r} = 1.42, H_{\infty l} = 0.398$. The prescribed model is simulated until the steady state solution is reached, starting from the initial conditions: $H_I^0 = 0.63$, $H_E^0 = 0.63$, $L_I^0 = 1$ and $L_E^0 = 1$. We determine whether the steady state solution has been reached as in Figure 3.2.

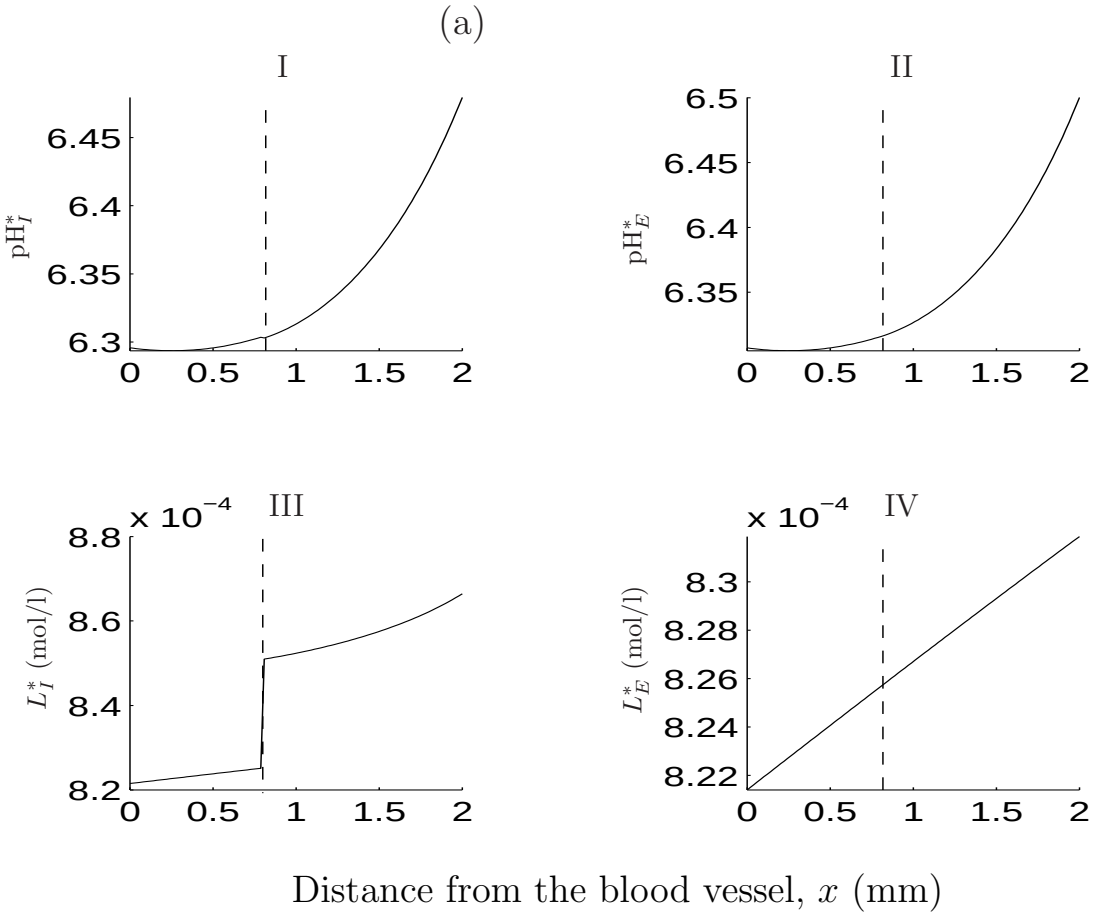

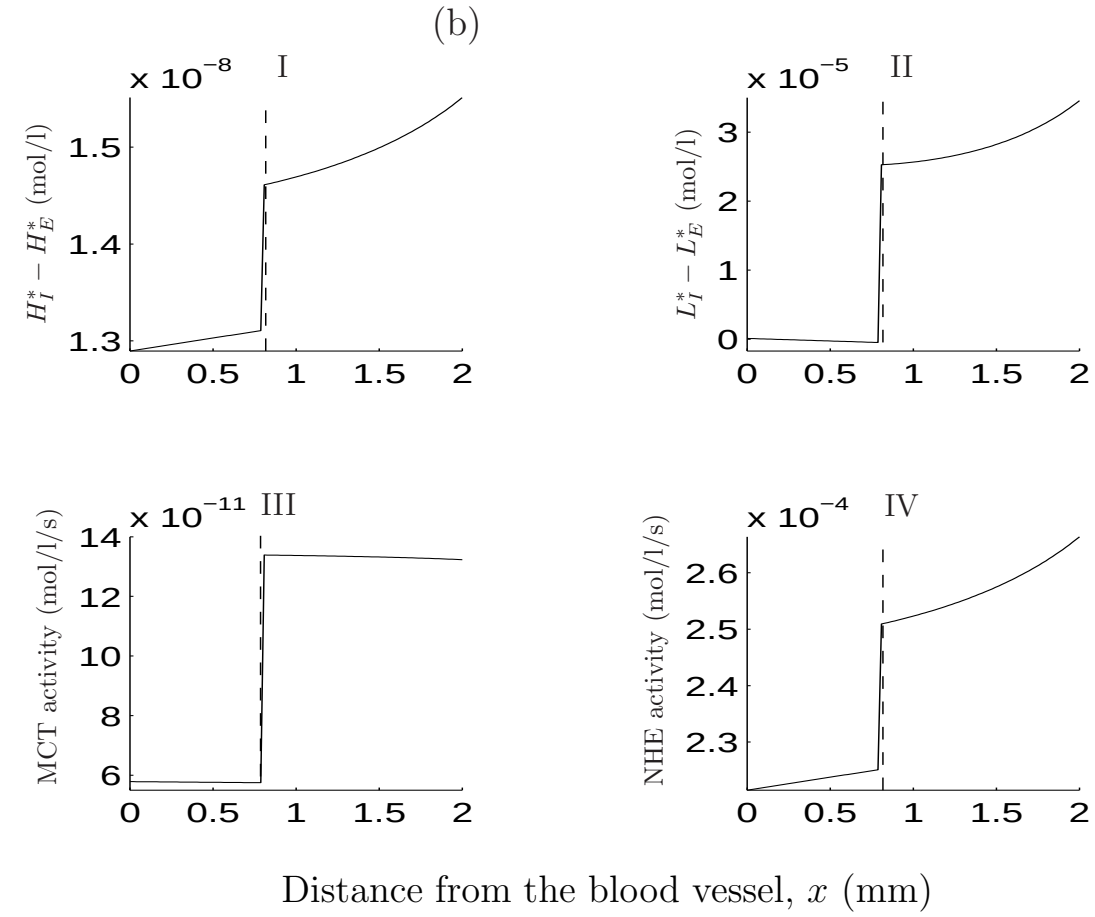

Figure 3.4: Caption on following page.

Figure 3.4: (Previous page). Numerical solution to the system (3.5)–(3.11) at steady state showing (a) a lack of spatial correlation between pH_E and L_E obtained using parameter values as in Figure 3.3 but with a reduced rate of leakage of H^+-ions and lactate into the blood stream (i.e. $\rho_{Hl}, \rho_{Ll} = 4.4$), compare (a)II with (a)IV. (b)I shows the hydrogen ion gradient, (b)II the lactate gradient, (b)III the MCT activity and (b)IV the NHE activity. The model is simulated until the steady state solution is reached, starting from the initial conditions: $H_I^0 = 0.63$, $H_E^0 = 0.63$, $L_I^0 = 1$ and L_E^0=1. We determine whether the steady state solution is reached the same way as stated in the caption for Figure 3.2.

3.3.4 Effect of parameter variations on the spatial cellular pH gradient

In Section 2.4.2.2, we investigate how the steady state solution varies against a number of model parameters. We also demonstrate that d_1, which is responsible for the background production of H^+-ions, plays a pivotal role in determining whether there is a reversed cellular pH gradient. In this section, we study the extent of the reversed cellular pH gradient in this spatial context and show that, in some cases, the extracellular environment is more acidic than the intracellular for all the cells in the domain or only for non-glycolytic cells or in other cases, no negative pH gradients are found in any region of the tissue section. We demonstrate in Figures 3.5–3.8 examples of this.

Varying the concentration of extracellular lactate in the blood vessel versus that in the tissue

Recall that $L_{\infty l}$ and $L_{\infty r}$ denote the concentrations of extracellular lactate in the blood and tissue respectively. We find that simply taking lower values of $L_{\infty l}$ gives a reversed cellular pH gradient across the tissue section independent of $L_{\infty r}$, as

illustrated in Figure 3.5. For example, with $L_{\infty l} = 0.1$, the pH gradient is reversed throughout the entire spatial domain considered. This is because if we take $L_{\infty l}$ to be very small, $L_E(0,t) - L_{\infty l}$ in the boundary term at $x = 0$ is likely to be positive and large, which means that extracellular lactate will leak into the blood stream at a high rate and hence the levels of extracellular lactate throughout the tissue section will be low. This will then facilitate the activity of the MCT (which functions according to the cellular lactate and H^+ gradient) and consequently result in a reversed cellular pH gradient as H^+-ions are exported outside the cells along with lactate. We note that in this case, the observed reversed cellular pH gradients occur at realistic values (pH_E 6.5–7.4 for the parameters used in Figure 3.5). As $L_{\infty l}$ increases, the perfusion rate of lactate into the blood decreases, tissue lactate then increases and the MCT activity decreases. This then results in a negative cellular pH gradient only in the non-glycolytic region, or, if $L_{\infty l}$ continues to increase, no negative pH gradient is observed at all. Our model therefore predicts that low levels of lactate found in the blood stream may indirectly cause a reversed cellular pH gradient in conjunction with an up-regulated tumour activity of the MCT.

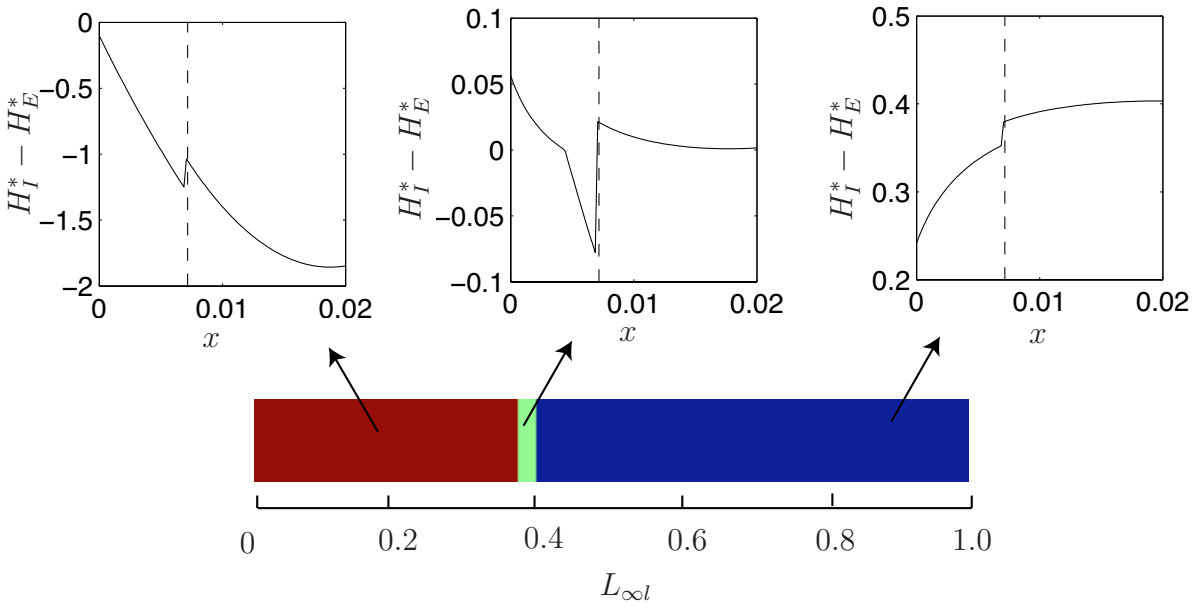

Figure 3.5: The effect of varying lactate levels in the blood vessel ($L_{\infty l}$) whilst keeping tissue lactate level ($L_{\infty r}$) fixed. The red region represents the parameter values for which all the cells in the spatial domain express a negative pH gradient; the green region represents a negative pH gradient for only non-glycolytic cells ($V \geq V^g$); the blue region represents parameter space where there are no negative pH gradients in any region of the tissue. Shown above the horizontal panel are typical profiles of the cellular hydrogen gradient for $L_{\infty l}$ values that lie in the region highlighted by the arrows. For each set of chosen parameters $(L_{\infty l}, L_{\infty r})$, the model is simulated until the steady state solution is reached, starting from the initial conditions: $H_I^0 = 0.63$, $H_E^0 = 0.63$, $L_I^0 = 1$ and $L_E^0 = 1$. We determine whether the steady state solution is reached the same way as stated in the caption to Figure 3.2. $L_{\infty r} = 1$ in each subplot and remaining parameters are the same as in the caption to Figure 3.3.

Varying the activity of MCTs versus other sources of intracellular H^+-ions

Figure 3.6 shows that the extent of the negative cellular pH gradient is strongly dependent on both the MCT activity, regulated by the parameter k_3, and the back-

ground production of intracellular H^+-ions, d_1. Not only is the negative cellular pH gradient attainable for a larger range of k_3 and d_1 values when blood lactate level ($L_{\infty l}$) is lowered (compare (a) with (b) in Figure 3.6), but when $L_{\infty l}$ is low, a reversed cellular pH gradient also occurs for the base case parameter values set in Chapter 2 as indicated by a "diamond" in the figure.

We now examine analytically what happens when d_1 and k_3 are varied. Looking at the H_I equation in (3.5), an increase in d_1 gives rise to an increase in the rate of H_I production. We now proceed by looking for an analytical solution to $H_E^*(x)$ (we denote by * the steady state level). To do this, as described above, we drop the $1/(H_I+1)$ factor from (3.5)–(3.8) and re-write $\mathrm{H}(V^g - V)$ as

$$\mathrm{H}(x^g - x) = \begin{cases} 1, & x > x^g \\ 0, & x \le x^g, \end{cases} \tag{3.14}$$

where $x = x^g$ is the point at which $V = V^g$. Adding (3.5) and (3.7), at steady state, gives $\dfrac{\partial^2 H_E^*}{\partial x^2} = -d_1 - 2\Phi_G\psi\mathrm{H}(x - x^g)$, which on integrating twice and using the given boundary conditions we get

$$\begin{aligned} H_E^*(x) \;=\; & -\left(\frac{d_1}{2} + \Phi_G\psi\mathrm{H}(x^g - x)\right)x^2 - \Big(\frac{1}{2(L\rho_{Hl}+1)}\big(2\rho_{Hl}\Phi_G\psi\mathrm{H}(L - x^g) \\ & \big(-L^2 - x^{g2} + 2x^gL\big) - \rho_{Hl}d_1L^2 - 2\rho_{Hl}H_{\infty r} + 2\rho_{Hl}H_{\infty l}\big) \\ & +2\Phi_G\psi\mathrm{H}(x^g - x)x^g\Big)x - \Phi_G\psi\mathrm{H}(x - x^g)x^{g2} \\ & +\frac{1}{2(L\rho_{Hl}+1)}\Big(\mathrm{H}(x^g - L)\big(2\Phi_G\psi L^2 + 2\Phi_G\psi x^{g2} - 4\Phi_G\psi x^gL\big) \\ & +d_1L^2 + 2L\rho_{Hl}H_{\infty l} + 2H_{\infty r}\Big). \end{aligned} \tag{3.15}$$

Now, differentiating (3.15) with respect to d_1 gives

$$\frac{\partial H_E^*}{\partial d_1}\Big|_{x \text{ fixed}} = \frac{-(\rho_{Hl}L+1)x^2 + \rho_{Hl}L^2x + L^2}{2(\rho_{Hl}L+1)},$$

so that

$$\frac{\partial H_E^*}{\partial d_1}\Big|_{x \text{ fixed}} > 0 \text{ iff} \left(\frac{-(\rho_{Hl}L+1)x^2 + \rho_{Hl}L^2x + L^2}{2(\rho_{Hl}L+1)}\right) > 0,$$

$$\Leftrightarrow \big((\rho_{Hl}L+1)x^2 - L^2\rho_{Hl}x - L^2\big) < 0. \tag{3.16}$$

The roots of (3.16) are $x = L$ and $x = -L/(\rho_{Hl}+1)$, where $\rho_{Hl} > 0$ and $L > 0$, so that the above inequality is satisfied for $-L/(\rho_{Hl}+1) < x < L$. Hence, H_E^* decreases as d_1 decreases for all $-L/(\rho_{Hl}+1) < 0 \leq x < L$. It is difficult to obtain a similar expression analytically for $H_I^*(x)$, so we numerically illustrate in Figure 3.7 (column (a)) that decreasing d_1 also decreases H_I, but we observe that there is a greater effect on H_I^* as d_1 varies than there is on H_E^*. That is, as d_1 decreases, H_I^* becomes much lower than H_E^* (see Figure 3.7(c)). On the other hand, H_E^* does not depend on k_3 at steady state (see equation (3.15)), but H_I^* decreases as k_3 is increased as shown in Figure 3.7(b). This, in turn, results in the levels of intracellular H^+-ions being lower than the extracellular (as shown in Figure 3.7(d)) as k_3 increases.

To interpret the above observations, we note that decreasing d_1 implies that the amount of H^+-ions available intracellularly is reduced. This influences the rate of activity of all the membrane-based transporters and the rate at which H^+-ions leak inside the cell from the extracellular space. So, the lower the background production of intracellular H^+-ions, the less H^+-ions are extruded and the lower the extracellular H^+ levels become. On the other hand, increasing k_3 implies that the amount of H^+-ions extruded extracellularly via the MCT increases. These extracellular H^+-ions, however, quickly diffuse across the tissue section and are removed by the supporting blood vessel.

(a) $L_{\infty l} = 0.2, L_{\infty r} = 0.3$ (b) $L_{\infty l} = 0.5, L_{\infty r} = 1.42$

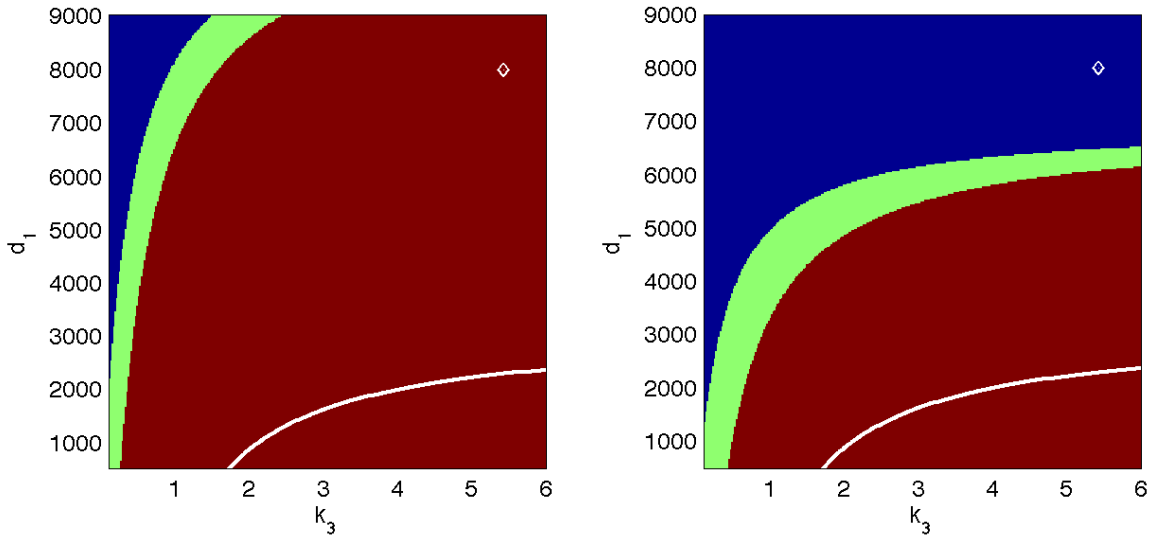

Figure 3.6: Parameter space of pH gradient reversal showing the effect of varying the rate of activity of MCT (k_3) and the total background production of H^+-ions (d_1) for: (a) $L_{\infty l} = 0.2, L_{\infty r} = 0.3$ and (b) $L_{\infty l} = 0.5, L_{\infty r} = 1.42$. The remaining parameters are the same as in the caption to Figure 3.3. The colour code is the same as in Figure 3.5. We superimpose our results from the ODE model in Chapter 2 which shows that parameter values below the white curve yield a reversed pH gradient and above the curve otherwise. The base case parameter set in Chapter 2 is depicted in the figure by a "diamond".

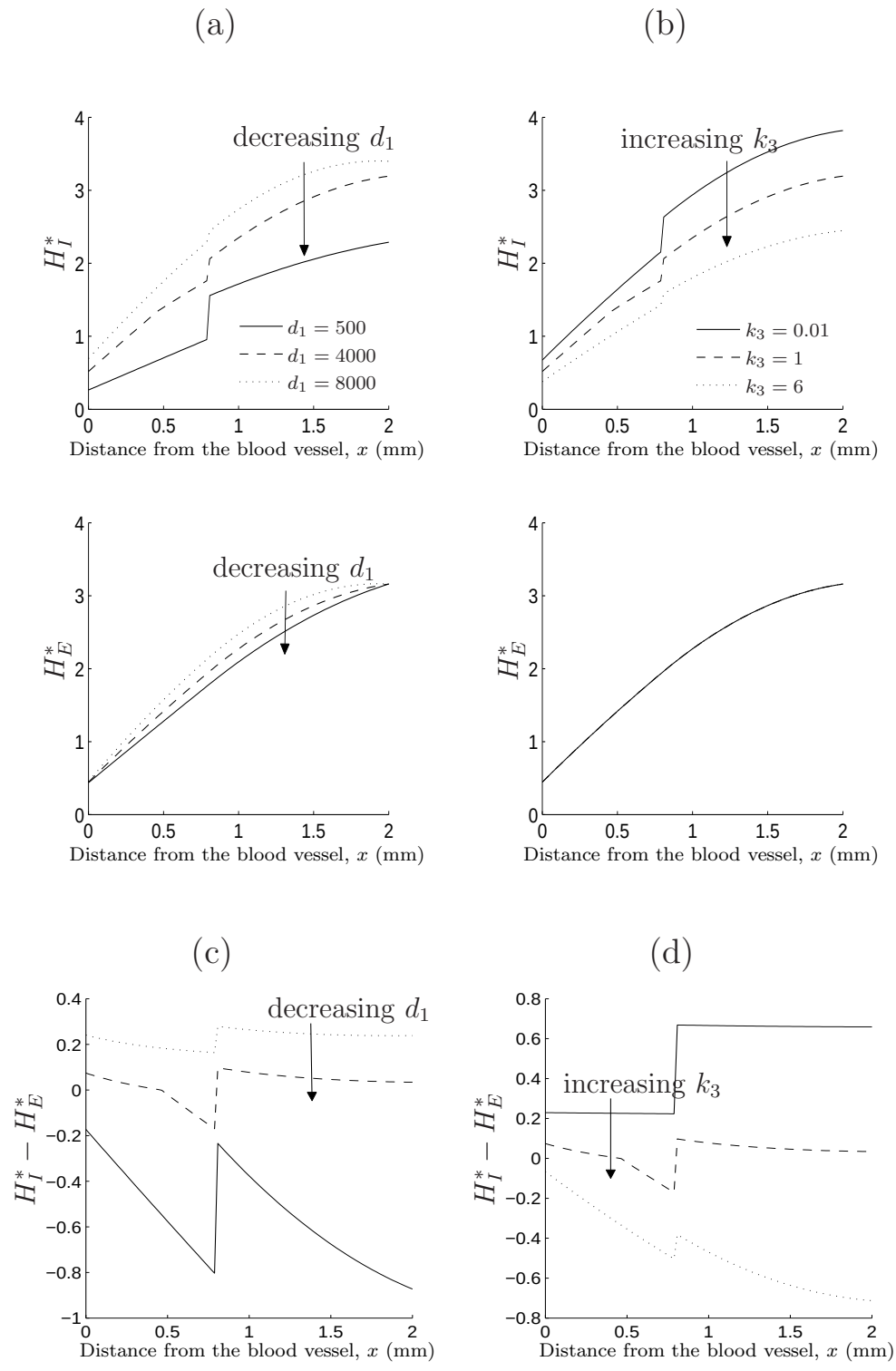

Figure 3.7: The effect of varying (a) d_1 (k_3 fixed at 1) and (b) k_3 (d_1 fixed at 4000) on H_I^* and H_E^* (in dimensionless form). We also show the effect on the cellular H^+ gradient ($H_I^* - H_E^*$) due to variations in the values of: (c) d_1 and (d) k_3. Remaining parameters are the same as in the caption to Figure 3.3. Here, $L_{\infty l} = 0.5$ and $L_{\infty l} = 1.42$.

Varying the the activity of NHEs versus other sources of intracellular H^+-ions

In contrast, we find that no matter how much the rate of activity of the NHEs, regulated by the parameter f_1, is varied the cellular pH gradient is reversed throughout the tissue section (for all values of d_1, as long as k_3 is sufficiently high) as Figure 3.8(a) demonstrates. Note that H_E^* at steady state does not depend on f_1 (see equation (3.15)) because the rate at which H^+-ions enter the extracellular space, in our model, via the membrane-based transporters is equal to the rate of their removal by the blood vessel or their subsequent leakage into a cell. So, an increase in f_1 does not affect H_E^* but will decrease H_I^* via extrusion by the NHE so that H_I^* quickly becomes smaller than H_E^* and the cellular pH gradient becomes reversed. In contrast, for higher values of tissue and blood lactate, the NHE only gives rise to a reversed pH gradient provided that the level of other sources of H^+-ions is small (i.e. d_1 below a certain threshold as shown in Figure 3.8(b)). This is because increasing the levels of blood lactate means that extracellular lactate leaks into the blood stream at a lower rate. This then lowers the activity of the MCT (which functions according to the cellular lactate and H^+ gradient) and consequently results in less intracellular H^+-ions being transported outside the cell along with lactate.

Note that, if we artificially set intracellular and extracellular lactate to be equal, we find no cellular pH gradient reversal for the range of parameters that we have explored thus far. Crucially, this suggests that lactate plays a pivotal role in determining a cellular reversed pH gradient, which further motivates its inclusion as separate intracellular and extracellular components in the model.

To summarise, we have shown so far in this chapter that by allowing diffusion of the extracellular metabolites across the tissue section, we are able to recover a more realistic acidic negative pH gradient throughout the tissue section—in the aerobic region as well as in the anaerobic region—which the well-mixed ODE model

in Chapter 2 does not capture. Recall from our discussion in Chapter 2 that in the well-mixed model a reversed cellular pH gradient is obtainable but is found to be too alkaline to be biologically realistic (with $\mathrm{pH}_i = 7.7$–9.75, $\mathrm{pH}_e = 7.5$–9.5, see Figures 2.6–2.7).

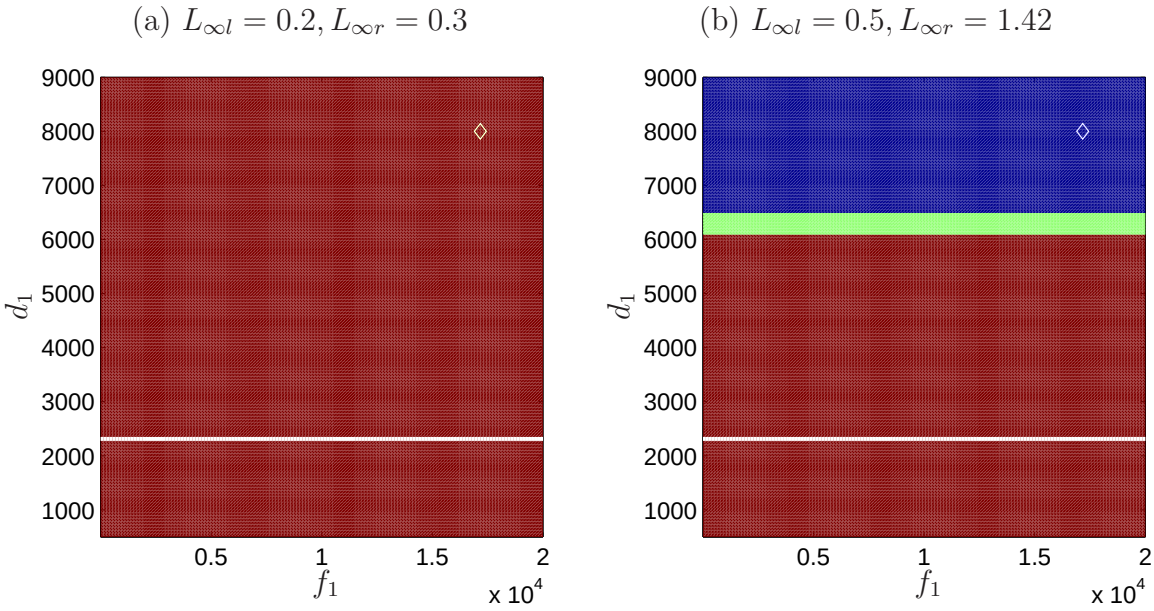

Figure 3.8: Same procedure described in Figure 3.5, but with parameter space (f_1, d_1) and with k_3 fixed at 5.43. In (a) $L_{\infty l} = 0.2, L_{\infty r} = 0.3$. In (b) $L_{\infty l} = 0.5, L_{\infty r} = 1.42$. The remaining parameters are the same as in the caption to Figure 3.3. The colour code is the same as in Figure 3.5. We superimpose our results from the ODE model in Chapter 2 which predicts that parameter values below the white line yield a reversed pH gradient and above the line otherwise. The base case parameter set in Chapter 2 is depicted in the Figure by a "diamond".

Our focus in the remainder of this chapter will be on the impact of a heterogeneous spatial distribution of NHEs and MCTs on the extent of the spatial pH gradient reversal and on the spatial correlation of extracellular lactate and low pH_e.

3.3.5 Heterogeneous distribution of MCT and NHE

So far, we have assumed that the MCTs and NHEs are homogeneously distributed throughout the spatial domain. However, recent experiments carried out by Grillon *et al.* [94] on C6 rat gliomas reveal that the relative intensity of NHE peaks at a distance of 0.33±0.027 mm away from the tumour edge and that the intensity of MCT is also up-regulated at 1.05±0.14 mm from the edge of the tumour. The authors represent this spatial organisation of the transporters across the tumour rim graphically as shown in Figure 3.9. With this in mind, we incorporate the following functions for the heterogenous expression of the NHE (f_1) and the MCT (k_3), namely

$$\begin{aligned} f_1 &= \left(1 + \frac{f_2 x}{f_3 + f_4 x^2}\right) f_1^{\text{base}} \\ k_3 &= \left(1 + \frac{k_4}{k_5 + k_6 x^2}\right) k_3^{\text{base}}, \end{aligned} \tag{3.17}$$

where, $f_i (i \in 2, 3, 4)$, $k_j (j \in 4, 5, 6)$ are chosen to best fit the curves shown in Figure 3.9, and f_1^{base}, k_3^{base} denote the base parameter values as presented in Table 2.1. It turns out, however, that incorporating these functions in our model has no qualitative effect on the pH and lactate profiles for the parameter values considered (see Figure 3.10). Quantitatively, there is relatively little change to the levels of pH_I and no observable change to pH_E and L_E. However, there is a considerable change in the levels of intracellular lactate which is due to the variations in MCT activity. That is, intracellular lactate levels increase near the tumour edge due to a higher NHE activity there (compared to MCT activity) which leaves less intracellular H^+ to bind with lactate for extrusion via the MCT and so intracellular lactate builds up. But as the NHE activity then drops further into the tumour (see Figure 3.9), intracellular lactate begins to fall due to an increased MCT activity. In comparison, a substantial change in the NHE activity only appears to result in a small change in intracellular pH (see Figure 3.10(b)IV). Therefore, it appears that the variations in MCT activity is the dominating factor here.

We show in Figure 3.11 that variations in the parameters that represent the maximum rate of activity of the NHE transporter, f_2, and the MCT transporter, k_4, results in a qualitatively similar profile to that seen in Figure 3.10. We see, however, a slight change in the qualitative profiles of intracellular lactate and intracellular pH near the blood vessel (near $x = 0$). This is attributed to a sharp increase in the NHE activity and a slight dip in the MCT activity which results in a sharp increase in intracellular lactate levels there (see Figure 3.11(b), III and IV). So in conclusion, our model suggests that an increased expression of the MCT and NHE near the tumour edge affects the intracellular levels of lactate significantly (the key effects being dominated by the MCT), and the effects on intracellular pH is much lower.

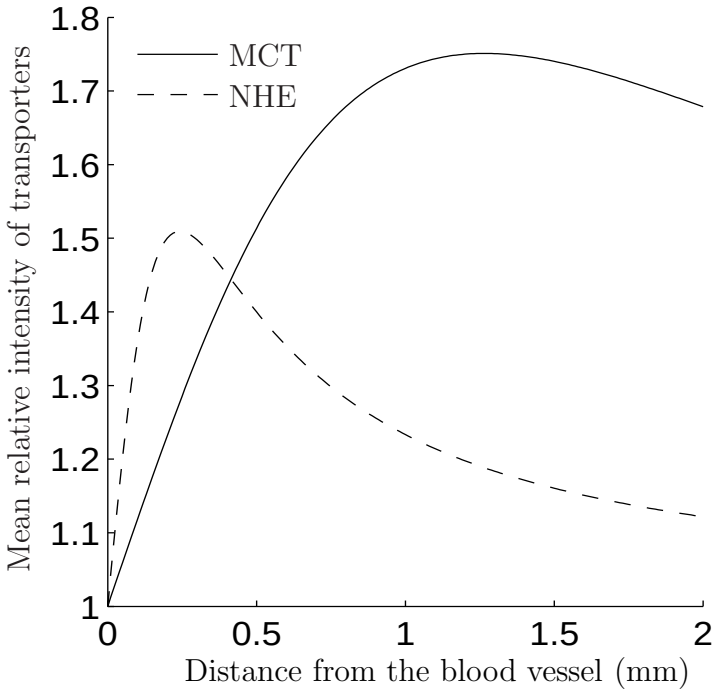

Figure 3.9: The spatial organisation of the NHE and the MCT near the tumour rim relative to outside the tumour as observed in [94]. The average intensity of the transporters outside the tumour is set to one.

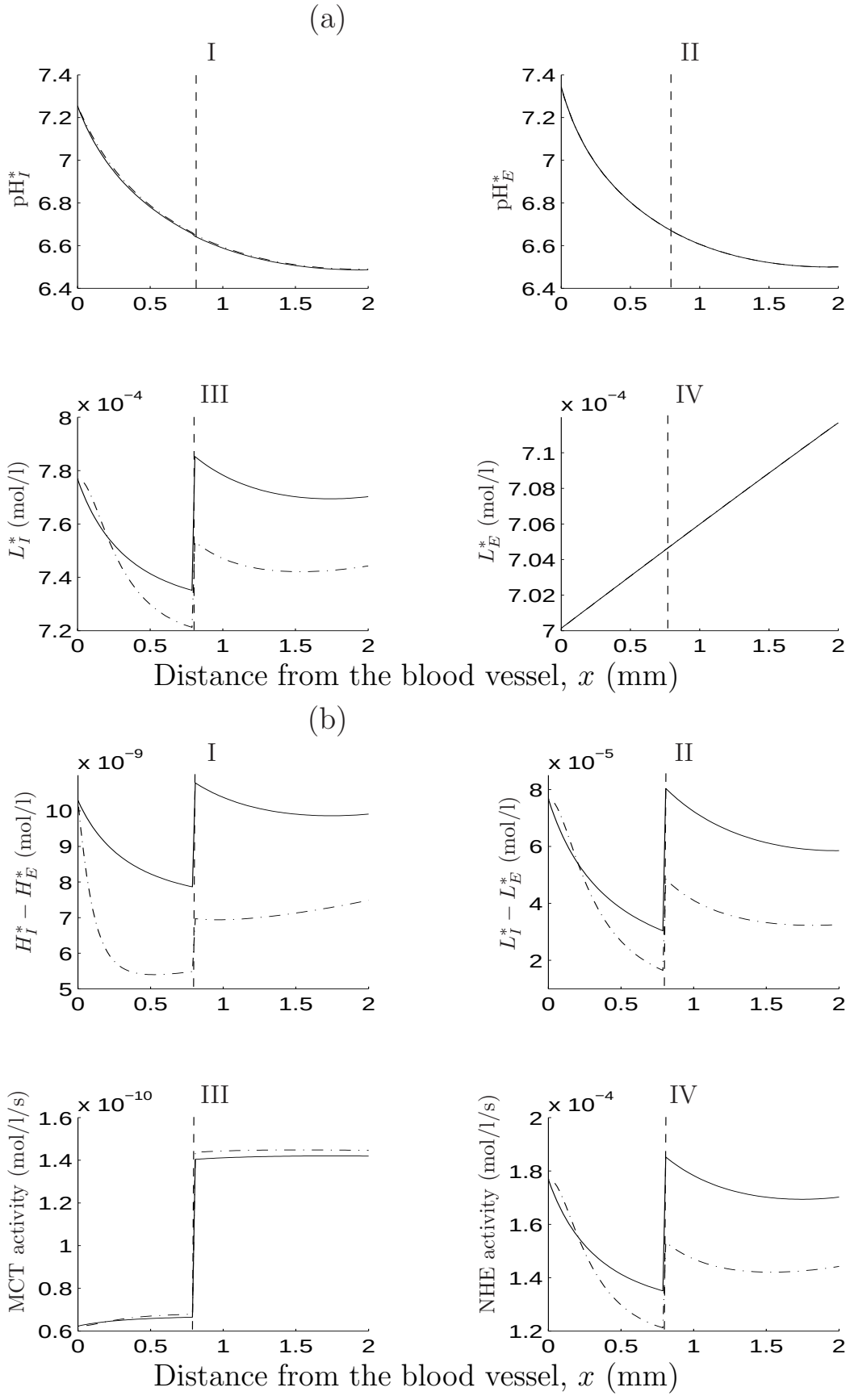

Figure 3.10: Caption on following page.

Figure 3.10: (Previous page). (a) The steady state profile of pH and lactate with heterogeneous (– · –·) and homogeneous (——) functions representing the activity of the NHEs and MCTs. (b) Shows hydrogen and lactate gradients and the rates of activity of NHE and MCT. Parameter values are the same as in Figure 3.3 but with $k_4 = 1.18, k_5 = 8 \times 10^{-3}, k_6 = 50, f_2 = 0.032, f_3 = 9.9 \times 10^{-5}, f_4 = 10$ representing the heterogenous distribution of NHE and MCT. $f_1^{\text{base}} = 1.71 \times 10^4, k_3^{\text{base}} = 5.43$.

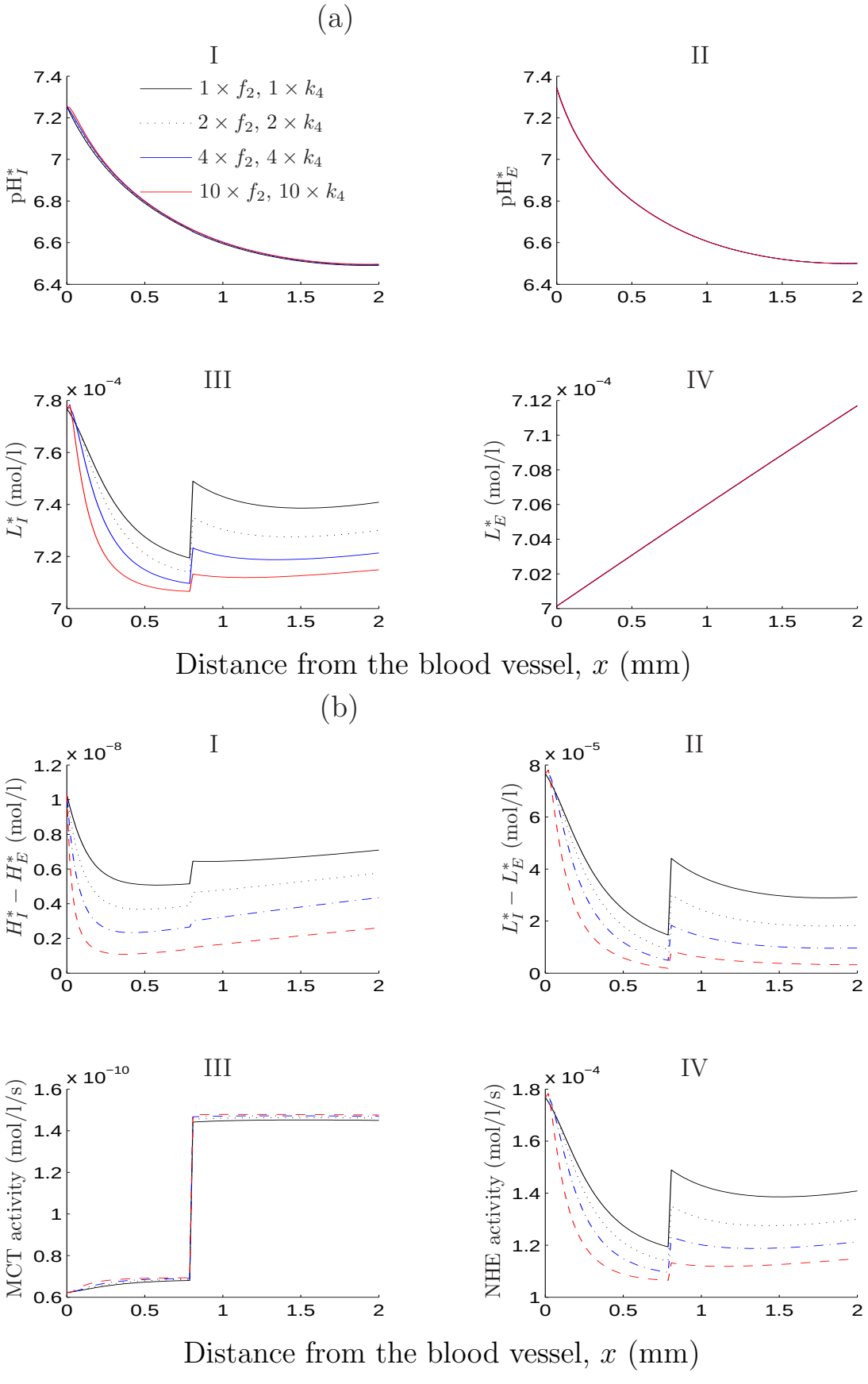

Figure 3.11: Caption on following page.

Figure 3.11: (Previous page). (a) shows the effect of increasing the magnitude of the maximum rate of activity near the tumour rim of the NHE, f_2, and MCT, k_4 on the spatial levels of the metabolites. It appears that intracellular lactate is the most sensitive metabolite to variations in f_2 and k_4. Intracellular pH is also affected, but to a lesser extent. (b)I shows hydrogen ion gradient, (b)II lactate gradient, (b)III the MCT activity and (b)IV the NHE activity. Base values: $f_2 = 0.032$, $k_3 = 1.18$. Remaining parameter values are the same as in the caption to Figure 3.3.

3.3.6 The inclusion of intercellular gap junctions for H^+-ions

It has been suggested that a lack of spatial correlation between an increase in extracellular lactate levels and a decrease in extracellular pH exists in some tumours because protons, which are exported extracellularly along with lactate in hypoxic regions, re-enter the cells indirectly via the HCO_3^-/Cl^- exchanger or simply leak back into the cell and then are transported cell-to-cell via gap junctions to make protons available for the NHE exchanger [183]. In this section, we examine if incorporating H^+-ions intercellular gap junctions in our model have any effect on whether high extracellular lactate is correlated with a decrease in extracellular pH.

We now introduce the following gap junction intercellular communication term,

$$g_j = k\left(H_I(j+1) - 2H_I(j) + H_I(j-1)\right), \tag{3.18}$$

into the spatially discretised form of equation (3.1), where j denotes the cell at spatial position j, $H_I(j)$ is the intracellular H^+-ion concentration in that cell and k represents the rate of transfer of H^+ between cells. Due to the lack of available

data, we vary the magnitude of k and illustrate the effect on the spatial profile of pH and lactate in Figure 3.12.

We observe that as k increases, the intracellular pH decreases in the aerobic region ($V \geq V^g$) and increases in the glycolytic region ($V < V^g$) due to the intracellular H^+-ions being transferred from the glycolytic region (where they are produced in excess) to the aerobic region. As a result, extracellular pH increases in the $V < V^g$ region (due to there being less intracellular H^+-ions to be pumped outside the cell via the NHE or MCT) and decreases in the $V \geq V^g$ region (due to there being more intracellular H^+-ions being pumped outside the cell). Extracellular lactate, however, remains largely insensitive which is attributed to their leakage to the surrounding tissue. Note that the concentrations of extracellular lactate and pH become spatially correlated (compare (a)I with (a)IV in Figure 3.12), contrary to the hypothesis provided in [94, 183] which associates the activity of the H^+ intercellular gap junctions with the lack of correlation between low pH_e and high extracellular lactate. Also, intracellular lactate decreases in the $V \geq V^g$ region (due to there being more intracellular H^+-ions being pumped outside the cell along with lactate via the MCTs) and increases in the $V < V^g$ region (due to there being less intracellular H^+-ions pumped outside the cell via the MCTs).

Furthermore, a reversed pH gradient is observed in the glycolytic region, which is due to the intracellular H^+-ions being transferred from the glycolytic region (where they are produced in excess) to the aerobic region and thus lowering the levels of intracellular H^+-ions in the glycolytic region and raising it in the aerobic region. Note that a sufficiently high value of k is required, $> O(10^6)$, to see a significant effect on the metabolite gradients (see Figure 3.12).

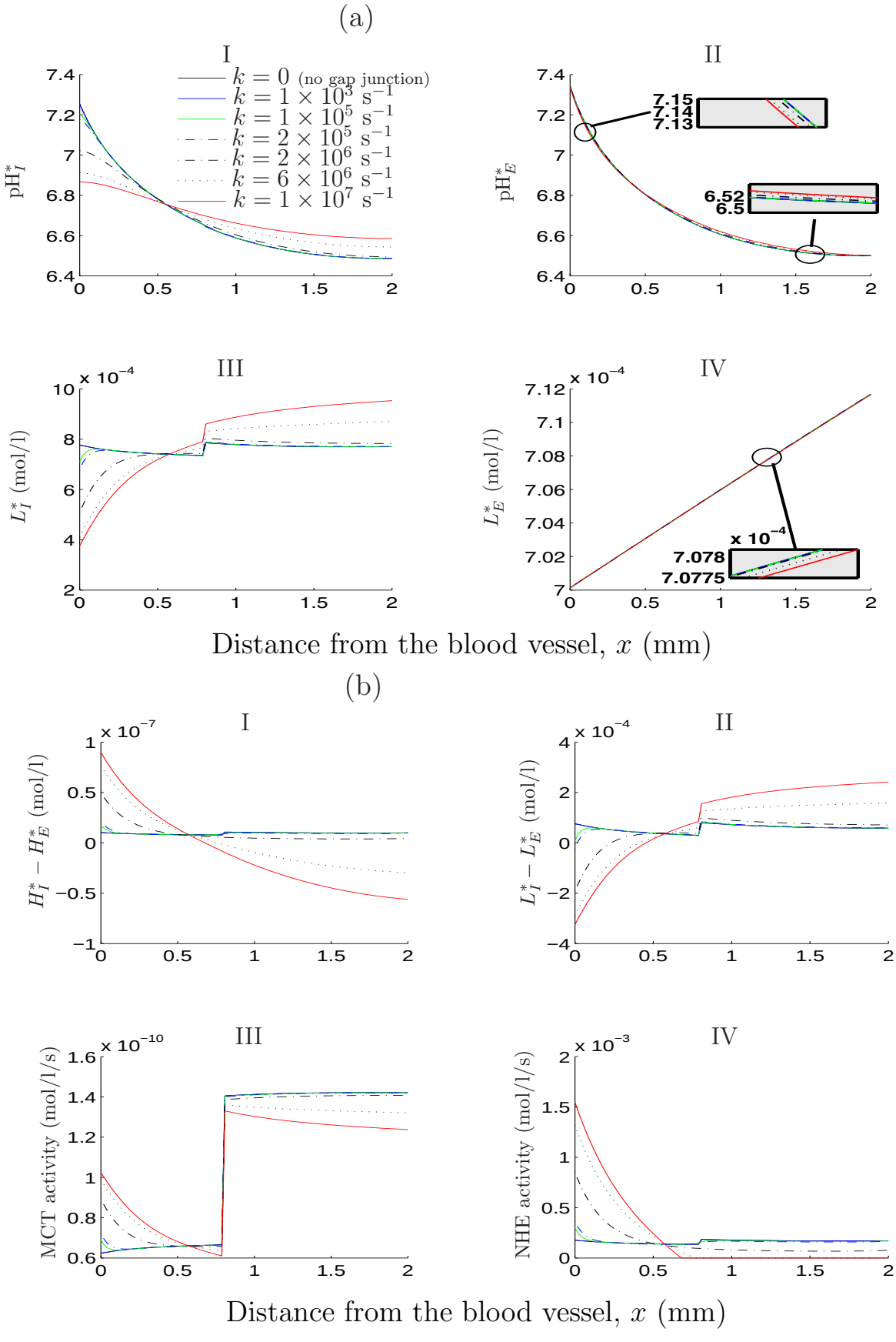

Figure 3.12: Caption on following page.

Figure 3.12: (Previous page). Plots showing how the spatial profile of: (a)I pH_I^* and (a)III L_I^* are affected as the rate of H^+ transfer between cells, k, is varied and how little (a)II pH_E^* and (a)IV L_E^* profiles change in comparison. (b)I shows hydrogen ion gradient, (b)II lactate gradient, (b)III the MCT activity and (b)IV the NHE activity. Parameter values are the same as in the caption to Figure 3.3.

3.4 Discussion and conclusions

The motivation of this chapter is to incorporate more realism into the modelling framework. By giving the tumour a spatial structure, the aim is to investigate if there is a spatial correlation between extracellular lactate and extracellular pH and if a reversed cellular pH gradient can be achieved with more realistic parameter values. Also, we include intercellular gap junctions and a heterogeneous expression of NHEs and MCTs, as suggested by experimentation, and study the effects.

Acidic extracellular environments are often-noted in solid tumours [149, 195, 218, 220]. It has long been anticipated that this low pH is largely due to lactic acid production by glycolytic tumours. The diagnostic significance of lactate has been implicated in numerous studies showing an association between high lactate levels and the incidence of metastasis [207, 246]. We have demonstrated in this model that areas with high extracellular lactate can coincide with high extracellular H^+-ion concentrations. However, when the rate of removal of H^+-ions and lactate by blood vessels is reduced, lower extracellular lactate concentrations can exist where extracellular H^+-ion concentrations are at their highest level. This result suggests a role for blood vessel perfusion rates in determining the spatial correlation of extracellular pH and lactate. Tumour blood vessels are chaotic and an order of magnitude leakier than normal vessels [145]. This is known to result in an in-

creased interstitial fluid pressure inside tumours which can hamper the uptake of therapeutic agents [187]. Recently, Martin *et al.* [141] extended the acid-mediated tumour invasion model [71] by including the effect of vessel permeability on the acid gradient from the centre of the tumour to the normal tissue. They find that leaky vasculature (those with high vessel permeability) can lead to an overall acidification of the normal tissue further from the tumour boundary, and our present study seems not to contradict this (if we take non-glycolytic cells to be representatives of normal cells). Moreover, our results are supported by Parkins *et al.* [168] who studied the relationship between extracellular lactate and extracellular pH in murine tumours after vascular occlusion (clamping) followed by reperfusion. Their study shows that, under conditions of severe stress, resulting in abolition of energy stores and cell death, the extracellular pH continues to decline in the absence of a corresponding accumulation of extracellular lactate [168].

The motivation of our work is to also determine the relative importance and inter-relationships between some of the main parameters involved in the spatial reversed cellular pH gradient, concentrating in particular on the influence of changes in tissue and blood lactate levels, background production of H^+-ions and the activity of the MCTs and NHEs. We find that simply taking lower values of blood lactate levels gives a reversed pH gradient throughout the spatial domain independent of the levels of tissue lactate. This is because, with lower blood lactate values, extracellular lactate leaks into the blood vessel until the level of lactate in the tissue equates that in the blood vessel. Hence, the lower the blood lactate level is, the lower the tissue extracellular lactate becomes, which in turn drives the MCTs to export lactate and H^+-ions outside the cell at a higher rate due to the larger lactate gradient. Likewise, we have found the existence of a negative pH gradient to be strongly dependent on the combined activity of the MCTs and other sources of H^+-ion. The ability of extracellular H^+-ions to leak into the neighbouring blood vessel and to diffuse across the tissue from higher to lower concentrations means that the reversed cellular pH gradient occurs at more realistic values and is less

alkaline (pH_e = 6.5–7.4) than that observed in the closed ODE system studied in Chapter 2 (pH_e = 7.5–9.5). In addition, we have found the pH gradient to be always reversed no matter how high or low the NHE activity is, provided that the level of other sources of H^+-ions is below a certain threshold.

Recent experiments carried out by Grillon *et al.* [94] on C6 rat gliomas reveal that the relative intensity of NHEs peak at a distance of 0.33±0.027 mm away from the edge of the tumour and that the intensity of MCTs is also up-regulated at 1.05±0.14 mm from the edge. The inclusion of heterogeneous expressions of the NHEs and the MCTs as in [94] has no qualitative effect on the model behaviour, but a considerable increase in their rate of activity can have some effect on intracellular levels of lactate and intracellular pH. Quantitatively, this has a significant difference to the intracellular levels of lactate which is attributed to the activity of the MCT. Also, there is a relatively small effect on the intracellular pH. Based on our model, we therefore suggest that an up-regulated expression of NHE and MCT in the growing rim of a carcinoma can give rise to a higher intracellular pH (which is known to aid tumour cell migration [139] and proliferation [85]) and a lower intracellular lactate (in regions further away from the tumour edge) but may not result in a reversed cellular pH gradient or a redistribution of protons away from the glycolytic source.

On the other hand, including intercellular gap junction communication can give rise to a reversed cellular pH gradient. Note that in order for this to happen, intercellular gap H^+-ion transfer needs to be more rapid compared to the other transporter processes in the model. This results in intracellular H^+-ions being transferred from the glycolytic region (where they are produced in excess) to the aerobic region and thus lowering the levels of intracellular H^+-ions in the glycolytic region and raising it in the aerobic region. Moreover, we observe that the intercellular H^+-ion gap junctions can influence the levels of extracellular pH in the model. There are numerous studies suggesting that gap junction intercellular communication (GJIC) is altered by changes in the extracellular pH [201, 255].

However, there is no evidence to suggest that intercellular-gap junctions can change the extracellular acidity of a cell and it would be interesting to test these results experimentally.

Chapter 4

A cellular automaton model examining the effects of H^+-ions and lactate on early tumour growth

4.1 Introduction

In Chapter 3, we have presented a continuum reaction-diffusion model of pH and lactate which has provided us with insight into the conditions that give rise to a spatial reversed cellular pH gradient. It was assumed that all the tumour cells are of one type and are large in number. In this chapter, however, our aim is to model the growth of a small number of tumour cells which are supplied with nutrients from distally located blood vessels. To this end, we use a hybrid cellular automaton model with reaction-diffusion equations as described in Chapter 3 to describe the evolution of extracellular metabolites (oxygen, H^+-ions and lactate) and discrete elements describing the individual tumour cells and the interaction of the cells with each other and the microenvironment. The model is intended to represent a

two dimensional slice through the centre of a three-dimensional avascular tumour spheroid.

Existing hybrid cellular automaton models have tended to utilise simple reaction-diffusion differential equations when examining the effect of extracellular pH on tumour growth (see for example [78, 79, 112, 170]). The main difference between the model we develop in this chapter and previous models (e.g. [112, 170]) is that we couple the dynamics of intra- and extracellular pH, as well as the intra- and extracellular lactate levels. This is achieved by taking explicit account of the membrane-bound ion transporters (such as the Na^+/H^+ and lactate/H^+ exchangers) used to regulate intracellular pH and lactate. In so doing, we are able to examine the effect of these transporters on the cellular pH gradient and early tumour growth.

We first assume, in Section 4.3.1, that oxygen is the only metabolite that drives the growth and phenotypic transformations of the tumour cells. We then allow oxygen, in Section 4.3.2, to influence a cell's glycolytic phenotype and assume that only the extracellular pH drives the growth and transformations of the tumour cells. In Section 4.3.3, we focus on the effects of intracellular pH on tumour cell growth and phenotypic transformations. Then, using experimental findings we allow both oxygen and extracellular pH to drive the simulations in Section 4.3.4.

4.2 Model framework

Our cellular model consists of two spatial scales. At the microscopic scale, a discrete lattice stochastic model utilising a set of probabilistic rules for cell growth and death. At the macroscopic scale, a system of partial differential equations describing the diffusion and transport of extracellular lactate, H^+-ions and oxygen. Both of these are coupled to a system of ordinary differential equations describing the production, decay and transport of intracellular lactate and H^+-ions in each tumour cell.

4.2.1 Metabolite fields

We denote by V the oxygen levels that enter the system via the blood vessels which are located on the perimeter of a regular square domain. We assume that oxygen diffuses with diffusivity D_V throughout the domain and is consumed by tumour cells at a rate d_V (rate per cell), namely

$$\frac{\partial V(\mathbf{x},t)}{\partial t} = D_V \nabla^2 V(\mathbf{x},t) - d_V(\mathbf{x}) V(\mathbf{x},t), \tag{4.1}$$

where, $\mathbf{x}= (x, y)$ is the position vector in the simulation space with $-L \leq x \leq L$ and $-L \leq y \leq L$ where L is the distance from the tumour centre, and t is time. Note that $d_V(\mathbf{x})$ will be a function of cell phenotype, and is taken to be equal to a constant d_V (the value of which varies with phenotype defined below) if viable cell is present at $\mathbf{x} = (x, y)$ and zero otherwise. As the tumour grows, the supply of oxygen by diffusion to the central core of the growing mass decreases, resulting in cells becoming starved of oxygen and incapable of proliferating (a cell state termed as quiescent, see Figure 4.1 for an illustration). Quiescent cells are generally characterised by a lower metabolic rate [67] which is represented in our model by a lower oxygen consumption rate, d_V (see below). The extent of the decrease is not well determined experimentally [67], but we find that the key qualitative features of the solutions are largely insensitive to this factor and so for simplicity we assume a decrease by a factor of two, namely,

$$d_V = d_c \times \begin{cases} 1, & \forall \mathbf{x} = \text{proliferative cells}, \\ 1/2, & \forall \mathbf{x} = \text{quiescent cells}, \\ 0, & \forall \mathbf{x} = \text{necrotic cells or empty space}, \end{cases}$$

where d_c corresponds to the base oxygen consumption rate in proliferating tumour cells. While some tumour cells have been shown to metabolise using anaerobic glycolysis instead of aerobic despite a plentiful supply of oxygen [74], here we assume that only if oxygen levels become low do tumour cells undergo glycolysis. The result is an excess production of hydrogen ions and lactate which must then

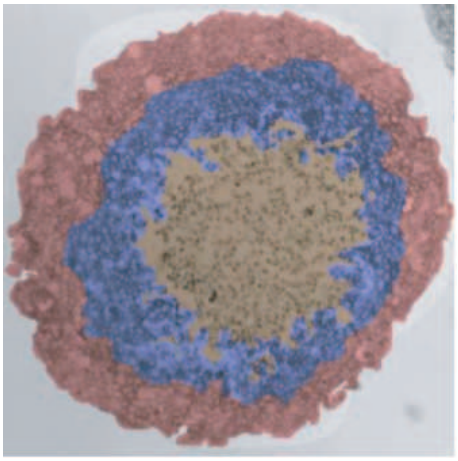

Figure 4.1: Transverse section of a T47D multicellular tumour spheroid shows a characteristic viable rim consisting of proliferative (red) and quiescent cells (blue), and an inner necrotic core (brown). Spheroid diameter$\sim$1200 μm. Image courtesy of [164].

be exported extracellularly in regions of cellular glycolysis via several membrane bound transporters to ensure cell viability. This is represented by the following ordinary differential equation for a cell located at position $\mathbf{x}$,

$$\frac{dH_I(\mathbf{x},t)}{dt} = \frac{2\Phi_G \mathrm{H}(V^g - V(\mathbf{x},t))}{H_I(\mathbf{x},t)+b} + d_1 + \phi(\mathbf{x},t), \tag{4.2}$$

where,

$$\begin{aligned}\phi(\mathbf{x},t) = {} & l_H(H_E(\mathbf{x},t) - H_I(\mathbf{x},t)) - f_1 \mathrm{H}\left(H_I(\mathbf{x},t) - H_E(\mathbf{x},t)\right)\left(H_I(\mathbf{x},t) - H_E(\mathbf{x},t)\right) \\ & - k_3\left(H_I(\mathbf{x},t)L_I(\mathbf{x},t) - H_E(\mathbf{x},t)L_E(\mathbf{x},t)\right).\end{aligned}$$

Recall that Φ_G represents the rate at which a tumour cell glycolytically produces H^+-ions and lactate; d_1 denotes the background production of H^+-ions; l_H denotes the rate of intracellular leakage of H^+-ions from the extracellular space; f_1 denotes the NHE rate activity and k_3 represents the MCT rate activity.

Extracellular hydrogen ions diffuse with diffusivity D_H and are governed by the following reaction-diffusion equation

$$\frac{\partial H_E(\mathbf{x},t)}{\partial t} = D_H \nabla^2 H_E(\mathbf{x},t) - \phi(\mathbf{x},t). \tag{4.3}$$

Note that in this equation we take

$$\phi(\mathbf{x},t) = \begin{cases} \phi(\mathbf{x},t), & \text{if a cell is present} \\ 0, & \text{otherwise (i.e. empty space or a dead cell)} \end{cases}$$

so that there is no transporter activity at locations where there are dead cells or empty space. Similarly, tumour cells produce excess lactate as a by-product of glycolysis which are exported outside the cell via the MCTs to avoid cell toxicity or is converted back to glucose. This is represented for a cell at location $\mathbf{x}$ via,

$$\frac{dL_I(\mathbf{x},t)}{dt} = \frac{2\Phi_G \mathrm{H}(V^g - V(\mathbf{x},t))}{H_I(\mathbf{x},t)+b} + d_4 - \alpha_4 L_I(\mathbf{x},t) - \theta(\mathbf{x},t), \tag{4.4}$$

where,

$$\theta(\mathbf{x},t) = k_3 \left(H_I(\mathbf{x},t)L_I(\mathbf{x},t) - H_E(\mathbf{x},t)L_E(\mathbf{x},t)\right).$$

Recall that d_4 and α_4 represent the rate of lactate background production and decay respectively.

Extracellular lactate also diffuses (with diffusion co-efficient D_L) and is transported via the MCTs in the form,

$$\frac{\partial L_E(\mathbf{x},t)}{\partial t} = D_L \nabla^2 L_E(\mathbf{x},\mathbf{t}) + \theta(\mathbf{x},t). \tag{4.5}$$

Again, as above, in this equation we take

$$\theta(\mathbf{x},t) = \begin{cases} \theta(\mathbf{x},t), & \text{if a cell is present at } \mathbf{x} \\ 0, & \text{otherwise (i.e. empty space or a dead cell)} \end{cases}$$

to prevent lactate influx/efflux at spatial locations of dead cells or empty space. We take fixed boundary conditions. On this perimeter, we fix O_2, H_E and L_E at their normal physiological levels: $V(\mathbf{x},t) = V^0$ mol/l, $H_E(\mathbf{x},t) = H_E^0$ mol/l, $L_E(\mathbf{x},t) = L_E^0$ mol/l. Our initial conditions for O_2, H_I, H_E, L_I and L_E are, respectively, $V(\mathbf{x},0) = V^0$ mol/l, $H_I(\mathbf{x},0) = H_I^0$ mol/l, $H_E(\mathbf{x},0) = H_E^0$ mol/l, $L_I(\mathbf{x},0) = L_I^0$ mol/l, $L_E(\mathbf{x},0) = L_E^0$ mol/l.

4.2.2 Automaton rules

In the automaton framework, we discretise the $[-L, L] \times [-L, L]$ domain by an $N \times N$ regular square grid. Each grid site can either be occupied by a tumour cell (proliferative, quiescent or necrotic) or it can be empty. Initially, we introduce a population of sixteen tumour cells at the centre of the lattice. At each time step, the state of each grid cell evolves according to predefined automaton rules: (a) if the grid cell is unoccupied, it does not evolve directly but may evolve indirectly if a daughter cell is placed into it by a neighbouring proliferative tumour cell; (b) if the grid cell is occupied, then the phenotype of the occupying tumour cell will be altered depending on environmental conditions, such as the levels of oxygen and acidity. We update the automaton according to the following rules:

Proliferation

At each time step, we loop over each tumour cell and check if oxygen levels at the cell locations are permissive for cell division, i.e. if oxygen level (V) is bigger than or equal to a predefined quiescence threshold, V^q.

For each tumour cell such that $V \geq V^q$ at its location, we then examine the state of the neighbouring sites in the von Neumann neighbourhood of the cell (i.e. the four cells orthogonally surrounding a central cell). If there are any empty sites in this local neighbourhood, we then choose one of these sites randomly and insert a daughter cell in that site provided that the time since the last division of that cell exceeds a predefined average cell cycle time, T_σ.

Cell state

Almost 60 years ago, the first indication that hypoxia (low oxygen) exists in tumours was observed by Thomlinson and Gray [228] in histological studies of human lung adenocarcinomas. Since then, many studies have shown that hypoxic cells are present in most solid tumours, such as, melanomas [124], prostate cancer [152], in-

vasive breast cancer [229] and non-small cell lung cancer [225]. It is well-established that hypoxia alters cells progression through the cell cycle [69]. Whereas normal cells undergo apoptosis when faced with intensive prolonged hypoxia, tumour cells are shown to be able to resist for longer and enter into a quiescent state [26, 31]. At each time step in our model, we update the state of each tumour cell according to the level of oxygen. If oxygen concentration is lower than the value we predefine for quiescence, V_q, but above that which we define for necrosis, V_n, then we set the cell state to quiescent. If the oxygen concentration is lower than the value set for necrosis, we set the cell state to dead. Otherwise, we leave the state of the cell to proliferative. Note that once a cell dies it is no longer updated but still occupies a grid point. The reason for this is that when cell death occurs by necrosis the cell keeps its shape for a period of time and thus still occupies a physical space during this period [131].

pH effects on phenotype and proliferation

As well as being dependent on oxygen availability, cell division and phenotypic transformations are also influenced by intracellular and extracellular pH [84]. In the simulations in this chapter we either focus just on the effects of oxygen (and ignore the effects of pH on cell phenotype and proliferation) or we include pH effects. We will vary whether it is pH_I or pH_E that drives the cell proliferation and cell phenotype transformations in our simulations. If pH_E (or pH_I) is above or equal to a quiescence threshold level, which we define as pH_E^q (or pH_I^q), then we allow the cell to proliferate. If the pH_E (or pH_I) is lower than or equal to a necrotic threshold, which we define as pH_E^n (or pH_I^n), the cell dies. Otherwise the cell becomes quiescent.

An overview of the automaton process is shown in Figure 4.2 when growth and phenotypic transformations are dependent only on oxygen levels.

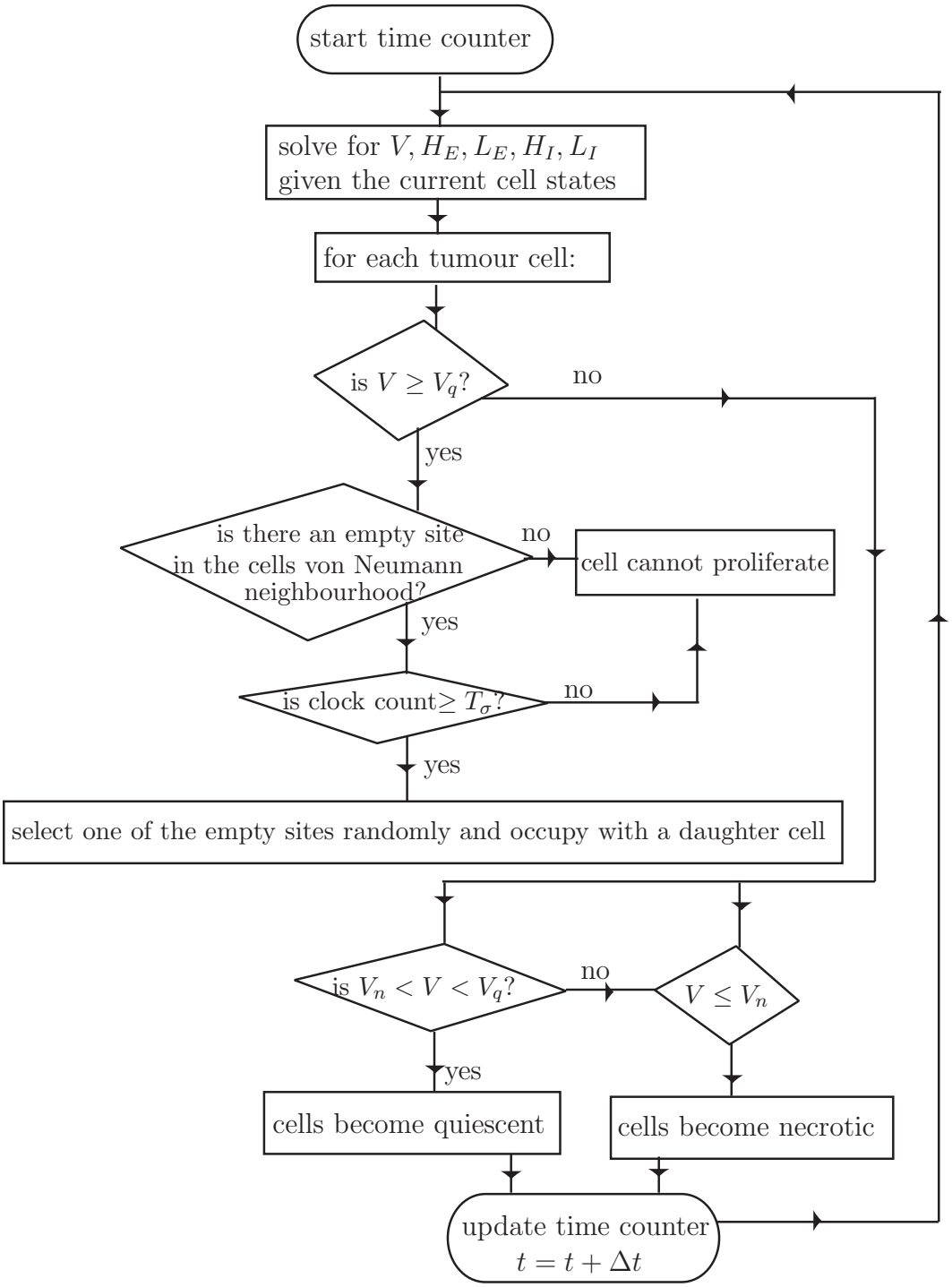

Figure 4.2: Schematic representation of the automaton process showing the effects of oxygen. Note that by replacing 'V' with 'H_I' or 'H_E' in the above rules, one can get similar automaton process for the effects of intra- and extracellular H^+-ions. See main text for full details.

Non-dimensionalising

Note that the average doubling time of a tumour cell is of the order of 10–24 hours [39] which can vary depending on tumour cell type. The diffusion times for the metabolites in our model (lactate, hydrogen ions and oxygen), on the other hand, are of the order of 1–10 seconds (e.g. with mean intervessel distance, $\Delta x = 10^{-2}$cm, and lactic acid diffusion constant, $D_L = 1.08 \times 10^{-5}$ cm^{-2}s^{-1}, the diffusion time is given by $\Delta\tau = \Delta x^2/D_L = 9.3$ seconds [170]). Under the timescale of interest (tumour cell growth$\sim$ days, chemical reaction/diffusion$\sim$ hours), we can therefore assume quasi-steady conditions for oxygen, hydrogen ions and lactate, so that the time derivatives in (4.1)–(4.5) can be set to zero. To facilitate our numerical study of the model, we also non-dimensionalise by letting $\tilde{V} = V/V^g$, and as in the previous chapters we take

$$\tilde{x} = \sqrt{\frac{\alpha_4}{D_H}}x,\ \tilde{H}_I = \frac{H_I}{b},\ \tilde{H}_E = \frac{H_E}{b},\ \tilde{L}_I = \frac{\alpha_4 L_I}{d_4},\ \tilde{L}_E = \frac{\alpha_4 L_E}{d_4}.$$

The leading order quasi-steady dimensionless equations read

$$0 = \nabla^2\tilde{V}(\tilde{\mathbf{x}}) - \tilde{d}_V\tilde{V}(\tilde{\mathbf{x}}), \tag{4.6}$$

$$0 = \frac{2\tilde{\Phi}_G\psi\mathrm{H}(1-\tilde{V})}{\tilde{H}_I(\tilde{\mathbf{x}})+1} + \tilde{d}_1 + \tilde{\phi}(\tilde{\mathbf{x}}), \tag{4.7}$$

$$0 = \nabla^2\tilde{H}_E(\tilde{\mathbf{x}}) - \tilde{\phi}(\tilde{\mathbf{x}}), \tag{4.8}$$

$$0 = \frac{2\tilde{\Phi}_G\mathrm{H}(1-\tilde{V})}{\tilde{H}_I(\tilde{\mathbf{x}})+1} + 1 - \tilde{L}_I(\tilde{\mathbf{x}}) - \tilde{\theta}(\tilde{\mathbf{x}}), \tag{4.9}$$

$$0 = \nabla^2\tilde{L}_E(\tilde{\mathbf{x}}) + \tilde{D}_{HL}\tilde{\theta}(\tilde{\mathbf{x}}), \tag{4.10}$$

where,

$$\begin{aligned}
\tilde{\theta} &= \tilde{k}_3(\tilde{H}_I\tilde{L}_I - \tilde{H}_E\tilde{L}_E), \\
\tilde{\phi} &= \tilde{l}_H(\tilde{H}_E - \tilde{H}_I) - \tilde{f}_1\mathrm{H}(\tilde{H}_I - \tilde{H}_E)(\tilde{H}_I - \tilde{H}_E) - \tilde{k}_3\psi(\tilde{H}_I\tilde{L}_I - \tilde{H}_E\tilde{L}_E), \\
\tilde{D}_{HL} &= \frac{D_H}{D_L},\ \tilde{l}_H = \frac{l_H}{\alpha_4},\ \tilde{f}_1 = \frac{f_1}{\alpha_4},\ \tilde{k}_3 = \frac{k_3 b}{\alpha_4}, \\
\tilde{\Phi}_G &= \frac{\Phi_G}{bd_4},\ \tilde{d}_1 = \frac{d_1}{b\alpha_4},\ \psi = \frac{d_4}{b\alpha_4},\ \tilde{d}_V = \frac{D_H d_V}{D_V\alpha_4}.
\end{aligned}$$

The initial and boundary parameters become

$$\tilde{H}_I^0 = \frac{H_I^0}{b},\ \tilde{H}_E^0 = \frac{H_E^0}{b},\ \tilde{L}_I^0 = \frac{\alpha_4 L_I^0}{d_4},\ \tilde{L}_E^0 = \frac{\alpha_4 L_E^0}{d_4},\ \tilde{V}^0 = \frac{V^0}{V^g}.$$

Recall that equations (4.7) and (4.9) are only valid at spatial locations of viable cells (i.e. proliferative, quiescent). So that $\tilde{\phi}(\tilde{x})$ and $\tilde{\theta}(\tilde{x})$ in equations (4.8) and (4.10) are set to zero where there are necrotic cells or empty space. Similarly, $\tilde{d}_V$ in equations (4.6) is set to zero where there are necrotic cells or empty space.

At each time step, we solve the algebraic equations in (4.6)–(4.10) simultaneously given the previous cell states (proliferative, quiescent, dead).

4.2.3 Parameter estimation

We are able to estimate some of the new model parameters from the literature. A study by Kallinowski *et al.* [113] finds that the oxygen consumption rate of L929 and DS-carcinosarcoma cells *in vitro* and *in vivo* lie within the range of 0.10–0.83 fmol/s/cell. Using the fact that one mole contains 10^{15} femtomole [171] and one cell has a typical volume of approximately 10^{-12} litres [131], the oxygen consumption rate becomes 1×10^{-4} – 8.3×10^{-3} mol/l/s. To convert from mol/l/s to s^{-1}, we use the fact that one mole of oxygen is equivalent to 26.2 litres of oxygen [127], so that d_c becomes 2.63×10^{-3} – 21.83×10^{-3} s^{-1}. Typically, cells become hypoxic if the oxygen partial pressure falls below 10 mmHg [2]. We convert this value into

mol/l using the conversion rates in [162] to get $V_q = 1.25 \times 10^{-5}$ mol/l. A study by Casciari *et al.* [39] finds that oxygen levels below $8.2{\times}10^{-6}$ mol/l (at pH 6.6) inhibits cell growth of EMT6IRo mouse mammary tumour cells and so we take this value to be the minimum oxygen concentration for cell survival, V_n.

As well as being dependent on oxygen, virtually all biological processes are pH sensitive, for example, glycolysis, protein synthesis, DNA synthesis, are all permissive at a specific pH range and a slight deviation from the norm has a detrimental effect on their functionality [34, 123]. Low intracellular pH is a hallmark of non-proliferative cells [85, 180] and a rapid increase in pH_I may be vital to bring these cells from a quiescent state to a proliferative state [137]. It has been shown that a pH_I threshold of ~ 7.2 for quiescence exists, below which growth factors cannot set the transformation of fibroblasts back into proliferative [180]. Intracellular acidification in mammalian cells undergoing apoptosis was first observed about two decades ago [15] and since then, several studies have confirmed that this is a common apoptotic characteristic. Although apoptosis and necrosis are two separate modes of cell death [262] and since we are not concerned with the morphological or chemical changes that occur to cells following their death (which distinguishes necrosis from apoptosis), we adopt apoptotic values for our model. A study by Park *et al.* [167] shows that the intracellular pH of HL-60 Human Leukemia cells undergoing apoptosis lies between 6.6–6.9 with a corresponding extracellular pH of 6.2–6.4. We denote these values by pH_I^n and pH_E^n respectively. Along with Patel *et al.* [170] we use a quiescence threshold of $\mathrm{pH}_E^q = 6.4$ when we consider effects due to extracellular pH.

We simulate the model on a 200×200 square grid where the tumour tissue under consideration is surrounded by a blood vessel with optimal oxygen concentration, V^0, of 2.8×10^{-3} mol/l [193]. In dimensionless form: $\tilde{V}^0 = 22.4, \tilde{H}_I^0 = 0.6309, \tilde{L}_I^0 = 1, \tilde{H}_E^0 = 0.6309, \tilde{L}_E^0 = 1$. Assuming that the diameter of each cell in this model is of the order of 10 μm, the 200×200 domain corresponds to a physical size of 2 mm. The parameter values used in the model are summarised in

Table 4.1: (a) Model parameter values which appear in equations (4.1)–(4.5). (b) The tildes represent the non-dimensional values used in (4.6)–(4.10).

(a)

Description	Symbol	Value	Units	Ref.
O_2 diffusion co-efficient	D_V	1.82×10^{-5}	cm^2s^{-1}	[238]
H^+ diffusion co-efficient	D_H	1.1×10^{-5}	cm^2s^{-1}	[53]
Lactate diffusion co-efficient	D_L	1.08×10^{-5}	cm^2s^{-1}	[127]
O_2 consumption rate	d_c	2.6×10^{-3}	s^{-1}	[113]
Necrosis O_2 threshold	V_n	8.2×10^{-6}	mol/l	[39]
Cell hypoxia	V^g, V_q	1.25×10^{-5}	mol/l	[236]
Necrosis pH_i threshold	pH_I^n	6.6–6.9	mol/l	[167]
Necrosis pH_e threshold	pH_E^n	6.2–6.4	mol/l	[170]
Quiescence pH_i threshold	pH_I^q	7.2	mol/l	[180]
Quiescence pH_e threshold	pH_E^q	6.4	mol/l	[170]

(b)

Parameter	Value
$\tilde{D}_{HL}$	1
$\tilde{d}_V$	$0.0016/\alpha_4$
$\tilde{V}_q$	1
$\tilde{V}_n$	0.65
$\tilde{H}_I^q$	0.63
$\tilde{H}_I^n$	2.51
$\tilde{H}_E^q$	3.98
$\tilde{H}_E^n$	6.30

Table 4.1. We will work with the non-dimensional model hereafter but drop the tildes for notational convenience. We discretise the spatial derivatives in equations (4.6), (4.8) and (4.10) on the $N \times N$ (200×200) cell grid and solve the resulting systems of algebraic coupled equations using 'backslash' in Matlab.

4.3 Model results

We begin by presenting our model results in the case where cellular growth and phenotypic change depend solely on oxygen levels. We later allow cellular growth and phenotypic change to depend also on extracellular and intracellular H^+-ions. We focus on the effects of various key parameters on tumour morphology and cellular pH gradient and, in particular, examine whether varying activities of the

NHE or MCT transporters has any effect at this early stage of tumour growth.

4.3.1 Effect of oxygen on tumour growth

In this section, we neglect any pH effects on cell growth and phenotypic transformations and allow only oxygen to drive tumour growth and cell state. Due to the lack of available data on α_4, we begin by estimating d_V ($= 0.0016/\alpha_4$) by fitting our model output to the experimental results [Personal communication with Craig Murdoch, School of Dentistry, University of Sheffield, T47D breast cancer cell line] shown in Figure 4.3. A comparison between our simulation and this experimental data is shown in Figure 4.4. It is clear that the viable rim size in our model does not match very well with the experimental results for early time which is, in part, due to the empty spaces formed inside the tumour mass at the initial stage of the growth (see Figure 4.3(a)). Our simulated tumour, however, has no intratumoural empty spaces at this early stage and as a result we have a smaller radius compared to the experimental results. Moreover, as the necrotic radius becomes bigger, our simulated viable rim remains roughly constant in size compared to the experimental rim which decreases. It has been previously suggested that necrotic cells secrete toxic chemicals that act as growth or viability inhibitors which diffuse from the core to the edge of the tumour and play a part in bringing tumour growth to a saturation level [66]. It is possible that such an effect could explain the observed differences between the data and our simulations. Our simulated tumour shows a three layered structure (see Figure 4.5) comparable to that typically observed in an avascular tumour that does not possess a blood supply (as shown in Figure 4.1). Figure 4.6 shows how the simulated tumour in our model does not reach a saturation level with time but continues to grow linearly. This is because although oxygen is consumed by the viable cells and is diminished in the inner core of the spheroid (see Figure 4.7), oxygen levels at the outer layer of the tumour mass are still permissive for cell proliferation. Note that the best fit shown in Figure 4.3 is obtained with a value of 750 for d_V.

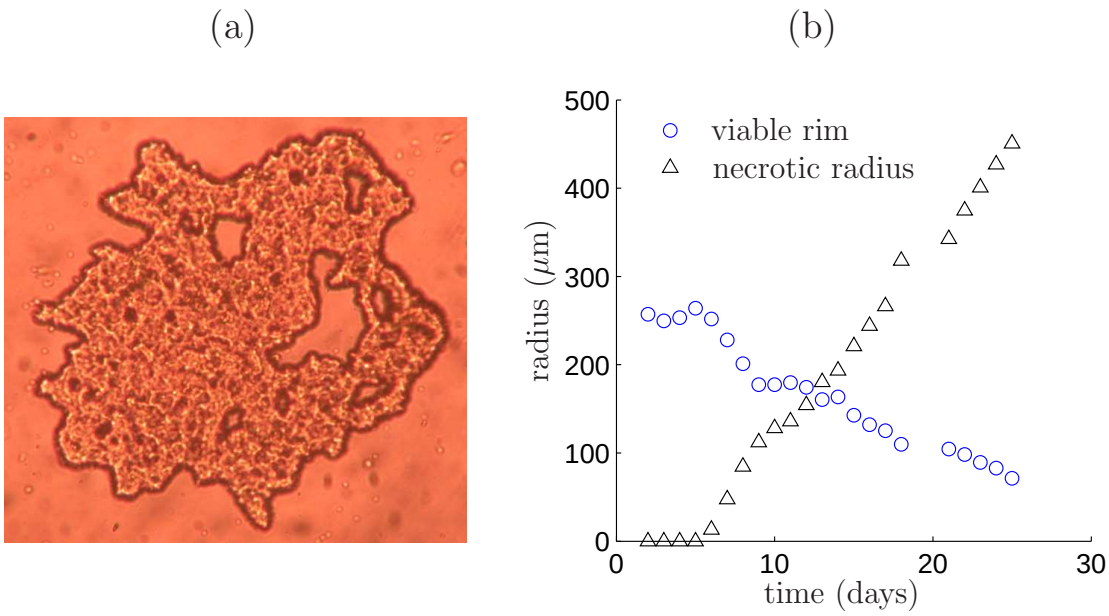

Figure 4.3: (a) A snapshot of T47D breast cancer growth line at day one (diameter 500μm) shows intratumoral empty spaces [Craig Murdoch, School of Dentistry, University of Sheffield, Personal communication]. (b) The evolution of the viable rim (circles) and necrotic radius (triangles) over a period of 26 days of the T47D breast cancer shown in (a).

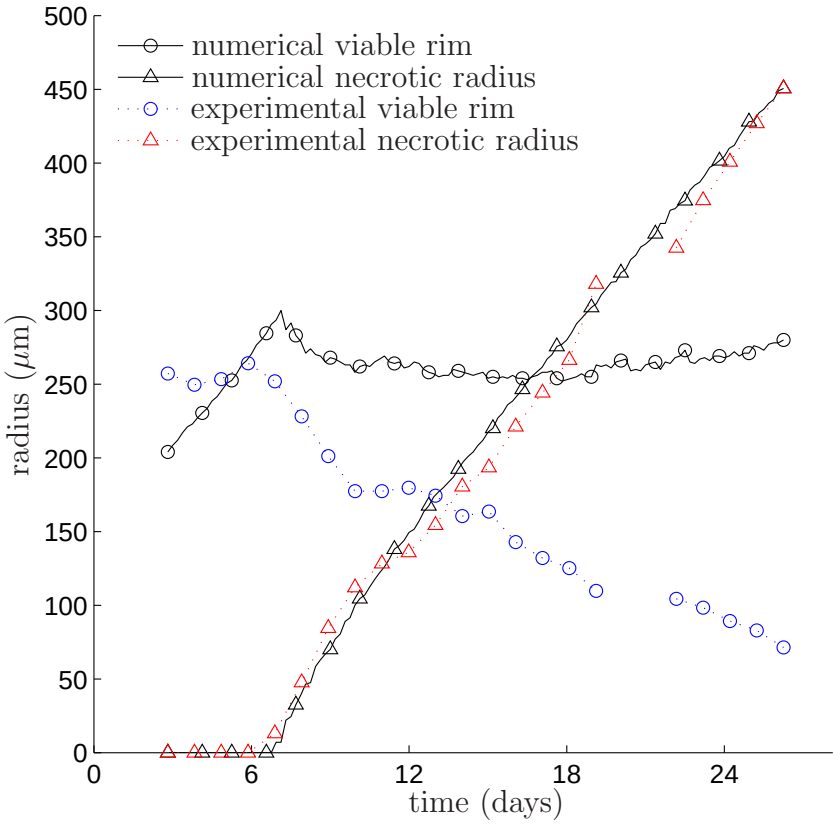

Figure 4.4: Comparison of our numerical solution (—○—,—△—) to the experimental data (··· ○ ···,··· △ ···) presented in Figure 4.3. Our numerical plot corresponds to the mean of 10 simulations with standard deviations at 20 time intervals {0, 0, 0, 0, 0.98, 1.08, 1.07, 1.09, 1.00, 1.23, 1.18, 1.31, 1.28 1.21, 1.42, 1.00, 1.09, 1.27, 1.40, 1.19} for the necrotic radius and {2.12, 2.03, 1.53, 1.76, 2.16, 2.04, 1.55, 1.65, 1.69, 2.08, 1.18, 1.65, 1.17, 1.58, 1.51, 1.58, 1.42, 0.99, 0.99, 1.70} for the viable rim. Parameter values are as in Table 4.1 and with $d_V = 750, N = 200, L = 0.02$. Note that the best comparison between the data and the simulations is achieved when one simulation time step is taken to be roughly five hours.

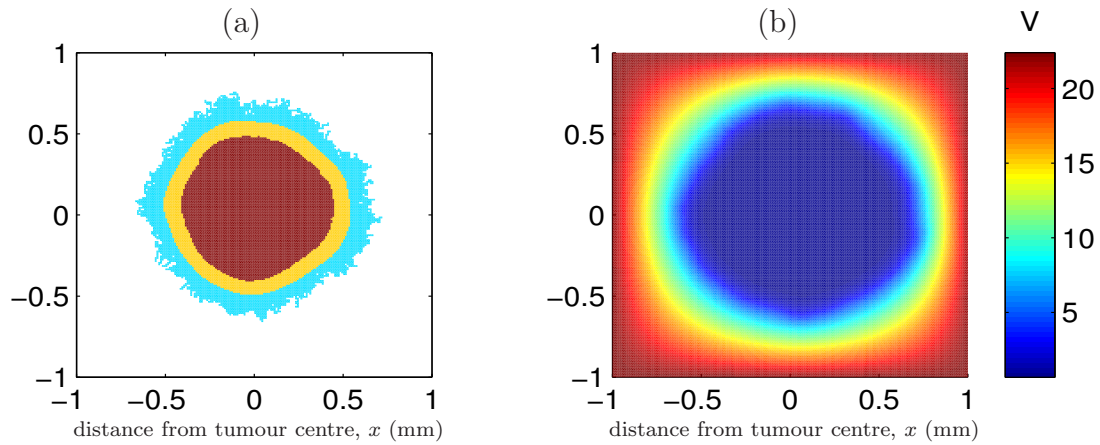

Figure 4.5: Plots showing (a) a layered tumour comprised of necrotic (dark red), quiescent (yellow) and proliferating (blue) tumour cells. Empty space is represented as white. The corresponding oxygen profile is shown in (b). The tumour centre is designated as the 0 point on the x and $y-$axis. After 26 days the tumour reaches a radius of 765 μm with a total number of 13,000 cells. Parameter values: initial number of tumour cells=16, $V_q = 1, V_n = 0.65, V^0 = 22.4, d_V = 750, N = 200, L = 0.02, t = 180, T_\sigma = 12$.

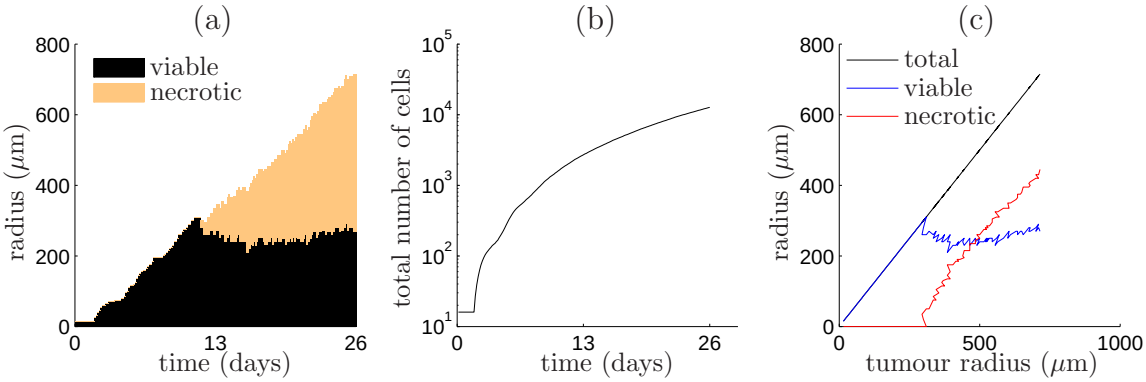

Figure 4.6: Plots of simulation output showing how: (a) the size of the viable rim and the necrotic core change with time; (b) the total number of cells within the tumour spheroid continues to increase and does not reach a saturation level; (c) the onset of necrosis occurs at a tumour radius of ~ 250 μm (in agreement with [228]) and continues to increase in size. Parameter values are as given in the caption to Figure 4.5.

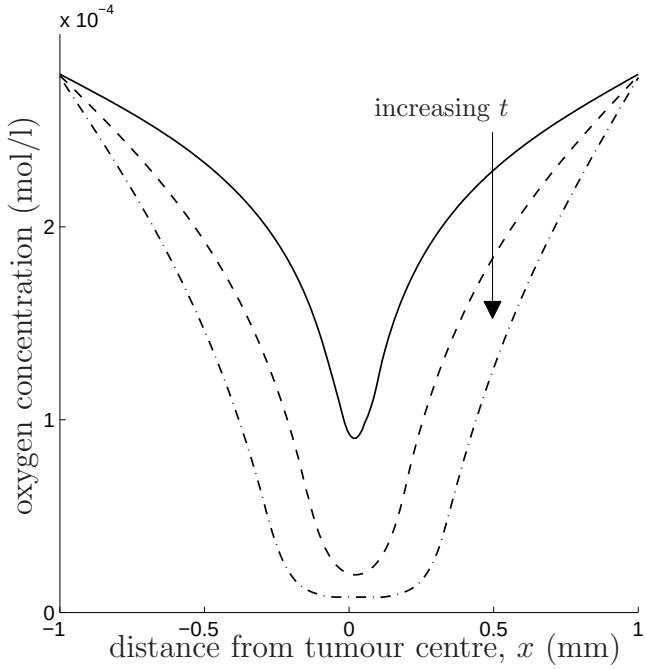

Figure 4.7: Oxygen concentration along row 100 of the 200 × 200 grid at: (——, day 6), (– – –, day 11) and (– · –, day 19). Oxygen levels decrease as time increases due to consumption by the rapidly dividing cells. The lowest concentration is found at the centre of the tumour spheroid. Parameter values are as given in the caption to Figure 4.5.

4.3.1.1 Effect of parameter variations on tumour morphology

Metastasis is when a tumour cell leaves the primary tumour mass and colonises in a neighbouring tissue [17]. This is a sign of a high grade invasive tumour as established by pathological specimens [68]. Moreover, the irregular finger-like projections (as seen in Figure 4.8) or completely disconnected regions of tumour cells are attributable to aggressive tumours compared to more benign ones which are usually distinguished by a smooth non-invasive edge [60]. We illustrate in Figure 4.9 an example of this feature obtained simply by increasing the value of the dimensionless oxygen consumption rate, $\tilde{d}_V$, which can be written in terms of

dimensional parameters as $\tilde{d}_V = D_H d_V / D_V \alpha_4$. A large $\tilde{d}_V$ could then be a result of one, or, a combination of the following: 1) an increase in oxygen consumption rate, d_V; 2) a decrease in oxygen diffusion rate, D_V; 3) an increase in extracellular H^+-ions diffusion rate, D_H; 4) a decrease in the rate of lactate decay/conversion, α_4. Biologically, this implies that high oxygen-consuming tumour cells can possibly give rise to a tumour with a "fingering" morphology. Alternatively, an aggressive morphology can be attained if the diffusion rate of extracellular H^+-ions is high or the tumour cells are not oxygenated well-enough to allow the conversion of intracellular lactate to glucose or pyruvate.

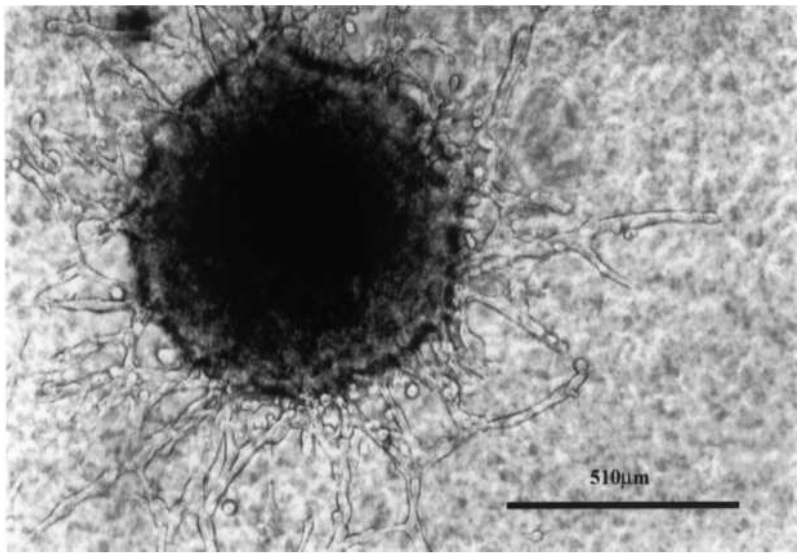

Figure 4.8: Multi-cellular tumour spheroid (MCS) gel assay showing multiple projections of "fingering"-like invasion pathways (magnification:×200). Image courtesy of [115].

This is because as oxygen is utilised by proliferating cells in the outermost layer of the spheroid, less oxygen is left in the innermost region and so tumour cells become quiescent or die if oxygen levels become too intolerable. This means that higher $\tilde{d}_V$ implies an earlier onset of necrosis; the larger the necrotic core; and the smaller the viable rim. Rough tumour edges then form due to there being fewer

proliferative cells along the tumour border than there are necrotic cells (which are incapable of proliferating). Note that although the tumour develops rough "fingered" edges as $\tilde{d}_V$ increases, the necrotic zone is large and the number of proliferating and quiescent cells is small suggesting that one should not only focus on the morphology of the invading mass to predict the aggressiveness, but also to the type of cells comprising it.

Our results are in-line with previous continuum (e.g. see [136]) and discrete-continuum models (e.g. see [78]) which study the effect of tumour microenvironment on tumour growth. More specifically, Gerlee & Anderson [78] predict that a low oxygen concentration in the tissue gives rise to a tumour with a fingered morphology, while a high oxygen concentration in the tissue gives rise to a tumour with a round morphology. Also, Macklin & Lowengrub [136] predict that tissue invasion via fragmentation can be caused by a hypoxic microenvironment.

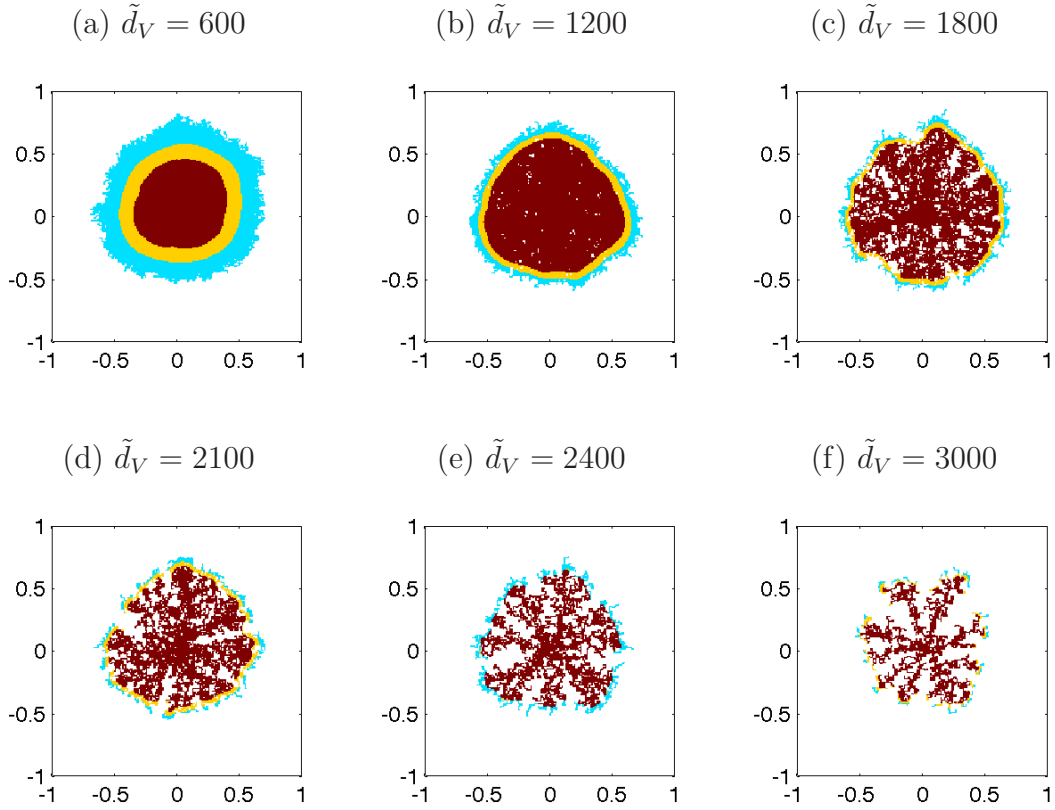

Figure 4.9: Tumour morphology changes as the dimensionless oxygen consumption rate ($\tilde{d}_V$) is varied. Note also how the thickness of the protruding "fingers" change as $\tilde{d}_V$ varies. Axes: space x, y (mm). Colouration: blue (proliferating cells), yellow (quiescent cells), dark red (necrotic material), white (empty space). Parameter values: $V_q = 1, V_n = 0.65, V^0 = 22.4, t = 26$ days in each simulation.

4.3.2 Effect of extracellular H^+ ions on tumour growth

In this section, we remove the effects of oxygen on cell proliferation and phenotypic transformations and instead focus on the effects of extracellular pH. That is, we take cellular proliferation and phenotypic transformations to depend solely on the extracellular levels of H^+-ions and update the state of each cell as mentioned in Section 4.2.2. Note that oxygen levels, however, still play a role in our simulations

in determining whether a tumour cell undergoes anaerobic glycolysis or not, but does not directly influence cell growth or phenotypic change. A typical simulation result in this case is shown in Figure 4.10 with the corresponding temporal mean (over the viable cells) of pH and lactate shown in Figure 4.11. Tumour cells which are located in the innermost region of the spheroid become glycolytic (enclosed by a black curve in the left hand panel of Figure 4.10) when oxygen levels decrease below the glycolytic threshold (V_q) which in turn lowers pH_I and pH_E, and increases L_I and L_E in this region because of excess production of H^+-ions and lactate. Note that the spatial concentration of extracellular lactate is roughly homogeneous due to the estimated dimensionless diffusion co-efficient value being low ($D_{LH} = D_H/D_L \sim 1$).

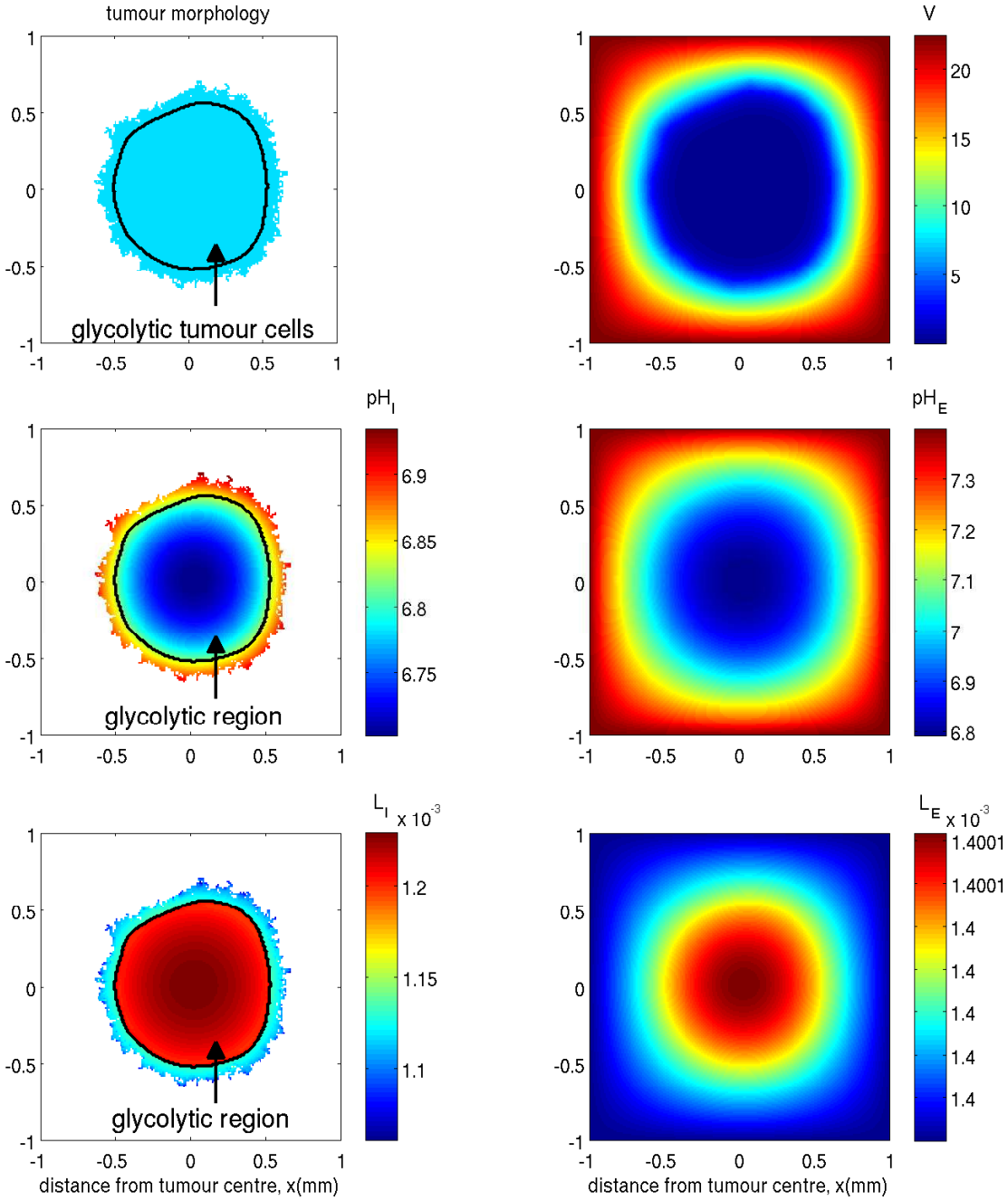

Figure 4.10: Plots with cellular growth and phenotypic transformations entirely dependent on extracellular H^+-ions. A tumour comprised of only proliferative cells is formed, with an inner hypoxic (glycolytic) region, compared to the three layered structure shown in Figure 4.5. Parameter values are as given in the caption to Figure 4.5 but with also $pH_E^q = 6.4$, $pH_E^n = 6.2$, $H_I^0 = 0.39, H_E^0 = 0.39, L_I^0 = 1, L_E^0 = 1$.

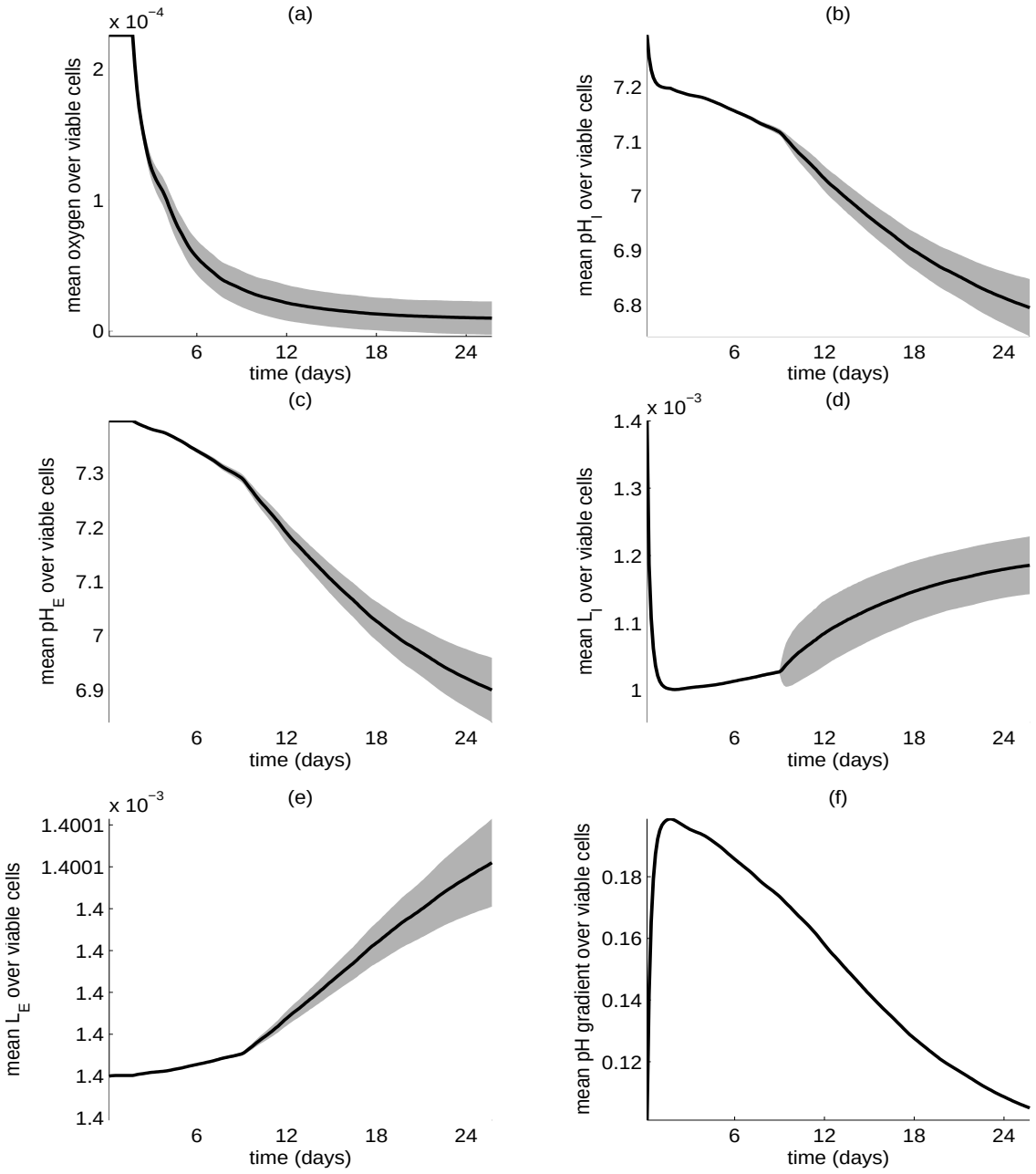

Figure 4.11: Plots showing the mean concentrations of (a) oxygen, (b and c) pH and (d and e) lactate over the viable cells in the spheroid when cellular growth and phenotypic change are entirely dependent on the extracellular levels of H^+-ions. Note that the mean cellular pH gradient (pH_E-pH_I) shown in (f) is positive. The grey shades represent the standard deviations. We observe that the mean pH decreases and lactate increases rapidly when oxygen levels become low (roughly at day 9) because of the rise in the glycolytic production of H^+-ions.

4.3.2.1 Effect of parameter variation on transmembrane pH gradient and tumour morphology

In this section, we vary some of the key parameters in our model and observe the effect on tumour morphology and cellular pH gradient. Since we use three-dimensional tumour spheroid studies to estimate the quiescence and necrosis threshold and our model is only a two-dimensional representative, we begin by varying these thresholds. We show the effect of varying the quiescence threshold, pH_E^q, on tumour morphology and cellular pH gradient in Figure 4.12. We observe that as pH_E^q is increased from the base value (i.e. from $\mathrm{pH}_E^q = 6.40$) quiescent cells start to appear and the tumour develops a "fingering" morphology. This is because a high pH_E^q means that the tumour cells are less resistant to extracellular acidity and quickly become quiescent instead of proliferating. The cellular pH gradient remains positive and largely the same across the various morphologies shown.

We now vary the extracellular pH necrosis threshold level, pH_E^n, and show the effect on tumour morphology and cellular pH gradient in Figure 4.13. Note that if we assume the base value for pH_E^q (i.e. $\mathrm{pH}_E^q = 6.40$) and vary pH_E^n, the tumour morphology does not change. This is because the extracellular pH in our model does not go below 6.4. However if we choose $\mathrm{pH}_E^q = 6.98$ and vary pH_E^n we see from Figure 4.13 that the tumour starts to develop a necrotic zone when pH_E^n is significantly increased. This is because increasing pH_E^n means that the tumour cells become less resistant to extracellular acidosis and die quickly instead of proliferating or becoming quiescent. The cellular pH gradient remains positive and largely the same as that shown in Figure 4.12.

Recall that Φ_G represents the rate at which intracellular hydrogen ions are produced glycolytically when oxygen concentrations are low. We observe from Figure 4.14 that increasing Φ_G results in the appearance of quiescent and necrotic cells. This is because as Φ_G increases, the production of intracellular H^+-ions from anaerobic glycolysis increases which are then exported outside the cell and as a

result raise the levels of extracellular H^+-ions. This then results in cells quickly becoming necrotic or quiescent. Note that the cellular pH gradient remains positive but increases with increasing rate of glycolysis which is to be expected.

We also observe that as the background production of intracellular H^+-ions (d_1) in tumour cells increases, the tumour changes from that with a "compact" well-rounded edges to one exhibiting several "fingers" (see Figure 4.15). However, a considerable increase in the background production of intracellular H^+-ions (other than from glycolysis) is needed to achieve this. The cellular pH gradient remains positive but increases with increasing values of d_1 which is to be expected since there are more intracellular H^+-ions available.

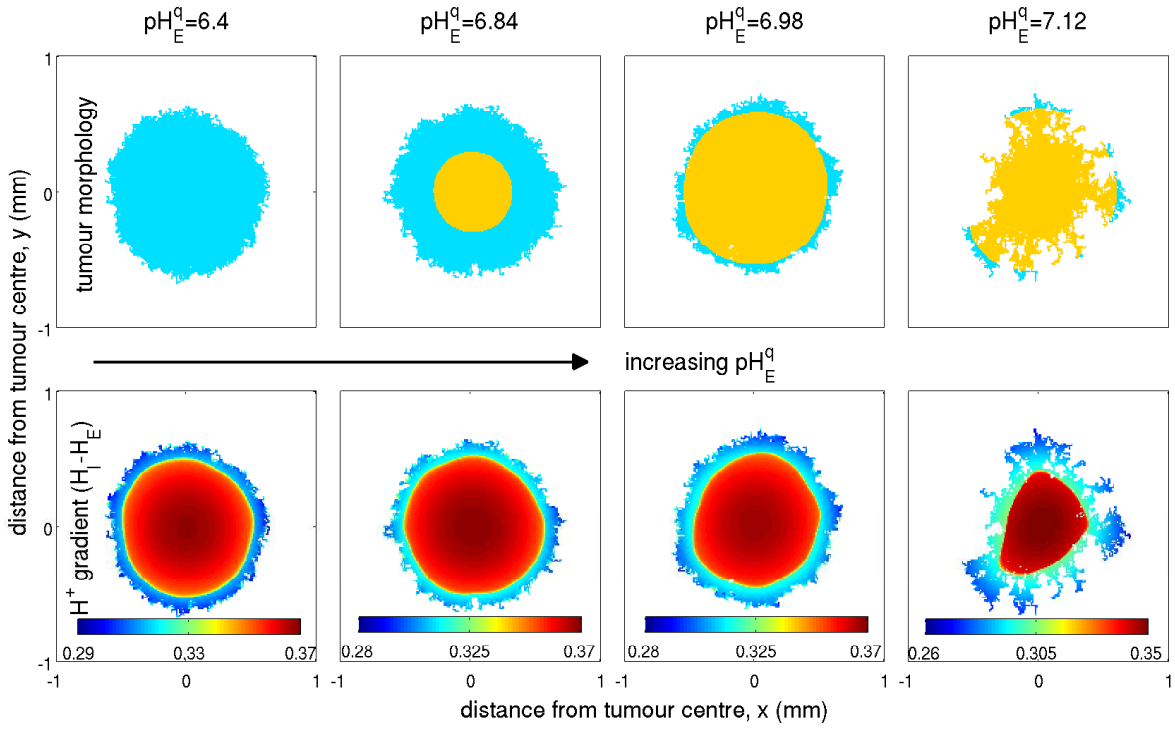

Figure 4.12: Plots showing the effect of increasing the extracellular pH quiescence threshold level, pH_E^q, on tumour morphology (top panel) and cellular H^+ gradient (bottom panel, $H_I - H_E$ in dimensionless form). Colouration is the same as in Figure 4.9. Here, $\mathrm{pH}_E^n = 6.2$ and the remaining parameter values are fixed as in the caption to Figure 4.10. Note that the pH gradient slightly decreases as the tumour develops a "fingering" morphology.

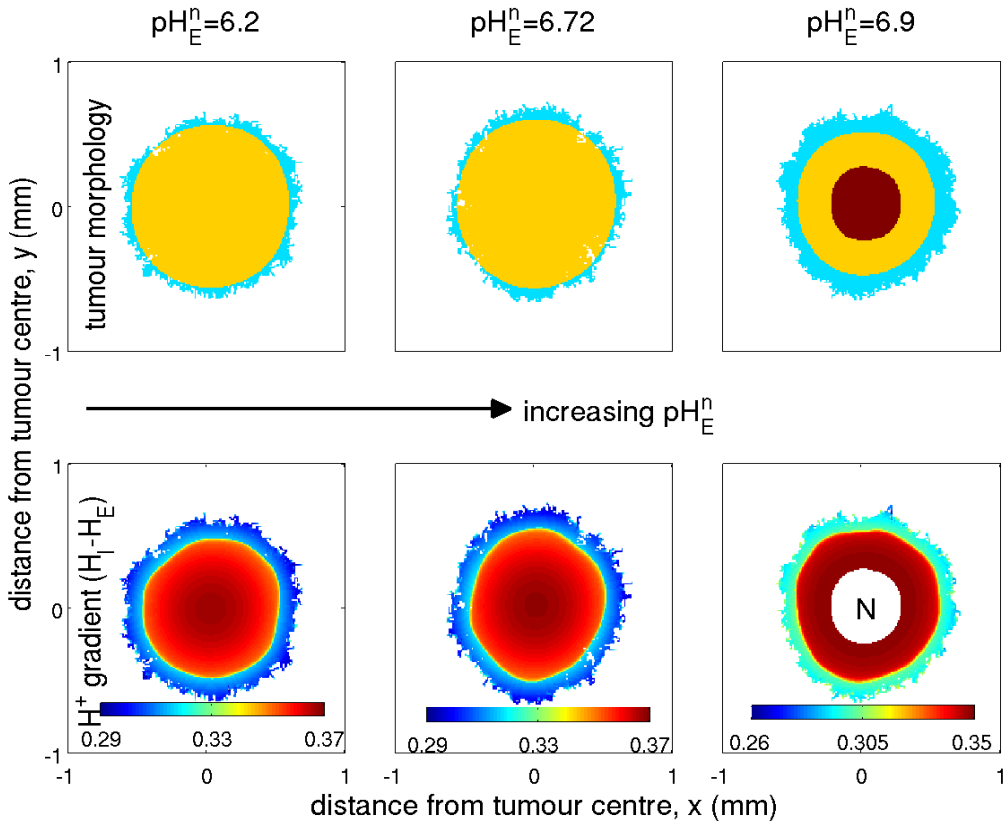

Figure 4.13: Plots showing the effect of increasing the extracellular pH necrosis threshold level, pH_E^n, on tumour morphology (top panel) and cellular H^+ gradient (bottom panel, $H_I - H_E$ in dimensionless form). Colouration is the same as in Figure 4.9. Here, pH_E^q is chosen to be 6.98 and the remaining parameter values are as given in the caption to Figure 4.10. 'N' denotes necrosis.

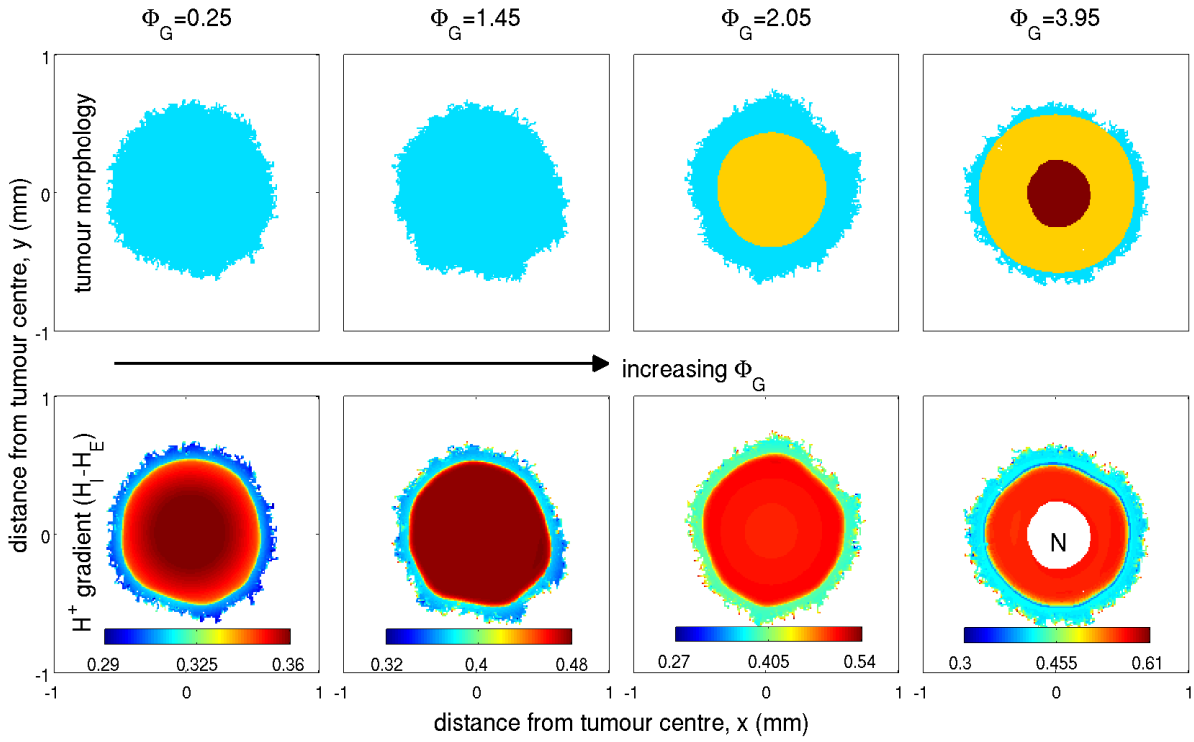

Figure 4.14: Plots showing the effect of increasing the rate of glycolysis, Φ_G, on tumour morphology (top panel) and cellular H^+ gradient (bottom panel, $H_I - H_E$ in dimensionless form). Colouration is the same as in Figure 4.9. $\mathrm{pH_E^q} = 6.4, \mathrm{pH_E^n} = 6.2$ and the remaining parameter values are as in the caption to Figure 4.10. 'N' denotes necrosis.

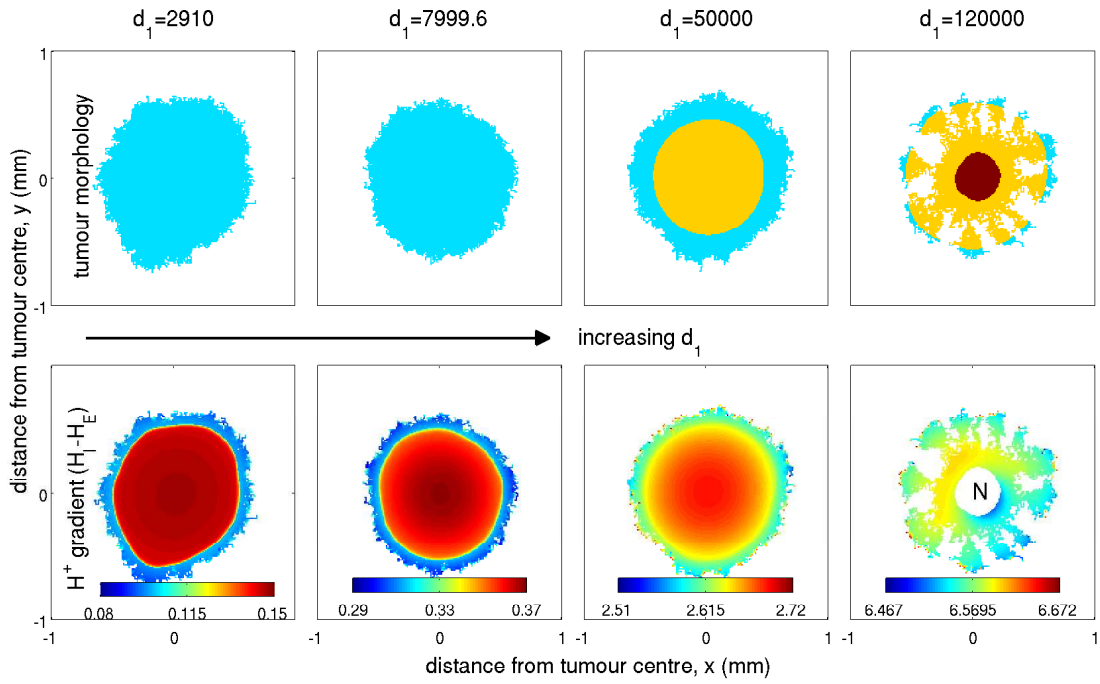

Figure 4.15: Plots showing the effect of increasing the rate of background production of H^+-ions, d_1, on tumour morphology (top panel) and cellular H^+ gradient (bottom panel, $H_I - H_E$ in dimensionless form). $pH_E^q = 6.4, pH_E^q = 6.2$ and the remaining parameter values are as in the caption to Figure 4.10. 'N' denotes necrosis.

4.3.3 Effect of intracellular H^+ ions on tumour growth

In this section, we now allow cellular growth and phenotypic transformations to depend solely on the levels of intracellular hydrogen ions, and observe any differences, to the tumour size and cellular pH gradient. Note that we now assume that neither oxygen nor pH_e affects cellular growth or phenotypic change but oxygen is still assumed to play a role in determining whether a tumour cell undergoes glycolysis or not as in the previous section. Note, in this case, that with our initial estimate of the quiescence threshold (i.e. $pH_I^q = 7.2$) and the necrotic threshold (i.e. $pH_I^n = 6.6$), the initial cluster of cells quickly become quiescent before prolifer-

ating (see Figure 4.16). So, we lower the pH threshold for quiescence to $\mathrm{pH}_I^q = 6.84$ and show a typical simulation with this new threshold level in Figure 4.17 with the corresponding temporal mean (over the viable cells) of pH and lactate shown in Figure 4.18. As we can see, the tumour now consists of a typical layered structure comprising a quiescent core with proliferating cells at the rim.

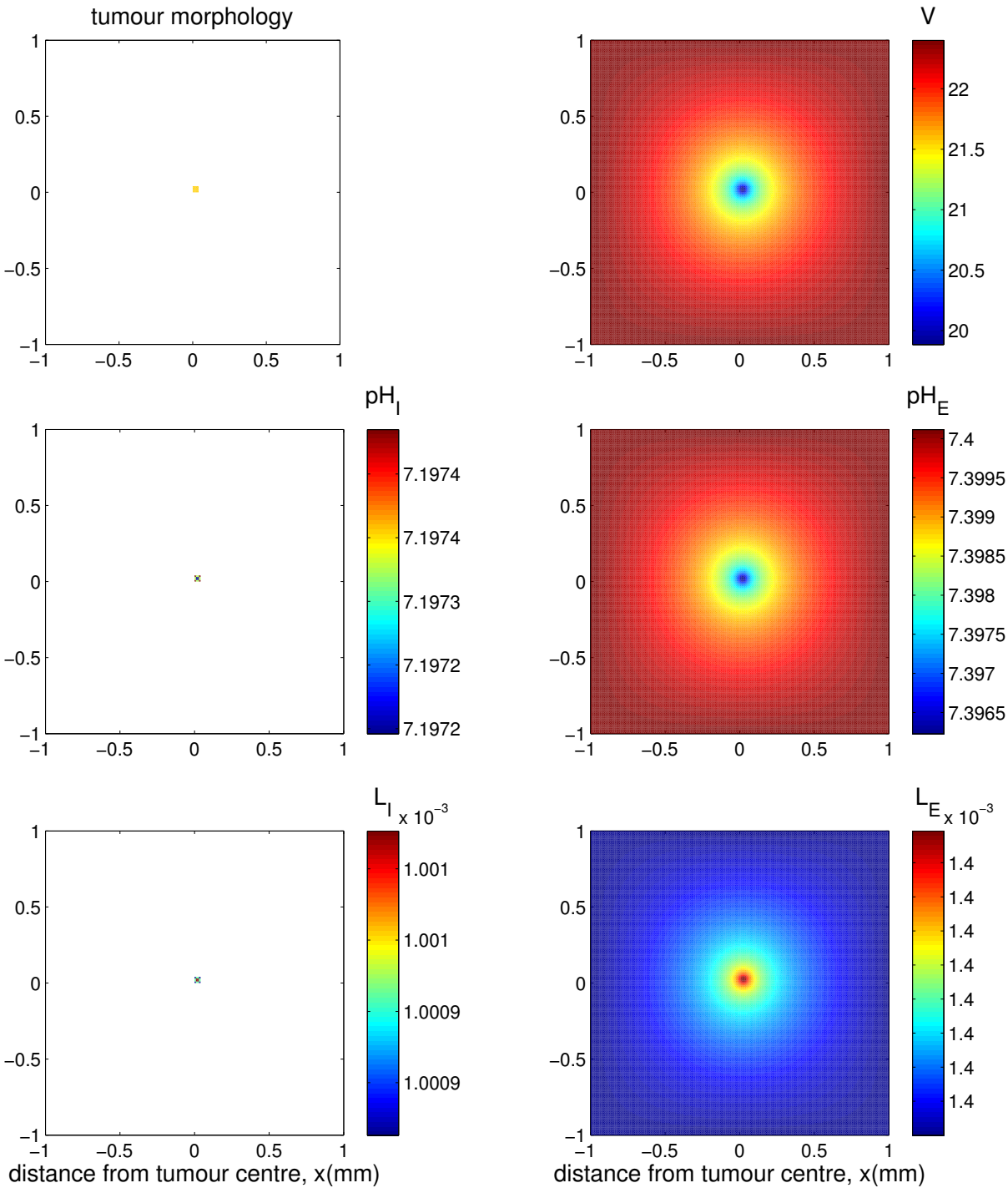

Figure 4.16: Plots with tumour growth and phenotypic change entirely dependent on pH_I. The tumour cells do not grow but quickly became quiescent (yellow). $\mathrm{pH}_I^q = 7.2$ and $\mathrm{pH}_I^n = 6.6$. Remaining parameter values are as shown in the caption to Figure 4.5.

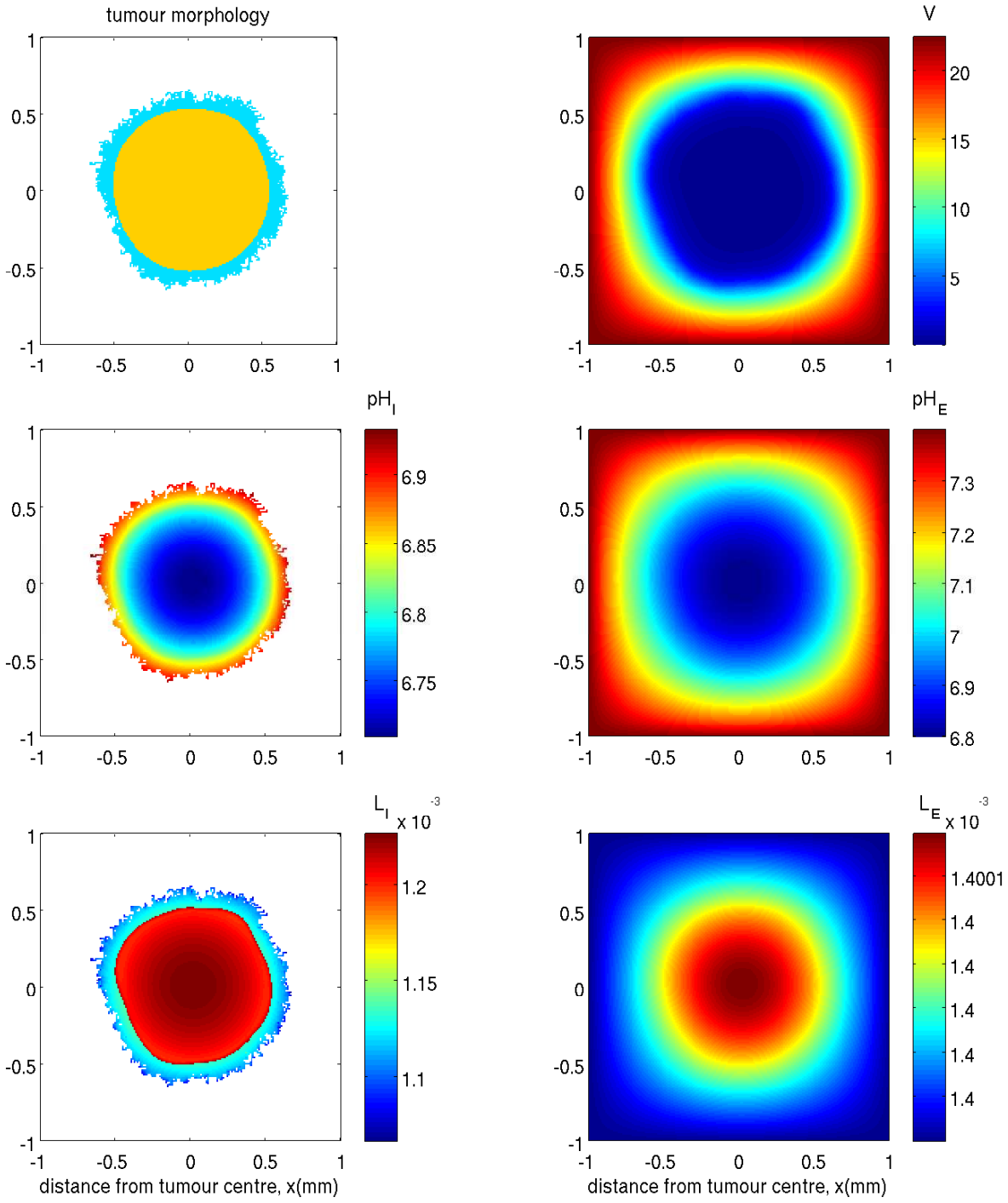

Figure 4.17: Plots with tumour growth and phenotypic change entirely dependent on pH_I. A layered tumour has formed consisting of quiescent (yellow) and proliferating (blue) tumour cells. Parameter values are is in the caption to Figure 4.16 but with a lowered quiescence threshold, $\mathrm{pH}_I^q = 6.84$.

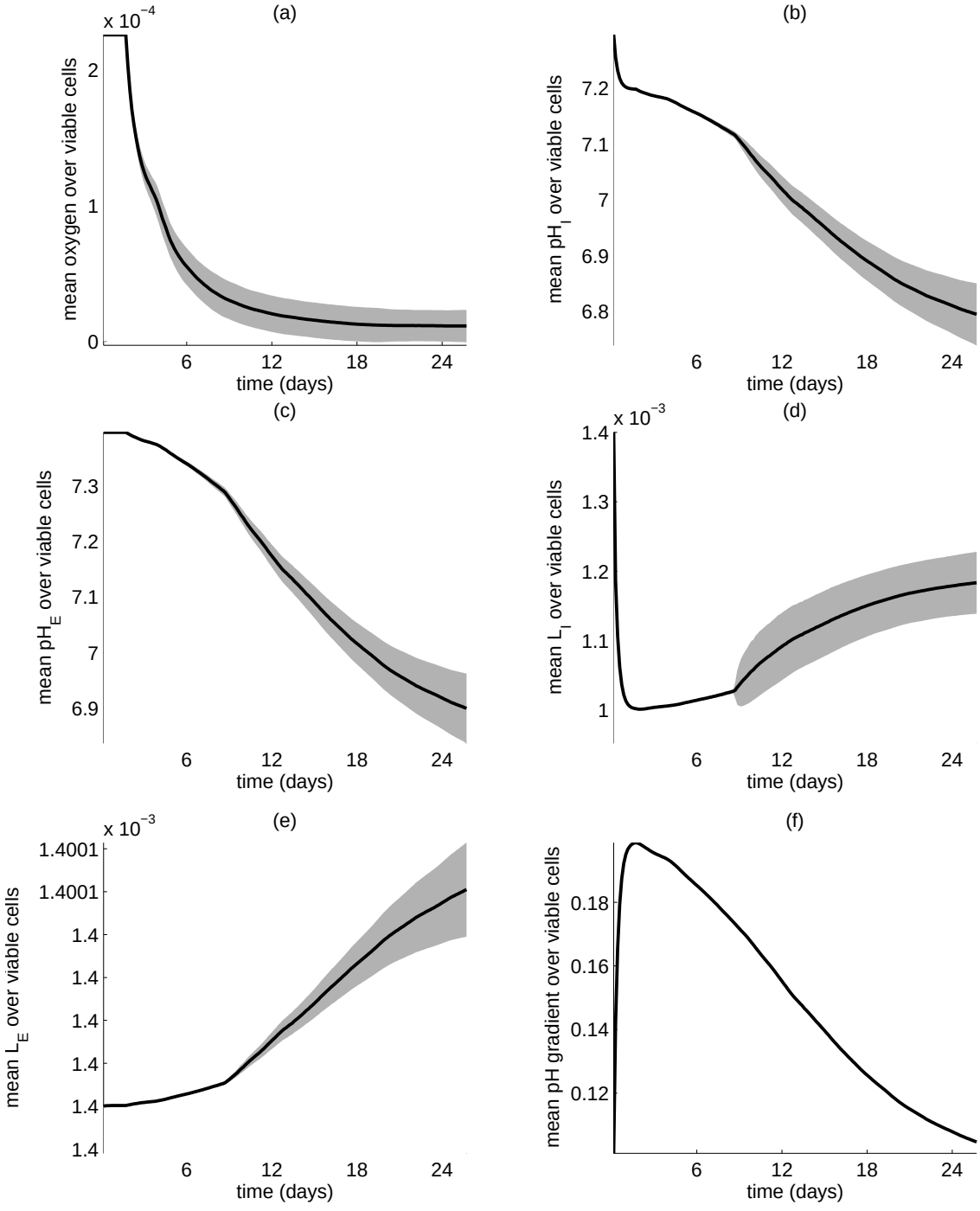

Figure 4.18: Plots showing the mean concentrations of (a) oxygen, (b and c) pH and (d and e) lactate over the viable tumour rim. We also show that the cellular pH gradient (pH_E-pH_I shown in (f)) is positive. This is when cellular growth and phenotypic change is entirely dependent on intracellular H^+-ions.

4.3.3.1 Effect of parameter variation on transmembrane pH gradient and tumour morphology

As before, we vary some of the key parameters in the model and observe the effect on tumour morphology and cellular pH gradient, but this time we let the levels of intracellular pH drive the growth and phenotypic transformation of cells. Note that the levels of oxygen still play a role in the "glycolytic switch" but not in the growth and phenotypic transformations of cells. We begin by varying the intracellular pH threshold for quiescence, pH_I^q. We can see from Figure 4.19 that as pH_I^q increases, the tumour develops a fingering morphology. This is because increasing pH_I^q means that cells are less resistant to intracellular acidity and quickly become quiescent instead of proliferating. Note how the cellular pH gradient becomes smaller when the "fingers" appear which is due to the tumour mass being smaller in size and hence cells which are undergoing anaerobic glycolysis are smaller in number (or none at all for $\mathrm{pH}_I^q = 7.12$). Increasing the intracellular pH threshold for necrosis, pH_I^n (see Figure 4.20) gives rise to a "compact" tumour comprised of the three characteristic layers: necrotic core surrounded by quiescent and proliferative layers. This is to be expected since a high pH_I^n means that cells become less resistant to an increase in intracellular acidity and die, giving rise to a necrotic core.

Figure 4.21 shows that as the background production of intracellular H^+-ions (d_1) increases the tumour begins to develop a quiescent core with some "contorted" edges. However, compared to when cellular growth and phenotypic transformations is dependent on extracellular pH, tumour growth is halted as d_1 further increases. Moreover, the cellular pH gradient remains positive but significantly increases with increasing values of d_1, which is to be expected since more intracellular H^+-ions are produced which are made available for extrusion extracellularly via the cellular transporters.

In addition, as the rate of glycolysis, Φ_G, increases (see Figure 4.22) the tumour consists of necrotic cells as well as proliferative and quiescent cells with

the "fingering" morphology becoming more prominent as Φ_G is increased further. Again, the cellular pH gradient remains positive but significantly increases with increasing values of Φ_G, which is to be expected since more intracellular H^+-ions are glycolytically produced at a higher rate when oxygen levels become low.

We also examine the effect of varying the magnitudes of the rate of activity of the Na^+/H^+ exchanger, f_1, and the lactate/H^+ symporter, k_3 in Figures 4.23–4.24. As can be seen from Figure 4.23 the tumour develops a "fingering" morphology when f_1 is low and the pH gradient becomes high but remains positive. However, as k_3 increases the tumour begins to exhibit a reversed cellular pH gradient and a "compact" morphology consisting of only proliferative cells. The cellular pH gradient becomes more negative as k_3 increases further. This implies that, in our model, the MCT plays a major role in not only regulating the intracellular pH, but also in causing a 'reversed' cellular pH gradient.

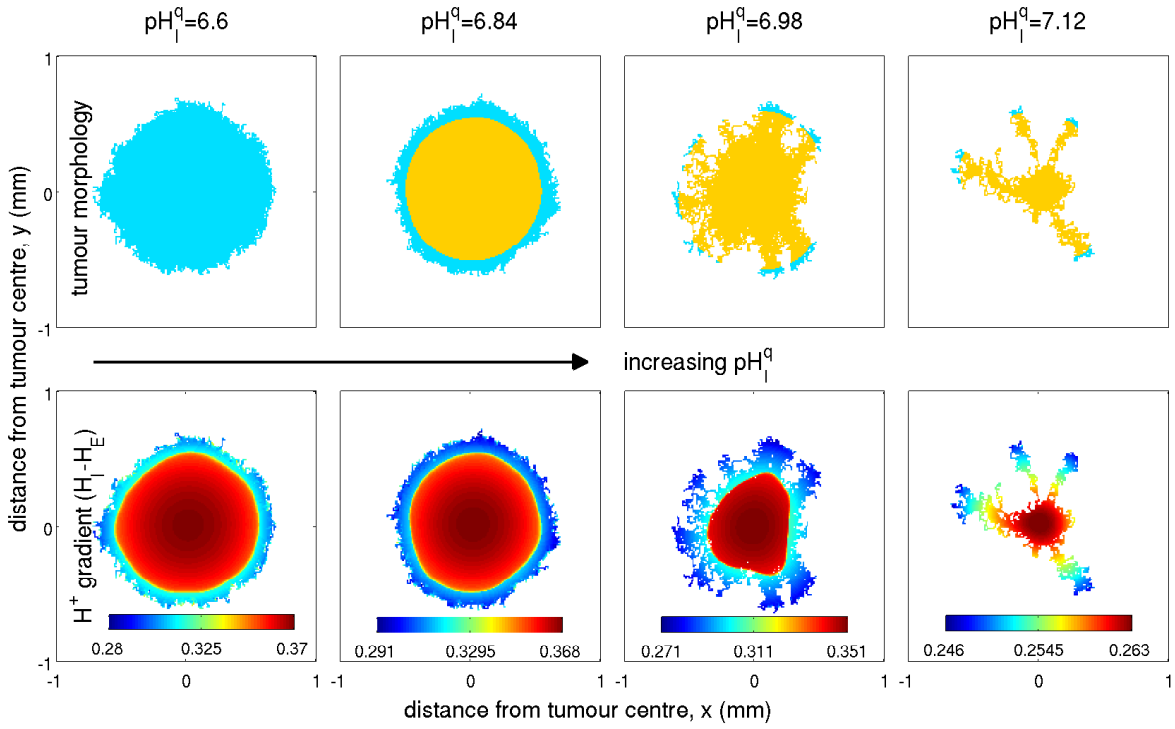

Figure 4.19: Plots showing the effect of increasing the intracellular pH quiescence threshold level, pH_I^q, on tumour morphology (top panel) and cellular H^+ gradient (bottom panel, $H_I - H_E$ in dimensionless form). Colouration is the same as in Figure 4.9. Here, $\mathrm{pH}_I^n = 6.6$ and the remaining parameter values are fixed as in the caption to Figure 4.16. 'N' denotes necrosis.

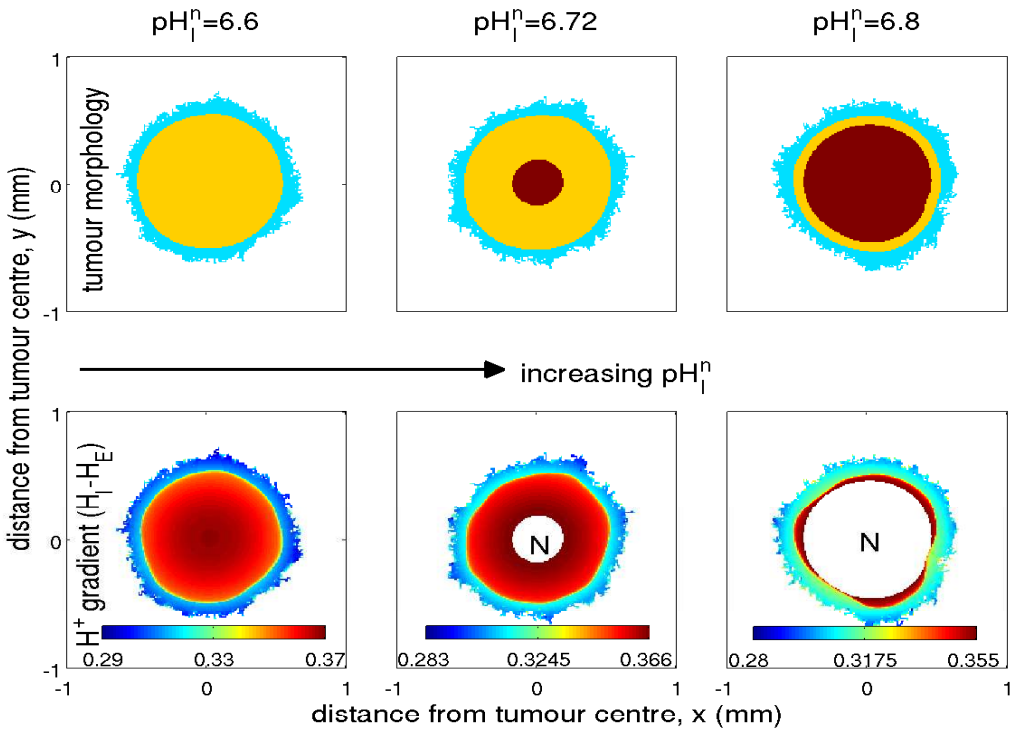

Figure 4.20: Plots showing the effect of increasing the intracellular pH necrosis threshold level, pH_I^n, on tumour morphology (top panel) and cellular H^+ gradient (bottom panel, $H_I - H_E$ in dimensionless form). Colouration is the same as in Figure 4.9. Here, $\mathrm{pH}_I^q = 6.84$ and the remaining parameter values are fixed as in the caption to Figure 4.16. 'N' denotes necrosis.

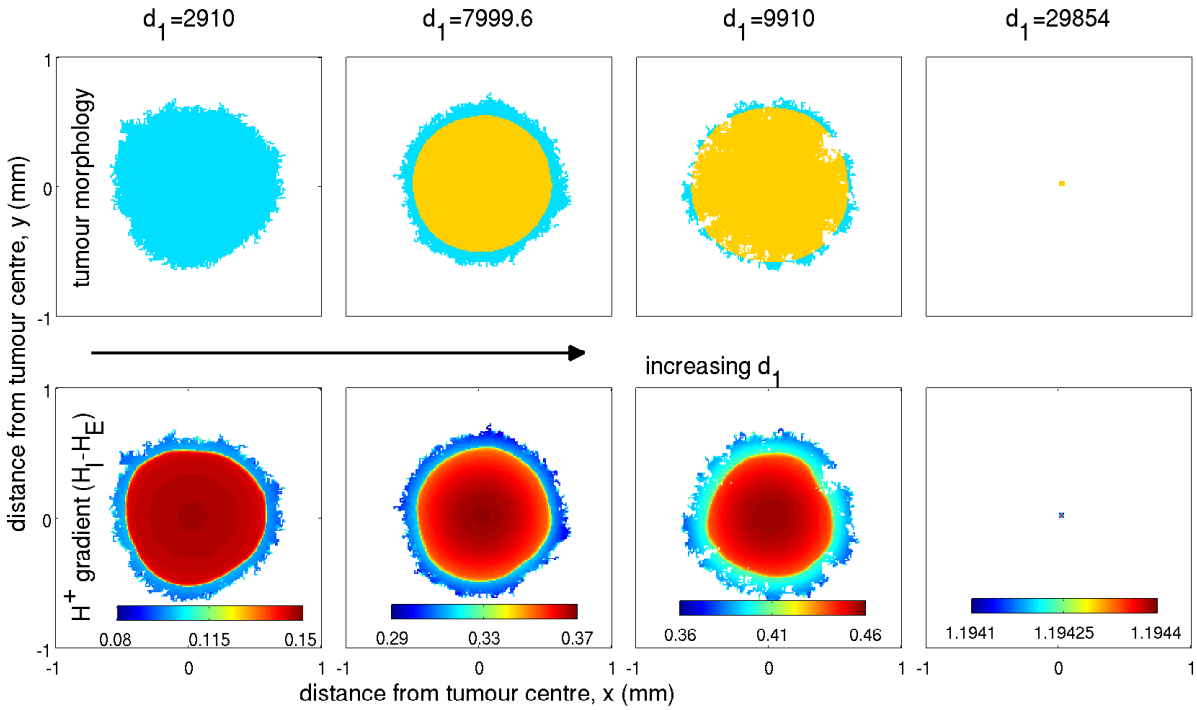

Figure 4.21: Plots showing the effect of increasing the background production of H^+-ions, d_1, on tumour morphology (top panel) and cellular H^+ gradient (bottom panel, $H_I - H_E$ in dimensionless form). Colouration is the same as in Figure 4.9. Here, $pH_I^q = 6.84$, $pH_I^n = 6.6$ and the remaining parameter values are fixed as in the caption to Figure 4.16.

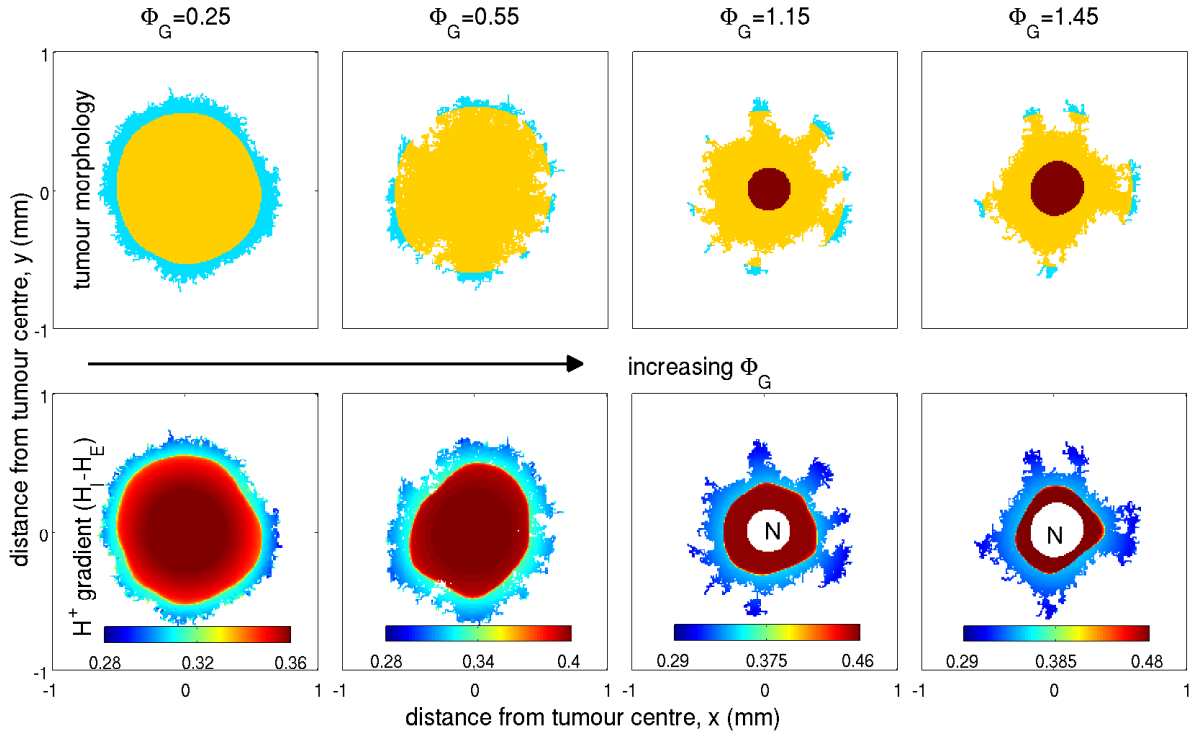

Figure 4.22: Plots showing the effect of increasing the rate of glycolysis, Φ_G, on tumour morphology (top panel) and cellular H^+ gradient (bottom panel, $H_I - H_E$ in dimensionless form). Colouration is the same as in Figure 4.9. Here, $pH_I^q = 6.84$, $pH_I^n = 6.6$ and the remaining parameter values are fixed as in the caption to Figure 4.16. 'N' denotes necrosis.

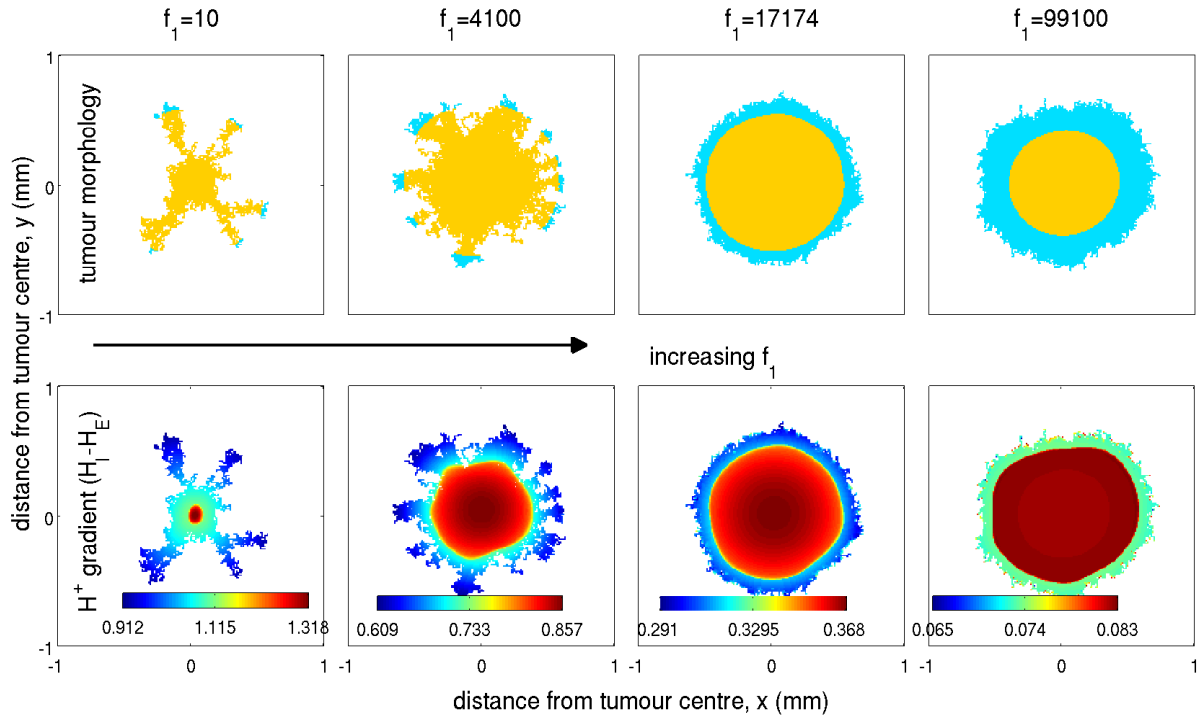

Figure 4.23: Plots showing the effect of increasing the rate of activity of the Na^+/H^+ exchanger, f_1, on tumour morphology (top panel) and cellular H^+ gradient (bottom panel, $H_I - H_E$ in dimensionless form). Colouration is the same as in Figure 4.9. Here, $pH_I^q = 6.84$, $pH_I^n = 6.6$ and the remaining parameter values are fixed as in the caption to Figure 4.16.

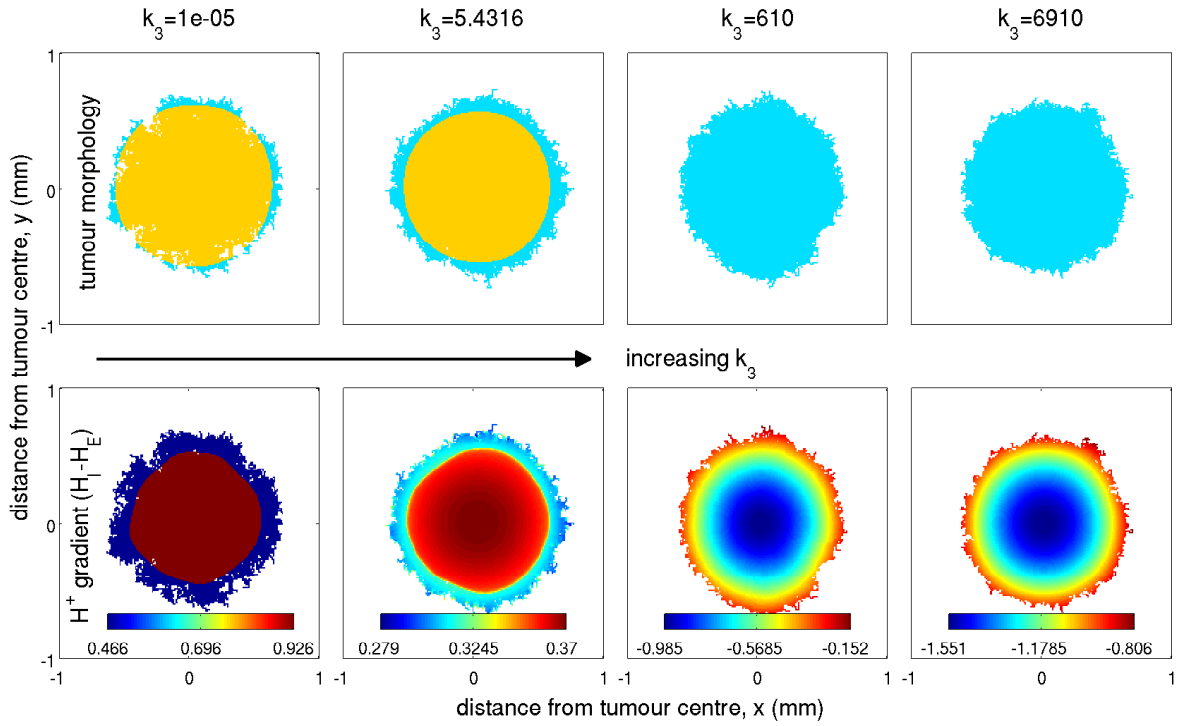

Figure 4.24: Plots showing the effect of increasing the rate of activity of the lactate/H^+ symporter, k_3, on tumour morphology (top panel) and cellular H^+ gradient (bottom panel, $H_I - H_E$ in dimensionless form). Colouration are the same as in Figure 4.9. Here, $\text{pH}_I^q = 6.84$, $\text{pH}_I^n = 6.6$ and the remaining parameter values are fixed as in the caption to Figure 4.16.

4.3.4 The combined effect of extracellular H^+-ions and oxygen on tumour growth

Guided by experimental findings, we couple the automaton rules derived in Section 4.2.2 in order to investigate the combined effect of pH_E and O_2 on cell proliferation and phenotypic transformations. A study by Casciari *et al.* [39] in which the growth rate of EMT6IRo mouse mammary tumour cells is measured at several values of extracellular pH (pH_E 7.25, 6.95, 6.67, 6.60) and under various oxygen

concentrations ([4.43, 2.32, 0.82]$\times 10^{-5}$ mol/l) finds that very low levels of oxygen and pH are required to cease the growth of EMT6IRo cells (i.e. pH_E 6.60, $O_2 = 8.2 \times 10^{-6}$ mol/l). See Table 4.2(a) for a summary of their results. In the context of our model, we infer from their data that if cells take 20 hours or more to proliferate then they are assumed to be in a quiescent state, greater than 200 hours means a necrotic cell state, otherwise we assume that the cell is proliferative (see Table 4.2(b)).

In our simulation code, we examine the concentration of oxygen and the extracellular pH at each cell location, if it falls within the range of values shown in Table 4.2 then we assign to the cell the appropriate state as indicated. We show a typical simulation in Figure 4.25 and the corresponding metabolite profiles in Figure 4.26 for the combined pH_E, O_2 simulation. We see that by allowing both oxygen and extracellular pH to influence the evolution of the cells, the tumour mass consists of a proliferative rim and a quiescent core as before but there appears to be some gaps within the tumour which could be due to the early onset of "fingers". However, these appear to be later masked by the rapid cell division. The impact on the tumour phenotypical structure is significant relative to when cells are assumed to be strongly sensitive to oxygen or pH_E individually, which is primarily due to the differing thresholds for quiescence, necrosis and proliferation. When the tumour cells are taken to be strongly sensitive to oxygen levels, the tumour mass consists of three layers: proliferative, quiescent and necrotic (e.g. see Figure 4.5). Whereas when the tumour cells are taken to be strongly sensitive to the extracellular pH, the tumour mass consists of only proliferative cells (see Figure 4.10). In terms of tumour phenotypic composition and response to therapies, it appears that when pH_E and oxygen effects are combined we observe a large inner core of quiescent cells rather than a quiescent layer with a large necrotic inner core. Quiescent cells are known to be resistant to some chemotherapeutics (which tend to target highly proliferative cells) and so can often be left untouched by treatment. The issue is that these quiescent cells can become nourished again

once the proliferative cells have been therapeutically removed and are often shown to be aggressive and invasive [151].

Figure 4.26 shows that the metabolic profiles for the combined pH_E and O_2 simulation is largely the same as that when oxygen or pH_E effects are considered individually. This is because, even with this dual effect, there is still hypoxia and the subsequent rise in pH and lactate is roughly the same.

Table 4.2: (a) Doubling times (hours) of EMT6/Ro cells grown at various oxygen concentrations, extracellular pH and a plentiful supply of glucose (5.5×10^{-3}mol/l). Data taken from [39]. Assuming that cells which take 20 hours or more to double in number are in a quiescent state, greater than 200 hours means a necrotic cell state, otherwise we assume that the cell is proliferative and obtain the cell state as shown in (b). 'P', 'Q' and 'N' denote proliferative, quiescent and necrotic cell state respectively.

(a)

oxygen (mol/l) \ extracellular pH	6.60	6.67	6.95–7.25
4.4×10^{-5}	24	17	12
2.3×10^{-5}	38	20	13
8.2×10^{-6}	226	26	16

(b)

oxygen (mol/l) \ extracellular pH	6.60	6.67	6.95–7.25
4.4×10^{-5}	Q	P	P
2.3×10^{-5}	Q	Q	P
8.2×10^{-6}	N	Q	P

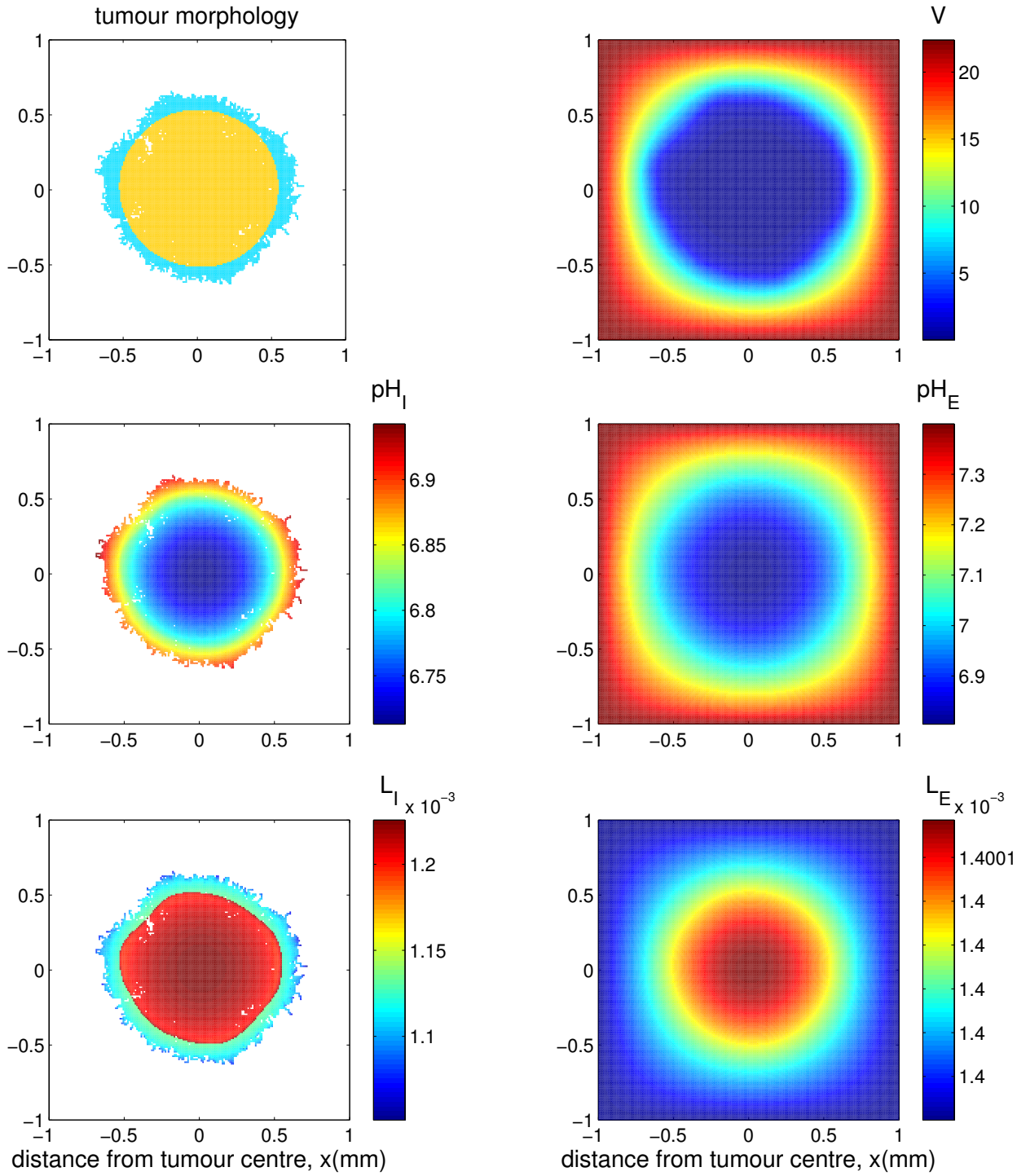

Figure 4.25: Plots showing the profile of the tumour spheroid, oxygen, pH and lactate at 26 days when cellular growth and phenotypic change are dependent on both extracellular H^+-ions and oxygen levels. Parameter values for the phenotypic transformation of cells in this case are summarised in Table 4.2. Remaining parameter values are as in Table 4.1.

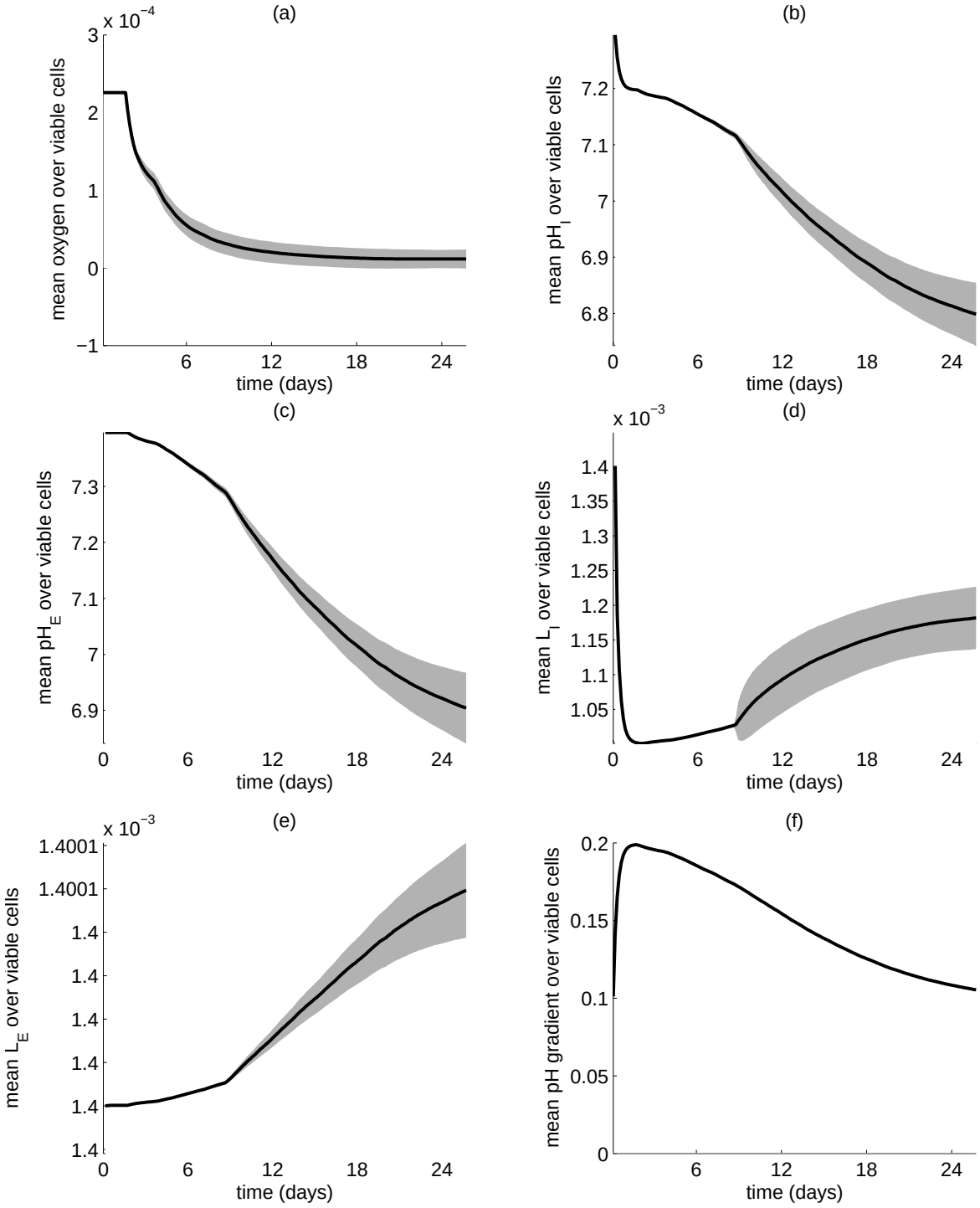

Figure 4.26: Plots showing the mean concentration of oxygen, pH and lactate over the course of tumour growth. We also show that the cellular pH gradient (pH_E-pH_I) is positive. Note that cellular growth and phenotypic change are dependent on extracellular H^+-ions and oxygen levels.

4.3.5 Effect of lactate on transmembrane pH gradient

Recall from our singular perturbation analysis of the outer solution of pH and lactate in Section 2.4.2 that, to leading order, $\mathrm{pH}_E < \mathrm{pH}_I$ (i.e. the pH gradient is negative) if $L_I > L_E$. In this section, we find that by simply taking the value of extracellular lactate at the boundary of the domain to be lower than some threshold (see Figure 4.27), we obtain a reversed cellular pH gradient. In Figure 4.27, we show the proportion of cells in the spheroid exhibiting a reversed cellular pH gradient when only oxygen (part (a)) or intracellular pH (part (c)) or extracellular pH (part (b)) drives the growth and phenotypic transformations of the cells. It is clear that there is no qualitative difference between the figures. We show (in Figure 4.28) a typical simulation when L_I^0 and L_E^0 are chosen such that 50% of cells are predicted to have a reversed cellular pH gradient. We illustrate the case when extracellular pH drives the phenotypic change and growth in the simulations. It is interesting to note that, for some L_E^0 values, the reversed cellular pH gradient is spatially organised within the tumour spheroid, with a positive pH gradient in an intermediate layer within the spheroid (as depicted in Figure 4.28). We suggest that the reversed pH gradient occurs when lactate outside the cell is decreased because the activity of the MCT becomes higher (due to L_E being low and L_I becoming high when oxygen levels fall below the threshold to initiate glycolysis) and so more intracellular lactate are exported outside the cell along with H^+-ions and thus the intracellular pH is raised, whilst the extracellular pH remains roughly constant. This suggests that there is a crucial role for extracellular lactate in not only determining the cellular pH gradient across the membrane but also the spatial extent of the pH gradient within the spheroid. And it is clear from Figure 4.27 that this result is independent of the initial intracellular lactate levels.

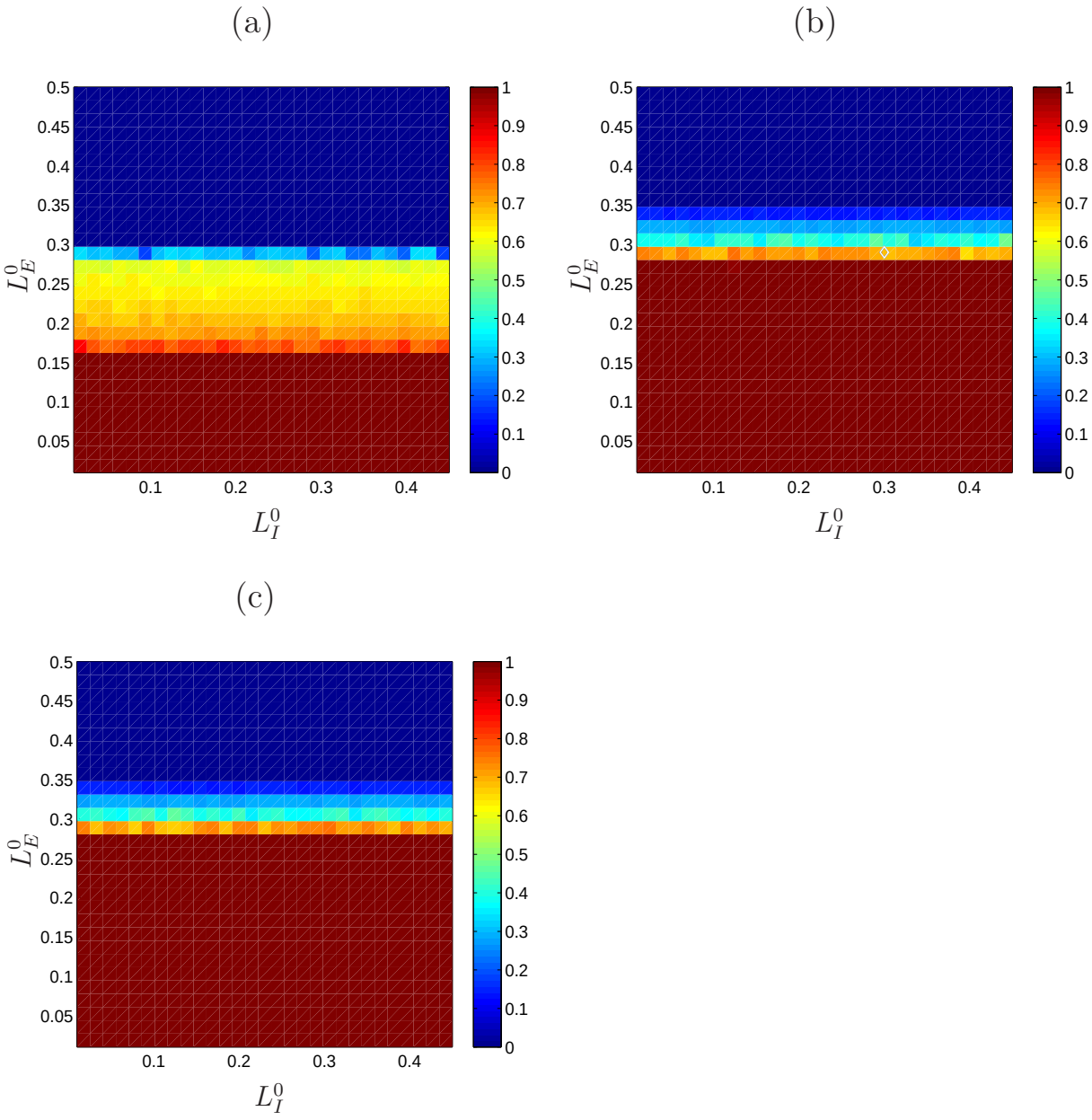

Figure 4.27: Plots showing the proportion of tumour cells in the spheroid with a reversed cellular pH gradient (ie. $\mathrm{pH}_E < \mathrm{pH}_\mathrm{I}$) for various initial values of intracellular lactate, L_I^0, and initial (and boundary) values of extracellular lactate, L_E^0. This figure shows the results of one simulation for each L_I^0 and L_E^0. In (a) cellular growth and phenotypic transformations depend solely on the levels of oxygen (as in Section 4.3.1). In (b) cellular growth and phenotypic transformations depend solely on extracellular H^+-ions concentrations (as in Section 4.3.2). In (c) cellular growth and phenotypic transformations depend solely on intracellular H^+-ions concentrations (as in Section 4.3.3). $\mathrm{pH}_I^q = 6.84$, $\mathrm{pH}_I^n = 6.60$, $\mathrm{pH}_E^q = 6.20$, $\mathrm{pH}_E^n = 6.20$, $d_V = 750$. Remaining parameters are the same as in Table 4.1. $t = 26$ days.

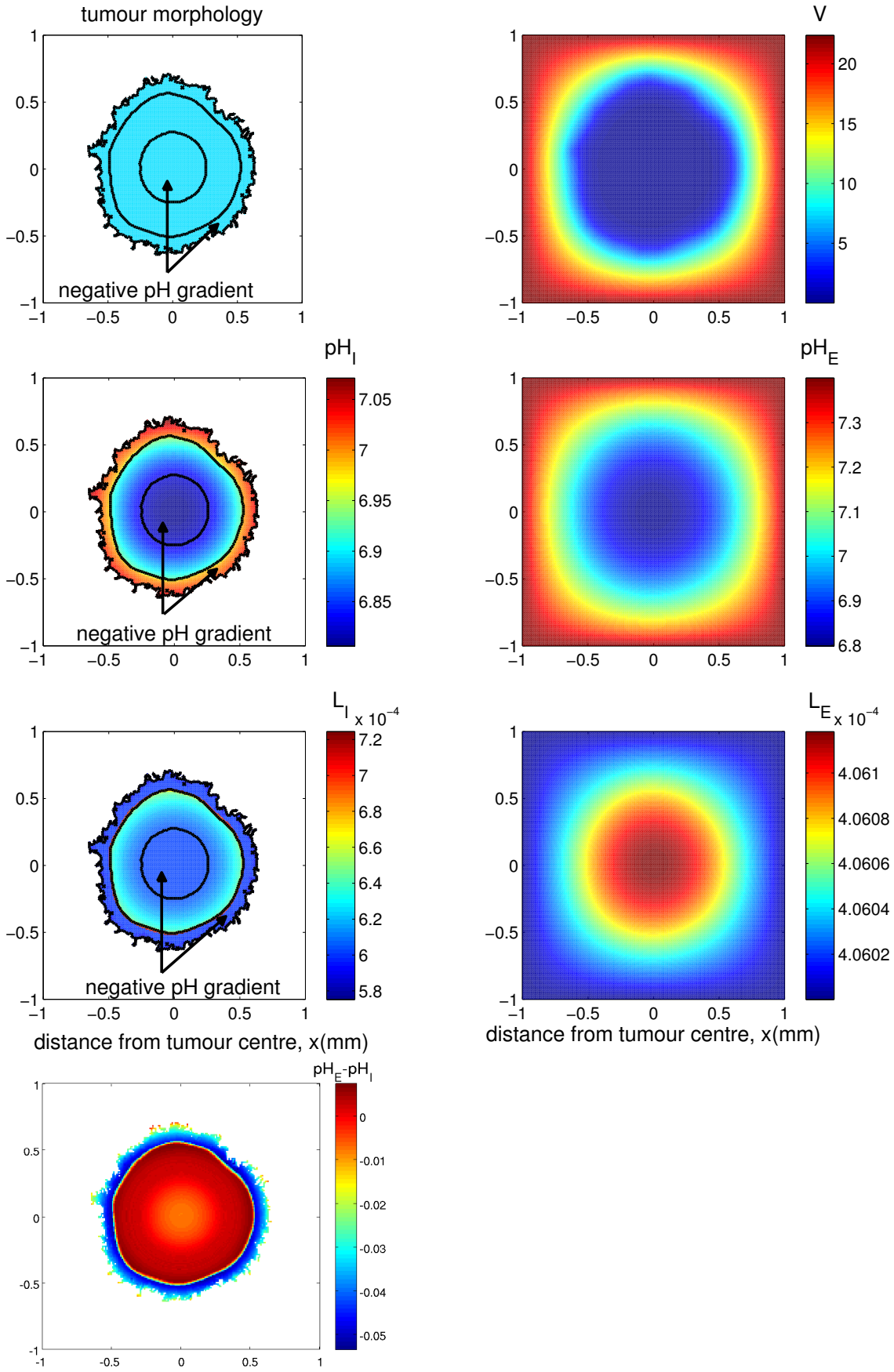

Figure 4.28: Caption on following page.

Figure 4.28: (Previous page.) Plots when cellular growth and phenotypic change are dependent on extracellular H^+-ions. A tumour comprised of only proliferating cells is formed compared to the three layered structure shown in Figure 4.5. A reversed cellular pH gradient exists ($pH_E < pH_I$) in the outermost and innermost region of the tumour mass with the exclusion of a thin region in-between. Parameter values and colouration are as in the caption to Figure 4.10 but with $L_E^0 = 0.28$. See Figure 4.29 for the temporal evolution of the metabolites.

4.4 Discussion and conclusions

Our model differs from previous studies mainly in our explicit inclusion of intracellular pH regulatory mechanisms compared to, for example, the study of [170] where extracellular pH effects are examined but there are no consideration of the membrane-bound cellular transporters, such as the Na^+/H^+ exchanger and the lactate/H^+ symporter. These transporters have been shown to be up-regulated in some tumours and are implicated in tumour growth and invasion [37, 102, 118]. In this respect, our model is the first to investigate the effect of these crucial membrane transporters, during the early stage of tumour growth, on the tumour morphology and the cellular pH gradient. This chapter begins by assuming that tumour growth and phenotypic transformation is sensitive to only the levels of oxygen. Then in Section 4.3.2, we remove the effect of oxygen on tumour growth and phenotypic transformation, but still allow oxygen to determine the "glycolytic switch" of cells, and take cellular growth and phenotypic transformation instead to be sensitive only on the levels of extracellular pH. In Section 4.3.3 we remove both the effects of oxygen and the extracellular pH on growth and cell state and focus instead on the intracellular pH. In Section 4.3.4, we take cellular growth and phenotypic transformation to depend on both oxygen and extracellular pH.

Our most significant findings in this chapter are that, when tumour cells are

strongly sensitive to changes in the intracellular pH, a low activity of the NHE or a high rate of anaerobic glycolysis can give rise to a "fingering" morphology. This is a new observation which has not been noted before in this context. The glycolytic phenotype is a characteristic of some human cancers and there is much biological evidence which has consistently correlated poor prognosis and increased tumour aggressiveness with an increased glycolytic rate [72, 73]. The effect of the glycolysis on tumour invasiveness has also been investigated mathematically via tumour-host interface models [71, 212]. For example, the acid-mediated model by Gatenby *et al.* [71] (see Section 1.3.1) predicts a hypocellular interstitial gap at the tumour-host interface which is thought to be caused by the pH gradient extending from the tumour into the normal tissue.

Furthermore, we show that as the activity of the MCT increases, when tumour cells are strongly sensitive to changes in the intracellular pH, all the tumour cells within the spheroid exhibit a reversed transmembrane pH gradient. This is an interesting result which has not been reported before in any mathematical modelling framework. Our results are supported by biological postulations in [37, 244] that the MCT increases the intracellular pH and gives rise to the onset of the acidic interstitial microenvironment and the reversed transmembrane pH gradient.

The current model has some limitations. Firstly, in reality, tumour growth may exhibit some strong dependencies on all of pH_i, pH_e and oxygen, and as such it would be more biologically reasonable to also allow all of these variables to simultaneously influence the growth and phenotypic transformation of cells. The difficulty in doing this is in finding data to sufficiently model these combined dependencies. Secondly, one could investigate whether the activity of the membrane-based cellular transporters (i.e. the NHEs and MCTs) is higher when cells become quiescent or hypoxic and incorporate this into the model equations. Thirdly, it would be interesting to investigate whether lactate levels have any effect on tumour growth.

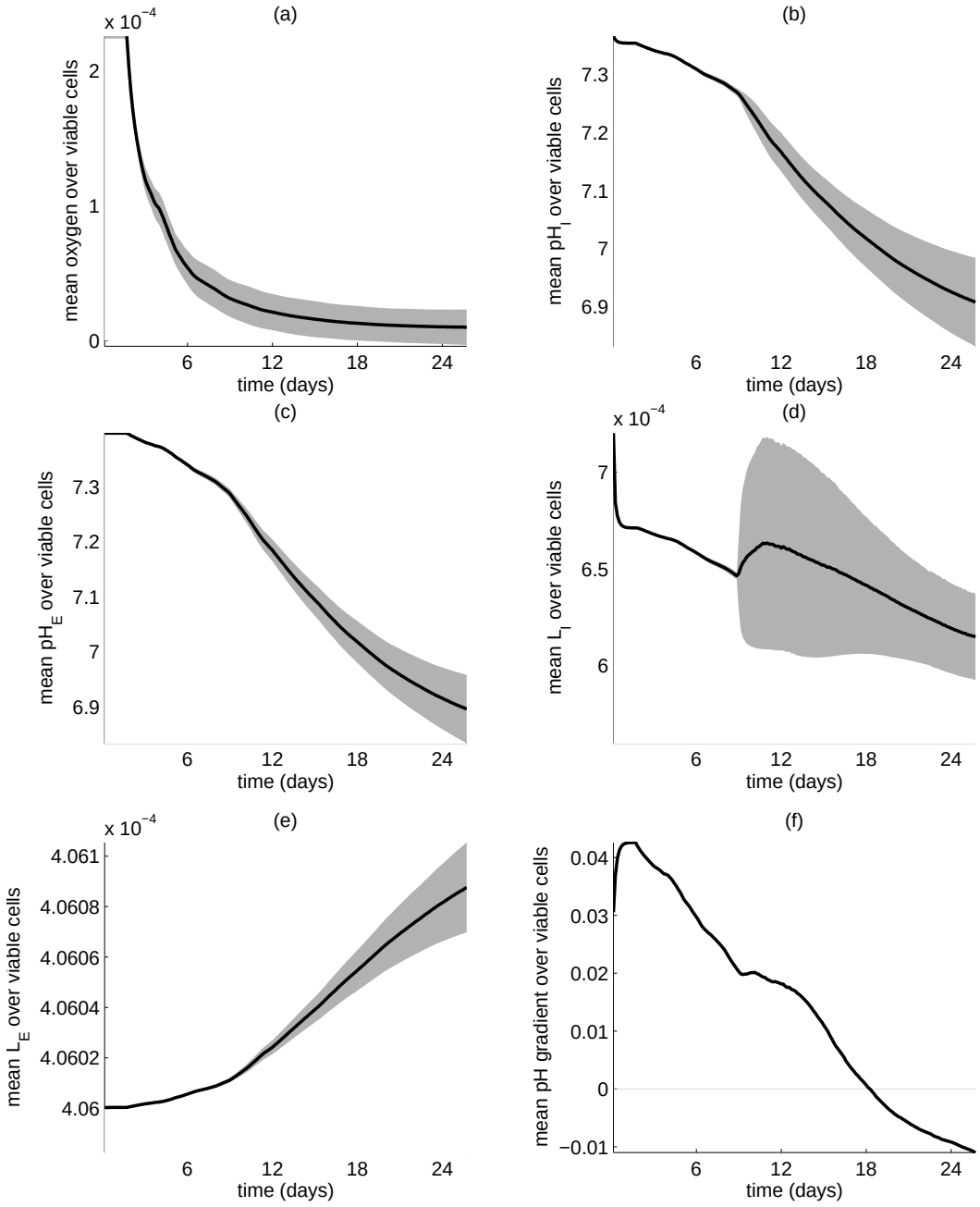

Figure 4.29: Plots showing the mean concentration of (a) oxygen, (b and c) pH and (d and e) lactate over the course of the tumour growth in Figure 4.28. We also show that the mean cellular pH gradient (pH_E-pH_I shown in (f)) becomes negative as the tumour grows. Note that in this simulation cellular growth and phenotypic change is taken to be entirely dependent on extracellular H^+-ions. We observe that the mean pH decreases for a short time (until the 9^{th} day) but decreases because of the rise in the glycolytic production of H^+-ions when oxygen levels become low.

Chapter 5

Modelling tumour cell invasion using the extended Potts model

5.1 Introduction

In this chapter we use the extended cellular Potts model, based on energy minimisation techniques, to model the interactions between tumour cells and the extracellular matrix under acidic and physiological pH. Such interactions have also been modelled using a continuum approach, see for example [5, 11]. Unlike our cellular automaton modelling approach of tumour growth in Chapter 4, here we explicitly account for cell geometry and the adhesive interactions between cells. An advantage of this approach is that migrating cells are able to change shape as they manoeuvre through the matrix [256].

There has been a lot of interest in using the cellular Potts model to understand different aspects of tumour growth (see for example [7, 112, 177, 200, 210, 233, 234], a detailed discussion of a selection of these studies can be found in Section 1.3.2). Inspired by the work of Turner *et al.* [233] on tumour cell invasion, we begin by developing a general formalism to reproduce their model results. Tumour invasiveness in this model is quantified by measuring the maximum cell penetration distance into the extracellular matrix at every time step, and, the time at which

a cell reaches a predefined maximal invasion distance. Moreover, the morphology of the invading tumour mass can be a useful indicator of the degree of tumour invasiveness. Tumours with "fingering" morphology are known to be more aggressive than those with smooth edges [60]. Additionally, those that shed cells which then migrate through the matrix and escape into the bloodstream are known to be associated with poor prognosis [96]. There are many known factors implicated in this metastatic cascade which begins when cells detach from each other and adhere to the supporting matrix [41]. We investigate in Section 5.3.2 the effect of cellular adhesion strength on the invasiveness of the tumour and the effect of haptotaxis in Section 5.3.3. We then incorporate an important feature of tumour growth—cell proliferation—into our model in Section 5.3.4. We finally use this model in Section 5.4 to examine the effect of extracellular acidity on tumour invasiveness using experimental data from the literature.

5.2 Model Development

We divide our domain into $N \times N$ equally spaced lattice sites with indices (i, j). Each site is assigned a label, $\sigma_{i,j} \in \{1, 2, 3, \ldots, M\}$, where M is the maximum number of biological cells. A collection of adjacent lattice sites, $(i,' j')$, sharing the same value of $\sigma_{i,j}$ are defined to lie within the same cell. Each cell has an associated "cell type", denoted by $\tau(\sigma_{i,j})$, used to model the different types of cells within the tissue in question, e.g. cancerous or normal cells. In this study, we model only one type of cell: a tumour cell. See Figure 5.1 for a schematic representation of our modelled tumour mass.

Biological cells interact with one another through their surface membrane, and we model this interaction by using a coupling constant, $J_{\tau(\sigma_{ij}),\tau(\sigma_{i'j'})}$, to quantify the adhesive energy between cells in a Hamiltonian, E. The energy function is made up of a number of parts relating to cell-cell adhesion, cell-matrix adhesion,

cell volume and haptotaxis. For example,

$$E_{\text{adhesion}} = \sum_{ij} \sum_{i'j'} J_{\tau(\sigma_{ij}),\tau(\sigma_{i'j'})} \left(1 - \delta_{\tau(\sigma_{ij}),\tau(\sigma_{i'j'})}\right), \tag{5.1}$$

where the boundary energy coefficients are symmetric, $J_{\tau(\sigma_{ij}),\tau(\sigma_{i'j'})} = J_{\tau(\sigma_{i'j'}),\tau(\sigma_{ij})}$. The outer sum runs over all occupied sites in the lattice, whereas the inner sum is over the eight nearest neighbours of (i, j). The Kronecker delta, $\delta_{\tau(\sigma_{ij}),\tau(\sigma_{i'j'})}$, is equal to one when $\sigma_{ij} = \sigma_{i'j'}$ and zero otherwise. This ensures that only surface interactions between different biological cells contribute to the cell-cell adhesion energy.

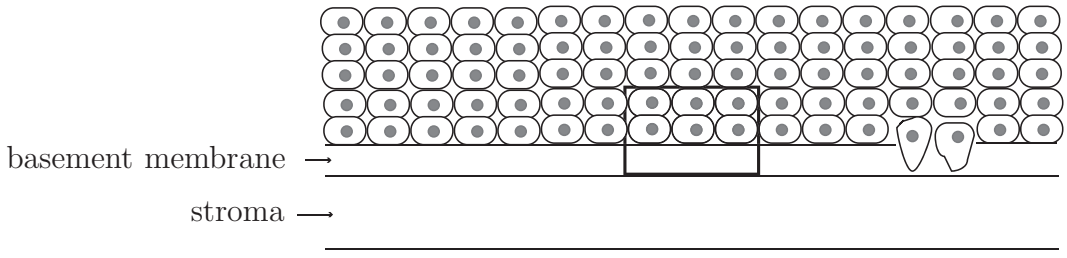

Figure 5.1: Diagrammatic representation showing five layers of epithelial cells invading the basement membrane. See Figure 5.2 for a representation of a portion of the cells (boxed area) and the extracellular matrix (or basement membrane) using the cellular Potts model. Note that we do not incorporate blood vessels in our model.

Cells change volume during growth [39], hence we prescribe an elastic constraint, E_{volume}, to prevent cells from growing unbounded or shrinking too small

$$E_{\text{volume}} = \sum_{\text{all domains } \lambda \neq 0} \lambda \left(v_\sigma - V_T\right)^2, \tag{5.2}$$

where, the summation runs over the total number of cells in the lattice and λ denotes the cellular volume elasticity. The target volume, V_T, is the volume a cell relaxes to in the absence of deformation or stress. This term ensures that the

instantaneous volume of a cell, v_σ, remains close to the target volume (depending on the value of λ).

The above formulation is the basic set-up of the classical cellular Potts model [89]. To include other cellular phenomenon, one simply adds terms to the Hamiltonian in the usual form of an elastic constraint or a potential energy.

Cells not only adhere to each other and to the medium, but they can also move up or down gradients of chemicals or substratum. The first stage of metastasis is believed to be when tumour cells invade the basement membrane in order to gain access to the surrounding blood vessels and colonise in different locations of the body [129]. This is thought to be facilitated by proteolytic enzymes which break down components of the extracellular matrix (e.g. fibronectin) and thereby create a gradient along which cells move [59] (this movement is termed "haptotaxis"). To model haptotaxis, we adopt a similar approach used by Savill & Hogeweg [203], so that the energy change due to cells moving up a fibronectin gradient is given by

$$\Delta E_{\text{haptotaxis}} = k_H(f_{i'j'} - f_{ij}), \tag{5.3}$$

where, $f_{i,j}$ is the fibronectin concentration at the point (i, j) on the lattice, $f_{i',j'}$ is the neighbouring fibronectin concentration and k_H is a constant that determines the strength of the haptotactic gradient. There is accumulating evidence suggesting that endosomal vesicles which contain matrix-degrading enzymes tend to relocate to the surface of the cell to aid invasion [90, 154, 232]. For this reason, we assume, in line with Turner *et al.* [233], that cells which are situated directly on top of the ECM secrete larger quantities of active proteolytic enzymes than those which are further up. Consequently, the rate of change of fibronectin in our model is governed by the proteolytic enzyme activity at each time step according to

$$f(t+1) = f(t) \times \begin{cases} e^{-k_i}, & \text{if lattice point is occupied by a cell,} \\ e^{-k_n}, & \text{if adjacent point(s) are occupied,} \\ 1, & \text{empty space,} \end{cases} \tag{5.4}$$

where t refers to the Monte-Carlo time step (MCS) and we assume that k_i is larger than k_n to account for higher matrix degradation rate associated with cells that are in close contact with the ECM. In line with Turner *et al.* [233], we take $k_i = 2k_n$.

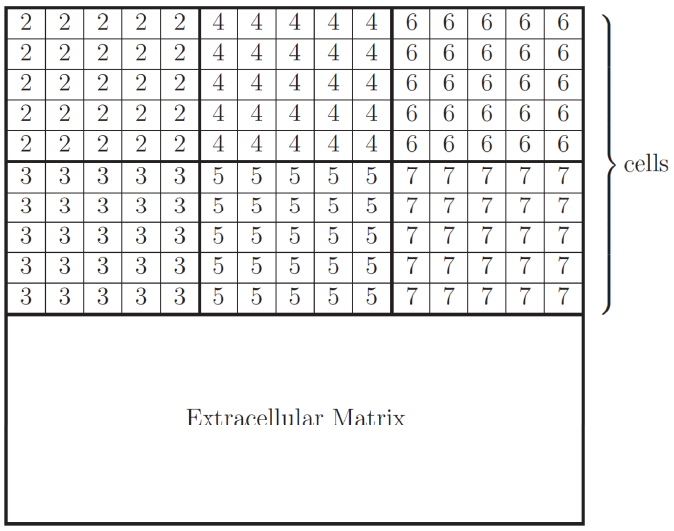

Figure 5.2: An example of a 2-D lattice configuration of our extended Potts model. The numerals (referred to in the text by $\sigma_{i,j}$) represent cell index values. Each biological cell is modelled as a collection of lattice sites with the same index value. The number of lattice sites in each biological cell denotes its volume (here, the volume of each cell, V_T is taken to be 25). In this example, there are two layers of cells, each layer containing three biological cells.

Thus, the total energy change of our system, ΔE is

$$\Delta E = \Delta E_{\text{adhesion}} + \Delta E_{\text{volume}} + \Delta E_{\text{haptotaxis}}. \tag{5.5}$$

To simulate the above Hamiltonian, we generate a standard Monte Carlo simulation using a modified Metropolis algorithm [89, 150], where each Monte-Carlo time step is defined to be as many iterations as the number of occupied lattice points in the model. The algorithm is as follows: we randomly choose a lattice point (i, j), then randomly choose one of the eight neighbouring points, (i', j'). If

$\sigma_{i,j} = \sigma_{i',j'}$, i.e. the lattice points lie in the same biological cell, then we repeat the selection. If the lattice sites lie in different biological cells, we calculate the energy change, ΔE, associated with changing the state of the lattice site (i, j) to that of site (i', j'). If $\Delta E \leq 0$, we accept the copy; otherwise we accept with Boltzmann weighted probability according to $e^{-\Delta E/\beta}$. That is,

$$p(\sigma_{ij} \to \sigma_{i'j'}) = \begin{cases} 1, & \text{if } \Delta E \leq 0, \\ e^{-\Delta E/\beta}, & \text{if } \Delta E > 0, \end{cases} \tag{5.6}$$

where β affects the probability of unfavourable configurations being accepted. A high β leads to a higher acceptance rate of a configuration and the greater the area across which a cell will move in a given time. In this sense, β is physically comparable to the diffusion coefficient considered in a diffusion equation. In other physical systems such as in Ferromagnetism and the Ising model, β is analogous to thermal fluctuations [89].

Initial conditions

We simulate the model on a 100×100 grid, with each biological cell initially represented by a square occupying 25 lattice sites (i.e. $V_T = 25$ in equation (5.2)). The lattice is initialised with five layers of cells, each layer containing 20 biological cells. A homogeneous sheet of fibronectin (100×100 in size) acts as a medium to which cells adhere and migrate along. We normalise the fibronectin concentration so that $f_{ij} = 1$ within this fibronectin sheet.

Boundary conditions

We impose zero flux boundary conditions at the top and bottom of the lattice to reflect the fact that epithelial cells are enclosed by lumen from the top and by the basement membrane from below [125] (see Figure 5.1 for a schematic). We assume periodic boundary conditions at the left and right of the lattice to reflect the fact that we are modelling only a small segment of a large tumour.

5.3 Numerical Results under physiological pH

5.3.1 Parameter values

Wherever possible, experimental data is used to estimate values for our model parameters. Firstly, to prevent cells from dissociating we set all $J_{\tau(\sigma_{ij}),\tau(\sigma_{i'j'})}$ positive. Note that a high J value is energetically demanding and therefore corresponds to low adhesivity. We use $J_{\mathrm{c,ECM}}$ to denote the cell-ECM adhesion energy; $J_{\mathrm{ECM,ECM}}$ the ECM-ECM adhesion energy; and $J_{\mathrm{c,c}}$ the cell-cell adhesion energy. Owing to the fact that the dynamics of the simulations are controlled by the relative value of ΔE to β, the absolute values of J's are less significant than their relative values. We thus assume a typical value of 3 for $J_{\mathrm{c,c}}$ and 6 for $J_{\mathrm{c,ECM}}$ in line with Turner *et al.* [233]. On the contrary, there is no adhesive energy between neighbouring lattice sites constituting just ECM, and so we take $J_{\mathrm{ECM,ECM}} = 0$ [177].

The Boltzmann probability in (5.6) is at the heart of the cellular Potts model, and as such β plays a central role in determining the configuration of a system. At high β, the acceptance rate of a configuration increases and as a result the boundaries of the cells become contorted. The volume elasticity constant, λ, controls the extent of cell growth and a high value gives rise to a system where cells barely grow (because of the resulting increase in the overall energy). Increasing λ/β gives rise to a computationally inefficient system because the acceptance rate becomes very small [89]. We have experimented with various values of β and λ, and choose $\beta = 6, \lambda = 1$ (in line with various other models such as [200, 233]) in all our simulations to ensure that the model is computationally efficient.

To relate our spatial scale to real space, we assume that the size of one simulated tumour cell is equivalent to the average size of a typical biological cell, that is, approximately 10 μm in diameter [16]. With each simulated tumour cell initially occupying 25 lattice sites arranged in a square of length five, each lattice site then corresponds to 2 μm and the size of our domain corresponds to a physical size of around 200 μm.

For a typical simulation, with the parameter values outlined above, shown in Figure 5.3, the mean maximum translocation distance (d_{max}) per 2100 MCS (taken from an average of ten runs) is 67 lattice sites—equivalent to 134 μm. To relate our temporal scale to real time, we use the mean translocation distance of human melanoma cells (MV3) following their exposure to various extracellular pH [218]. For example, at pH_e 7.45, the mean translocation distance in five hours is 20 μm [218]. Comparing with the translocation distance of our simulated tumour cells, this gives that one MCS corresponds to roughly 58 seconds.

Throughout the rest of this chapter, the model is run for 3000 MCS which corresponds to roughly 48 hours, or, is terminated when a cell reaches the bottom of the lattice.

5.3.2 Effect of cellular adhesion strengths on tumour morphology and invasion

Figure 5.3 shows how the initially rectangular tumour mass develops fingering morphology which eventually break from the main tumour and migrate into the extracellular matrix; an example of the cross-section of the corresponding fibronectin profile is shown in Figure 5.4. The depth of tumour cell penetration into the extracellular matrix has long been established as a marker of the extent of tumour aggression [28]. A higher depth is associated with more aggressive tumours and poor prognosis [107, 117]. To quantify the extent of invasion, we measure the maximum cell penetration distance into the extracellular matrix, d_{max}. We also introduce another parameter, n_m, to denote the number of Monte-Carlo time steps that it takes for a tumour cell to reach the bottom of the lattice (we terminate the simulation at that time).

Alterations in the adhesive properties of the tumour cells is thought to have an important role in tumour development and progression [41, 204]. Figure 5.5 shows the evolution of the tumour mass for a higher cell-cell adhesion energy.

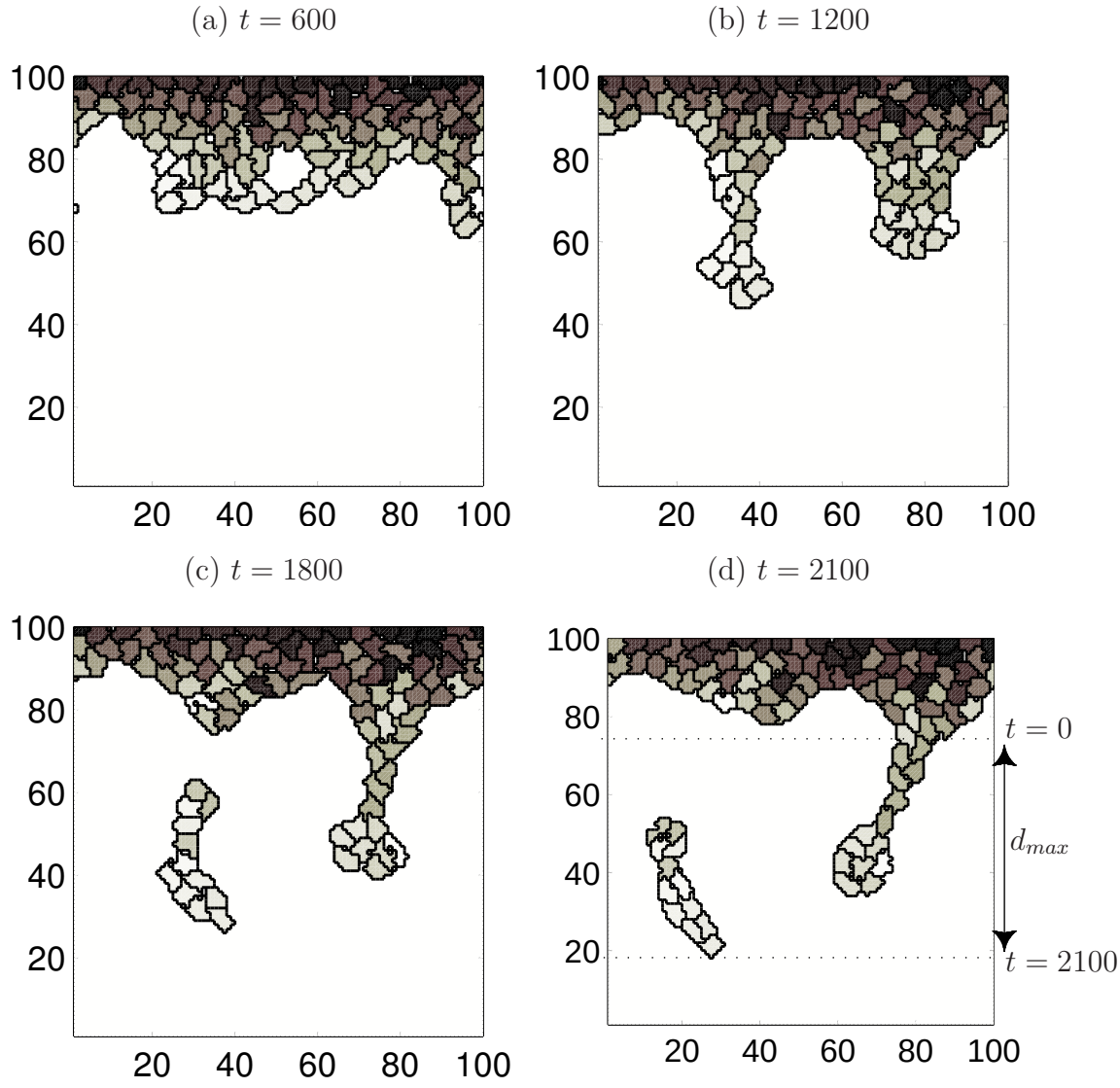

Figure 5.3: A typical simulation of our model showing the temporal evolution of the tumour mass. The initially rectangular tumour mass develops fingering morphology which then break from the main tumour and migrate into the extracellular matrix. d_{max} denotes the maximum cell penetration distance into the extracellular matrix. Here, $J_{c-c} = 3, J_{c-ECM} = 6, \lambda = 1, \beta = 6, k_H = 40, k_n = 0.003$.

Here, we take $J_{c-c} = 6$ instead of $J_{c-c} = 3$ (as in Figure 5.3). Compared to Figure 5.3, in Figure 5.5 cells break from the main tumour earlier and migrate

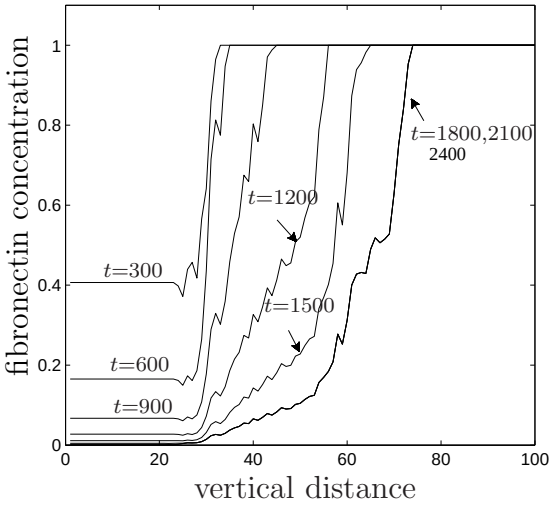

Figure 5.4: A vertical slice through the centre of the corresponding fibronectin profile of Figure 5.3. Taken from column number 50 of the 100×100 grid and for t ranging from 300 to 2400.

individually as well as in cohorts. We illustrate in Figure 5.6 the effect of varying the cell-cell adhesion energy, J_{c-c}, on (a) d_{max} and (b) n_m. A high J_{c-c} value corresponds to low intercellular adhesivity, which leads to more cells spreading into the surrounding matrix and consequently a higher depth of invasion as shown in Figure 5.6(a). Following their detachment from neighbouring cells, an adequate adherence to the ECM is required in order for cells to migrate [154]. This is evident from Figure 5.6(a) where a stronger attachment to the ECM ($J_{c-ECM} = 3$) results in a higher depth of invasion compared to weaker ones ($J_{c-ECM} = 6$). This is because it is energetically favourable for a cell to bind with the ECM in the case of a low J_{c-ECM} and so cells are more likely to migrate through the ECM. Moreover, Figure 5.6(b) shows that as the intercellular adhesion becomes weaker, the time it takes for a cell to reach the maximal invasion distance decreases, with those expressing a low cell-ECM adhesion ($J_{c-ECM} = 6$) taking longer. On the other hand, decreasing the strength of cell-cell attachment (from $J_{c-c} = 3$ to

$J_{c-c} = 6$) across a range of J_{c-ECM} values does not have such a noticeable effect (see Figure 5.7). Not only does the depth of invasion differ as the strength of the

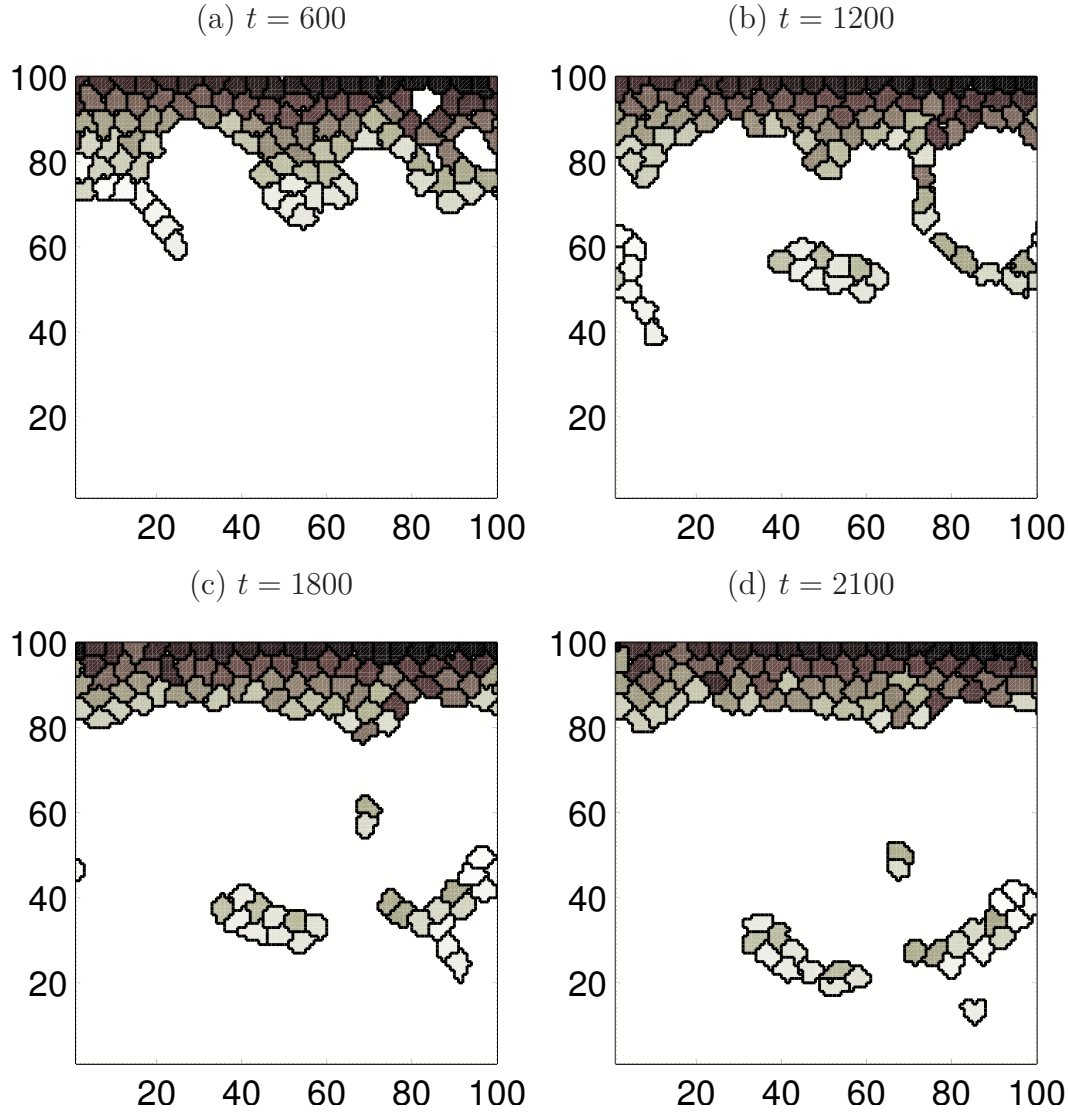

Figure 5.5: A typical simulation showing the effect of a higher cell-cell adhesion energy, J_{c-c}. The parameter values are the same as in the caption to Figure 5.3 except that $J_{c-c} = 6$. The difference in this case is that cells break from the main tumour mass earlier and migrate individually as well as collectively.

adhesion energy varies, but so does the morphology of the tumour mass. As the

intercellular adhesion gradually becomes weaker, compact "fingers" break from the main tumour and move into the ECM (as illustrated in Figure 5.8). Note that cells exhibiting stronger intercellular adhesions (e.g. $J_{c-c} = 2$) tend to break off collectively in large lumps compared to those with lower adhesions which break off in smaller lumps as well as individually. In contrast, Figure 5.9 demonstrates how a more defined fingering morphology is obtained with less shedding of individual tumour cells as the cell-ECM adhesion energy becomes weak.

The results obtained in this section demonstrate that an increase in malignant invasion can result from a decrease in the cohesiveness between the invading cells and/or from an increase in their adhesiveness to the extracellular matrix—a result which is well-established in cellular migration assays [217]. For example, the loss of E-cadherin, the most abundant epithelial intercellular adhesion molecule, is shown to correlate with increased invasiveness and metastasis of tumours [241]. Several studies show that restoring E-cadherin adhesion complex impedes the invasiveness of several types of tumour cells [17]. Moreover, increased expression of certain integrin molecules that bind cells to the ECM is associated with increased cell migration and metastasis in several cancer cells, for example breast [252], melanoma [126] and prostate [261].

Changes in the adhesive properties of cells and their proteolytic activity can facilitate their movement through the basement membrane [154]. We next investigate how tumour cell invasion can be affected by variations in the enzyme degradation rate of the ECM, under various strengths of cellular adhesion energies.

5.3.3 Effect of haptotactic strength and cell adhesion on tumour cell invasion

Figure 5.10(a) shows that increasing the haptotactic co-efficient (k_H in equation 5.3) results in a slightly larger depth of invasion, which is more pronounced

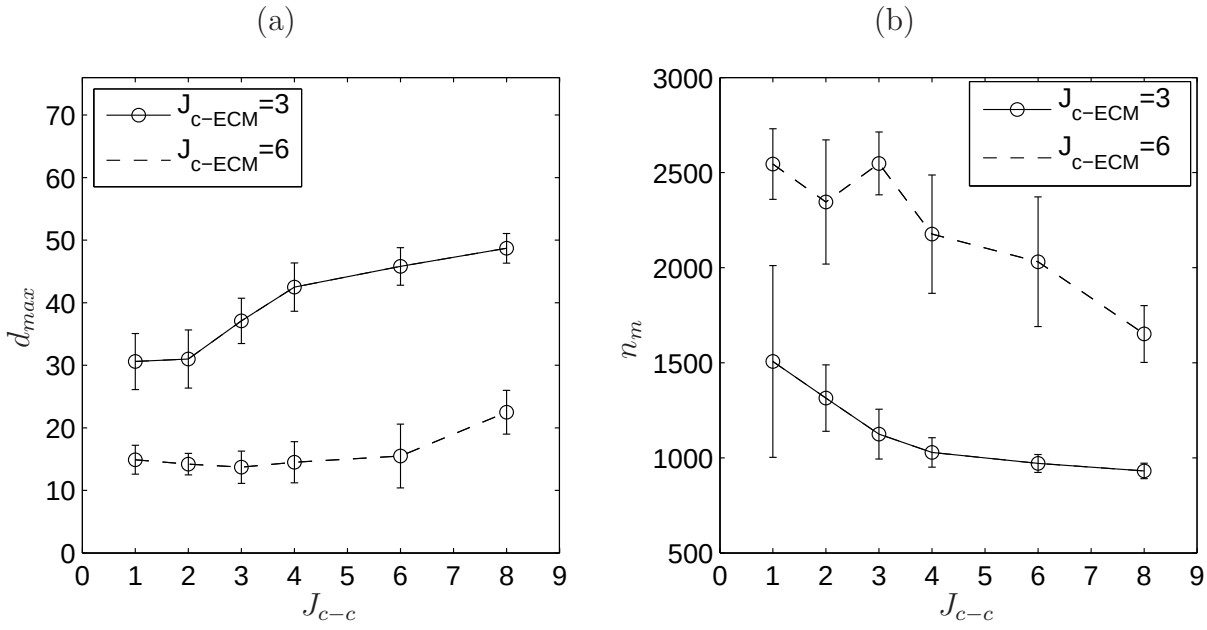

Figure 5.6: Effect of varying cell-cell adhesion energy, J_{c-c}, on (a) maximum depth of invasion, d_{max} and (b) the time it takes a single cell to reach the bottom of the lattice, n_m. We show the results for two values of cell-ECM adhesion energy: $J_{c-ECM} = 3$ (——) and $J_{c-ECM} = 6$ (− − −). The profile in (a) is obtained at $t = 600$. Each circle represents the mean of ten duplicate simulations with the associated standard deviations represented by error bars. Note that a high J corresponds to low adhesivity and vice versa. Increasing J_{c-c} results in an increase in the depth of invasion, which is much higher when J_{c-ECM} is decreased. Parameter values: $\lambda = 1, \beta = 6, k_H = 40, k_n = 0.003$.

if the rate of enzyme degradation of the fibronectin matrix, k_n, is also increased. We can see that the gap between the two solutions is small when k_H is small but increases for large k_H. Figure 5.10(b) shows the effect of varying k_H and k_n on the time taken for a cell to reach the bottom of the lattice, n_m. Biologically, this implies that a greater sensitivity to the haptotactic gradient coupled with a high secretion rate of active proteolytic enzymes would result in an increased depth of invasion in a short period of time.

We illustrate in Figures 5.11–5.12 the relationship between tumour invasion

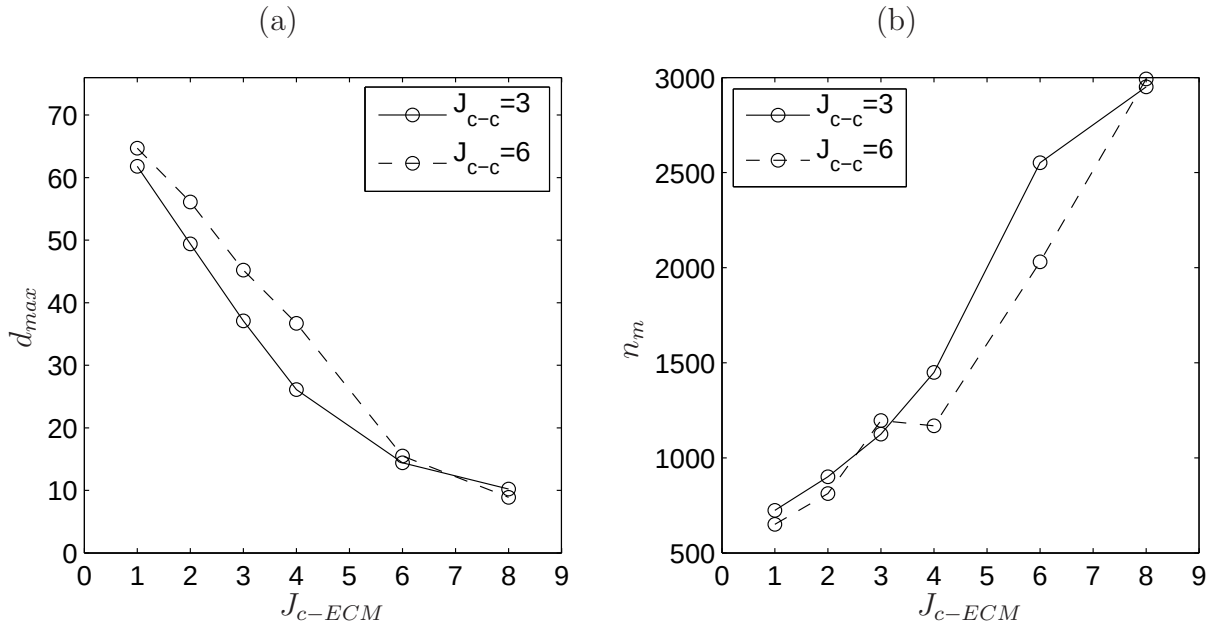

Figure 5.7: Effect of varying cell-ECM adhesion energy, J_{c-ECM}, on (a) maximum depth of invasion, d_{max} and (b) the time at which a cell reaches the bottom of the lattice, n_m. We show the results for two values of cell-cell adhesion energy: $J_{c-c} = 3$ (——) and $J_{c-c} = 6$ (− − −). The profile shown in (a) is obtained at $t = 600$. Each circle represents the mean of ten duplicate simulations with standard deviations: in (a) $\sigma = \{4.71, 2.17, 3.28, 2.28, 5.10, 1.51\}$ for $J_{c-c} = 6$ and $\sigma = \{3.57, 2.20, 3.62, 3.21, 1.85, 1.54\}$ for $J_{c-c} = 3$; and in (b) $\sigma = \{55, 45, 605, 70, 341, 23\}$ for $J_{c-c} = 6$ and $\sigma = \{45, 42, 131, 171, 250, 108\}$ for $J_{c-c} = 3$. Note that a high J corresponds to low adhesivity and vice versa. Increasing J_{c-ECM} results in a profound decrease in the depth of invasion and an increase in the time a cell reaches the bottom of the lattice. The two lines in the figure lie close to each other, indicating that weakening intercellular adhesion does not have a significant impact on invasion compared to cell-ECM adhesion (see Figure 5.6). Parameter values: $\lambda = 1, \beta = 6, k_H = 40, k_n = 0.003$.

depth and the rate of proteolytic degradation of the fibronectin matrix (k_n), under various values of cellular adhesion energies. As expected, we observe from both

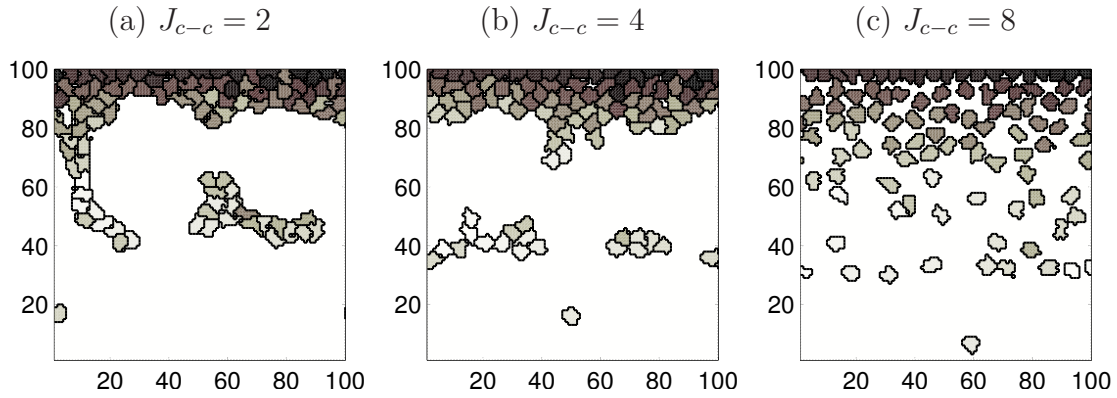

Figure 5.8: Simulations showing the way in which the strength of cell-cell adhesion energy modulates tumour morphology (at $t = 900$). We take cell-ECM adhesion to be $J_{c-ECM} = 3$ and vary the cell-cell adhesion energy: (a) $J_{c-c} = 2$ (strong adhesion), (b) $J_{c-c} = 4$ (medium adhesion), (c) $J_{c-c} = 8$ (weak adhesion). The remaining parameter values are the same as those in the caption to Figure 5.3.

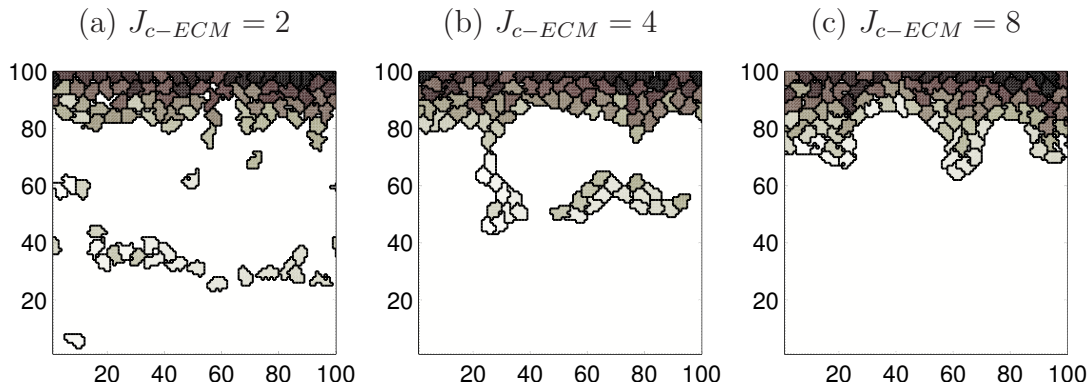

Figure 5.9: Simulations showing the way in which the strength of cell-ECM adhesion energy modulates tumour morphology (at $t = 900$). We take cell-cell adhesion to be $J_{c-c} = 3$ and vary the cell-ECM adhesion energy: (a) $J_{c-ECM} = 2$ (strong adhesion), (b) $J_{c-ECM} = 4$ (medium adhesion), (c) $J_{c-ECM} = 8$ (weak adhesion). The remaining parameter values are the same as those in the caption to Figure 5.3.

figures that a large k_n (high proteolytic degradation rate) gives a high invasion depth compared to a low k_n. However, there is a marked difference in the slope of the two solution curves in Figure 5.11(b) for lower values of k_n, pointing again, to the significance of cell-ECM adhesion on tumour invasiveness. On the other hand, varying the cell-cell adhesivity has a comparably less significant effect (Figure 5.12). That is, the speed of invasion shows a much wider range of variation as k_n varies when the cell-ECM adhesivity is low.

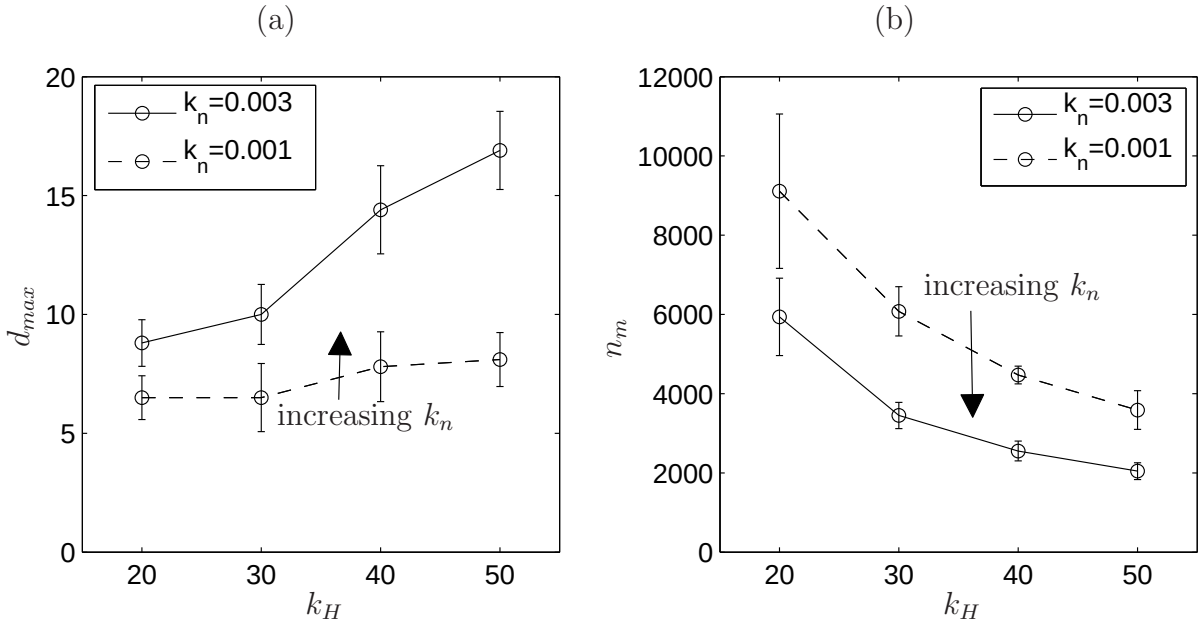

Figure 5.10: Effect of varying the strength of the haptotactic gradient, k_H, on (a) maximum depth of invasion, d_{max} and (b) the time at which a cell reaches the bottom of the lattice, n_m. The profile in (a) is obtained at $t = 600$. We show the results for two values of matrix-degrading rate: $k_n = 0.003$ (——) and $k_n = 0.001$ (− − −). Each circle represents the mean of ten duplicate simulations with the associated standard deviations represented by error bars. Parameter values: $J_{c-c} = 3, J_{c-ECM} = 6, \lambda = 1, \beta = 6$.

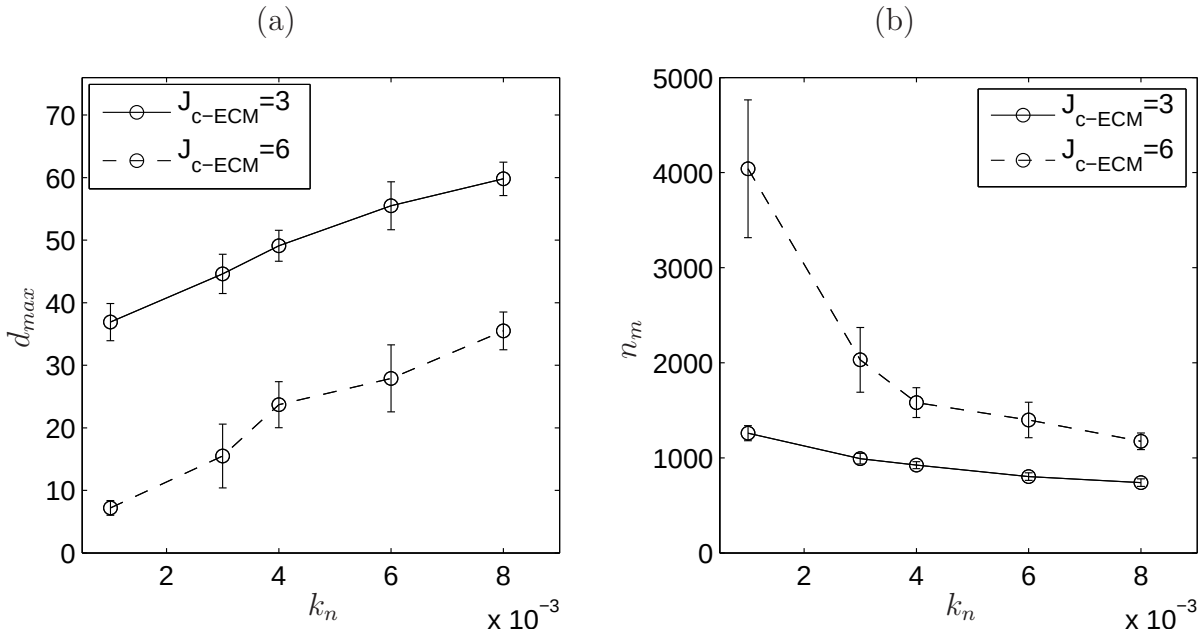

Figure 5.11: Effect of varying the rate at which fibronectin is degraded by proteolytic enzymes, k_n, on (a) maximum depth of invasion, d_{max} and (b) the time at which a cell reaches the bottom of the lattice, n_m. The profile in (a) is obtained at $t = 600$. With $J_{c-c} = 6$, we show the results for two values of cell-ECM adhesion: $J_{c-ECM} = 3$ (——) and $J_{c-ECM} = 6$ (− − −). Each circle represents the mean of ten duplicate simulations with the associated standard deviations represented by error bars. Parameter values: $\lambda = 1, \beta = 6, k_H = 40$.

5.3.4 The inclusion of cell proliferation

So far in our model, cells can grow in size but do not multiply. In reality, once a cell reaches a certain size, it attempts to proliferate and after several divisions (50–60 times), it is no longer capable of dividing [239]. The average cell doubling time is about ten hours [39], but this varies between different cell types. For example, nerve cells do not divide; liver cells divide roughly every two years; whereas skin cells divide approximately every 12 hours [16]. The axis along which cells divide depends on their type and their associated morphology [161]. It is, however, typical

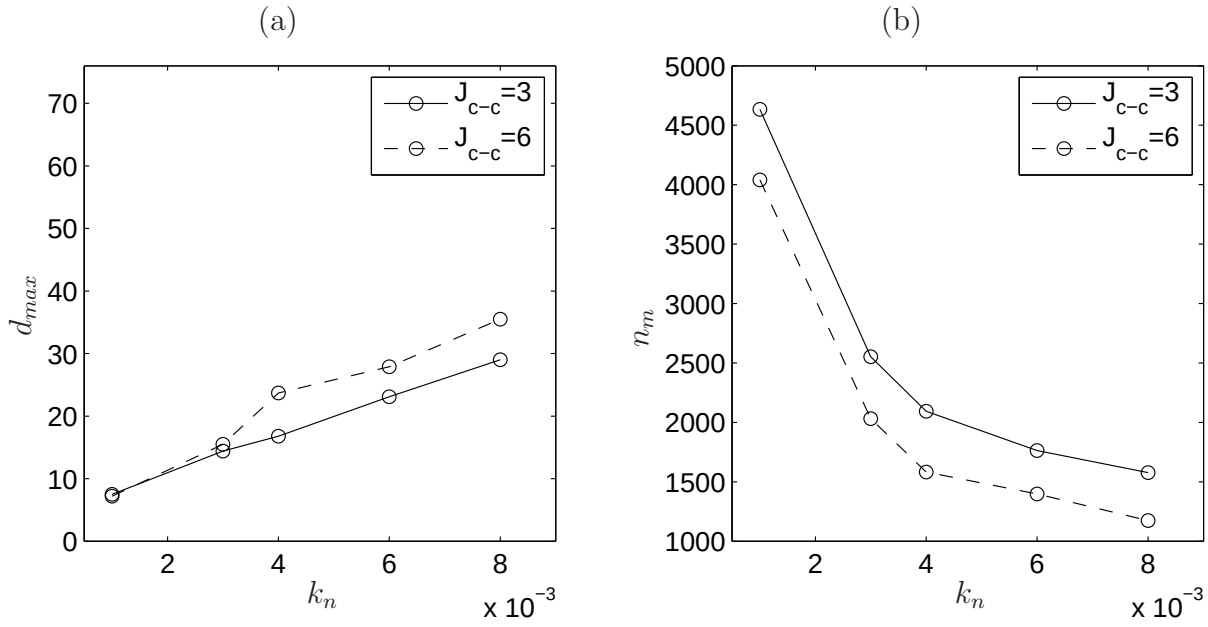

Figure 5.12: Effect of varying the rate at which fibronectin is degraded by proteolytic enzymes, k_n, on (a) maximum depth of invasion, d_{max} and (b) the time at which a cell reaches the bottom of the lattice (n_m, maximal invasion). With $J_{c-ECM} = 6$, we show the results for two values of cell-cell adhesion: $J_{c-c} = 3$ (——) and $J_{c-c} = 6$ (− − −). The profile in (a) is obtained at $t = 600$. Each circle represents the mean of ten duplicate simulations with standard deviations: in (a) $\sigma = \{1.02, 1.85, 2.44, 2.21, 4.67\}$ for $J_{c-c} = 3$ and $\sigma = \{1.17, 5.10, 3.69, 5.36, 3.01\}$ for $J_{c-c} = 6$; and in (b) $\sigma = \{444, 250, 393, 465, 504\}$ for $J_{c-c} = 3$ and $\sigma = \{724, 341, 156, 186, 88\}$ for $J_{c-c} = 6$. Parameter values: $\lambda = 1, \beta = 6, k_H = 40$.

of cells to divide along the shortest axis through their centre of mass [161].

We model cell division the same way as in [233]. We begin by assuming that there exists a time period, T_d, during which cells are not permitted to divide. This is to account for the time it takes for cells to double their content and prepare for cell division. Moreover, we assume, along with Turner *et al.* [233], that cells tend to proliferate when intercellular adhesions are strong relative to the cell-ECM adhesions. This is conveyed in the ratio, $k_s = J_{c-ECM}/J_{c-c}$, which we introduce

into a probability function for cell division. Namely, we assign to each cell a clock which records the time since last division, T_σ, and the instantaneous volume, v_σ. If $T_\sigma > T_d$ and $v_\sigma > V_T$, then we assume that the probability of division gradually increases and reaches one as T_σ becomes very large. That is,

$$p_\sigma = \frac{T_\sigma^2}{T_\sigma^2 + (\alpha k_s)^2}, \tag{5.7}$$

where αk_s is the time (T_σ) at which $p_\sigma = 1/2$.
We calculate the horizontal, vertical and diagonal distances passing through the centre of mass of each cell and divide the cell along the shortest axis. The result is two daughter cells roughly equal in size ($v_\sigma^{\text{new}} \sim v_\sigma^{\text{old}}/2$).

Now, with one MCS being equivalent to 58 seconds (see section 5.3.1 for details), we take $T_d = 745$ so that it is comparable with the average cell doubling time ($\sim$12 hours). A low value of T_d represents a fast-growing tumour whereas a high value represents a slow-growing tumour.

A typical simulation with cell proliferation included is shown in Figure 5.13 for $J_{c-c} = 3$ and $J_{c-ECM} = 6$. Here, we observe that the protruding "fingers" are much thicker and the depth of invasion is higher than that in the absence of proliferation (shown in Figure 5.3). We vary α in Figure 5.14 and note the effect on d_{max} and the total number of tumour cells, n_{cells}. For both strong and weak intercellular adhesions ($J_{c-c} = 3$, left column; $J_{c-c} = 6$, right column), the number of cells and the depth of invasion decrease as α becomes large (see Figures 5.14(a)–5.14(b)). One would expect cell proliferation to increase the invasiveness of the tumour, but we find that within a small range of α, proliferation has a counter-intuitive effect on invasion. More specifically, values of α in the range of 10^4–10^5 have no effect on d_{max} (Figure 5.14(c)), and a negative effect when intercellular adhesions are weakened (Figure 5.14(d)) which is largely attributed to the stochastic nature of the model. This is because increasing α means that the probability of proliferation, for T_σ considered in the simulations, becomes smaller and tends to zero for very large values of α and hence the observed lack of proliferation for $\alpha = 10^5$ (see

Figure 5.14 (c) and (d)).

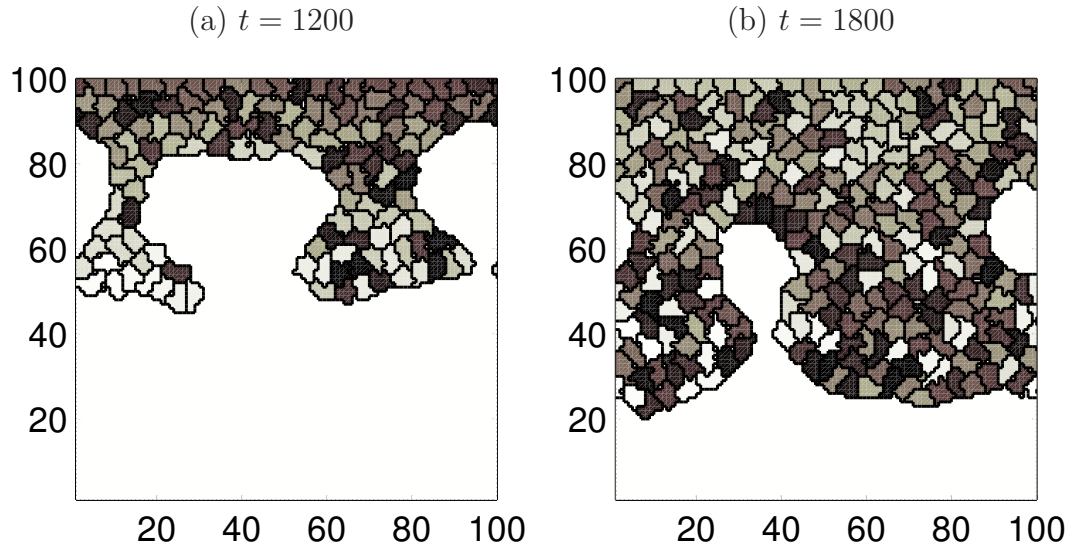

Figure 5.13: A typical simulation of our model with the inclusion of cell proliferation. The invading "fingers" are much thicker than in the absence of proliferation (compare with Figure 5.3). Parameter values here: $J_{c-c} = 3, J_{c-ECM} = 6, \lambda = 1, \beta = 6, k_H = 40, k_n = 0.003, \alpha = 7 \times 10^3, T_d = 745, k_s = 2$.

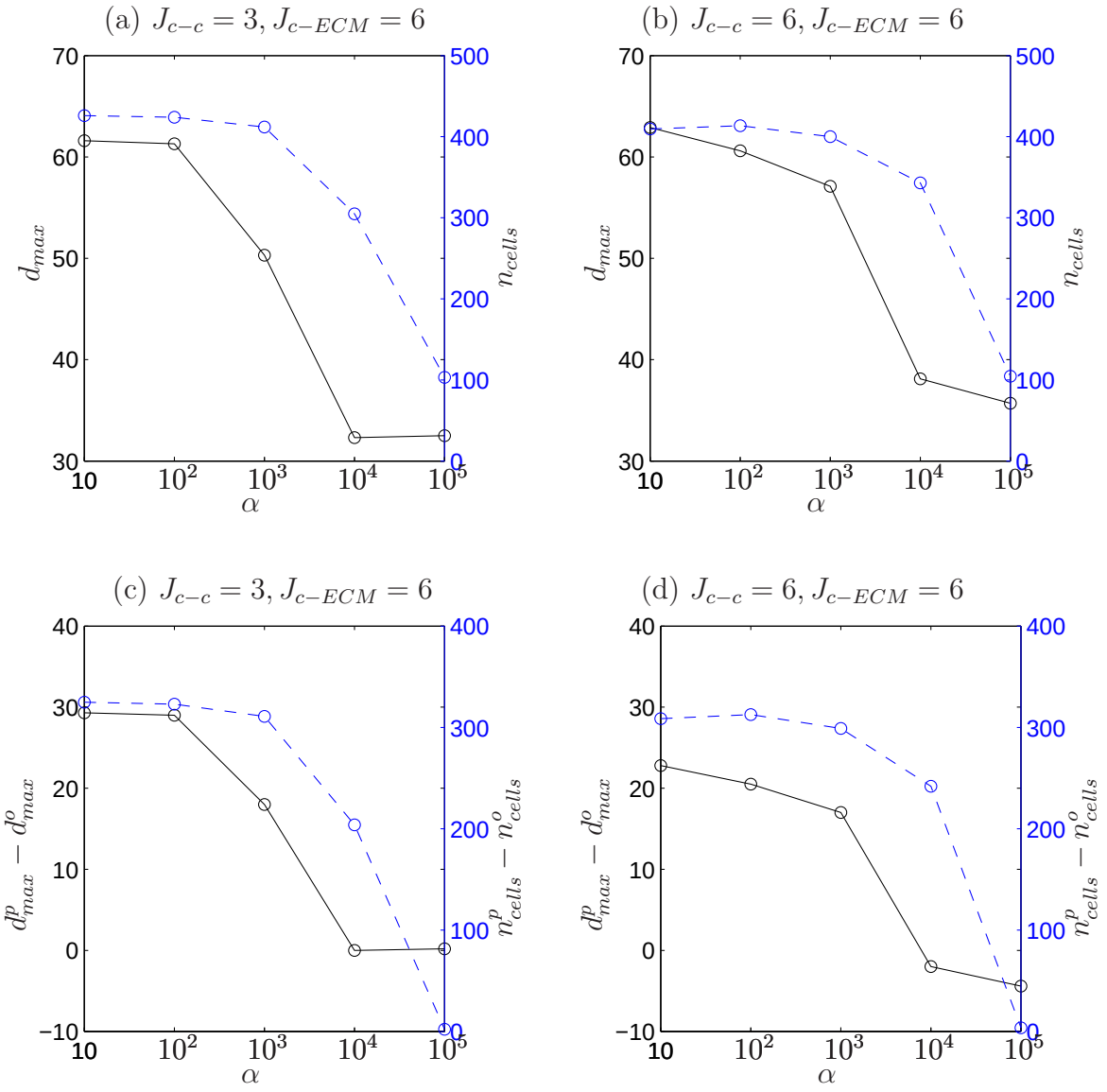

Figure 5.14: Plots showing the relationship between α, d_{max} and n_{cells} under two different values of intercellular adhesions: (a) $J_{c-c} = 3$ and (b) $J_{c-c} = 6$, with $J_{c-ECM} = 6$ in both cases. We also show the difference proliferation has on the depth of invasion and the number of cells for these two cases (d^p_{max}, n^p_{cells}) compared to the non-proliferative case (d^o_{max}, n^o_{cells}). The profiles shown are obtained at $t = 1200$. Each circle represents the mean of ten duplicate simulations. Standard deviations: in (a) $\sigma = \{3.26, 3.66, 5.42, 4.03, 3.20\}$ for d_{max} and $\sigma = \{12.82, 11.73, 10.09, 48.71, 1.79\}$ for n_{cells}. Standard deviations: (b) $\sigma = \{6.50, 5.48, 5.19, 5.89, 3.32\}$ for d_{max} and $\sigma = \{24.30, 20.03, 19.58, 59.64, 1.43\}$ for n_{cells}. Parameter values: $\lambda = 1, \beta = 6, k_H = 40, k_n = 0.003$. Note that the total number of cells in the absence of proliferation is 100. For both strong and weak intercellular adhesions, n_{cells} and d_{max} decrease as α becomes large. Note that proliferation has a counter-intuitive effect on invasion for α in the range of 10^4–10^5.

We now use this model to examine the effect of extracellular acidity on tumour invasiveness.

5.4 Effects of extracellular pH

Many cellular processes are highly dependent on extracellular pH [109, 196] and a small perturbation can cause drastic changes in cell behaviour [142, 195]. Acidic extracellular pH is a hallmark of most solid tumours and is often associated with tumour progression [195] and response to therapies [81]. For instance, acidic extracellular pH is shown to facilitate metastasis by modulating the adhesion properties of cells [47, 166], inducing cell elongation [166] and upregulating the secretion of several proteolytic enzymes [142]. Our study is, to the best of our knowledge, the first to use the extended cellular Potts model to examine the effect of extracellular pH on tumour cell invasion. We study pH effects implicitly by determining how pH variations will affect the model parameters, e.g. cell-ECM adhesion strength, and then studying the effects of these parameter changes in the Potts model. We first investigate the effects of pH on each model parameter in turn. Then we simulate a tumour with all the relevant model parameters being sensitive to acidic pH. Note that throughout this section we ignore intracellular pH and focus on variations and associated effects of pH_e.

5.4.1 Sensitivity of cellular adhesion to acidic pH

The empirical studies that have lead to the existing model parameter values were performed under physiological pH_e (pH$\sim$ 7.2–7.4). We now use experimental data to work out the relative change in their values under acidic pH (6.0–6.6) and hence obtain new model parameter values applicable to acidic conditions. For example, a study by Chen *et al.* [47] shows that cells cultured at pH 6.6 have a 75% reduced junctional E-cadherin level relative to those cultured at pH 7.4. We assume that the J_{c-c} value used so far (i.e. $J_{c-c} = 3$) [233] corresponds to 100% inten-

sity of intercellular adhesion molecules (such as E-cadherins). Now, taking into consideration that a high J value corresponds to low adhesivity and vice versa, we can approximate $J_{c-c} = 5.25$ to be the cell-cell adhesivity at pH_e 6.6 (i.e. a 75% reduction in adhesivity). Figure 5.15(a) shows the morphology of the tumour mass where we assume that only cell-cell adhesion energy is affected by acidic pH_e (namely, we increase J_{c-c} from 3 to 5.25). We observe that the "fingering" morphology is similar to that under physiological pH (shown in Figure 5.15(d)). We can therefore predict that certain mechanisms which cause intercellular adhesions to be weakened under acidic conditions do not, alone, have a significant effect on the invasiveness of the tumour.

To investigate the influence of pH_e on cell-ECM adhesion, Stock *et al.* [218] measure the number of cells that remain adhered to collagen matrix at various extracellular pH values. They find that there is a 45% increase in the number of cells adhered to the matrix at pH_e 6.6 relative to those at pH_e 7.4. Again, keeping in mind that a high adhesivity corresponds to a low J value, we can approximate $J_{c-ECM} = 3.3$ to be the cell-ECM adhesivity at pH 6.6 (compared to $J_{c-ECM} = 6$ at physiological pH [233]). We present in Figure 5.15(b) the results of exposing our tumour mass to acidic pH_e if only cell-ECM adhesion is taken to be sensitive to the acidic medium. Here, we see a marked difference in tumour morphology compared to that at physiological pH.

Moreover, we illustrate in Figure 5.15(c) the effect, on the depth of invasion, of sensitising both cellular adhesion energies (i.e. cell-cell and cell-ECM) to acidic pH_e. We summarise the key effects in Figure 5.16. As we can see, when cell-ECM adhesion energy is decreased in response to acidic pH_e, the depth of invasion is significantly greater than in the base case and that of an increased cell-cell adhesion energy. We may therefore conclude that the combined over-expression of cell-ECM adhesion molecules, such as integrins, and under-expression of cell-cell adhesion molecules, such as, cadherins, under acidic conditions is associated with a higher degree of invasiveness. We can suggest from our model predictions that

the dominant effect appears to be due to the change in cell-ECM adhesivity at low pH rather than due to variations in cell-cell adhesivity.

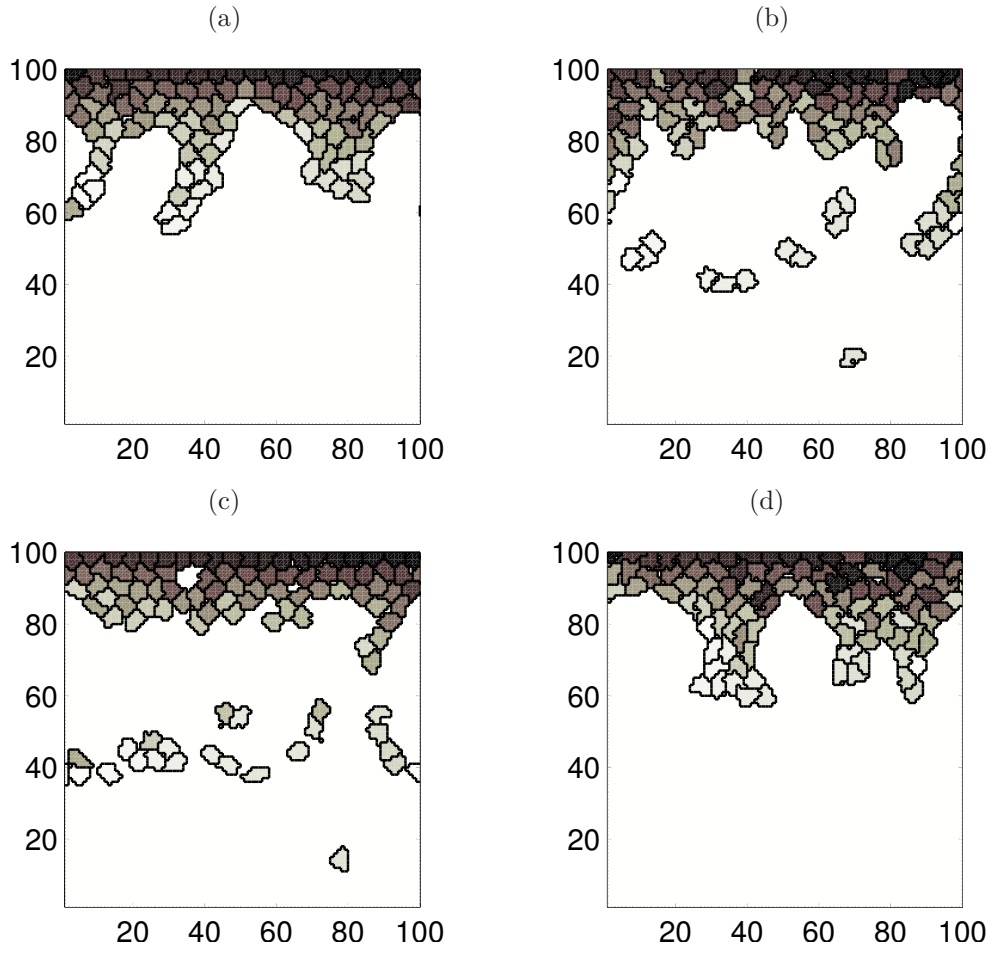

Figure 5.15: Effect of acidic extracellular pH on tumour morphology. In (a) only intercellular adhesion molecules are taken to be sensitive to the acidic medium ($J_{c-c} = 5.25$ and $J_{c-ECM} = 6$). In (b), only cell-ECM adhesion molecules are taken to be sensitive to the acidic extracellular pH ($J_{c-c} = 3$ and $J_{c-ECM} = 3.3$). In (c), both cell-ECM and cell-cell adhesion molecules are taken to be sensitive to the acidic extracellular pH ($J_{c-c} = 5.25$ and $J_{c-ECM} = 3.3$). In (d), cell- cell and cell-ECM adhesiveness are taken to be at the physiological values ($J_{c-c} = 3, J_{c-ECM} = 6$). Here $t = 900$ and the remaining parameter values are the same as those in the caption to Figure 5.3.

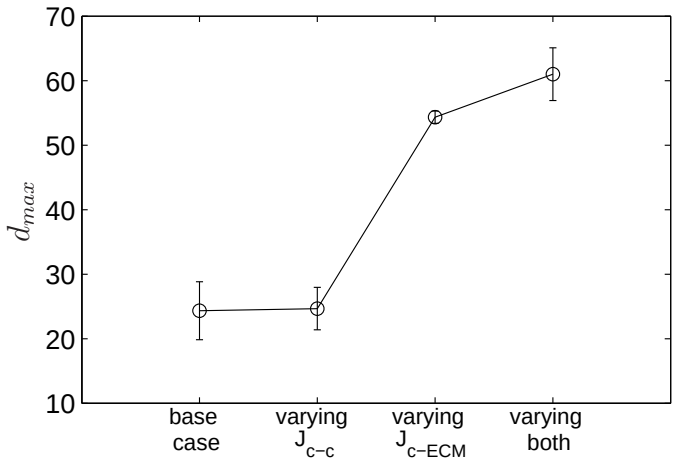

Figure 5.16: We show how the depth of invasion (d_{max}) in the base case ($J_{c-c} = 3, J_{c-ECM} = 6$) compares with that when J_{c-c}, alone, is varied in response to acidic extracellular pH ($J_{c-c} = 5.25$), or, J_{c-ECM} alone is varied ($J_{c-ECM} = 3.3$), or, both J_{c-c} and J_{c-ECM} are varied ($J_{c-c} = 5.25, J_{c-ECM} = 3.3$). Each circle represents the mean of three duplicate simulations at $t = 900$, with the associated standard deviations represented by error bars.

5.4.2 Effect of acidic pH on the rate of proteolytic degradation of the ECM

The local secretion of proteolytic enzymes by tumour cells or surrounding stromal cells is a prerequisite to the loss of the structural integrity of the extracellular matrix [59]. The acidic extracellular environment of most solid tumour cells is permissive for the over-production of several proteolytic enzymes, such as cathepsin B [88, 199], cathepsin D [195], proangiogenic factors [195], matrix metalloproteinases (MMPs) [116, 195]. There are 23 members of MMPs, and we focus in this study on MMP-2 because the pH dependency in this enzyme is readily available. Although the catalytic activity of MMP-2 exhibits a broad bell-shaped pH dependency with pK_a values of 6.0–9.0 [61], a study by Rofstad *et al.* [195] shows that

human melanoma cells cultured at acidic pH_e secrete 1.8–2.8 times more MMP-2 in pro and active form than those cultured at pH_e 7.4. Assuming that the matrix degradation rate used so far (i.e. $k_n = 0.003, k_i = 2k_n$) applies to physiological pH medium, we can approximate $k_n = 0.0036$–0.0084 to be the matrix degradation rate at acidic pH_e. We illustrate the effect of increased enzyme secretion rate by factors of 1.8–2.8 [195] on tumour morphology (Figure 5.17) and on the depth of invasion (Figure 5.18). It is clear from both figures that increased secretion of proteolytic enzymes due to acidic conditions yields a more invasive tumour than when the medium is kept at physiological pH (see Figure 5.17(c)). However, an increase in the secretion rate of proteolytic enzymes by a factor of 2.8 gives rise to a similar depth of invasion to that when cell-ECM adhesion is taken to be sensitive to acidic pH_e (see Figure 5.16).

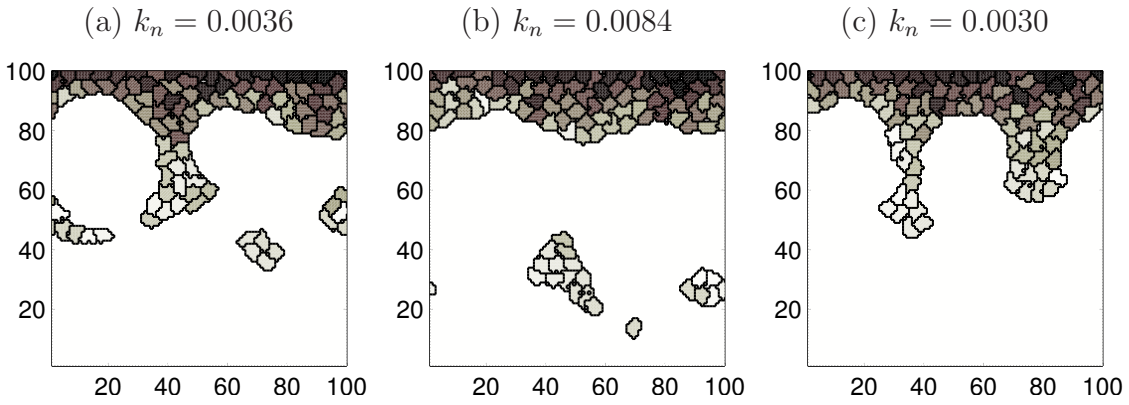

Figure 5.17: Plots showing the morphology of the tumour following increased production of proteolytic enzymes (such as MMP-2) at acidic pH by a factor of: (a) 1.8, (b) 2.8, relative to secretions under pH 7.2–7.4. Compare with (c) where $k_n = 0.003$, which is the assumed value under physiological pH. Here $t = 1200, J_{c-c} = 3, J_{c-ECM} = 6, \lambda = 1, \beta = 6$.

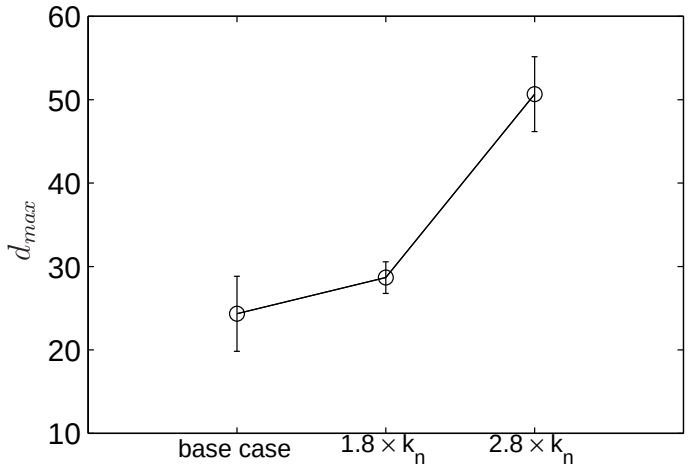

Figure 5.18: Plot showing how d_{max} is altered when proteolytic enzyme secretion rate is increased, from the base case, under acidic pH. Each circle represents the mean of three duplicate simulations obtained at $t = 900$, with the associated standard deviations represented by error bars. k_n=0.003 in the base case.

5.4.3 Effect of acidic pH on cell area

As cells migrate along a matrix their shape changes, the extent of which is believed to vary with exposure to different degrees of extracellular acidity [37, 46, 166, 218, 222] (see Figure 5.19 for an illustration). For example, a study by Paradaise *et al.* [166] shows that cells develop an elongated morphology following an exposure to extracellular pH of 6.0, with a 42% increase in mean cell area. Now, with V_T =25 taken to be the average cell area at physiological pH [233], a 42% increase will then give V_T =36 to be the average cell area at acidic pH. To simulate an elongated cell of volume 36, we initialise each biological cell to be either a 12×3 or 9×4 or 18×2 rectangle. We find that, compared to the physiological pH case, there is no effect on either the morphology of the main tumour mass or the depth of invasion (figures not shown). This is because the Potts model is driven by the

change in energy in the system and not the number of adhesive bonds gained or lost. Our model therefore predicts that cell elongation and increased cell area, due to changes in extracellular pH, does not predict an increase in the invasiveness of the tumour.

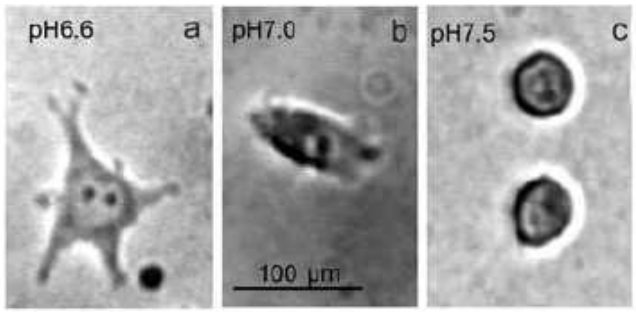

Figure 5.19: Morphology of human melanoma (MV3) cells following a three-hour exposure to various extracellular pH. Image courtesy of [218].

5.4.4 Effect of acidic pH on cell proliferation

Once cells reach a prescribed volume, they can proliferate. Before proliferating, many conditions have to be met, amongst them is a viable extracellular pH [39, 63]. A study by Casciari *et al.* [39] shows that the growth rate of EMT6/Ro mouse mammary tumour cells decreases with decreasing extracellular pH. They measure tumour cell doubling time at various extracellular pH and O_2 concentrations. For instance, under oxygen levels of 0.0443 mmol/l, cell doubling time increases by 118% at pH 6.6 relative to pH 7.25. With even lower oxygen levels of 0.0232 mmol/l and 0.0082 mmol/l, there is, respectively, a 238% and a 1.46×10^3% increase in cell doubling time at pH 6.6 relative to pH 7.25. Now, if we assume that $T_d = 745$ is the cell doubling time under physiological pH, we can then take for pH 6.6: $T_d = 1.62 \times 10^3$, 2.52×10^3, and 1.15×10^4, respectively, for pH 6.6 conditions at O_2 concentrations of (0.0443, 0.0232, 0.0082) mmol/l [39].

Figures 5.20(a)–(c) show how the tumour morphology changes from well-defined

"fingers" to that where the "fingers" split from the main tumour mass. The reason for this is that the doubling time in (a)–(c) is long (due to low pH and oxygen levels), so that cells do not have the chance to proliferate and populate the areas behind the advancing "finger" tip. Cells cultured under physiological pH are known to produce a "diffuse" morphology (Figure 5.13). We show in Figure 5.21 how d_{max} is little affected by variations in pH_e. Proliferation under acidic pH yields a similar d_{max} to the case where no proliferation is included, with the highest d_{max} recorded under physiological pH (see Figure 5.21). In view of those results, we suggest that the increased invasion distances observed in low pH cultured cells is not a result of the pH effects on cell proliferation. However, as we can see in Figure 5.20(d), there are clear morphological differences in low pH and physiologically cultured tumours, with break-away tumour clusters readily observed in the low pH case.

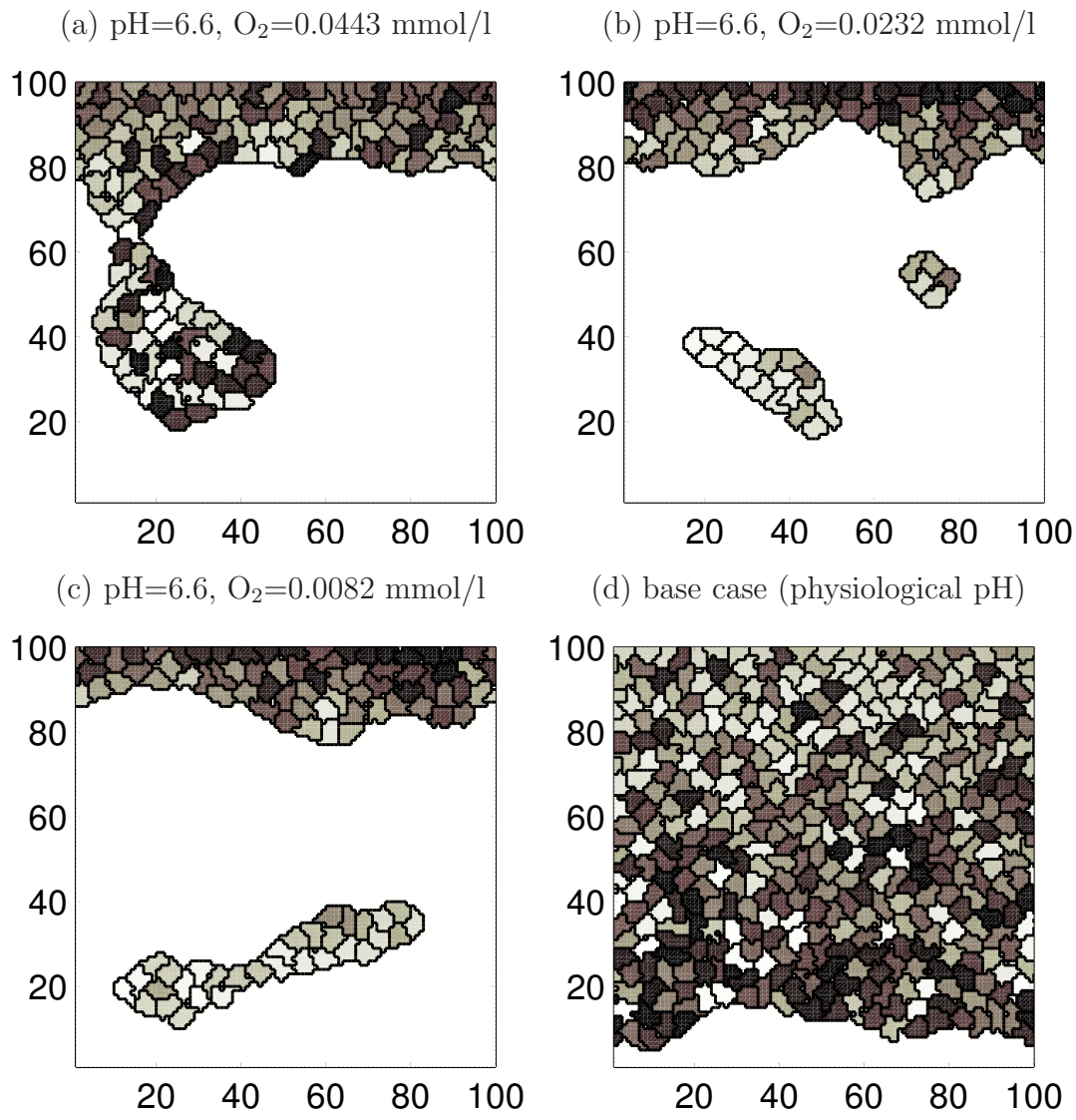

Figure 5.20: We show the profile of the tumour mass cultured at pH 6.6 and at three different concentrations of oxygen: (a) 0.0443 mmol/l ($T_d = 1.62 \times 10^3$), (b) 0.0232 mmol/l ($T_d = 2.52 \times 10^3$), (c) 0.0082 mmol/l ($T_d = 1.15 \times 10^4$). We also show the tumour profile under physiological pH and O_2 (T_d=745) in (d). It is clear that under pH 6.6 the tumour mass exhibits "fingering" morphology, whereas at physiological pH the morphology is more "diffuse". Note that in (b) and (c) the doubling time is very large that cells break off the main mass and reach the bottom of the lattice before proliferation occurs. Here $t = 2100$. The remaining parameters are the same as in the caption to Figure 5.3.

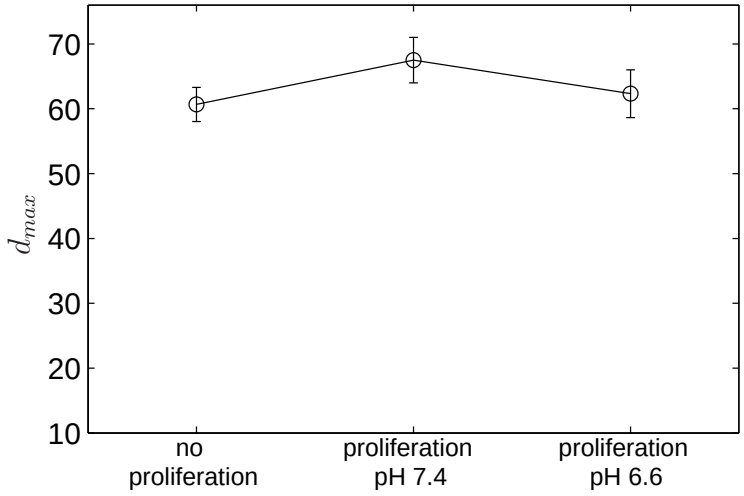

Figure 5.21: Plot showing how d_{max} is little affected by proliferation at acidic pH. Each circle represents the mean of three duplicate simulations obtained at $t = 900$, with the associated standard deviations represented by error bars. Parameter values are the same as in the caption to Figure 5.13 with $T_d = 745$ at physiological pH, $T_d = 1.62 \times 10^3$ at pH 6.6 and $\alpha = 7 \times 10^3$ in both cases.

5.4.5 Effect of acidic pH on cellular adhesion, cell area, proteolytic enzymes and proliferation

So far we have illustrated the effects of acidic pH on each of the relevant model parameters one by one (Figures 5.15–5.21). We now show the results when all of these parameters are simultaneously modified to replicate more realistically a tumour cultured in acidic conditions (see Figure 5.22(a)). We observe that, compared with the physiological pH case (Figure 5.22(b)), cells split from the main tumour mass much earlier and migrate further into the extracellular matrix in a very short period of time. We summarise in Figure 5.23 how the depth of invading cells is affected over the course of their growth, under physiological and acidic pH. We may deduce that, cell-ECM adhesion strength, or, proteolytic enzyme secretion

rate appear to be dominating processes driving an increase in tumour invasiveness under acidic conditions. Variations in processes such as cell-cell adhesivity, moderate ($\times 1.8$) variations in proteolytic activity and cell proliferation do not appear to significantly affect the speed of invasion. Therefore, it appears that optimal therapeutic targets are predicted to be cell-ECM adhesions and preventing large increases in proteolytic activity.

(a) tumour cultured at acidic pH (b) tumour cultured at physiological pH

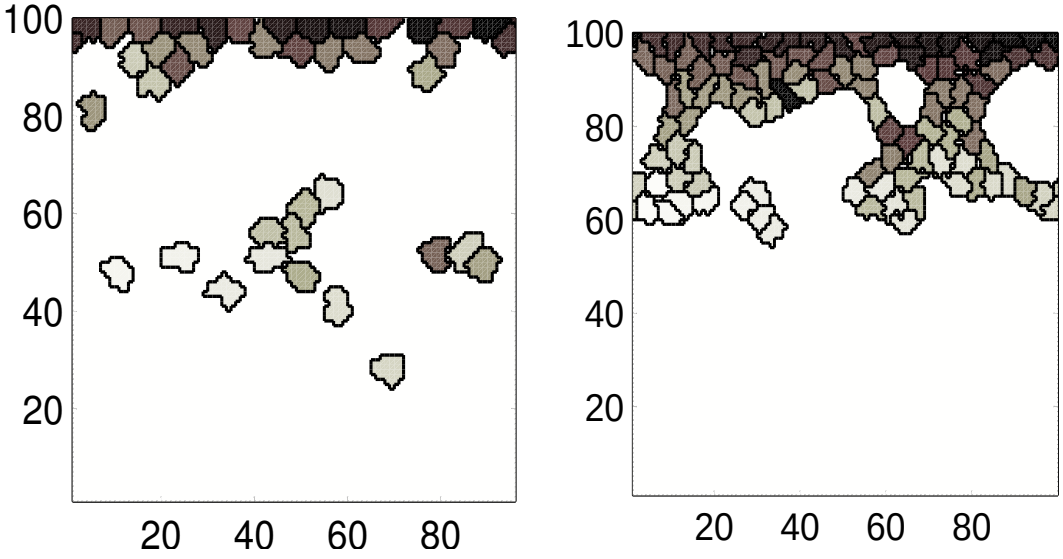

Figure 5.22: A typical profile of the migration of tumour cells cultured (a) at acidic pH (b) at physiological pH. Profiles shown at $t = 900$. Parameter values for (a) are those applicable to acidic conditions: $k_n = 0.0036, J_{c-c} = 5.25, J_{c-ECM} = 3.3, V_T = 36$ (initially cells are 3 grids long and 12 grids wide), $\alpha = 7 \times 10^3, T_d = 1.9 \times 10^3$. Parameter values for (b) are those corresponding to physiological pH, i.e. $k_n = 0.003, J_{c-c} = 3, J_{c-ECM} = 6, V_T = 25, \alpha = 7 \times 10^3, T_d = 1.9 \times 10^3$. In both figures: $\lambda = 1, \beta = 6, k_H = 40$.

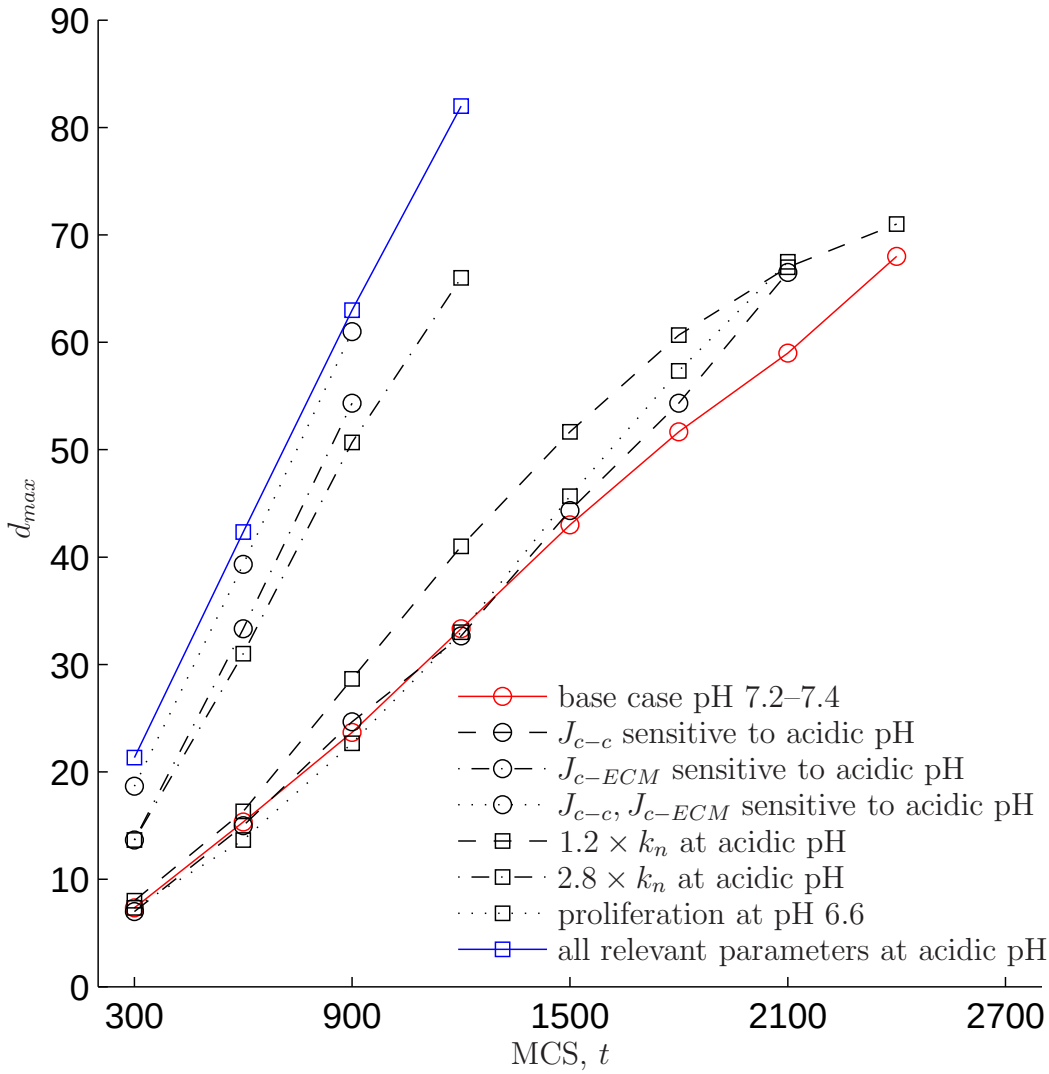

Figure 5.23: Plot showing how d_{max} is affected when a tumour is cultured at acidic pH (squared solid line) compared to physiological pH (circled solid line). In between these two lines we show how d_{max} is affected if only one parameter is taken to be sensitive to acidic pH medium. Each circle and square represent the mean of three duplicate simulations.

5.5 Discussion and conclusions

In this chapter we have reproduced key findings obtained by Turner *et al.* [233] in their study of tumour cell invasion using the extended cellular Potts model. We then examined the effect of acidic pH on cell adhesion, proteolytic degradation of the ECM and cell proliferation and how it can affect the invasiveness of the tumour mass. While previous studies, such as in [112, 210], have considered reaction-diffusion equations to represent chemicals such as oxygen, nutrients and lactate, here we simply vary the relevant parameters using experimental data in the literature to reflect the relevant pH effects.

In summary, our numerical simulations have shown that a strong cell-ECM adhesion and a weak cell-cell adhesion can result in a 'fingering' and more invasive morphology. This is consistent with previous multi-scale individual-based (e.g. [7]) and continuum models (e.g. [6, 165]). We have also shown that under acidic extracellular pH, cell-ECM adhesion strength have a comparable effect on tumour invasiveness as the rate at which the ECM is degraded by proteolytic enzymes. More specifically, cells which are strongly attached to the ECM, or, have a high rate of proteolytic degradation of the ECM, tend to infiltrate further into the matrix than those which are weakly attached or have a low rate of proteolytic degradation of the ECM. On the other hand, intercellular adhesion strength appears to have a less significant effect on tumour invasiveness. Moreover, we have also shown that proliferation can have a counter-intuitive effect on invasion. That is, tumour cells cultured under physiological pH tend to be larger and develop a "diffuse" morphology compared to those cultured at acidic pH which display protruding "fingers" at the advancing front. Amongst the many factors that affect the prognosis and treatment of cancer is their morphology. For instance, in colorectal cancer, whether a tumour has an infiltrative or smooth border at the advancing edge has been shown to have a prognostic significance and may predict liver metastasis [52, 111, 163].

Our study is the first to use the extended cellular Potts model to examine the effect of extracellular acidity on tumour cell invasion and as such there is plenty of scope for improvement. Firstly, we model the effects of pH in a simplistic manner by assuming a constant pH_e throughout the tissue section and that cellular membrane transporters are distributed evenly. However, there are numerous studies suggesting that certain cellular membrane transporters such as the NHEs localise at the leading edge of migrating tumour cells [57, 139, 218, 222]. In particular, Stock *et al.* [218] observe in their study of human melanoma cells that the NHE activity plays a key role in controlling cell migration and morphology. Inhibition of the NHE reduces the speed and translocation of migrating cells by 70% [218]. Secondly, we assume a homogeneous concentration of fibronectin in our model. However, a study by Paradise *et al.* [166] shows that the fibronectin levels required for maximum migration speed is lower at acidic pH compared to physiological pH. Therefore, in order to increase the biological realism of our model, it would be interesting in the future to simulate our model with a heterogenous concentration of fibronectin and a reaction diffusion equation (such as the one presented Chapter 3) to represent pH_e with the NHE term being localised near the leading edge of tumour cells.

Chapter 6

Conclusions and future work

Compared to normal tissue, the microenvironment of some solid tumours are littered with variable regions of hypoxia and acidity [93, 227]. This has been partly attributed to the poorly-formed tumour vasculature and irregular perfusion [187]. However, even under aerobic conditions, tumour cells have been sometimes shown to still metabolise anaerobically [247] and produce excess amounts of lactate and H^+-ions, which has been shown to have a detrimental effect on cell function and survival if accumulated intracellularly [85, 109, 123, 167]. Cells respond to the acidic intracellular load by upregulating their membrane-based ion transporters to extrude these ions extracellularly [35, 176]. It is thought that a high rate of anaerobic glycolysis coupled with an upregulated extrusion of these ions and a poor extracellular clearance gives rise to an acidic extracellular pH [73, 87, 93].

In this thesis, we develop mathematical models that examine the role of various membrane-based ion transporters in tumour pH regulation, in particular, with a focus on the interplay between lactate and H^+ ions and whether the lactate/H^+ symporter activity is sufficient to give rise to the observed reversed pH gradient that is seen in some tumours. We examine the problem of tumour acidity using two different mathematical approaches: a continuum (as in Chapters 2 and 3) and a multi-scale individual cell-based approach (as in Chapters 4 and 5).

In this chapter, we bring together the key findings of this thesis in the light

of current biological and mathematical contributions. We also set out some key questions that we suggest can be answered through further research.

In Chapter 2, we develop a mathematical model representing the various cell membrane transporters involved in pH regulation. Analysis of the model show that, with the inclusion of lactate explicitly in the model, a reversed pH gradient is attainable under aerobic conditions when 'other sources of hydrogen ions' are decreased and MCT activity is increased—but we find the pH conditions that this reversed gradient is found to be biologically unrealistic. Under anaerobic conditions, we find that decreasing 'other sources of H^+-ions' and the glycolytic rate gives rise to a reversed cellular pH gradient, but again it is too alkaline to be biologically realistic. Other sources of hydrogen ions can include those produced from glutaminolysis or the intracellular hydration of carbon dioxide by carbonic anhydrase.

In Chapter 3, we extend this model by giving the tumour a spatial structure. Spatially, we assume a 1-d cartesian geometry. We find that simply taking lower values of blood lactate levels gives a reversed cellular pH gradient throughout the spatial domain independent of the levels of tissue lactate. Likewise, we find the existence of a negative cellular pH gradient to be strongly dependent on the combined activity of the lactate/H^+ symporters (MCTs) and other sources of H^+-ion. The ability of extracellular H^+-ions to leak into the neighbouring blood vessel and to diffuse across the tissue causes the reversed cellular pH gradient to occur at more realistic values and is less alkaline than that found in the none spatial model. This is because as the extracellular H^+-ions and lactate are cleared by the blood vessel, more intracellular H^+-ions and lactate are extruded via the MCTs and NHEs which cause the extracellular pH to become less alkaline. In addition, we find the pH gradient to be always reversed no matter how high or low the Na^+/H^+ exchanger (NHE) activity is provided the level of other sources of H^+-ions is below a certain threshold. We also find that including intercellular gap junctional communication can give rise to a reversed cellular pH gradient but only

if the rate of intercellular transport is significantly high.

In Chapter 4, we model early tumour growth using a hybrid cellular automaton model with reaction-diffusion equations as described in Chapter 3 but with also an additional equation for oxygen and discrete elements describing the individual tumour cells and the interaction of the cells with each other and the microenvironment. Our most significant contribution in this chapter is that, when tumour cells are strongly sensitive to changes in the intracellular pH, a low activity of the NHE or a high rate of anaerobic glycolysis can give rise to a "fingering" morphology. Furthermore, we show that as the activity of the MCT increases all the tumour cells within the spheroid exhibit a reversed transmembrane pH gradient.

As a way of validating the model developed in Chapter 5, we reproduce key findings obtained by Turner *et al.* [233] in their study of tumour cell invasion using the extended cellular Potts model. We then examine the effect of acidic pH on cell adhesion, proteolytic degradation and cell proliferation on the invasiveness of the tumour cells. Our simulations show that, under acidic extracellular pH, cell-ECM adhesion strength has a comparable effect on tumour invasiveness as the rate at which the ECM is degraded by proteolytic enzymes. We also show that tumour cells cultured under physiological pH tend to be larger and develop a "diffuse" morphology compared to those cultured at acidic pH which display protruding "fingers" at the advancing front.

Our analysis have allowed us to draw several important conclusions regarding tumour acidity and the reversed cellular pH gradient. We now ask what their significance may be in terms of therapeutic strategies. We suggest that simply lowering the MCT activity may prevent the onset of a negative cellular pH gradient when the tumour is growing. This intervention, however, can cause a 'fingering' tumour morphology and the onset of quiescent cell state which have been shown to be resistant to some anti-cancer therapies [151]. Also, we suggest that interventions which lower the rate of glycolysis may result in a 'rounded' tumour which is a characteristic of less invasive tumours [60]. Also, artificially increasing the

glycolytic rate will acidify the intracellular space and result in inner core of dead cells, but with 'fingering' morphology which is a characteristic of invasive tumours [60]. Furthermore, we suggest that mechanisms which render cell-ECM adhesion molecules weak particularly under acidic extracellular conditions tend to give rise to a less invasive tumour. As expected, we also find that reducing proteolytic enzyme activity will also give rise to a less invasive tumour.

One criticism that may arise from our model is that we assume anaerobic glycolysis is the only source of excess production of H^+-ions above the normal background production. However, in addition to lactic acid production, intracellular buffering of H^+-ions with bicarbonate can release carbon dioxide which can then freely leave the cell [202]. Expression of the enzyme carbonic anhydrase 9 on the tumour cell surface catalyses the extracellular cell-generated carbon dioxide into bicarbonate and H^+ [223]. This will then contribute to the acidity of the extracellular environment [224]. It would be interesting to study the effects of this in our model.

The CA model presented in Chapter 4 provides a novel framework for understanding the important factors driving early tumour growth. In reality, tumour growth does not exclusively depend on, for example, oxygen or pH and as such it would be more biologically reasonable to allow all of oxygen, glucose, intra- and extracellular pH to simultaneously influence, in our model, the growth and phenotypic transformation of cells rather than just oxygen and extracellular pH. Also, rather than just assuming a distally located blood vessel at the boundary, our model can be extended by investigating the effect of the tumour microenvironment during angiogenesis. For example, it would be interesting to incorporate the effect of acidity on MMP secretion and degradation of the extracellular matrix into the sophisticated model of angiogenesis developed by McDougall *et al.* [146]. This model focuses on the effect of blood perfusion during angiogenesis and the delivery of chemotherapeutic drugs.

Appendix A

Glossary

Acidic pH high levels of H^+-ions.

Benign non-cancerous mass.

Carcinoma any type of cancer that arises in the epithelial tissue of the skin or of the lining of the internal organs.

Cell adhesion molecules proteins located on the cell surface that bind cells with other cells or with the extracellular matrix (ECM).

Cellular ion-transporter membrane-bound protein that transports ions in or out of the cell.

Extracellular matrix (ECM) is a non-cellular component that provides essential structural support for the tissues or organs and also initiates crucial biochemical and biomechanical signalling that are required for tissue morphogenesis, differentiation and homeostasis.

Glioma a type of malignant tumour that originates from the the brain or spine.

Glycolysis the breakdown of glucose to release energy in the form of ATP. In the presence of oxygen, 36 ATP molecules are produced, whereas in the absence of oxygen, only 2 ATP molecules are produced.

Hypoxia low oxygen.

Intracellular inside the cell.

Extracellular outside the cell.

In vitro experiments performed on cells outside the organism.

In vivo an experimental procedure using an intact live organism.

Metastasis the spread of cancer cells from one organ or tissue to another.

Necrosis cell death.

Phenotype an organism's observable characteristics, such as its morphology, development, biochemical or physiological features.

Proteolytic enzymes enzymes that catalyse the digestion of proteins into smaller peptide fractions and amino acids by a process known as proteolysis.

Proliferation the process whereby a parent cell gives rise to two daughter cells that share the same genetic make up.

Reversed, or negative, pH gradient the intracellular pH is higher than the extracellular.

pH scale measures how acidic or alkaline a substance is, with pH 14 being strongly alkaline, pH 1 being strongly acidic and pH 7 neutral.

Quiescence cell in resting state.

Vasculature arrangement of blood vessels in the body or an organ.

Bibliography

[1] http://info.cancerresearchuk.org/cancerstats/incidence/, Sep 2012.

[2] M F Adam, E C Gabalski, D A Bloch, J W Oehlert, J M Brown, A A Elsaid, H A Pinto, and D J Terris. Tissue oxygen distribution in head and neck cancer patients. *Head Neck*, 21:146–153, 1999.

[3] J A Adams and N Bellomo. *A Survey of models for tumour-immune system dynamics*. Birkhauser, Boston, 1997.

[4] M Alber, M Kiskowski, J Glazier, and Y Jiang. *IMA Series on mathematical systems theory in biology, communication and finance*, volume 142, chapter On cellular automaton approaches to modeling biological cells, pages 1–40. Springer, New York, 2002.

[5] V Andasari and M A J Chaplain. Intracellular modelling of cell-matrix adhesion during cancer cell invasion. *Math Model Nat Phenom*, 7(01):29–48, 2012.

[6] V Andasari, A Gerisch, G Lolas, A P South, and M A J Chaplain. Mathematical modeling of cancer cell invasion of tissue: biological insight from mathematical analysis and computational simulation. *J. Math. Biol.*, 63:141–171, 2011.

[7] V Andasari, R T Roper, M H Swat, and M A J Chaplain. Integrating intracellular dynamics using CompuCell3D and bionetsolver: applications

to multiscale modelling of cancer cell growth and invasion. *PLoS ONE*, 7(3):e33726, 2012.

[8] A R A Anderson. A hybrid mathematical model of solid tumour invasion: the importance of cell adhesion. *Math. Med. Biol.*, 22:163–186, 2005.

[9] A E Aplin, A K Howe, and R L Juliano. Cell adhesion molecules, signal transduction and cell growth. *Curr. Opin. Cell Biol.*, 11(6):737–744, 1999.

[10] R P Araujo and D L S McElwain. A history of the study of solid tumour growth: the contribution of mathematical modelling. *Bull. Math. Biol.*, 66:1039–1091, 2004.

[11] N J Armstrong, K J Painter, and J A Sherratt. A continuum approach to modelling cell-cell adhesion. *J. Theor. Biol.*, 243(1):98–113, 2006.

[12] P S Aronson. Kinetic properties of the plasma membrane Na^+-H^+ exchanger. *Ann. Rev. Physiol.*, 47:545–560, 1985.

[13] N Avril, J Dose, F Janicke, S Bense, S Ziegler, C Laubenbacher, W Romer, H Pache, M Herz, B Allgayer, W Nathrath, H Graeff, and M Schwaiger. Metabolic characterization of breast tumors with positron emission tomography using F-18 fluorodeoxyglucose. *J. Clin. Oncol.*, 14(6):1848–1857, 1996.

[14] A H Baker, D R Edwards, and G Murphy. Metalloproteinase inhibitors: biological actions and therapeutic opportunities. *J. Cell. Sci.*, 115:719–3727, 2002.

[15] M A Barry and A Eastman. Endonuclease activation during apoptosis: The role of cytosolic Ca^{2+} and pH. *Biochem. Bioph. Res. Co.*, 186(2):782—789, 1992.

[16] W M Becker, L J Kleinsmith, J Hardin, and G P Bertoni. *The world of the cell.* Perarson Benjamin Cummings, San Francisco, 2008.

[17] J Behrens. The role of cell adhesion molecules in cancer invasion and metastasis. *Breast Cancer Res. Tr.*, 24:175–184, 1993.

[18] S Bekku, H Mochizuki, T Yamamoto, H Ueno, E Takayama, and T Tadakuma. Expression of carbonic anhydrase I or II and correlation to clinical aspects of colorectal cancer. *Hepato-Gastroenterol.*, 47(34):998–1001, 2000.

[19] J M Berg, J L Tymoczko, and L Stryer. *Biochemistry.* W. H. Freeman, New York, 5th edition, 2003.

[20] G Berx and F van Roy. Involvement of members of the cadherin superfamily in cancer. *Cold Spring Harb. Perspect. Biol.*, 1:a003129, 2009.

[21] J Boldt, B Kumle, S Suttner, and G Haisch. Point-of-care (POC) testing of lactate in the intensive care patient. *Acta. Anaesthesiol. Scand.*, 45:194–199, 2001.

[22] W F Boron. Intracellular pH-regulating mechanisms for the squid axons: Relation between the external Na^+ and HCO_3^- dependences. *J. Gen. Physiol*, 85(3):325–345, 1985.

[23] W F Boron. Intracellular pH regulation in epithelial cells. *Annu. Rev. Physiol.*, 48:377–388, 1986.

[24] M J Boyer and I F Tannock. Regulation of intracellular pH in tumour cell lines: Influence of microenvironmental conditions. *Cancer Res.*, 52:4441–4447, 1992.

[25] P Boyle and B Levin. World cancer report. Technical report, World Health Organisation, 2008.

[26] M C Brahimi-Horn, J Chiche, and J Pouyssegur. Hypoxia signalling controls metabolic demand. *Curr. Opin. Cell Biol.*, 19:223–229, 2007.

[27] R Breban, A Bisiaux, C Biot, C Rentsch, P Bousso, and M L Albert. Mathematical model of tumor immunotherapy for bladder carcinoma identifies the limitations of the innate immune response. *Oncoimmunology*, 1(1):9–17, 2012.

[28] A Breslow. Thickness, cross-sectional areas and depth of invasion in the prognosis of cutaneous melanoma. *Ann. Surg.*, 172(5):902–908, 1970.

[29] J M Brown. Tumor microenvironment and the response to anticancer therapy (review). *Cancer Biol. Ther.*, 1(15):453–458, 2002.

[30] J M Brown and A J Giaccia. The unique physiology of solid tumors: Opportunities (and problems) for cancer therapy. *Cancer Res.*, 58(7):1408–1416, 1998.

[31] J M Brown and W R Wilson. Exploiting tumour hypoxia in cancer treatment. *Nat. Rev. Cancer*, 4:437–447, 2004.

[32] S Bunimovich-Mendrazitsky, H Byrne, and K Stone. Mathematical model of pulsed immunotherapy for superficial bladder cancer. *Bull. Math. Biol.*, 70(7):2055–2076, 2008.

[33] A V Burton. Rate of growth of solid tumours as a problem of diffusion. *Growth*, 30:157–176, 1966.

[34] W B Busa. Mechanisms and consequences of pH-mediated cell regulation. *Ann. Rev. Physiol.*, 48:389–402, 1986.

[35] G Busco, R A Cardone, M R Greco, A Bellizzi, M Colella, E Antelmi, M T Mancini, M E Dell'Aquila, V Casavola, A Paradiso, and S J Reshkin. NHE1 promotes invadopodial ECM proteolysis through acidification of the peri-invadopodial space. *FASEB J*, 24(10):3903–3915, 2010.

[36] S K Calderwood and J A Dickson. pH and tumor response to hyperthermia. *Adv. Radiat. Biol.*, 10:135–190, 1983.

[37] R A Cardone, V Casavola, and S J Reshkin. The role of distributed pH dynamics and the Na^+/H^+ exchanger in metastasis. *Nat. Rev. Cancer*, 5:786–795, 2005.

[38] P Carmeliet and R K Jain. Angiogenesis in cancer and other diseases. *Nature*, 407:249–257, 2000.

[39] J J Casciari, S V Sotirchos, and R M Sutherland. Variations in tumour cell growth rates and metabolism with oxygen concentrations, glucose concentration, and extracellular pH. *J. Cell. Physiol.*, 151(2):386–394, 1992.

[40] U Cavallaro and G Christofori. Cell adhesion and signalling by cadherins and ig-CAMs in cancer. *Nat. Rev. Cancer*, 4:118–132, 2004.

[41] F Ceteci, S Ceteci, C Karreman, B W Kramer, E Asan, R Götz, and U R Rapp. Disruption of tumor cell adhesion promotes angiogenic switch and progression to micrometastasis in RAF-driven murine lung cancer. *Cancer Cell*, 12(2):145–159, 2007.

[42] D A Chan and A J Giaccia. Hypoxia, gene expression, and metastasis. *Cancer Metast. Rev.*, 26:333–339, 2007.

[43] M A J Chaplain, S R McDougall, and A R A Anderson. Mathematical modeling of tumour-induced angiogenesis. *Annu. Rev. Biomed. Eng.*, 8:233–257, 2006.

[44] M A J Chaplain, G D Singh, and J C McLachlan, editors. *On Growth and Form: Spatio-temporal Pattern Formation in Biology*. Wiley-Blackwell, 2000.

[45] N Chaudary and R P Hill. Hypoxia and metastasis. *Clin. Cancer Res.*, 13:1947–1949, 2007.

[46] K-H Chen, P-Y Tung, J-C Wu, Y Chen, P-C Chen, S-H Huang, and S-M Wang. An acidic extracellular pH induces Src kinase-dependent loss of β-catenin from the adherens junction. *Cancer Lett.*, 267:37–48, 2008.

[47] Y Chen, C-H Chen, P-Y Tung, S-H Huang, and S-M Wang. An acidic extracellular pH disrupts adherens junctions in HepG2 cells by Src kinases-dependent modification of E-cadherin. *J. Cell. Biochem.*, 108:851–859, 2009.

[48] Y Chen, H-N Kung, C-H Chen, S-H Huang, K-H Chen, and S-M Wang. Acidic extracellular pH induces p120-catenin-mediated disruption of adherens junctions via the Src kinase-PKCd pathway. *FEBS Letters*, 585:705–710, 2011.

[49] Y Chiang, C Y Chou, K F Hsu, Y F Huang, and M R Shen. EGF upregulates Na^+/H^+ exchanger NHE1 by post-translational regulation that is important for cervical cancer cell invasiveness. *J. Cell. Physiol.*, 214:810–819, 2008.

[50] G L Chu and W C Dewey. The role of low intracellular or extracellular pH in sensitization to hyperthermia. *Radiat. Res.*, 114(1):154–167, 1988.

[51] C B Colen, Y Shen, F Ghoddoussi, P Yu, T B Francis, B J Koch, M D Monterey, M P Galloway, A E Sloan, and S P Mathupala. Metabolic targeting of lactate efflux by malignant glioma inhibits invasiveness and induces necrosis: An in vivo study1. *Neoplasia*, 13(7):620–632, 2011.

[52] C C Compton. Colorectal carcinoma: Diagnostic, prognostic, and molecular features. *Mod. Pathol.*, 16(4):376–388, 2003.

[53] C Crone and D G Levitt. Capillary permeability to small solutes. In E M Renkin and C C Michel, editors, *Handbook of Physiology: A critical, comprehensive presentation of physiological knowledge and concepts*, volume IV,

chapter 2: The Cardiovascular System, pages 414 and 434–437. Bethesda, ML: American Physiological Society, 1984.

[54] S Curran and G I Murray. Matrix metalloproteinases in tumour invasion and metastasis. *J. Pathol.*, 189(3):300–308, 1999.

[55] G D Dakubo. *Mitochondrial Genetics and Cancer*. Springer, 2010.

[56] K E de Visser, A Eichten, and L M Coussens. Paradoxical roles of the immune system during cancer development. *Nat. Rev. Cancer*, 6:24–37, 2006.

[57] S P Denker and D L Barber. Cell migration requires both ion translocation and cytoskeletal anchoring by the NaH exchanger NHE1. *J. Cell Biol.*, 159:1087–1096, 2002.

[58] W Düchting and T Vogelsaenger. Analysis, forecasting and control of three-dimensional tumor growth and treatment. *J. Med. Syst*, 8:461–475, 1984.

[59] M J Duffy. The role of proteolytic enzymes in cancer invasion and metastasis. *Clin. Exp. Metastas.*, 10:145–155, 1992.

[60] N A Epstein and L P Fatti. Prostatic carcinoma: Some morphological features affecting prognosis. *Cancer*, 37:2455–2465, 1976.

[61] G F Fasciglione, S Marini, S D'Alessio, V Politi, and M Coletta. pH- and temperature-dependence of functional modulation in metalloproteinases. A comparison between neutrophil collagenase and gelatinases A and B. *Biophys. J.*, 79:2138–2149, 2000.

[62] S C Ferreira, M L Martins, and M J Vilela. Reaction-diffusion model for the growth of avascular tumor. *Phys. Rev. E*, 65(021907):1–8, 2002.

[63] R C Fitzgerald, M B Omary, and George Triadafilopoulos. Acid modulation of HT29 cell growth and differentiation. *J. Cell Sci.*, 110(5):663–671, 1997.

[64] J Folkman and M Hochberg. Self-regulation of growth in three-dimensions. *J. Exp. Med.*, 138:745–753, 1973.

[65] M L Freeman, W C Dewey, and L E Hopwood. Effect of pH on hyperthermic cell survival. *J. Nati. Cancer Inst.*, 58:1837–1839, 1977.

[66] J P Freyer and R M Sutherland. Regulation of growth saturation and development of necrosis in EMT6/Ro multicellular spheroids by the glucose and oxygen supply. *Cancer Res.*, 46:3504–3512, 1986.

[67] J P Freyer, E Tustanoff, A J Franko, and R M Sutherland. In situ oxygen consumption rates of cells in V-79 multicellular spheroids during growth. *J. Cell. Physiol.*, 118:53–61, 1984.

[68] P Friedl, Y Hegerfeldt, and M Tusch. Collective cell migration in morphogenesis and cancer. *Int. J. Dev. Biol.*, 48:441–449, 2004.

[69] L B Gardner, Q Li, M S Park, W M Flanagan, G L Semenza, and C V Dang. Hypoxia inhibits G1\S transition through regulation of p27 expression. *J. Biol. Chem.*, 276(11):7919–7926, 2001.

[70] M Gardner. The fantastic combinations of john conway's new solitaire game "life". *Sci. Am.*, 223:120–123, 1970.

[71] R A Gatenby and E T Gawlinski. A reaction diffusion model of cancer invasion. *Cancer Res.*, 56:5745–5753, 1996.

[72] R A Gatenby and E T Gawlinski. The glycolytic phenotype in carcinogenesis and tumour invasion: insights through mathematical models. *Cancer Res.*, 63:3847–3854, 2003.

[73] R A Gatenby and R J Gillies. Why do cancers have high aerobic glycolysis? *Nature Rev.*, 4:891–899, 2004.

[74] R A Gatenby and R J Gillies. Glycolysis in cancer: a potential target for therapy. *Int. J. Biochem. Cell B.*, 39:1358–1366, 2007.

[75] R A Gatenby, K Smallbone, P K Maini, F Rose, J Averill, R B Nagle, L Worrall, and R J Gillies. Cellular adaptations to hypoxia and acidosis during somatic evolution of breast cancer. *Br. J. Cancer*, 97:646–653, 2007.

[76] M Gerhardt, H Schuster, and J J Tyson. A cellular automation model of excitable media including curvature and dispersion. *Science*, 247(4950):1563–1566, 1990.

[77] A Gerisch and M A J Chaplain. Mathematical modelling of cancer cell invasion of tissue: Local and non-local models and the effect of adhesion. *J. Theor. Biol.*, 250:684–704, 2008.

[78] P Gerlee and A R A Anderson. An evolutionary hybrid cellular automaton model of solid tumour growth. *J. Theor. Biol.*, 246(4):583–603, 2007.

[79] P Gerlee and A R A Anderson. A hybrid cellular automaton model of clonal evolution in cancer: the emergence of the glycolytic phenotype. *J. Theor. Biol.*, 250(4):705–722, 2008.

[80] L E Gerweck and B Richards. Influence of pH on the thermal sensitivity of cultured human glioblastoma cells. *Cancer Res.*, 41:845–849, 1981.

[81] L E Gerweck, S Vijayappa, and S Kozin. Tumour pH controls the *in vivo* efficacy of weak acid and base chemotherapeutics. *Mol. Cancer Ther.*, 5:1275–1279, 2005.

[82] G Giannelli, E Fransvea, F Marinosci, C Bergamini, S Colucci, O Schiraldi, and S Antonaci. Transforming growth factor-β_1 triggers hepatocellular carcinoma invasiveness via $\alpha_3\beta_1$ integrin. *Am. J. Pathol.*, 161:183–193, 2002.

[83] R J Gillies, Z Liu, and Z Bhujwalla. 31P-MRS measurements of extracellular pH of tumors using 3-aminopropylphosphonate. *Am. J. Physiol.*, 267(1):C195–C203, 1994.

[84] R J Gillies and R Martinez-Zaguilan. Regulation of intracellular pH in BALB/c 3T3 cells. *J. Biol. Chem.*, 226(3):1551–1556, 1991.

[85] R J Gillies, R Martinez-Zaguilan, EP Peterson, and R Perona. Role of intracellular pH in mammalian cell proliferation. *Cell Physiol. Biochem.*, 2:159–79, 1992.

[86] R J Gillies, N Raghunand, G S Karczmar, and Z M Bhujwalla. MRI of the tumor microenvironment. *J. Magn. Reson. Imaging*, 16:430–450, 2002.

[87] R J Gillies, I Robey, and R A Gatenby. Causes and consequences of increased glucose metabolism of cancers. *J. Nucl. Med.*, 49(Suppl 2):24S–42S, 2008.

[88] I Giusti, S D'Ascenzo, D Millimaggi, G Taraboletti, G Carta, N Franceschini, A Pavan, and V Dolo. Cathepsin B mediates the pH-dependent proinvasive activity of tumor-shed microvesicles. *Neoplasia*, 10(5):481–488, 2008.

[89] J A Glazier, A Balter, and N J Poplawski. Magnetization to morphogenesis: a brief history of the glazier-graner-hogeweg model. In A R A Anderson, M A J Chaplain, and K A Rejniak, editors, *Single-cell-based models in Biology and Medicine*. Birkhäuser Basel, 2007.

[90] K Glunde, S E Gugginoy, M Solaiyappan, A P Pathak, Y Ichikawaz, and Z M Bhujwalla. Extracellular acidification alters lysosomal trafficking in human breast cancer cells. *Neoplasia*, 5(6):533–545, 2003.

[91] F Graner and J A Glazier. Simulation of biological cell sorting using a two dimensional extended potts model. *Phys. Rev. Lett.*, 69:2013–2016, 1992.

[92] H P Greenspan. Models for the growth of a solid tumour by diffusion. *Stud. Appl. Math.*, 52:317–340, 1972.

[93] J R Griffiths. Are cancer cells acidic? *Br. J. Cancer*, 3(64):425–427, 1991.

[94] E Grillon, R Farion, K Fablet, M D Waard, C M Tse, M Donowitz, C Segebarth, C Rémy, and J A Coles. The spatial organization of proton and lactate transport in a rat brain tumor. *PloS ONE*, 6(2):1–9, 2011.

[95] P Gu, X Xing, M Tänzer, C Röcken, W Weichert, A Ivanauskas, M Pross, U Peitz, P Malfertheiner, R M Schmid, and M P Ebert. Frequent loss of TIMP-3 expression in progression of esophageal and gastric adenocarcinomas. *Neoplasia*, 10(6):563–572, 2008.

[96] S Günther, C Ruhe, M G Derikito, G Böse G, H Sauer, and M Wartenberg. Polyphenols prevent cell shedding from mouse mammary cancer spheroids and inhibit cancer cell invasion in confrontation cultures derived from embryonic stem cells. *Cancer Lett.*, 250(1):25–35, 2007.

[97] G P Gupta and J Massagu. Cancer metastasis: Building a framework. *Cell*, 127(4):679–695, 2006.

[98] G M Hahn and E C Shiu. Adaptation to low pH modifies thermal and thermochemical responses of mammaliar cells. *Int. J. Hyperthermia*, 2:379–387, 1986.

[99] A P Halestrap and D Meredith. The SLC16 gene family-from monocarboxylate transporters (MCTs) to aromatic amino acid transporters and beyond. *Pflug. Arch. Eur. J. Phy.*, 447:619–628, 2004.

[100] S Han, F R Khuri, and J Roman. Fibronectin stimulates non-small cell lung carcinoma cell growth through activation of Akt/mammalian target of rapamycin/S6 kinase and inactivation of LKB1/AMP-activated protein kinase signal pathways. *Cancer Res.*, 66(1):315–323, 2006.

[101] D Hanahan and R A Weinberg. The hallmarks of cancer. *Cell*, 100:57–70, 2000.

[102] S Harguindey, G Orive, J Luis Pedraz, A Paradiso, and S J Reshkin. The role of pH dynamics and the Na^+/ H^+ antiporter in the etiopathogenesis and treatment of cancer. two faces of the same coin—one single nature. *Biochim. Biophys. Acta*, 1756:1–24, 2005.

[103] G Helmlinger, A Sckell, M Dellian, N S Forbes, and R K Jain. Acid production in glycolysis-impaired tumors provides new insights into tumor metabolism. *Clin. Cancer Res.*, 8:1284–1291, 2002.

[104] T Henning, M Krausb, M Brischweina, A M Ottoa, and B Wolfa. Relevance of tumor microenvironment for progression, therapy and drug development (review). *Anti-Cancer Drugs*, 15:7–14, 2004.

[105] P W Hochachka and T P Mommsen. Protons and anaerobiosis. *Science*, 219:1391–1397, 1983.

[106] E V Holahan, P K Stuart, and W C Dewey. Enhancement of survival of CHO cells by acidic pH after X-irradiation. *Radiat. Res.*, 89:433–435, 1982.

[107] S M Hong, T M Pawlik, H Cho, B Aggarwal, M Goggins, R H Hruban, and R A Anders. Depth of tumor invasion better predicts prognosis than the current American joint committee on cancer T classification for distal bile duct carcinoma. *Surgery*, 146(2):250–257, 2009.

[108] J D Hood and D A Cheresh. Role of integrins in cell invasion and migration. *Nat. Rev. Cancer*, 2:91–100, 2002.

[109] S Humez, M Monet, F V Coppenolle, P Delcourt, and N Prevarskaya. The role of intracellular pH in cell growth arrest induced by ATP. *Am. J. Physiol. Cell Physiol.*, 287:C1733–C1746, 2003.

[110] H Izumi, T Torigoe, H Ishiguchi, H Uramoto, Y Yoshida, M Tanabe, T Ise, T Murakami, T Yoshida, M Nomoto, and K Kohno. Cellular pH regulators: potentially promising molecular targets for cancer chemotherapy. *Cancer Treat. Rev.*, 29:541–549, 2003.

[111] J R Jass, W S Atkin, J Cuzick, H J Bussey, B C Morson, J M Northover, and I P Todd. The grading of rectal cancer: historical perspectives and a multivariate analysis of 447 cases. *Histopathology*, 10(5):437–459, 1986.

[112] Y Jiang, J Pjesivac-Grbovic, C Cantrell, and J P Freyer. A multiscale model for avascular tumor growth. *Biophys. J.*, 89:3884–3894, 2005.

[113] F Kallinowski, G Tyler, W Mueller-Klieser, and P Vaupel. Growth-related changes of oxygen consumption rates of tumor cells grown in vitro and in vivo. *J. Cell. Physiol.*, 191:138–183, 1989.

[114] E Kaminskas. The pH-dependence of sugar-transport and glycolysis in cultured ehrlich ascites-tumour cells. *Biochem. J.*, 174(2):453–459, 1978.

[115] A R Kansal, S Torquato, G R I V Harsh, E A Chiocca, and T S Deisboeck. Simulated brain tumor growth dynamics using a three-dimensional cellular automaton. *J. Theor. Biol.*, 203(4):367–382, 2000.

[116] Y Kato, S Ozawa, M Tsukuda, E Kubota, K Miyazaki, Y St-Pierre, and R-I Hata. Acidic extracellular pH increases calcium influx-triggered phospholipase D activity along with acidic sphingomyelinase activation to induce matrix metalloproteinase-9 expression in mouse metastatic melanoma. *FEBS J.*, 274:3171–3183, 2007.

[117] D Katsumata, H Fukui, Y Ono, K Ichikawa, S Tomita, J Imura, A Abe, M Fujita, O Watanabe, M Tsubaki, M Sunagawa, and T Fujimori. Depth of tumor invasion in locally advanced rectal cancer correlates with patients'

prognosis: the usefulness of elastic stain for its measurement. *Surg. Today*, 38(2):115–122, 2008.

[118] K M Kennedy and M W Dewhirst. Tumor metabolism of lactate: the influence and therapeutic potential for MCT and CD147 regulation. *Future Oncol.*, 6:127–148, 2010.

[119] D Kirschner and J C Panetta. Modeling immunotherapy of the tumor-immune interaction. *J. Math. Biol.*, 37:235–252, 1998.

[120] L Kostakoglu, H Agress Jr, and S J Goldsmith. Clinical role of FDG PET in evaluation of cancer patients. *Radiographics*, 23:315–340, 2003.

[121] E M Kovacs, R G Ali, A J McCormack, and A S Yap. E-cadherin homophilic ligation directly signals through rac and phosphatidylinositol 3-kinase to regulate adhesive contacts. *J. Biol. Chem.*, 277:6708–6718, 2002.

[122] M Kunkel, T E Reichert, P Benz, H A Lehr, J H Jeong, S Wieand, P Bartenstein, W Wagner, and T L Whiteside. Overexpression of glut-1 and increased glucose metabolism in tumors are associated with a poor prognosis in patients with oral squamous cell carcinoma. *Cancer*, 97(4):1015–1024, 2003.

[123] D Lagadic-Gossmann, L Huc, and V Lecureur. Alterations of intracellular pH homeostasis in apoptosis: origins and roles. *Cell Death Differ.*, 11:953–961, 2004.

[124] E Lartigau, H Randrianarivelo, M F Avril, A Margulis, A Spatz, F Eschwege, and M Guichard. Intratumoral oxygen tension in metastatic melanoma. *Melanoma Res.*, 7:400–406, 1997.

[125] E Lawrence. *A Guide to Modern Biology: Genetics, Cells and Systems*. Addison-Wesley Longman Ltd, 1989.

[126] X Li, J Regezi, F P Ross, S Blystone S, D Ilic, S P Leong, and D M Ramos. Integrin $\alpha_v\beta_3$ mediates K1735 murine melanoma cell motility *in vivo* and *in vitro*. *J. Cell Sci.*, 114:2665–2672, 2001.

[127] D R Lide. *Handbook of Chemistry*. Boca Raton, FL:CRC Press, 74 edition, 1994.

[128] H S Lim, W Yoon, T W Chung, J K Kim, J G Park, H K Kang, H S Bom, and J H Yoon. FDG PET/CT for the detection and evaluation of breast diseases: Usefulness and limitations. *Radiographics*, 27:S197–S213, 2007.

[129] L A Liotta and W G Stetler-Stevenson. Tumor invasion and metastasis: An imbalance of positive and negative regulation. *Cancer Res.*, 51(18 Suppl.):5054s–5059s, 1991.

[130] C-M Liu, Y-M Lin, K-T Yeh, M-K Chen, J-H Chang, C-J Chen, M-Y Chou, S-F Yang, and M-H Chien. Expression of carbonic anhydrases I II and the correlation to clinical aspects of oral squamous cell carcinoma analyzed using tissue microarray. *J. Oral Pathol. Med.*, pages 1–7, 2012.

[131] H Lodish, A Berk, S L Zipursky, P Matsudaira, D Baltimore, and J E Darnell. *Molecular Cell Biology*. W. H. freeman, New York, 4th edition, 2008.

[132] J S Lowengrub, H B Frieboes, F Jin, Y-L Chuang, X Li, P Macklin, S M Wise, and V Cristini. Nonlinear modelling of cancer: bridging the gap between cells and tumours. *Nonlinearity*, 23:R1–R91, 2010.

[133] H Lu, C L Dalgard, A Mohyeldin, T McFate, A S Tait, and A Verma A. Reversible inactivation of HIF-1 prolyl hydroxylases allows cell metabolism to control basal HIF-1. *J. Biol. Chem.*, 280:41928–41939, 2005.

[134] H Lu, R A Forbes, and A Verma. Hypoxia-inducible factor 1 activation by aerobic glycolysis implicates the Warburg effect in carcinogenesis. *J. Biol. Chem.*, 277:23111–23115, 2002.

[135] C G Mackenzie, J B Mackenzie, and P Beck. The effect of pH on growth, protein synthesis, and lipid-rich particles of cultured mammalian cells. *J. Biophys. Biochem. Cytol.*, 9(1):141–156, 1961.

[136] P Macklin and J Lowengrub. Nonlinear simulation of the effect of microenvironment on tumor growth. *J. Theor. Biol.*, 245(4):677–704, 2007.

[137] I H Madshus. Regulation of intracellular pH in eukaryotic cells. *Biochem. J.*, 250:1–8, 1988.

[138] N V Mantzaris, S D Webb, and H G Othmer. Mathematical modeling of tumor-induced angiogenesis. *J. Math. Biol.*, 49(2):111–187, 2004.

[139] C Martin, S F Pedersen, A Schwab, and C Stock. Intracellular pH gradients in migrating cells. *Am. J. Physiol. Cell Physiol.*, 300:C490–C495, 2011.

[140] G R Martin and R K Jain. Non invasive measurement of interstitial pH profile in normal and neoplastic tissue using fluorescent ration imaging microscopy. *Cancer Res.*, 54:5670–5674, 1999.

[141] N K Martin, E A Gaffney, R A Gatenby, and P K Maini. Leaky vessels as a potential source of stromal acidification in tumours. *J. Theor. Biol.*, 267(3):454–460, 2010.

[142] R Martinez-Zaguilan, E A Seftor, R E Seftor, Y W Chu, R J Gillies, and M J Hendrix. Acidic pH enhances the invasive behaviour of human melanoma cells. *Clin. Exp. Metastas.*, 14(2):176–186, 1996.

[143] S Matsuyama, J Llopis, Q L Deveraux, R Y Tsien, and J C Reed. Changes in intramitochondrial and cytosolic pH: early events that modulate caspase activation during apoptosis. *Nat. Cell Biol.*, 2(6):318–325, 2000.

[144] J C McDermott and A Bonen. Lactate transport by skeletal muscle sarcolemmal vesicles. *Mol. Cell. Biochem.*, 122(2):113–121, 1993.

[145] D M McDonald and P Baluk. Significance of blood vessel leakiness in cancer. *Cancer Res.*, 62:5381–5385, 2002.

[146] S R McDougall, A R A Anderson, and M A J Chaplain. Mathematical modelling of dynamic adaptive tumour-induced angiogenesis: clinical implications and therapeutic targeting strategies. *J. Theor. Biol.*, 241(3):564–589, 2006.

[147] L A McLean, J Roscoe, N K Jorgensen, F A Gorin, and P M Cala. Malignant gliomas display altered pH regulation by NHE1 compared with nontransformed astrocytes. *Am. J. Physiol. Cell Physiol.*, 278:C676–C688, 2000.

[148] N U Meldrum and F J W Roughton. Carbonic anhydrase:its preparation and properties. *J. Physiol.*, 80:113–141, 1933.

[149] P Mellergard, Y Ou-Yang, and B K Siesjo. Relationship between intra- and extracellular pH in primary cultures of rat astrocytes. *Am. J. Physiol. Cell Physiol.*, 267(2):C581–C589, 1994.

[150] N Metropolis and S Ulam. The Monte Carlo method. *J. Am. Stat. Assoc.*, 44:335–341, 1949.

[151] S Missailidis. *Anticancer Therapeutics*. Wiley-Blackwell, 2008.

[152] B Movsas, J D Chapman, A L Hanlon, E M Horwitz, R E Greenberg, C Stobbe, G E Hanks, and A Pollack. Hypoxic prostate/muscle pO2 ratio predicts for biochemical failure in patients with prostate cancer: Preliminary findings. *Urology*, 60:634–639, 2002.

[153] S Mukherjee. *The Emperor of All Maladies: A Biography of Cancer*. Thorndike Press, 2012.

[154] G Murphy and J Gavrilovic. Proteolysis and cell migration: creating a path? *Curr. Opin. Cell Biol.*, 11:614–621, 1999.

[155] G Murray, M Duncan, E Arbuckle, W Melvin, and J Fothergill. Matrix metalloproteinases and their inhibitors in gastric cancer. *Gut*, 43(6):791–797, 1998.

[156] H Nagase, R Visse, and G Murphy. Structure and function of matrix metalloproteinases and TIMPs. *Cardiovasc. Res.*, 69:562–573, 2006.

[157] S Negrini, V G Gorgoulis, and T D Halazonetis. Genomic instability–an evolving hallmark of cancer. *Nat. Rev. Mol. Cell. Bio.*, 11:220–228, 2010.

[158] A A Neville. *Biomedical Modelling incorporating growth.* PhD thesis, University of Nottingham, 2003.

[159] K Newell, A Franchi, J Pouysségur, and I Tannock. Studies with glycolysis-deficient cells suggest that production of lactic acid is not the only cause of tumor acidity. *Proc. Natl. Acad. Sci.*, 90(3):1127–1131, 1993.

[160] P Nyberg, T Salo, and R Kalluri. Tumor microenvironment and angiogenesis. *Front Biosci.*, 1(13):6537–6553, 2008.

[161] S Oliferenko, T G Chew, and M K Balasubramanian. Positioning cytokinesis. *Gene Dev.*, 23:660–674, 2009.

[162] A R Oller, C W Buser, M A Tyo, and W G Thilly. Growth of mammalian cells at high oxygen concentrations. *J. Cell Sci.*, 94(1):43–49, 1989.

[163] M Ono, M Sakamoto, Y Ino, Y Moriya, K Sugihara, T Muto, and S Hirohashi. Cancer cell morphology at the invasive front and expression of cell adhesion-related carbohydrate in the primary lesion of patients with colorectal carcinoma with liver metastasis. *Cancer*, 78(6):1179–1186, 1996.

[164] M R Owen, H M Byrne, and C E Lewis. Mathematical modelling of the use of macrophages as vehicles for drug delivery to hypoxic tumour sites. *J. Theor. Biol.*, 226:377–391, 2004.

[165] K J Painter, N J Armstrong, and J A Sherratt. The impact of adhesion on cellular invasion processes in cancer and development. *J. Theor. Biol.*, 264(3):1057–1067, 2010.

[166] R K Paradise, D A Lauffenburger, and K J V Vliet. Acidic extracellular pH promotes activation of integrin $\alpha_v\beta_3$. *PLoS ONE*, 6(1):e15746, 2010.

[167] H J Park. Effects of intracellular pH on apoptosis in HL-60 human leukemia cells. *Yonsei Med. J.*, 36(6):473–479, 1995.

[168] C S Parkins, M R L Stratford, M F Dennis, M Stubbs, and D J Chaplin. The relationship between extracellular lactate and tumour pH in a murine tumour model of ischaemia-reperfusion. *Brit. J. Cancer*, 75(3):319–323, 1997.

[169] S Parkkila, H Rajaniemi, A Parkkila, J Kivelä, A Waheed, S Pastoreková, J Pastorek, and W S Sly. Carbonic anhydrase inhibitor suppresses invasion of renal cancer cells *in vitro*. *Proc. Natl. Acad. Sci. USA*, 97(5):2220–2224, 2000.

[170] A A Patel, E T Gawlinski, S K Lemieux, and R A Gatenby. A cellular automaton model of early tumor growth and invasion. *J. Theor. Biol.*, 213:315–331, 2001.

[171] C J Pennycuick. *Conversion Factors: S.I. Units and Many Others*. University of Chicago Press, 19 edition, 1988.

[172] S A Peralta, K A Knudsen, M C Jaurand, K R Johnson, M J Wheelock, A J Klein-Szanto, and H Salazar. The differential expression of N-cadherin and E-cadherin distinguishes pleural mesotheliomas from lung adenocarcinomas. *Hum. Pathol.*, 26:1363–1369, 1995.

[173] S A Peralta, K A Knudsen, A Tecson-Miguel, F X McBrearty, A C Han, and H Salazar. Expression of E-cadherin and N-cadherin in surface epithelial-stromal tumors of the ovary distinguishes mucinous from serous and endometrioid tumors. *Hum. Pathol.*, 28:734–739, 1997.

[174] L Petruzzelli, M Takami, and H D Humes. Structure and function of cell adhesion molecules. *Am. J. Med.*, 106(4):467–476, 1999.

[175] C Pinheiro, A Longatto-Filho, L Ferreira, S M Pereira, D Etlinger, M A Moreira, L F Jubé, G S Queiroz, F Schmitt, and F Baltazar. Increasing expression of monocarboxylate transporters 1 and 4 along progression to invasive cervical carcinoma. *Int. J. Gynecol. Pathol.*, 27:568–574, 2008.

[176] C Pinheiro, A Longatto-Filho, C Scapulatempo, L Ferreira, S Martins, L Pellerin, M Rodrigues, V A Alves, F Schmitt, and F Baltazar. Increased expression of monocarboxylate transporters 1, 2, and 4 in colorectal carcinomas. *Virchows Arch.*, 452:139–146, 2008.

[177] N J Poplawski, U Agero, J S Gens, M Swat, J A Glazier, and A R A Anderson. Front instabilities and invasiveness of simulated avascular tumors. *B. Math. Biol.*, 71:1189–1227, 2009.

[178] C M Porth. *Pathophysiology: concepts of altered health states*. Lippincott company, Pennsylvania, 4th edition, 1995.

[179] J Pouysségur, F Dayan, and NM Mazure. Hypoxia signalling in cancer and approaches to enforce tumour regression. *Nature*, 441(13):437–443, 2006.

[180] J Pouysségur, A Franchi, G L'Akmain, and S Paris. Cytoplasmic pH, a key determinant of growth factor-induced DNA synthesis in quiescent fibroblasts. *Federation of European Biochemical Societies*, 190(1):115–119, 1985.

[181] G C Powathil, K E Gordon, L A Hill, and M A J Chaplain. Modelling the effects of cell-cycle heterogeneity on the response of a solid tumour to

chemotherapy: biological insights from a hybrid multiscale cellular automaton model. *J. Theor. Biol.*, 308:1–19, 2012.

[182] L Preziosi, editor. *Cancer Modelling and Simulation*. Chapman & Hall/CRC Mathematical & Computational Biology, 2003.

[183] P Provent, M Benito, B Hiba, R Farion, P López-Larrubia, P Ballesteros, C Rémy, C Segebarth, S Cerdán, J A Coles, and M L García-Martín. Serial *In vivo* spectroscopic nuclear magnetic resonance imaging of lactate and extracellular pH in rat gilomas shows redistribution of protons away from sites of glycolysis. *Cancer Res.*, 67(16):7638–7645, 2007.

[184] L K Putney and D L Barber. Na-H exchange-dependent increase in intracellular pH times G2/M entry and transition. *J. Biol. Chem.*, 278(45):44645–4469, 2003.

[185] V Quennet, A Yaromina, D Zips, A Rosner, S Walenta, M Baumann, and W Mueller-Kliesera. Tumor lactate content predicts for response to fractionated irradiation of human squamous cell carcinomas in nude mice. *Radiother. Oncol.*, 81(2):130–135, 2006.

[186] N Raghunand. pH and chemotherapy and drug resistance in tumours. *Drug Resist. Update*, 3:39–47, 2000.

[187] N Raghunand, R A Gatenby, and R J Gillies. Microenvironmental and cellular consequences of altered blood flow in tumours. *Br. J. Radiol.*, 76:S11–S22, 2003.

[188] I Ramis-Conde, M A J Chaplain, and A R A Anderson. Mathematical modelling of cancer cell invasion of tissue. *Math. Comp. Mod.*, 47:533–545, 2008.

[189] I Ramis-Conde, M A J Chaplain, A R A Anderson, and D Drasdo. Multi-scale modelling of cancer cell intravasation: the role of cadherins in metastasis. *Phys. Biol.*, 6(1):016008 (12pp), 2009.

[190] I Ramis-Conde, D Drasdo, M A J Chaplain, and A R A Anderson. Modelling the influence of the E-Cadherin-β-catenin pathway in cancer cell invasion and tissue architecture: A multi-scale approach. *Biophys. J.*, 95(155–165), 2008.

[191] R Rathinam and S K Alahari. Important role of integrins in the cancer biology. *Cancer Metast. Rev.*, 29(1):223–237, 2010.

[192] J C Reed. Dysregulation of apoptosis in cancer. *J. Clin. Oncol.*, 17(9):2941–2953, 1999.

[193] K A Rejniak. A single-cell approach in modeling the dynamics of tumor microregions. *Math. Biosci. Eng.*, 2(3), 2005.

[194] T Y Reynolds, S Rockwell, and P M Glazer. Genetic instability induced by the tumor microenvironment. *Cancer Res.*, 56:5754–5757, 1996.

[195] E K Rofstad, B Mathiesen, K Kindem, and K Galappathi. Acidic extracellular pH promotes experimental metastasis of human melanoma cells in athymic nude mice. *Cancer Res.*, 66(13):6699–6707, 2006.

[196] M. F. Romero. In the beginning, there was the cell: cellular homeostasis. *Adv. Physiol. Educ.*, 28:135–138, 2004.

[197] T Roose, S J Chapman, and P K Maini. Mathematical models of avascular tumor growth. *SIAM Rev.*, 49(2):179–208, 2007.

[198] E M Rottinger and M Mendonca. Radioresistance secondary to low pH in human glial cells and Chinese hamster ovary cells. *Int. J. Radiat. Oncol. Biol. Phys.*, 8:1309–1314, 1982.

[199] J Rozhin, M Sameni, G Ziegler, and B F Sloane. Pericellular pH affects distribution and secretion of cathepsin B in malignant cells. *Cancer Res.*, 54(24):6517–6525, 1994.

[200] B M Rubenstein and L J Kaufman. The role of extracellular matrix in glioma invasion: a cellular potts model approach. *Biophys. J.*, 95:5661–5680, 2008.

[201] R J Ruch, J E Klaunig, GA Kerckaert, and R A LeBoeuf. Modification of gap junctional intercellular communication by changes in extracellular pH in Syrian hamster embryo cells. *Carcinogenesis*, 11(6):909–913, 1990.

[202] A M Saleh, G Rombola, and C Batlle. Intracellular H^+ buffering power and its dependency on intracellular pH. *Kidney Int.*, 39:282–288, 1991.

[203] N J Savill and P Hogeweg. Modelling morphogenesis: From single cells to crawling slugs. *J. Theor. Biol.*, 184:229–235, 1997.

[204] O Schmalhofer, S Brabletz, and T Brabletz. E-cadherin, beta-catenin, and ZEB1 in malignant progression of cancer. *Cancer Metast. Rev.*, 28:151–166, 2009.

[205] M Schmitt, F Janicke, N Moniwa, L Chucholowski, H Pache, and H Graeff. Tumor-associated urokinase-type plasminogen activator: Biological and clinical significance. *Biol. Chem. H-S*, 373:611–622, 1992.

[206] W Schumer. Cell metabolism and lactate. In H Bossart and C Perret, editors, *Lactate in Acute Conditions International Symposium*, pages 1–9. Basel, 1978.

[207] G Schwickert, S Walenta, K Sundfør, E K Rofstad, and W Mueller-Kliesera. Correlation of high lactate levels in human cervical cancer with incidence of metastasis. *Cancer Res.*, 55:4757–4759, 1995.

[208] J A Sherratt, B T Eagan, and M A Lewis. Oscillations and chaos behind predator-prey invasion: mathematical artifact or ecological reality? *Phil. Trans. R. Soc. Lond. B*, 352:21–38, 1997.

[209] J M Shipley, R L Wesselschmidt, D K Kobayashi, T J Ley, and S D Shapiro. Metalloelastase is required for macrophage-mediated proteolysis and matrix invasion in mice. *Proc. Natl. Acad. Sci. USA*, 93:3942–3946, 1996.

[210] A Shirinifard, J S Gens, B L Zaitlen, N J Popławski, M Swat, and J A Glazier. 3D multi-cell simulation of tumor growth and angiogenesis. *PLoS ONE*, 4(10):e7190, 2009.

[211] E Skrzydlewska, M Sulkowska, M Koda, and S Sulkowski. Proteolytic-antiproteolytic balance and its regulation in carcinogenesis. *World J. Gastroenterol.*, 11(9):1251–1266, 2005.

[212] K Smallbone, R A Gatenby, R J Gillies, P K Maini, and D J Gavaghan. Metabolic changes during carcinogenesis: Potential impact on invasiveness. *J. Theor. Biol.*, 244:703–713, 2007.

[213] K Smallbone, R A Gatenby, and P K Maini. Mathematical modelling of tumour acidity. *J. Theor. Biol.*, 255:106–112, 2008.

[214] K Smallbone, D J Gavaghan, R A Gatenby, and P K Maini. The role of acidity in solid tumour growth and invasion. *J. Theor. Biol.*, 235:476–484, 2005.

[215] P Sonveaux, T Copetti, C J De Saedeleer, F Vegran, J Verrax, K M Kennedy, E J Moon, S Dhup, P Danhier, Francoise Frerart, B Gallez, A Ribeiro, C Michiels, M W Dewhirst, and O Feron. Targeting the lactate transporter MCT1 in endothelial cells inhibits lactate-induced HIF-1 activation and tumor angiogenesis. *PLoS ONE*, 7(3):e33418, 2012.

[216] P Sonveaux, F Vegran, T Schroeder, M C Wergin, J Verrax, Z N Rabbani, C J De Saedeleer, K M Kennedy, C Diepart, B F Jordan, M J Kelley, B Gallez, M L Wahl, O Feron, and M W Dewhirst. Targeting lactate-fueled respiration selectively kills hypoxic tumor cells in mice. *J. Clin. Invest.*, 118(12):3930–3942, 2008.

[217] M S Steinberg and R A Foty. Intercellular adhesions as determinants of tissue assembly and malignant invasion. *J. Cell Physiol.*, 173:135–139, 1997.

[218] C Stock, B Gassner, C R Hauck, H Arnold, S Mally, J A Eble, P Dieterich, and A Schwab. Migration of human melanoma cells depends on extracellular pH and Na^+/H^+ exchange. *J. Physiol.*, 567:225–238, 2005.

[219] E L Stott and N F Britton. Stochastic simulation of benign avascular tumour growth using the Potts Model. *Math. Comput. Model.*, 30:183–198, 1999.

[220] M Stubbs, P M J McSheehy, J R Griffiths, and C L Bashford. Causes and consequences of acidity in tumours: A magnetic resonance study. *Advan. Enzyme Regul.*, 39:13–30, 1999.

[221] M Stubbs, L Rodrigues, F A Howe, J Wang, K-S Jeong, R L Veech, and J R Griffiths. Metabolic consequences of a reversed pH gradient in rat tumors. *Cancer Res.*, 54:4011–4016, 1994.

[222] L Stüwe, M Müller, A Fabian, J Waning, S Mally, J Noël, A Schwab, and C Stock. pH dependence of melanoma cell migration: protons extruded by NHE1 dominate protons of the bulk solution. *J. Physiol.*, 585:351–360, 2007.

[223] P Swietach, R D Vaughan-Jones, and A L Harris. Regulation of tumor pH and the role of carbonic anhydrase 9. *Cancer Metast. Rev.*, 26:299–310, 2007.

[224] P Swietach, S Wigfield, P Cobden, C T Supuran, A L Harris, and R D Vaughan-Jones. Tumour-associated carbonic anhydrase 9 spatially co-

ordinates intracellular pH in three-dimensional multicellular growths. *J. Biol. Chem.*, 283(29):20473–20483, 2008.

[225] D E B Swinson, J L Jones, D Richardson, C Wykoff, H Turley, J Pastorek, N Taub, A L Harris, and K J O'Byrne. Carbonic anhydrase IX expression, a novel surrogate marker of tumor hypoxia, is associated with a poor prognosis in non-small-cell lung cancer. *J. Clin. Oncol.*, 21:473–482, 2003.

[226] I F Tannock and D Rotin. Acid pH in tumours and its potenial for therapeutic exploitation. *Cancer Res.*, 49:4373–4384, 1989.

[227] R H Thomlinson. Hypoxia and tumours. *J. clin. Path.*, 11:105–113, 1977.

[228] R H Thomlinson and L H Gray. The histological structure of some human lung cancers and the possible implications for radiotherapy. *Br. J. Cancer*, 4:539–549, 1955.

[229] L Tomes, E Emberley, Y Niu, S Troup, J Pastorek, K Strange, A Harris, and P H Watson. Necrosis and hypoxia in invasive breast carcinoma. *Breast Cancer Res. Treat.*, 81:61–69, 2003.

[230] G M Tozer, R J Maxwell, J R Griffiths, and P Pham. Modification of the 31P magnetic resonance spectra of a rat tumour using vasodilators and its relationship to hypotension. *Br. J. Cancer*, 62(4):553–560, 1990.

[231] O Trédan, C M Galmarini, K Patel, and I F Tannock. Drug resistance and the solid tumour microenvironment review. *J. Natl. Cancer Inst.*, 99:1441–1454, 2007.

[232] C Tu, C F Ortega-Cava, G Chen, N D Fernandes, D Cavallo-Medved, B F Sloane, V Band, and H Band. Lysosomal Cathepsin B participates in the podosome-mediated extracellular matrix degradation and invasion via secreted lysosomes in v-Src fibroblasts. *Cancer Res.*, 68(22):9147–9156, 2008.

[233] S Turner and J A Sherratt. Intercellular adhesion and cancer invasion: A discrete simulation using the extended Potts model. *J. Theor. Biol.*, 216:85–100, 2002.

[234] S Turner, J A Sherratt, and D Cameron. Tamoxifen treatment failure in cancer and the nonlinear dynamics of TGFb. *J. Theor. Biol.*, 229:101–111, 2004.

[235] J W van der Stappen, A C Williams, R A Maciewicz, and C Paraskeva. Activation of cathepsin B, secreted by a colorectal cancer cell line requires low pH and is mediated by cathepsin D. *Int. J. Cancer*, 67:547–554, 1996.

[236] P Vaupel, F Kallinowski, and P Okunieff. Blood flow, oxygen and nutrient supply, and metabolic microenvironment of human tumors. *Cancer Res.*, 49(23):6449–6465, 1989.

[237] F Vegran, R Boidot, C Michiels, P Sonveaux, and O Feron. Lactate influx through the endothelial cell monocarboxylate transporter MCT1 supports an NF-kappaB/IL-8 pathway that drives tumor angiogenesis. *Cancer Res.*, 71:2550–2560, 2011.

[238] R Venkatasubramanian, M A Henson, and N S Forbes. Incorporating energy metabolism into a growth model of multicellular tumor spheroids. *J. Theor. Biol.*, 242:440–453, 2006.

[239] R E Verdun and J Karlseder. Replication and protection of telomeres. *Nature*, 447(7147):924–931, 2007.

[240] K C Vinnakota and D A Beard. Kinetic analysis and design of experiments to identify the catalytic mechanism of the monocarboxylate transporter isoforms 4 and 1. *Biophys. J.*, 100:369–380, 2011.

[241] K Vleminckx, L Jr Vakaet L, M Mareel M, W Fiers, and F van Roy. Genetic manipulation of E-cadherin expression by epithelial tumor cells reveals an invasion supressor role. *Cell*, 66:107–119, 1991.

[242] J von Neumann. *Theory of Self-Replicating Automata*. University of Illinois Press, 1966.

[243] P R Wachsberger, J Landry, and C Storck. Mammalian cells adapted to growth at pH 6.7 have eleveted HSP27 levels and are resistant to cisplatin. *Int. J. Hyperther.*, 13:251–255, 1997.

[244] M L Wahl, J A Owen, R Burd, R A Herlands, S S Nogami, U Rodeck, D Berd, D B Leeper, and C S Owen. Regulation of intracellular pH in human melanoma: Potential therapeutic implications. *Mol. Cancer. Ther.*, 1:617–628, 2002.

[245] S Walenta, A. Salameh, H. Lyng, J. F. Evensen, M. Mitze, E. K. Rofstad, and W. Mueller-Klieser. Correlation of high lactate levels in head and neck tumors with incidence of metastasis. *Am. J. Pathol.*, 150(2):409–415, 1997.

[246] S Walenta, M Wetterling, M Lehrke, G Schwickert, K Sundfør, E K Rofstad, and W Mueller-Kliesera. High lactate levels predict likelihood of metastasis, tumor recurrence, and restricted patient survival in human cervical cancers. *Cancer Res.*, 16(4):916–921, 2000.

[247] O Warburg, F Wind, and E Negelein. The metabolism of tumours in the body. *J. Gen. Physiol.*, 8(6):519–530, 1926.

[248] B A Webb, M Chimenti, M P Jacobson, and D L Barber. Dysregulated pH: a perfect storm for cancer progression. *Nat. Rev. Cancer*, 11(9):671–700, 2011.

[249] S D Webb, J A Sherratt, and R G Fish. Alterations in proteolytic activity at low pH and its association with invasion: A theoretical model. *Clin. Exp. Metastas.*, 17:397–407, 1999.

[250] S D Webb, J A Sherratt, and R G Fish. Mathematical modelling of tumour acidity: Regulation of intracellular pH. *J. Theor. Biol.*, 196:237–250, 1999.

[251] J L Wike-Hooley, J Haveman, and H S Reinhold. The relevance of tumour pH to the treatment of malignant disease. *Radiother. Oncol.*, 2(4):343–366, 1984.

[252] N C Wong, B M Mueller, C F Barbas, P Ruminski, V Quaranta, E C Lin, and J W Smith. α_v integrins mediate adhesion and migration of breast carcinoma cell lines. *Clin. Exp. Metastas.*, 16:50–61, 1998.

[253] J K L Woodward, I Holen, E R Coleman, and D J Buttle. The roles of proteolytic enzymes in the development of tumour-induced bone disease in breast and prostate cancer. *Bone*, 41:912–927, 2007.

[254] M Yamagata, K Hasuda, T Stamato, and I F Tannock. The contribution of lactic acid to acidification of tumours: Studies of variant cells lacking lactate dehydrogenase. *Br. J. Cancer.*, 77:1726–1731, 1998.

[255] D T Yamaguchi, J T Huang, and D Ma. Regulation of gap junction intercellular communication by pH in MC3T3-E1 osteoblastic cells. *J. Bone Miner. Res.*, 10(12):1891–1900, 1995.

[256] X Yu and L M Machesky. Cells assemble invadopodia-like structures and invade into matrigel in a matrix metalloprotease dependent manner in the circular invasion assay. *PLoS ONE*, 7(2):e30605, 2012.

[257] J Yuan and P M Glazer. Mutagenesis induced by the tumor microenvironment. *Mutat. Res.*, 400:439–446, 1998.

[258] J Yuan, L Narayanan, S Rockwell, and P M Glazer. Diminished DNA repair and elevated mutagenesis in mammalian cells exposed to hypoxia and low pH. *Cancer Res.*, 60:4372–4376, 2000.

[259] X Zhang, C-G Li, C-H Ye, and M-L Liu. Determination of molecular self-diffusion coefficient using multiple spin-echo NMR spectroscopy with removal of convection and background gradient artifacts. *Anal. Chem.*, 73:3528–3534, 2001.

[260] X Zhang, Y Lin, and R J Gillies. Tumor pH and its measurement. *J. Nucl. Med.*, 51:1167–1170, 2010.

[261] D Q Zheng, A S Woodard, M Fornaro M, G Tallini, and L R Languino. Prostatic carcinoma cell migration via $\alpha_v\beta_3$ integrin is modulated by a focal adhesion kinase pathway. *Cancer Res.*, 59:1655–1664, 1999.

[262] W-X Zong and C B Thompson. Necrotic death as a cell fate. *Genes Dev.*, 20:1–15, 2006.